The control of metal-silicon carbide contacts using a silicon interlayer.

Lee, Wai Yee

PhD Thesis

The Control of Metal-Silicon Carbide Contacts Using a Silicon Interlayer

By

Wai Yee Lee

May 2004

A thesis submitted for the degree of Doctor of Philosophy

University of Wales Swansea
School of Engineering
Electronic and Electrical Engineering
Singleton Park, Swansea SA2 8PP
United Kingdom

ProQuest LLC.
789 East Eisenhower Parkway
P.O. Box 1346
Ann Arbor, MI 48106 – 1346

Declaration

This work has not previously been accepted in substance for any degree and is not being concurrently submitted in candidate for any degree.

Signed: .. ... (Candidate)

The work contained in this thesis, other than where stated within, is the result of the candidate's own investigation, performed under the guidance of the director of studies named below.

Signed: .... (Candidate)

Signed: ..... (Director of studies)

Date: 19 MAY 2009

Statement 1

This thesis is the result of my own investigations, except where otherwise stated. Other sources are acknowledged by footnotes giving explicit references. A bibliography is appended.

Signed: .. (Candidate)

Date: 19 MAY 2004

Statement 2

I hereby give my consent for my thesis, if accepted, to be available for photocopying and for inter-library loan, and for the title and summary to be made available to outside organisations.

Signed: ..... (Candidate)

Date: 19 MAY 2004

Acknowledgements

Firstly, I would like to express my gratitude to my supervisor, Prof. Stephen P. Wilks for giving me the opportunity to study in the Semiconductor Interface Laboratory and his support and guidance throughout the course of my study. My gratitude is extended to Dr. Thierry G. G. Maffies, Dr. Vincent Teng, Mr. Mark A. Pritchard and all my colleagues in the SIL lab for their support and assistance during the course of my research. Also, I would like to thank the guys from the Power Electronics group, in particular Dr. Gareth Pope and Dr. Guy Owen for all the discussion and assistance during my experiments.

A special thanks and appreciation to my beloved family, especially my parents, brothers and sister, for their enduring love and emotional encouragement. Nothing would have been done without their support.

Acknowledgements are also made to the Department of Electronic and Electrical Engineering grant EED165 and International Office grant IOH100 for its financial support for my tuition fees throughout the course of my research.

Abstract

The effect of Si interlayers within Ni-SiC contacts was studied using X-ray photoelectron spectroscopy (XPS), low energy electron diffraction (LEED) and scanning tunnelling microscopy (STM). Firstly an atomically clean surface was successfully obtained by depositing a 40Å layer of Si onto the SiC surface, followed by an immediate anneal at 1000°C to re-evaporate the Si and remove surface contaminants. The interlayer was formed in ultra-high vacuum (UHV) conditions by depositing a known thickness of Si onto the clean SiC surface at room temperature. The metal contact was then produced by a sequential deposition of various Ni thicknesses onto the interlayer so that contact formation could be accurately monitored. These contacts were then annealed sequentially from 400°C to 1200°C. At each stage the process was characterised by XPS. Si interlayer thicknesses of 20Å, 40Å and 60Å were tested. Results show that the consumption of Si atoms occurs, either from the Si interlayer or from the bulk SiC, with the evolution of Ni silicides and a Ni-Si-C ternary compound. In addition, chemical shifts associated with the formation of silicides and Fermi shifts (indicative of surface band bending) were also observed. When annealed at temperatures up to 1000°C, rapid formation of silicides is observed in the Si spectra, whilst the C spectra consisted of only bulk C and a small amount of free C. Conversely, for the Ni-SiC interface without a Si interlayer, the C spectra consisted of large amount of free C and hydrocarbon. As a result of annealing the interlayer samples, chemical shifts were observed as well as downward band bending, indicative of barrier lowering and complimentary to the generation of an Ohmic contact at these elevated temperatures. At 1200°C, all silicides had been re-evaporated leaving a carbon-rich surface, plus the formation of graphite on the surface.

The electrical properties of the Ni-SiC contacts with and without Si interlayer were assessed using current-voltage (I/V) measurements. The contacts with a Si interlayer exhibit various behaviour from Schottky to Ohmic depending on the thickness of the Si interlayer. An Ohmic contact, which required no annealing was obtained when using a thick Si interlayer of 60Å. However, Ni-Si-SiC Schottky contacts formed with 20Å and 40Å thick Si interlayers were shown to be able to operate, with Schottky barriers of ~1.7eV, up to 400°C higher than the normal Ni-SiC contact, indicating the superior control of these interfaces when Si is used as an interlayer.

Table of Contents

Chapter 1

Introduction

1.1 Introduction

The research on semiconductor materials had propagated rapidly since its invention due to the enormous demand in electronics industry. Up to date, the semiconductor industry had been dominated by silicon (Si) for its superior properties and its wide availability. Vast research and investigation on Si has been conducted, leading towards a detailed literature on its material properties. However, as the technology advances, there is a huge demand for better electronic devices, thus an alternative semiconductor material is required. Various potential substitution materials for Si are gallium arsenide (GaAs), gallium nitride (GaN) and silicon carbide (SiC). Among these proposed materials, SiC has gained a major interest as it has substantial advantages over Si. However, this material is considered to be new and its applications are challenged by the difficulty of controlling metal contact properties. In addition, research results shows that there are still problems associated with fabrication of this material. This chapter presents a brief comparison between Si and SiC plus a review on the scientific literature published for the formation of metal contacts onto Si together with the progression of SiC metal contacts. The electrical characteristics (i.e. Schottky barrier height, ϕ_b), thermal stability and chemical

reactions for these contacts will also be discussed. In addition, the use of a Si interlayer to overcome and to improve existing contact conditions is introduced. Note that this work is only based on nickel (Ni); hence the review is concentrated only on Ni contacts.

1.2 Literature Review

It is vital to understand the basic properties of SiC and the Ni-SiC contact properties, plus the problems associated with the contact in order to discover an effective technique to improve the existing contact conditions. To gain a deep understanding on the research progress of the Ni-SiC contact, a brief literature review starting from Ni-Si, Ni-SiC and Ni-Si-SiC contact is presented. In this section, the issues correlated with these contact properties emphasising on the materials properties, interface formation mechanism and contact performance at elevated temperature are highlighted. The fundamental theory in the art of controlling metal-semiconductor is also discussed.

1.3 Advantages of Silicon Carbide over Si

Si is still by far the most widely used substrate material in electronic industry. However, SiC has recently gained a major interest to semiconductor pioneers due to its advantages over Si, especially in terms of high power and high temperature applications. SiC exists in more than 170 different crystal structures known as polytypes, with each polytypes having its own unique electrical and optical properties. Among these polytypes, the hexagonal structure, mainly 4H-SiC and 6H-SiC, and also the 3C-SiC cubic structure are the most commonly used in semiconductor fabrication due to their suitable electronic properties. Several parameters of the most popular used semiconductor materials such as Si and GaAs are compared against 4H-SiC as illustrated in Figure 1.1 below.

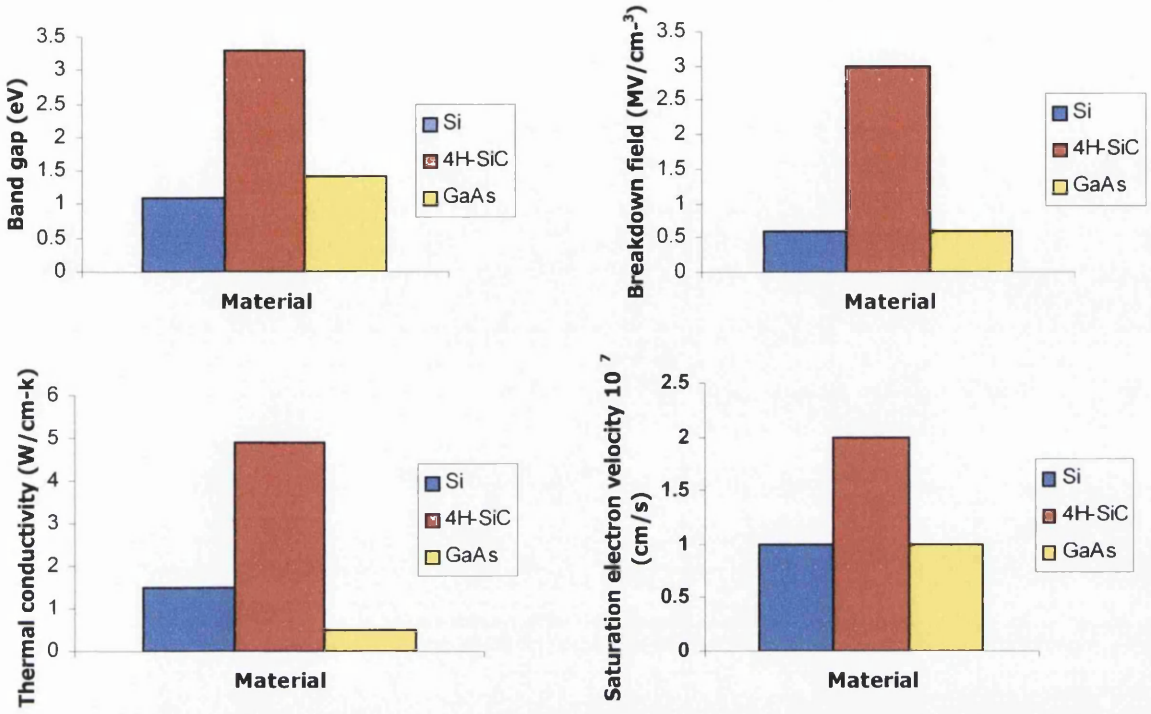

Figure 1.1: Comparison of parameters for Si, 4H-SiC and GaAs.

By comparison, it is clearly seen that SiC has superior properties over Si and GaAs. SiC is a group IV wide band gap compound formed by Si and carbon (C). Due to its large band gap, SiC has an extreme thermal conductivity and is able to withstand high temperature applications. Figure 1.2 shows the plot of operating temperature of a p-n junction based on various semiconductors versus band gap. From the plot, p-n junctions based on SiC operate well above 1000°C while p-n junctions made on Si operate at temperature below 500°C. In addition, the large breakdown field and high saturation electron velocity has made high power frequency switching possible. Hence, SiC devices are capable to operate in extreme harsh environment that conventional Si devices could not adequately operate in. With the figures of merit for its superior properties, it is predicted that SiC would be the dominant material for future electronics and next generation of high power devices.

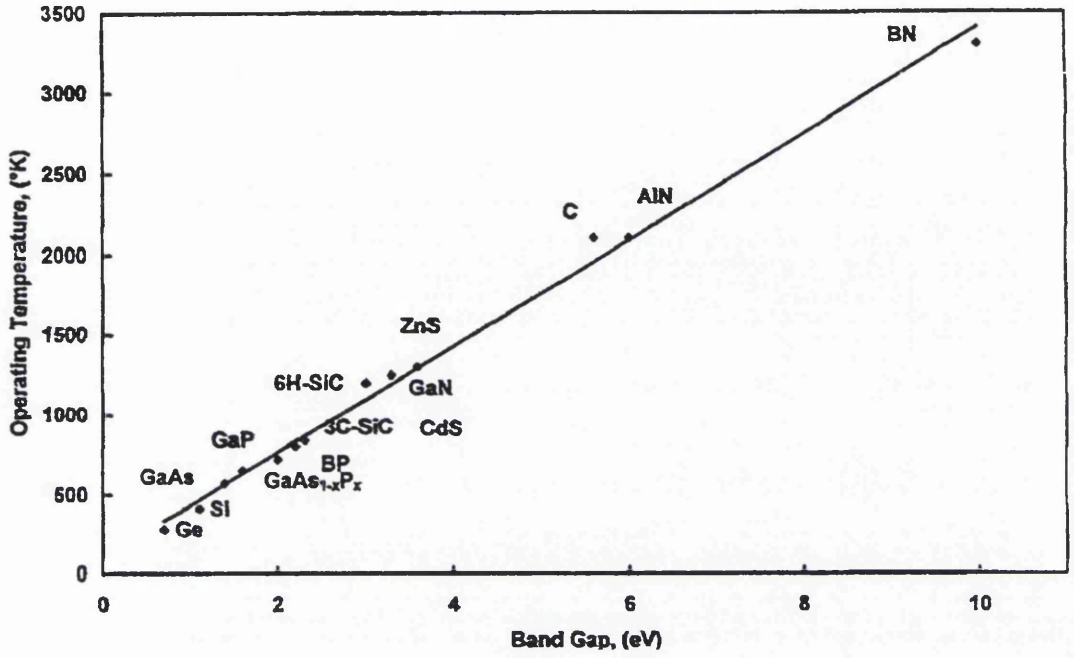

Figure 1.2: Operating temperature of p-n junctions based on different semiconductors versus band gap width [1].

1.4 Practical Contacts

- **Theory on the control of Schottky barrier height in metal semiconductor contacts**

The formation of a practical Schottky diode consists of a deposition of metal films onto a semiconductor surface, which is generally not an ideal surface with a few monolayers being contaminated by adsorbates or a thin layer of native oxide. Fundamentally, there are four primary parameters that control the Schottky barrier height, ϕ_b at the metal – semiconductor interface: the work function of the metal, ϕ_m; the crystalline structure at the metal – semiconductor interface; the diffusion of metal atoms across the interface into the semiconductor and the outermost electronic configuration of the metal atoms [2].

Various models have been proposed to examine these controlling factors on metal-semiconductor contacts. According to work proposed by *Schottky* [3]

and *Mott* [4] (see section 2.2.1), the control over the barrier height, ϕ_b is achieved by selecting the appropriate value of ϕ_m (i.e. choice of metals). The value of ϕ_m for various metals is listed in Table 1.1 below.

Metal	*Work Function*
Pt	5.65
Ni	**5.15**
Pd	5.12
Au	5.10
Cu	4.65
W	4.55
Cr	4.50
Sn	4.42
Ti	4.33
Al	4.28
Ag	4.26
Ga	4.20
In	4.12
Mg	3.66

Table 1.1: Values of work functions for selected metals (eV); from reference [5].

Meanwhile, another theory was proposed by *Bardeen* [6], which states that ϕ_b is independent of ϕ_m provided that the density of surface states is large enough to cause Fermi level *pinning*. These surface states are electronic states localised at the surface of the semiconductor caused by the natural material surface imperfections. However, later work by Kurtin *et al* [7] suggested a *'linear interface'* model where ϕ_b was assumed to be linearly dependant on the electronegativity of the metal, χ_m. According to this model, a dimensionless

parameter, *S*, known as the index of interface behaviour measures the closeness of the interface behaviour towards Schottky behaviour. In addition, the work from Kurtin *et al* concludes that Fermi level pinning is more pronounced in covalent materials than ionic materials. Based on these theories, a vast amount of research has been conducted and the highlight of the results is discussed below.

1.5 Semiconductor Metal Contacts

1.5.1 Nickel- Silicon (Ni – Si) Contacts

Over the years, Si has played a leading role in the world of semiconductors. Almost all of the electronic devices involved in our daily life, ranging from telecommunications to home appliances are made from Si. Meanwhile, Ni has gained a major interest as one of the most popular material in the fabrication of metal contacts onto semiconductor due to its low contact resistivity [8]. However, when these two useful materials are brought into contact to form a Schottky contact, it is observed that the interface system exhibits various species of metal-semiconductor compound (NiSi, $NiSi_2$, Ni_2Si etc.), known as silicides. Silicides are compounds formed from the interdiffusion between the metal and semiconductor, as they tend to lower the thermodynamic free energy when brought into contact [9]. These silicides are commonly used by the microelectronics industry to reduce the resistivity of gate and local interconnect metallisation in integrated circuits [10]. Despite being useful, the issue of thermal stability arises as constant operation above room temperature or even long periods at room temperature ambient can lead to degradation of these structures. In addition, there is a theme of interest about the amount of Si consumed by the metal to form silicide and the dominant moving species during formation of the metal-semiconductor interface.

Various investigations have been conducted to examine the Ni – Si interface. Tung *et al* [11] observed that initial $NiSi_2$ exhibits a (1 x 1) LEED pattern

and subsequent to an additional deposition of Ni at room temperature, the LEED pattern changed to a ($\sqrt{3}$ x $\sqrt{3}$). The process is also observed to be reversible when the interface is annealed from 450°C to 550°C. Meanwhile, Clabes *at al* [12] reported that by annealing at the higher temperature range of 350°C to 650°C, the ($\sqrt{3}$ x $\sqrt{3}$) structure changed into a ($\sqrt{19}$ x $\sqrt{19}$) and temperatures above 650°C exhibited a streak of Si (111) (7 x 7). These results were later explained by Yoshimura *et al* [13] by performing STM studies on the Ni-Si interface. Their results show that initial Ni deposition forms Ni clusters or islands on the surface. When the surface is annealed at 250°C, the clusters gradually coalesce with the substrate structure. At 400°C, some of the deposited Ni has already diffused into the bulk forming disordered ring clusters around the islands, which corresponds to the ($\sqrt{19}$ x $\sqrt{19}$) structure. The surface of the islands forms the ($\sqrt{3}$ x $\sqrt{3}$) structure. Annealing at 600°C results in further Ni diffusion towards the bulk indicated by the disappearance of the ($\sqrt{3}$ x $\sqrt{3}$) islands and the formation of larger island exhibiting a (2 x 2) structure. The (2 x 2) structure is presumably due to reconstruction on the interface between Si and $NiSi_2$. The ring clusters around the islands are still observable but forming more ordered ($\sqrt{19}$ x $\sqrt{19}$) structure. At 800°C, Ni is further diffused towards the bulk and the islands disappear completely giving a (1 x 1) structure. The surface exhibits the (7 x 7) structure indicating a complete Ni diffusion into the bulk for prolonged anneal at 1000°C. Therefore, it can be concluded that Ni is the dominant moving species in the formation of Ni-Si interface and the mechanism is enhanced by temperature.

The interface formation mechanism for Ni-Si contact is now well known. The performances of Si based devices need no further discussion as they are widely used in present electronics applications. Thus, one can easily find operating information or datasheets on these devices, which therefore will not be further discussed here. Even so, the reliability and the thermal stability of Si based devices has become an important issue. (For example, the operating

temperature of a p-n junction cannot exceed 500°C (see Figure 1.3)). Thus, an alternative semiconductor is required for high temperature applications.

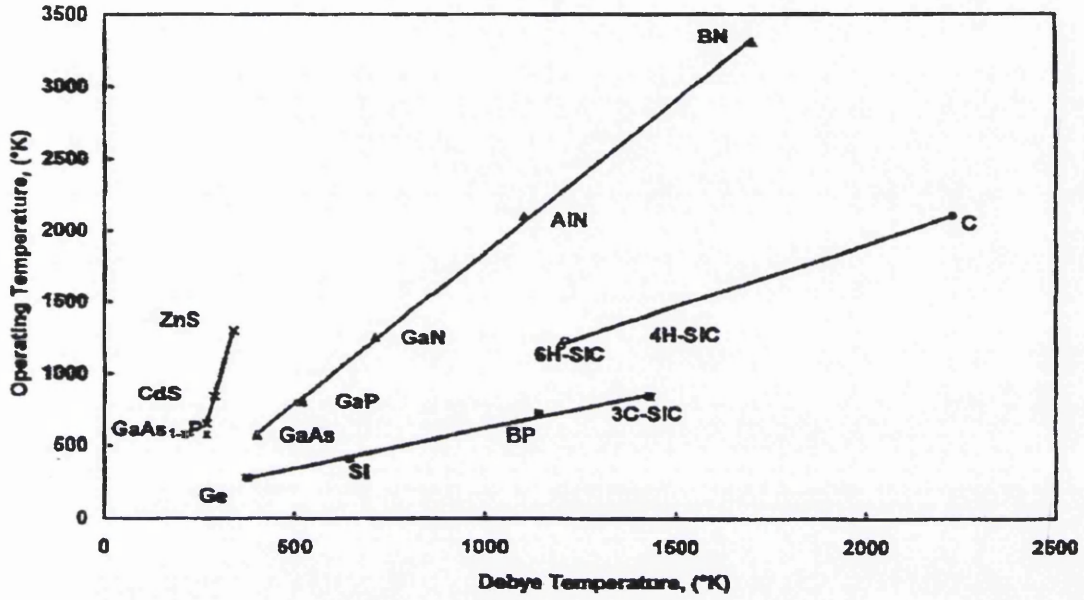

Figure 1.3: Operating temperature of p-n junctions based on different semiconductor versus Debye temperature of semiconductors [1].

1.5.2 Nickel – Silicon Carbide (Ni-SiC) Contacts

To achieve further progress in electronics technology, it is important to define a more appropriate material that could substantially withstand high temperature operation with reliability. As seen previously, SiC has outstanding properties as a candidate for high temperature and high power applications. The operating temperatures for 4H-SiC based devices in particular are well above 1500°C (see Figure 1.3). Therefore, a substantial interest into SiC had evolved in semiconductor research to discover the maximum potential of this material with the ultimate aim to produce leading edge devices.

The study on Ni-SiC is initiated with the formation mechanisms of the interface. As discussed previously, Ni reacts with Si, forming silicides. Similarly, for the case of Ni-SiC, Ni it is expected to react with SiC, producing silicides. Park

et al [14] have categorised the reaction between metal-SiC into two types of reaction based on equilibrium phase diagram. According to this diagram, illustrated in Figure 1.4, Ni-SiC incorporates into a reaction, where the final elements consists of interdiffused reaction silicides and free C in such a way that they satisfy the mass balanced requirements.

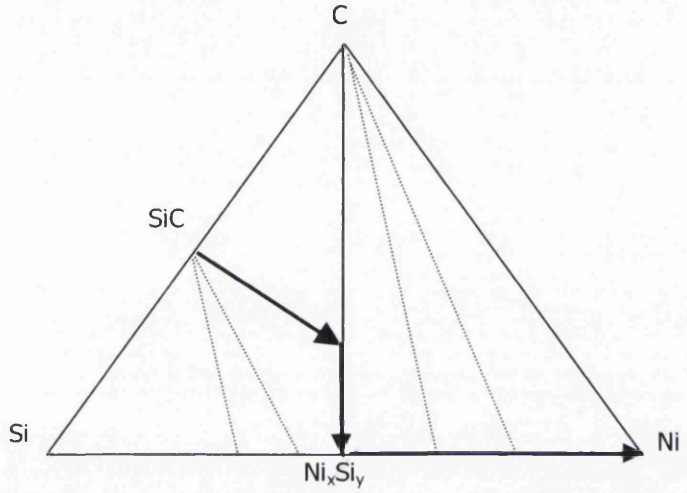

Figure 1.4: Schematic isothermal phase diagram and reaction pathway of Ni-SiC reaction [14].

Pécz *et al* [15, 16] have performed a Transmission Electron Microscopy (TEM) study on Ni Ohmic contacts to 4H-SiC. The TEM results show that the 'as-deposited' Ni layer is homogeneous in thickness and exhibits a smooth surface. On the other hand, Iwami *et al* [17] have performed a Scanning Tunnelling Microscopy (STM) study on the deposition of Ni onto a clean $\sqrt{3} \times \sqrt{3}$ SiC surface. Their result shows that Ni atoms were dispersed uniformly during the initial deposition of very thin layers of Ni. At later stages with thicker overlayers, Ni atoms are more likely to form islands on the surface.

Upon annealing, Ni silicides are rapidly formed. At low temperature (between 400°C to 700°C), the Ni overlayers are seen to be transformed into

several species of Ni silicides (Ni_2Si, $Ni_{13}Si_{12}$) [8]. The formation of silicides is via the diffusion of Si or Ni atoms reacted at the interface. The Ni layer was observed to be completely consumed in the formation of silicide, until equilibrium conditions are achieved. However, it is observed that Ni_2Si is the dominant species of silicides at the interface [8, 16, 17, 18, 19]. In addition, TEM results show that a large number of voids, mainly Kirkendall voids, consisting of empty states or vacancies are observed to be present at the original Ni-SiC interface [15, 16]. At this stage, the contact exhibits rectifying or Schottky behaviour. Above 900°C, periodic layers of silicides and carbon were observed. At such high temperature, the disassociation of SiC to Si and C is also observed [20-25]. This reaction results in Ni atoms reacting with the dissociated Si, leaving free C at the surface. These free C atoms are mainly in a graphite state, especially after being annealed at temperature above 1000°C. In addition, high-resolution microscopy and XTEM results show that the amounts of voids had also increased inside the contact layer [16]. Furthermore, the large number of voids also suggests the segregation of C to the surface through the voids. The presence of these C groups at the Ni-SiC interface has long been known to cause electrical instability and reduce device lifetime especially after prolonged operation at high temperature. Therefore, an alternative had to be developed to prevent this unwanted C formation in order to improve existing contact conditions.

1.5.3 Nickel-Silicon-Silicon Carbide (Ni-Si-SiC) Contacts

As discussed previously, although Ni-SiC contacts are capable of operating at a much higher temperature than Ni-Si contacts, the potential electrical instability and low reliability of contact due to the presence of unwanted free C and graphite within the contact remains unsolved. Thus, attempts to overcome such problems have been investigated.

Various studies have been reported [14, 16, 20, 24, 25]. These endeavours include implementing an alternative material composition such as Al/Ni, Si/Ni/Si or Ni/Si/Ni layers onto the contact, and theoretical calculations of reaction

products of the composite materials based on phase equilibrium diagram and thermodynamic properties. Although the results reported have showed improvements to the contact conditions, the consistency of the techniques employed remains uncertain. Hence, a reliable and consistent central theme to that matter is yet to be established.

The ultimate goal of this work is to investigate an approach to control Ni-SiC contact using a Si interlayer. Here, a thin Si interlayer is used to circumvent the problems associated with the free C formation at the Ni-SiC interface at elevated temperature. The thin layer of Si is implemented between Ni-SiC interface to act as a buffer layer with the aim to provide a source of Si atoms during Ni silicides formation in such a way that it does not alter the bulk SiC structure, preventing the formation of free C. Within this work, a central theme based on Si interlayers is investigated thoroughly in order to improve existing Ni-SiC contacts conditions. The interface formation mechanism including surface preparation, chemical and electrical properties of the Ni-Si-SiC contact are investigated. The results obtained from the study are presented gradually throughout the rest of this thesis.

1.4 References

[1] V. E. Chelnokov and A. L. Syrkin, Mat. Sci. and Eng., **B46**, 248-253 (1997).

[2] M. J. Bozack, Phys. Stat. Sol., (B) **202**, 549 (1997).

[3] W. Schottky, Naturwissenschaften, **26**, 843 (1938).

[4] N. F. Mott, Proc. Cambr. Phil. Soc., **34**, 568 (1938).

[5] E. H. Rhoderick and R. H. Williams, 'Metal - Semiconductor Contacts', Oxford University Press, (1988).

[6] J. Bardeen, Phys. Rev. Lett., **71**, 717-727 (1947).

[7] S. Kurtin, T. C. McGill and C.A. Mead, Phys. Rev. Lett., **22**, 1433 (1969).

[8] S. Y. Han, K. H. Kim, J. K. Kim, H. W. Jang, K. H. Lee, N. K. Kim, E. D. Kim and J. L. Lee, App. Phys. Lett. **79**, 12, 1816-1818 (2001).

[9] K. N. Tu, J. W. Mayer and L. C. Feldman, 'Electronic Thin Film Science for Electrical Engineers and Materials Scientists', Macmillan Publishing Company, (1992).

[10] E.G. Colgan, J. P. Gambino and B. Cunningham, Mat. Chem. and Phys., **46**, 209-214 (1996).

[11] R.T. Tung, J. M. Gibson and J.M. Poate, Phys. Rev. Lett., **50**, 429 (1983).

[12] J.G. Clabes, Surf. Sci., **145**, 87 (1984).

[13] M. Yoshimura, S. Shinabe, T.Yao, Surf. Sci., **357-358**, 917-920 (1996).

[14] J. S. Park, K. Landry and J. H. Perepezko, Mat. Sci. and Eng. **A259**, 279-286 (1999).

[15] B. Pécz, G.Radnóczi, S.Cassette, C. Brylinski, C. Arnodo and O. Noblanc, Dia. and Rel. Mat., **6**, 1428-1431(1997).

[16] B. Pécz, Appl. Surf. Sci., **184**, 287-294 (2001).

[17] M. Iwami, N. Hattori, T. Fujimoto, M. Hirai and M. Kusaka, T. Morii, H. Watabe and H. Watanabe, Surf. Rev.and Lett., **Vol 7**, No. 5-6, 679 –682 (2000).

[18] F. La Via, F. Roccaforte, A. Makhtai, V. Raineri, P. Musumeci and L. Calcagno, Microelec. Eng., **60**, 269-282 (2002).

[19] C. S. Pai, C. M. Hanson and S. S. Lau, J. Appl. Phys., **57**, 618 (1985).

[20] O. Noblanc, C. Arnodo, C. Brynlinski, S. Cassette, R. Kakanakov, L. Kassamakova, M. Neshev, A. Kakanakova-Georgieva, V. Krastev and Ts. Marinova, Inst. Phys. Conf. Ser., **No. 155**, 609-612 (1996).

[21] J. R. Waldrop and R. W. Grant, Appl. Phys. Lett., **62**, 2685 (1993).

[22] Ts. Marinova, V. Krastev, C. Hallin, R. Yakimova and E. Janzén, Appl. Surf. Sci., **99**, 119-125 (1996).

[23] Ts. Marinova, A. Kakanakova-Georgieva, V. Krastev, R. Kakanakov, M. Neshev, L. Kassamakova, O. Noblanc, C. Arnodo, S. Cassette, C.

Brynlinski, B. Pécz, G. Radnoczi and Gy. Vincze, Mat. Sci. and Eng., **B46**, 223-226 (1997).

[24] A. Kakanakova-Georgieva, Ts. Marinova, O. Noblanc, C. Arnodo, S. Cassette and C. Brynlinski, Thin Solid Films, **343-344**, 637-641 (1999).

[25] Ts. Marinova, V. Krastev, C. Hallin, R. Yakimova and E. Janzén, Mat. Sci Forum, **Vol. 207-209**, 293-296 (1996).

Chapter 2

Theory of Metal-Semiconductor Contacts

2.1 Introduction

The first step towards understanding the formation of metal-semiconductor contacts is to study the formation and the transport mechanism of the electrons between the interfaces. Detailed scientific literature has been published as a result of extensive investigations conducted throughout the years. In an attempt to describe and interpret the experimental data, this chapter presents various theoretical models of metal-semiconductor contact formation plus the transport mechanism of the electrons between these interfaces. Upon understanding the theoretical background of the contact formation, it is essential to extract the important electronic parameters associated with the interface. Hence, a discussion of the techniques that are used to extract these parameters is also included at the end of this chapter.

2.2 Models of Schottky Barrier Formation

In the late 19th century, Braun [1] performed the earliest recorded investigation of a metal-semiconductor contacts. When a metal and a semiconductor are brought into intimate contact, a barrier is established between the interfaces. This barrier is known as Schottky barrier and the simplest way to define this barrier is the contact potential that exists across the interface. The vital parameter used to evaluate this interface barrier is the *Schottky Barrier Height,* ϕ_b, which for the case of an n-type semiconductor is defined as the energy difference between the metal Fermi level and the semiconductor conduction band minimum at the interface. It is this barrier that determines the rectifying properties of the metal-semiconductor contact.

Over the years, the research on Schottky barrier formation at the metal-semiconductor interface remained active with the progression of semiconductor technology, exploring various promising new semiconductor materials such as Silicon Carbide (SiC). In this section, the formation of metal-semiconductor contacts is discussed in detail through various models proposed in the literature in order to elucidate the experimental results obtained (see chapter 6). For ease of discussion in the following section, the semiconductor is taken to be n-type material unless otherwise stated.

2.2.1 The Schottky-Mott Model

The most fundamental of the present Schottky barrier models was formulated independently by Schottky [2] and Mott [3]. In this model, ϕ_b is evaluated in terms of the physics and bulk parameters of the individual materials. The formation of the Schottky barrier mechanism modelled by the Schottky-Mott model is illustrated in Figure 2.1.

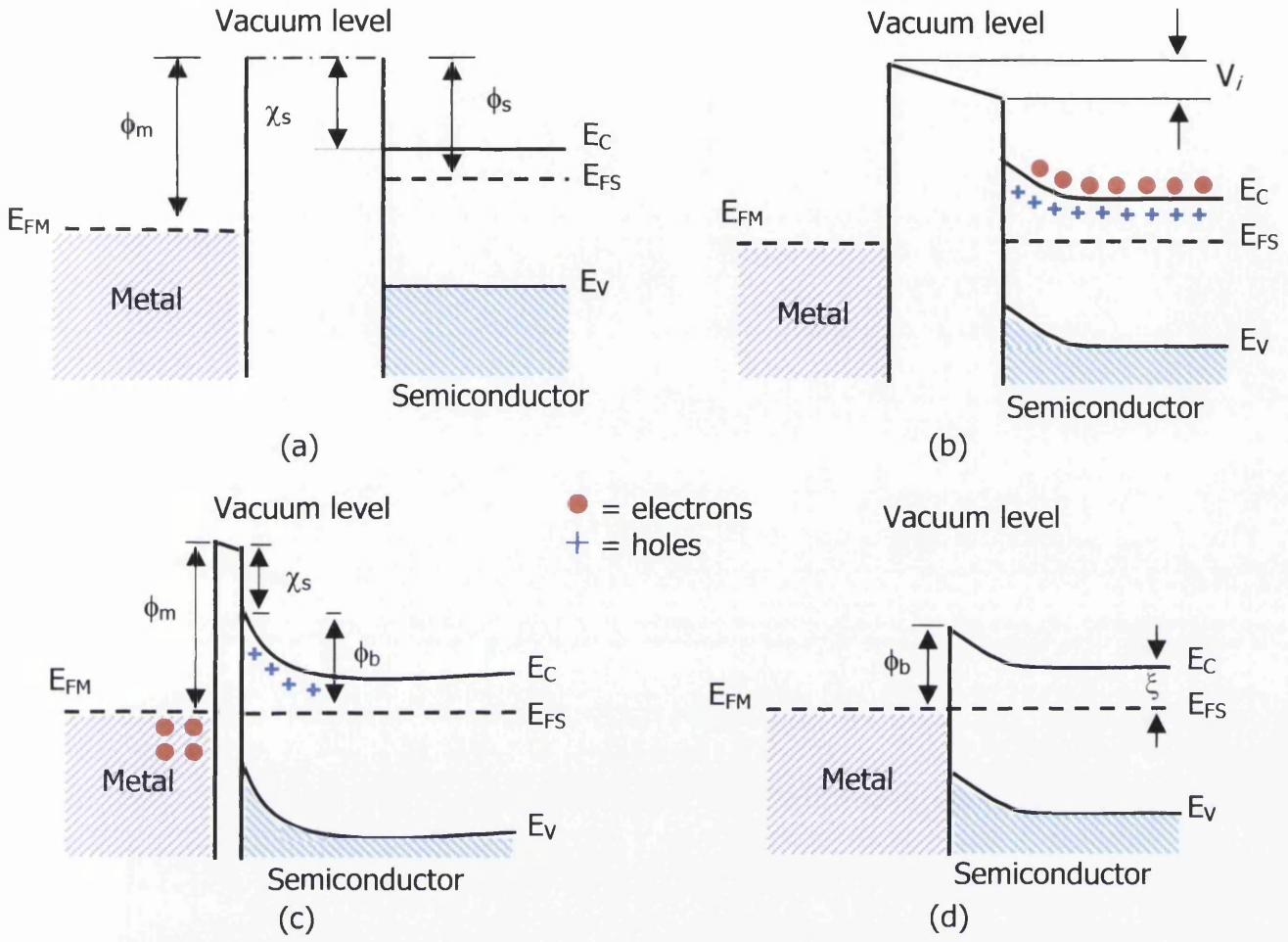

Figure 2.1: Formation of Schottky barrier between a metal and semiconductor (a) isolated, (b) electrically connected, (c) separated by a narrow gap, (d) perfect contact.

Initially, the metal and semiconductor are neutral and separated by vacuum as shown in Figure 2.1(a). In this state, the electron bands of the semiconductor are flat up to the surface and the vacuum levels of the metal and semiconductor are aligned. The metal is characterised by its Fermi level E_{FM} and its work function, ϕ_m, which is defined as the amount of energy required to raise an electron from the Fermi level to a state of rest outside the surface of the material (i.e. the vacuum level). Meanwhile, as there are no electrons at the

Fermi level in the semiconductor, it is more realistic to characterise the semiconductor by a parameter known as the electron affinity, χ_s, which is defined as the difference in energy between an electron at rest in the vacuum level and an electron at the bottom of the conduction band. Also, the work function of the metal is assumed to be higher than the electron affinity of the semiconductor ($\phi_m > \chi_s$).

When the metal is brought into intimate contact with the semiconductor, a charge transfer from the semiconductor into the metal arises. This phenomenon is continued until an equilibrium is reached where the two Fermi levels coincide as illustrated in Figure 2.1(b). As electrons migrated from the semiconductor to metal, there is an excess negative charge on the surface of the metal. This negative charge simply consists of the extra conduction electrons from the semiconductor. As the interface must be neutral, the negative charge on the metal is balanced by positive charge on the surface of the semiconductor. This positive charge is provided by the conducting electrons receding from the surface leaving uncompensated positive donor ions in a region of depleted electrons near the semiconductor surface. This positive space-charge causes a potential drop across the depletion region equal to the potential difference between the two materials. The semiconductor bands are then bend upward and thus form a Schottky barrier as illustrated in Figure 2.1(c). The height of this interface barrier (i.e. Schottky barrier), ϕ_b is given by the difference between the metal work function and the electron affinity of the semiconductor. Therefore, the Schottky-Mott model is defined as

$$\phi_b = \phi_m - \chi_s \qquad \text{(for n –type)} \qquad [2.1]$$

where

$$\chi_s = \phi_s - \xi$$

and

$$\xi = E_{CB} - E_F = \frac{kT}{q} \ln \frac{N_C}{N_D}$$

The parameters N_C and N_D are the effective density of states in the conduction band and donor concentration respectively. Also, k is the Boltzmann constant, T is the temperature in Kelvin and q is the elemental electronic charge. For the case of a p-type semiconductor where holes are the majority carriers, the barrier height is given by

$$\phi_b = E_g - (\phi_m - \chi_s) \quad \text{(for p-type)} \qquad [2.2]$$

where E_g is the semiconductor energy gap.

These equations are sometimes referred as the *Schottky limit*. Conclusively, the model predicts that ϕ_b is directly proportional to ϕ_m. An ideal Schottky barrier is illustrated in Figure 2.1(d). However, in practice, this ideal situation is never reached, as there is usually a thin interfacial layer (about 10-20Å) on the surface of the semiconductor [4]. Therefore, a practical contact is more likely to occur which will be discussed in section 2.2.2.

Practically, the parameter ϕ_b strongly determines the behaviour of the contact. If ϕ_b is large which corresponds to a wide depletion region for constant N_D, the contact is said to be Schottky or rectifying, and will be further discussed in section 2.8. Conversely, if ϕ_b is small or even a negative value, the contact has no rectifying properties, and is known as an *Ohmic* contact as there is no serious obstruction to the electron flow in either direction between the junction of the metal and semiconductor. The current-voltage characteristic of both Schottky and Ohmic contact is illustrated in Figure 2.2 below.

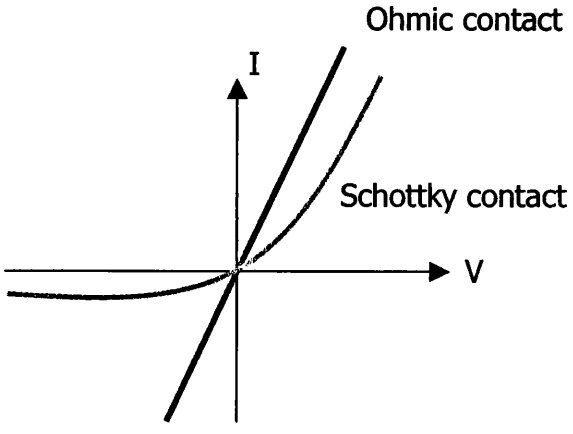

Figure 2.2: Current-voltage characteristic of Schottky and Ohmic contacts.

Generally speaking, a large ϕ_b is required for good Schottky contacts and a small ϕ_b for Ohmic contacts. Practically, an Ohmic contact plays an important role in achieving electrical continuity without forming a potential barrier at the semiconductor interface [5]. This criterion is compulsory for measurement of ϕ_b whenever an electrical method is implied. Hence, the standard structure used to measure ϕ_b consists of a back Ohmic contact and a front rectifying contact so that electrons only 'see' the required barrier as they traverse the metal-semiconductor front interface.

Up to this point, one can easily find that the Schottky-Mott model is rather straightforward. The reason for this is that the model assumes that ϕ_m and χ_s remains the same throughout the formation of the interface. Also, the model assumes that the interface formed is perfectly abrupt, without any surface or interface states (see section 2.3) present in the semiconductor band gap. The effect of surface states cannot be underestimated as they can significantly change the value of ϕ_b. Practical experimental data shows that these assumptions are not valid, thus equation [2.1] and [2.2] are not obeyed. There are also vagueness regarding the model's prediction that ϕ_b is linearly dependent on ϕ_m, (i.e. one can choose a metal with appropriate work function in order to predetermine the contact formation, either Schottky or Ohmic) as the observed experimental data shows that for most group III-V and II-IV semiconductors, the value of ϕ_b is almost independent of ϕ_m. When this occurs, the Fermi level is said to be *pinned*. The mechanism of Fermi level pinning is generated by the surface states and will be discussed in section 2.2.2. In conclusion, the main failure of the Schottky-Mott model is that the presence of the surface states is neglected. Consequently, a model accounting for these surface states was proposed by Bardeen [6] in 1947 as discussed in the next section.

2.2.2 The Bardeen Model

As mentioned previously, this model accounts for the effect of surface states during the formation of Schottky barrier. Bardeen proposed that if surface states exist in a sufficient density at the interface between the metal and the semiconductor, ϕ_b would be independent of ϕ_m [7]. The nature and origin of the surface states will be further discussed in the next section. In the Bardeen model, surface states are assumed to be uniformly distributed throughout the band gap with a density of D_{ss} $eV^{-1}cm^{-2}$. However, this is not necessarily true in real cases as surface states has been observed experimentally [8] to occur in discrete bands within the semiconductor band gap occasionally. Even so, the result would be more or less the same for both cases. When considering surface states in interface formation, an important parameter known as charge neutrality level, ϕ_o, is used to take into account the charge neutrality level of the surface states. By definition, the charge neutrality level is the energy level, measured relative to the valence band, to which the surface states must be filled when the surface is neutral. The states lying above ϕ_o are the acceptor-like states in which they hold a net negative charge when empty and neutral when filled. Conversely, states lying below ϕ_o are the donor-like states and hold a net positive charge when empty and neutral when occupied. To further demonstrate, consider the case of a semiconductor having a fresh clean surface (e.g. those generated by cleaving). Once the clean surface is formed, the surface states will be full up to the charge neutrality level ϕ_o and the corresponding bands are flat from the bulk to the surface. However, at the conduction band, there are surface states of lower energy that exist at the surface. Therefore, there is a charge flow into these empty states, which creates a depletion region. This process is continuous until the field opposes any further charge transfer resulting in band bending (i.e. Fermi level shift relative to band edges) that produces a potential barrier at the clean surface. At electrical equilibrium, the final position of the Fermi level relative to the ϕ_o will be determined by the total density of surface states, D_{ss}. If the surface states density is high (i.e. $D_{ss} > 10^{12}$ $eV^{-1}cm^{-2}$), the Fermi level will

approach ϕ_o. If this is the case, the Fermi level is said to be pinned by the high density of the surface states.

Consider now the approach of the metal in the formation of Schottky contact. As illustrated in Figure 2.3, the formation of Schottky contact is initiated with a clean semiconductor surface with the presence of a large density of surface states. Initially the metal and semiconductor are isolated (Figure 2.3(a)); with the semiconductor Fermi level pinned at ϕ_o via charge transfer to the surface states as described previously. When the metal is brought in close proximity with the semiconductor (Figure 2.3(b)), a charge double layer is required to compensate the difference in Fermi level positions relative to the vacuum levels in the metal and the semiconductor, i.e. the contact potential difference, V_i. When large densities of states are present, the electron flow between the metal and the surface states will cause a negligible movement in the semiconductor Fermi level position. Hence the Fermi level will appear to be pinned at ϕ_o and the barrier height ϕ_b will be independent of the metal contact used (Figure 2.3(c)). In this case, the Schottky barrier height modelled by Bardeen can be obtained by the relationship:

$$\phi_b = E_g - \phi_o \qquad [2.3]$$

The above equation is referred as *Bardeen limit*, where we can clearly see that there is no ϕ_m component. Therefore, as predicted by the Bardeen model, we can conclude that when a large density of surface states is present, ϕ_b is independent of ϕ_m. As mentioned previously, there is usually a thin interfacial layer (e.g. oxide) between the contacts preventing them from forming intimate contacts. Similarly, by using the Bardeen model quantitatively, the barrier height can be given by:

$$\phi_b = \gamma(\phi_m - \chi_s) + (1-\gamma)(E_g - \phi_o) \qquad [2.4]$$

where $\gamma = \left(\frac{\varepsilon_i}{\varepsilon_i + e^2 \delta D_{ss}}\right)$

The equation [2.4] assumes that the oxide layer has a thickness of δ and the semiconductor has a permitivity of ε_i. A more detailed and quantitative description of such a system can be found elsewhere [4]. Equation [2.4] shows that if there is large density of surface states i.e. $\gamma = 0$, $D_{ss} \to \infty$, then the Bardeen model is obeyed. However, in extreme cases where there are no surface states present, i.e. $\gamma = 1$, $D_{ss} \to 0$, and the Schottky-Mott model is obeyed.

2.3 Surface States

In crystallography, the sequence of atomic bonding of the bulk is abruptly terminated at the surface. These terminated edges consist of dangling and broken atomic bonds and the characteristics of such a structure is very different from those of the bulk. States can occur within the band gap, known as surface states and the earliest investigations were performed by Tamm [9] in 1932. More recent work has identified two categories of surface states, intrinsic and extrinsic, depending on how the states were generated. In this section, the characteristics and natural occurrence of these states in metal – semiconductor interfaces are discussed. In addition, those surface states generated through metal deposition known as *metal-induced gap states* (MIGS) are also presented to aid the understanding of the experimental results.

2.3.1 Intrinsic Surface States

When a surface of a material is abruptly terminated, the periodicity of the bulk will be interrupted. Hence, the Bloch wavefunctions will no longer describe the electron properties and the conditions which give rise to band gaps in the bulk no longer apply at the surface. In a quantum mechanics approach, these conditions give rise to electron states wavefunctions with an exponentially decaying characteristic from the surface into the bulk. These states are referred as *intrinsic surface states* since they can exist on the free surface of a perfect crystalline solid.

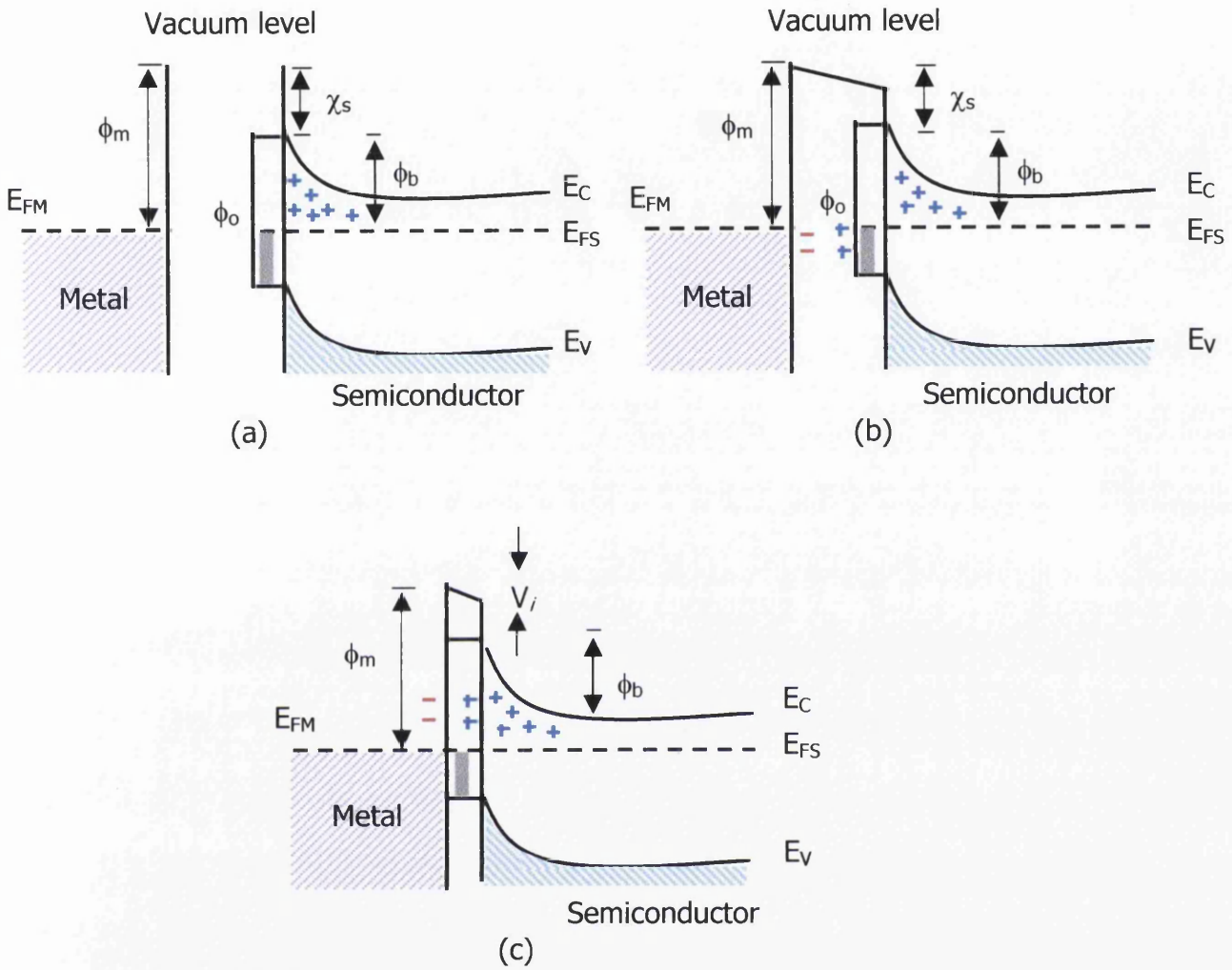

Figure 2.3: Metal contact to an n-type semiconductor surface in presence of a large density of surface states, (a) isolated, (b) charge transfer between metal and surface states, (c) for $D_{ss} \to \infty$, the contact potential difference V_i sustained by the surface state charge. The Fermi level is pinned at ϕ_o to give a metal independent barrier height, ϕ_b.

The first work considering these surface states was performed by Tamm [9] who showed that if a periodic square well potential were terminated by a high surface potential, there would be allowed levels in the energy gap corresponding to wavefunctions, which are localised at the surface. These surface states were studied in more detail by Shockley [10] in 1939, which suggested that there should be one surface state per surface atom. As the Bardeen model showed (section 2.2.2), it is clear that the structure and the density of this surface states which causes Fermi level pinning greatly affects ϕ_b. In this case, the states were intrinsic to the semiconductor such that the presence of metal has no influence on ϕ_b. Hence, this phenomenon is sometimes referred to as *intrinsically pinned* surface.

2.3.2 Extrinsic Surface States

The Bardeen model assumes that there is an insulation layer at the interface that prevents the metal-semiconductor from forming an intimate contact. Thus, Fermi level pinning originating from intrinsic surface states will not have any interaction between the states and the metal overlayer. Consequently, any physical or chemical reaction, which may occur as the interface is formed are inhibited. However, in reality, it appears highly likely that interactions between the metal and semiconductor will occur, which could also result in electronic states being generated at the interface. Such states are referred to as *extrinsic surface states* or *interface states.* The exact origin of these states is not fully understood but they are often acquainted with several factors ranging from a quantum mechanical approach to the physical effects of defects and chemical reaction at or near the interface. To date, the precise structure and their density within the semiconductor energy gap are rarely known. In spite of this, if the density is high enough, these interface states are capable of pinning the Fermi level in a way similar to that of the intrinsic surface states. Thus, the interface states can also be characterised by a charge neutrality level, ϕ_o as described in section 2.2.2. However, the extrinsic case is slightly different as the position of ϕ_o

is not fixed prior to the formation of the interface as described in the Bardeen model. Even so, the situation is generally 'Bardeen-like' since the final Fermi level position, thus ϕ_{b_r} is determined by the density of the interface states. Hence, it is sometimes referred as *extrinsically pinned* surface.

In the following sections, the origin of the extrinsically generated surface states is discussed to aid the understanding and correlation with experimental results. It is however important to note that the various mechanism described here can occur concurrently and contribute towards a single pinning process with one or more being dominant under certain circumstances.

2.3.2.1 Metal Induced Gap States (MIGS)

In 1965, Heine [14] was the first to describe the origins of the states liable for Fermi level pinning in a metal-semiconductor interface. Heine realised that there should be no intrinsic surface states at intimate metal-semiconductor junctions. Yet, if there are intrinsic surface states present on a free semiconductor surface, they will then be replaced by MIGS when a metal is deposited on that surface. This mechanism is driven by the tails of the electron wavefunctions from the metal contact penetrating into the semiconductor energy gap with a decaying nature and an attenuation length of the order of a few Angstroms (Å). The occurrence of this wavefunction is a direct result of the semiconductor wavefunctions coupling with those of the metal that tunnel into the band gap. The intrinsic surface states replaced by MIGS will generate a continuum of states, which behave in a similar manner to those states described in the Bardeen model. Thus, if these states are present in a sufficiently large density, they will also pin the Fermi level at the charge neutrality level, ϕ_o in the same manner as described in section 2.2.2.

Cohen and co-workers [15, 16, 17] had performed a more detailed analysis of the MIGS theory in terms of density of states at various locations from the metal through the interface and into the semiconductor using aluminium (Al) and various semiconductors including Si and GaAs. They implemented a 'jellium

model' to perform a self-consistent pseudo potential calculation by approximating Al with the model. The result of this study shows that at the interface, there are states, which exist in the gap and extend a few layers into the semiconductor. The penetration depth was found to be inversely proportional to the energy of the band gap. The barrier heights were calculated by determining the position of the Fermi level at the interface with respect to the position of the conduction band minimum in the bulk.

Another study by Tejedor and Flores [18] had suggested that the new density of interface states were associated with the loss in both the bulk conduction and valence band states at the semiconductor surface. They also proposed that when the metal-semiconductor intimate contact is formed, the intrinsic surface states were broadened into a continuous distribution with a charge neutrality level, ϕ_o, located approximately at the mid-gap. Hence, they suggested that the Fermi level pinning position would then be at the centre of the semiconductor band gap.

On the other hand, Tersoff [19] developed another similar theory, where he defined a charge neutrality position, E_B, such that the MIGS wavefunctions changed from the characteristic valence band-like to conduction band-like. In agreement with Tejedor and Flores, the theory had a similar conclusion that E_B, should lie near the centre of the mid-gap and there is an argument in this case that indirect gaps should be used instead of direct gap. Originally, the theory states that the interfacial barrier height should be metal independent. However, Tersoff [20] later amended the theory to allow for a weak dependence on the metal to vary the pinning position near the centre of the gap.

Until now, the elementary principles of MIGS have been widely adopted. However, the fact that the metal overlayer can induced states into the band gap, which are capable of pinning the Fermi level in similar manner as described in the Bardeen model if they are present in sufficient large density, has been the major problem in controlling metal-semiconductor contact formation. In addition, the MIGS model has several flaws. Firstly, the model cannot account for sub-

monolayer pinning effect as observed using surface sensitive technique such as Soft X-ray Photoelectron Spectroscopy (SXPS). Since the metal contact will only behave metallically after several monolayers of coverage, the early conditions of the pinning mechanism can then be dominated by other factors. Secondly, the model neglects the effect of atomic bonding and the differential geometries of the interface. These factors cannot be underestimated as they can significantly influence the Fermi level pinning position. Therefore, taking into account these important factors, several models have been proposed and are discussed in the next section.

2.4 Unified Defect Model (UDM)

One of the drawbacks of the MIGS theory is that the effect of atomic bonding has been neglected. An attempt of describing such effect was conducted by Spicer and co-workers [21, 22], which proposed a model that accounts for defects generated at the interface. The model assumes that the defects are generated near the semiconductor surface when the metal contact is deposited onto that surface. These defects are mainly native lattice defects, which include vacancies, substitutional impurities and lattice mismatch between semiconductor and metal. The model suggests that these defects can perturb the intrinsic surface states to form electronic bands of discrete energy within the band gap. The energy for the defect generation may arise from the heat of condensation of the metal, a reaction between the semiconductor and metal atoms or from metal cluster formation. In addition, surface imperfections such as atomic steps or dislocations may also be the origin of the nucleation sites where reactions may be initiated. When present in a sufficient high density, these defects can provide the dominant pinning process during Schottky barrier formation. Zur *et al* [23] have discussed that for a low metal coverage, only a small density of defects ($\sim 10^{12}cm^{-2}$) is required to pin the Fermi level. When thicker metal coverage is used,

a higher density (~ $10^{14}cm^{-2}$) is necessary to cause Fermi level pinning due to screening effects by the metal.

The model is based on vast experimental investigations on Fermi level movements and chemical reactions at the interface as a function of metal overlayers being deposited onto clean semiconductor surfaces conducted using XPS. The advantage of this model over the MIGS model is that it can be used to explain Fermi level pinning at sub-monolayer coverage. However, the model relies on the strength of XPS in measuring the Fermi level shifts and the interfacial barrier, ϕ_{b}, during metal-semiconductor contact formation. Nevertheless, this model has its flaw, as the agreement of XPS with other techniques is doubtful. Also, the presence of the photovoltaic effect [24] may also cause an inaccurate interpretation of the extracted information. In addition, due to the natural surface sensitivity of XPS, this technique can only be used to probe Fermi level shifts for thin metal coverage and there is a possibility that the barrier is not fully formed at this stage. Therefore, when a thick metal coverage is introduced onto the semiconductor surface, a different barrier height would be expected as measured by I-V or C-V techniques.

2.5 Chemical Reactivity

So far, the models discussed previously made the assumption that the interface formed between the metal and the semiconductor is ideal and abrupt, with the composition of the semiconductor being unaffected right up to the interface. Even in the defect model, the induced states are taken to be restricted in the semiconductor near the interface. However, this is not the case as deposition of metal overlayer can disrupt the semiconductor surface through interdiffusion and chemical reactions [12]. Often, these individual elements will diffuse or intermix together without causing a significant chemical reaction to form a new compound. These reactions at the interface can extend over many monolayers into both metal and semiconductor, and produce *chemically induced*

interface states and a reacted interfacial layer. The influence of such reactions to the magnitude of the barrier height is considered in the following section. Note that although these models are based on Si and III-V semiconductors, the basic principles are relevant and can be implied to SiC contact technology.

2.5.1 Effective Work Function Model

The effect of chemical reactions at the interface cannot be underestimated. The formation of compounds as a result of interdiffusion between the metal and semiconductor has been observed to change ϕ_b drastically. Freeouf and Woodall [25] have made an attempt in describing such an effect by proposing the effective work function model. The model makes the assumption that the interfacial region was left with an excess of semiconductor anions. This anion rich layer effectively replaces the metal and forms an intimate contact with the semiconductor. Thus, it is the properties of this layer that should be accounted for in any analysis performed on the interface. Under this circumstance, the Schottky-Mott model should apply by replacing the metal work function with the effective work function, ϕ_{eff}. Hence, the Schottky-Mott relationship can now be expressed as:

$$\phi_b = \phi_{eff} - \chi_s \qquad [2.5]$$

Since the deposition of the metal overlayer disrupts the surface causing an anion rich layer next to the semiconductor, the effective work function is then originated from this anion layer and is therefore metal independent.

Various theories have been proposed relating the thermodynamic properties of the formation of metallic-like compounds at the interface. For example, Andrew and Philips [26] plotted values of ϕ_b as a function of the heat of formation, ΔH_F, of silicides. They obtained a linear straight line from the plot of ϕ_b against ΔH_F, governed by the relationship ϕ_b (eV) = 0.83 - 0.18 (ΔH_F). According to this relationship, no values of ϕ_b should exceed 0.83eV. The variation of ϕ_b with ΔH_F on various semiconductors is observed to change rapidly around the critical heat formation $(\Delta H_F)_C$ with more reactive metals giving low

values of ϕ_b. However, the failure to predict ϕ_b greater than 0.83eV has results in other more accurate models being proposed such as the 'linear interface model' by Kurtin *et al* [27] (see section 2.6.1). Nevertheless, these models have many exceptions and they can only be partly correlated to any single thermodynamic quantity.

2.5.2 Thermally Activated Pinning

A later publication by Brillson and co-workers [28] experimentally proved that the Schottky-Mott model does apply under certain conditions. In their investigation, they performed an experiment using SXPS where metals were deposited on As de-capped Molecular Beam Epitaxy (MBE) grown GaAs (100) surface at a temperature of ~100K. Brillson and co-workers predicted that the ϕ_b formed by depositing the metal on the sample at room temperature is due to the pinning of the Fermi level by gap states that arise from chemically induced defects as the metal reacts with the semiconductor surface. Therefore, in the absence of such reactions, the Schottky-Mott model should apply. In an attempt to suppress these chemical reactions, the metal-semiconductor system was maintained at a temperature of 100K. The results from Brillson showed that if the metal-semiconductor system obeys the Schottky-Mott model, ϕ_b is then linearly scaled to the metal workfunctions. In addition, they also introduced the concept that the Fermi level pinning may be *thermally activated*.

2.5.3 Electronegativity

By definition, electronegativity, χ, is a measure of the power of an atom in a molecule to attract electrons to itself. The early study by Linus Pauling [29] on the concept is based on differences of bonding energy or the electronegativity of the atoms between the elements. According to Pauling's theory, the key in quantifying the electronegativity is the ionic character (determined by the difference of the atomic electronegativities) of the single bond. If the difference is large (ionic material), the valence (or bonding) electrons will be localised

around the atom with the highest electronegativity, thus creating an imbalanced in electronic charge allocation. Conversely, for a low difference in electronegativity (covalent material), the valence electrons do not distinguish any particular atom. An element with high electronegativities tends to form solids with large work functions, ϕ. However, a precise relationship between ϕ and χ cannot be defined, as χ cannot be readily measured. Additionally, it should be highlighted that the concept of electronegativity only applies to individual atoms and that it does not take into account surface dipoles. This inadequacy has lead to further work by Kurtin *et al* [27] in attempts to understand the variation of ϕ_b for metals on semiconductor, which will be further discussed in section 2.6.1. The variation of barrier height ϕ_b of various metal on three n-type semiconductors with electronegativity χ_M is illustrated in Figure 2.4. The slope of the straight linear line fitting the data points varies from nearly zero for covalent Si to approximately one for ionic SiO_2.

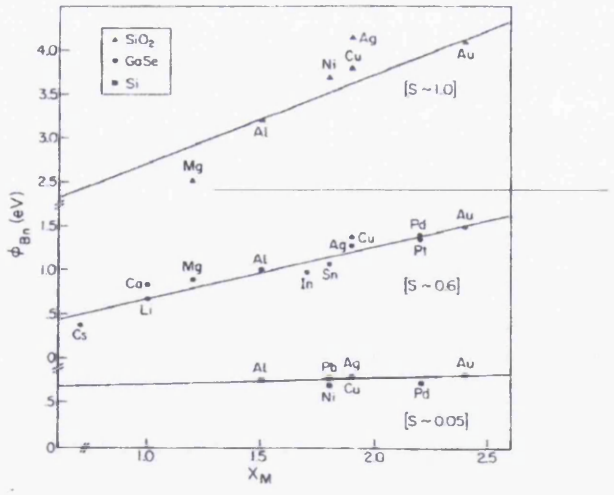

Figure 2.4: Plots of barrier height, ϕ_b of various metal on n-type semiconductors against Pauling electronegativity, χ_M of the metal [27].

2.6 Other Models

Apart from the Schottky-Mott and Bardeen model, there are other works performed in an attempt to understand the formation of metal-semiconductor contacts. Generally, these works are either the expansion of the models discussed previously or a universal model that can be implied to the metal-semiconductor interface formation phenomena. In the following sections, these models are further discussed.

2.6.1 Electronegativity Model

Recall previously in section 2.2, the proposed theoretical models only account for the reaction of Fermi level pinning due to surface states. Further on, other aspects such as MIGS and defects at the interface were considered in the unified defect model (UDM) while the effective work function model accounted for chemical effects at the interface. These early models of the metal-semiconductor interface were phenomenological in nature and were based on the empirical fact that ϕ_b for some semiconductors obeyed the Schottky limit whereas some other semiconductors followed closely the Bardeen limit. To fit this wide range of behaviour, Kurtin *et al* [27] proposed a '*linear interface model*' where the barrier energy ϕ_b was assumed to be linearly dependent on the work function of the metal, ϕ_m. This work was based on Pauling's electronegativity concept, where the ionic character of the single bonds in a diatomic molecule with the difference in atomic electronegativities determines the behaviour of the metal-semiconductor system. This concept describes the charge transfers across the metal-semiconductor interface via the difference of the metal and semiconductor electronegativities (i.e. the ionic character as described in section 2.5.3). By relating ϕ_b with the electronegativity of the metal, χ_M, instead of the work function of the metal, ϕ_m, the basic Schottky-Mott equation now becomes

$$\phi_b = S\chi_M + C \qquad [2.6]$$

where S is a dimensionless parameter that measures the sensitivity of ϕ_b to the metal known as the index of surface behaviour ($S = \delta\phi_b/\delta\chi_m$) and C is a constant. When $S \sim 1$, the system displays a pure Schottky behaviour and is determined by work function differences. Conversely, when $S \sim 0$, the system follows Bardeen behaviour and is dominated by surface states.

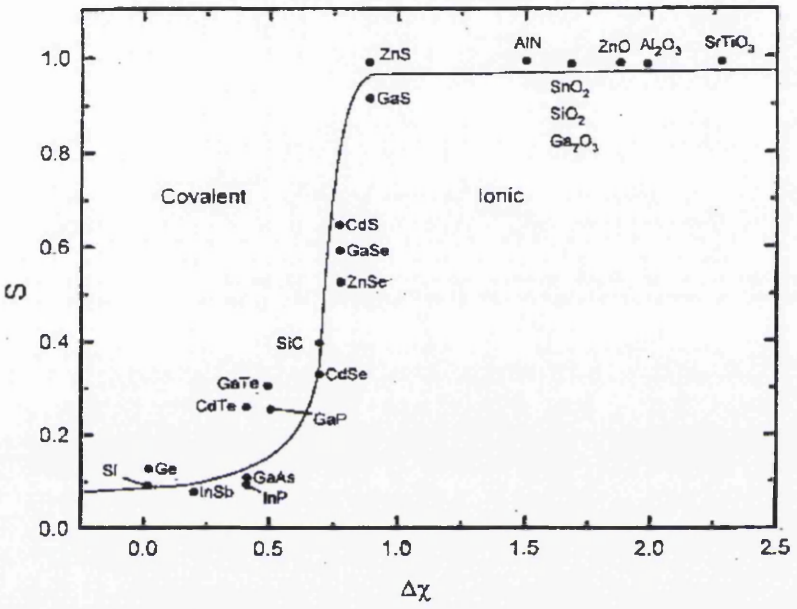

Figure 2.5: Index of interface behaviour S for various semiconductors versus the electronegativity difference $\Delta\chi$ in elemental components [27].

The plot of S against $\Delta\chi$ (as illustrated in Figure 2.5) reveals an important trend that classified the data into two regions. A region of low S (<0.1) for semiconductors with $\Delta\chi$ < 0.6 and a region of high S (>0.9) for semiconductors with $\Delta\chi$ > 0.8, connected by an abrupt transition region ($0.6<\Delta\chi<0.8$) [30]. Carbon and silicon have electronegativities of 2.55 and 1.90 respectively which corresponds to a $\Delta\chi$ = 0.65 for SiC. It has been known for years that Fermi level pinning is more common in covalent material than ionic materials [31, 32], which is in agreement with the data. However, SiC sits in the transition region ($0.6<\Delta\chi<0.8$) where Fermi level pinning plays a variable role in the mixture of

covalent and ionic bonding. Therefore, SiC is in the transition between strong Fermi level pinning (surface states) and no Fermi level pinning (no surface states). Although the linear interface model can be generally applied, the validity of S parameter is still in question. In addition, it is unlikely that this model is always applicable for interfaces formed between metals and a range of atomically clean semiconductor surfaces.

2.6.2 Cowley-Sze Model

Cowley and Sze [33] were the first to analyse the general case accounting for both surface states and work functions. Hence, this model is also referred to as the general case. This model assumes that there is a uniform density of surface states, D_S $cm^{-2}eV^{-1}$, throughout the band gap. These states are presumed to be independent of any chemical effect other than charge transfer that takes place during metal deposition. Neglecting any other contribution (such as image force lowering), the barrier height, ϕ_b, measured will then be expressed as the sum of the 'bare surface barrier height', ϕ_o, or band bending prior to metal deposition, and a Schottky-Mott term induced by the metal given by the expression:

$$\phi_b - \phi_0 = S(\phi_m - \chi) - S\phi_0 \qquad [2.7]$$

where ϕ_m is the metal work function and χ is the semiconductor electron affinity. S is a constant depending only on the density of the surface states D_S and can be written as:

$$D_S \approx 10^{13} \frac{(1-S)}{S} \qquad [2.8]$$

The common procedure in evaluating D_S is from the slope of the linear relationship between ϕ_b and ϕ_m for a range of metals on a given semiconductor. However, the values of ϕ_m quoted in the literature often vary over a range up to 0.5eV. In addition, the assumption of uniformly distributed surface states is unlikely to occur universally on all surfaces. Although the linear potential theory of Cowley and Sze has been extensively applied, it is clearly seen that the model

is too simple. Hence, taking into account the qualms of the model, care must be taken prior to application of model.

2.7 Intimate Contacts

It is important to note that commercial devices are more likely to be the case as illustrated in Figure 2.1(c), where a thin insulating layer (~ 10Å - 20Å) lies between the metal and the semiconductor preventing them from forming intimate contacts. Hence, the semiconductor surface is decoupled from the metal. However, this insulating layer is assumed to be thin enough for electrons to tunnel through it quite easily, but is thick enough to ensure that the interface states are, to a good approximation, a property of the insulator-semiconductor interface [4]. The most common type of such insulating layer is oxides (e.g. SiO_2).

Nevertheless, it is possible to obtain atomically clean surfaces through various techniques under an ultra-high vacuum environment. This includes annealing, ion sputtering or by cleaving the sample. Instead of cleaning the surface, fresh clean surfaces can also be prepared by MBE growth. These treated surfaces are free from the insulating layer and contacts deposited onto such a surface are referred to as intimate contacts. Within this work, all experiments are performed on an atomically clean surface, as it is essential to gain an understanding of such interfaces before considering more complex interfaces containing insulators.

Even though the surface is atomically abrupt and perfectly ordered, the interface is likely to change when forming intimate contacts. Firstly, the deposited metal will chemically react with the semiconductor via interdiffusion resulting in compound layers at the interface. Secondly, interface states are generated through structural changes from the initially ordered surface to the subsequently formed interface. These changes includes lattice mismatch between the metal and the semiconductor, lattice defects (atomic steps on cleaved surfaces, vacancies and anti-sites defects). These defects, existing in

large densities, will lead to Fermi level pinning as described by the unified defect model (UDM) [21, 22] in section 2.4.

On the other hand, it is possible that the wavefunctions of those electrons in the metal with energies corresponding to the forbidden gap in the semiconductor can penetrate into the semiconductor in the form of exponentially damped evanescent waves [14]. This phenomenon represents a transfer of charge from the metal to the semiconductor, generating new interface states. The existing intrinsic electron states, which might have been present at the semiconductor surface, will then be replaced by these new states, which is the MIGS. In a similar manner, when these MIGS exist in a sufficient amount, they will be able to cause Fermi level pinning as described in the MIGS theory in section 2.3.2.1.

Fermi level pinning for both UDM and MIGS is basically the same and they can be implied in the Bardeen theory, with the presence of a semiconductor layer between the surface of the metal and the centre of the depletion zone instead of an insulating layer as described in section 2.2.2. Also, it is often difficult to establish the precise crystallographic structure of the interfaces. Although modern surface science technique can provide information on interface structure at low overlayer coverage, there is no certainty that the interface remains the same as the film thickness increases. Hence, there is a possibility of uncertainties in such structures that needs to be considered when analysing the interfaces.

2.8 Current Transport Mechanisms

Previously, the mechanism of metal-semiconductor contact formation was discussed in terms of proposed models accounting for the Schottky barrier height ϕ_b. However, this investigation would not be complete if the electron transport mechanisms across this junction were not discussed. In this work, the extraction of ϕ_b is taken under the influence of an applied bias. Therefore, it is essential to

develop a strong theoretical background for an accurate interpretation of the current-voltage relationship to the extracted value of ϕ_b.

There are three main transport mechanisms in which the electron can cross the junction under applied bias, which are listed below and illustrated schematically in Figure 2.6.

-a- Emission of electrons from the semiconductor over the top of the barrier into the metal

-b- Quantum-mechanical tunnelling through the barrier

-c- Recombination in either the space-charge or neutral region

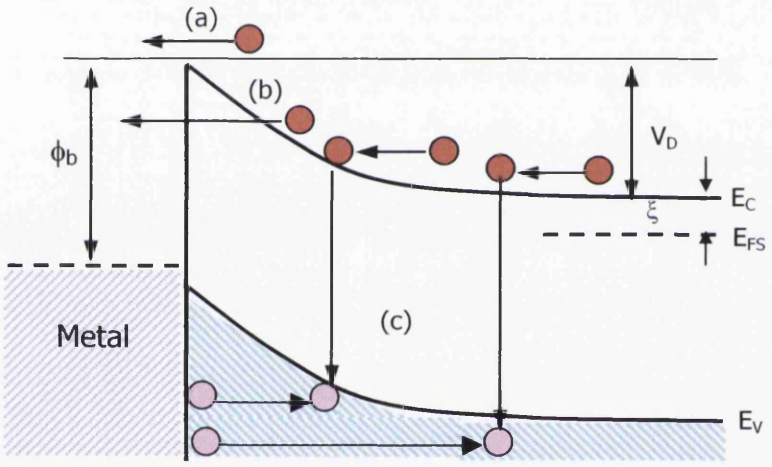

Figure 2.6: Schematic diagram of the electron transport mechanism across a forward-biased Schottky barrier (a) thermionic emission (b) quantum-mechanical tunnelling (c) recombination in the space charge or neutral region.

All the components listed above are present at the same time and they contribute to the current in different extents depending on the semiconductor fabrication process, temperature and doping concentration. Therefore, we could say that the transport mechanisms are only dependent on the shape and size of the barrier and not on the aspects that govern the formation of the interface. Although this is the case, under certain circumstances, it is possible to find a

single process that dominates the conduction mechanism, which dictates the main features of the current-voltage (I-V) characteristic of the interface. In this section, the conditions of the leading mechanism will be discussed in detail both quantitative and qualitatively.

2.8.1 Emission Over The Barrier

Prior to the emission from the semiconductor to the metal, the electrons will have to move within the semiconductor to the interface. The traversing route of the electrons from the depletion region of the semiconductor is regulated by diffusion and drift in the electric field of the barrier. Upon arrival at the interface, the electrons will then be emitted over the barrier into the metal. The emission into the metal is determined by the rate of transfer of electrons across the boundary between the metal and the semiconductor. This process occurs by thermionic emission, which acts concurrently in series with the drift and diffusion. The interfacial current will then be determined mainly by whichever causes the larger obstruction to the flow of the electrons. Although the real current is the combination of these two, experimental results shows that thermionic emission theory agrees best with the experimental data. A more detailed description of the mechanism can be found in Rhoderick and Williams [4].

2.8.1.1 Thermionic Emission

This section is based on the work by Bethe [11], where the thermionic emission theory is used to derive the I-V characteristic of the Schottky barrier when a metal-semiconductor interface is formed. The theory assumes that the effect of drift and diffusion in the depletion region is negligible and that the current is primarily controlled by the transfer of electron across the barrier. The positive direction of charge flow is taken as being from the semiconductor to the metal and any collisions in the depletion region are also neglected. The Maxwell-Boltzmann statistics is used to describe the electron density probability.

According to the kinetic theory, the current density, J, at the interface is given as [12]

$$J = q\,n\,v \qquad [2.9]$$

where q is the electrical charge of an electron, n is the number of electrons per unit volume and v is the mean velocity of the electrons. Thus the number of electrons passing in the x- direction will be

$$J = qn\left(\sqrt{\frac{kT}{2\pi m^*}}\right)\exp\left(\frac{-m^* v_{ox}^2}{2kT}\right) \qquad [2.10]$$

where v_{ox} is the minimum velocity required for an electron to pass through the barrier and m^* is the effective electron mass. Note that electrons with velocity less than v_{ox} do not contribute to J. At thermal equilibrium, we have

$$\frac{1}{2}m^* v_{ox}^2 = qV_D \qquad [2.11]$$

where V_D is the built-in potential of the semiconductor. Applying a forward bias, V_F, we now have

$$\frac{1}{2}m^* v_{ox}^2 = q(V_D - V_F) \qquad [2.12]$$

Therefore, the forward current density J_+ will be

$$J_+ = qn\left(\sqrt{\frac{kT}{2\pi m^*}}\right)\exp\left(\frac{-q(V_D - V_F)}{kT}\right) \qquad [2.13]$$

From Boltzmann statistics, the electron concentration at the interface is given by:

$$n = 2\left(\frac{2\pi m^* kT}{h^2}\right)^{3/2}\exp\left(\frac{-q(\phi_b - V_F)}{kT}\right) \qquad [2.14]$$

Substituting equation [2.14] into [2.13] yields:

$$J_+ = A^* T^2 \exp\left(\frac{-q\phi_b}{kT}\right)\exp\left(\frac{qV_F}{kT}\right) \qquad [2.15]$$

where ϕ_b is the Schottky barrier height and A^* is the Richardson constant given as

$$A^* = \frac{4\pi q m^* k^2}{h^3} \qquad [2.16]$$

The number of electrons flowing from the metal into the semiconductor is independent of the bias condition and the barrier height encountered by the electrons is constant. Therefore the total current density, J_{Total}, at equilibrium (V=0) must be zero and thus also equal to the total current density flowing through in either direction (i.e. $J_{Total} = J_+ + J_-$), which gives

$$J_+ = -(J_-)_{V=0} = -A^* T^2 \exp\left(\frac{-q\phi_b}{kT}\right) \qquad [2.17]$$

Hence, the total current density due to thermionic emission is:

$$J_{Total} = A^* T^2 \exp\left(\frac{-q\phi_b}{kT}\right)\left(\exp\left(\frac{qV}{kT}\right) - 1\right) \qquad [2.18]$$

2.8.2 Quantum Mechanical Tunnelling

Classically, electrons cannot be emitted without possession of energy greater than the potential maximum of the barrier. However, this is not the case as electrons can tunnel through the barrier. In quantum mechanics, an electron has a non-zero probability of crossing a barrier with a potential greater than its energy. The wave vector of the electron wave becomes imaginary within the barrier and the wave function decays exponentially with distance.

The tunnelling phenomenon can occur in two ways as illustrated in Figure 2.7. When a semiconductor is heavily doped (degenerate) and at very low temperature, the electrons whose energy lies close to the Fermi level in the semiconductor can tunnel across the barrier, which generates a forward current. This type of tunnelling is known as *field emission*. However, when the temperature or the doping is increased, the probability of tunnelling increases rapidly as electrons are excited to higher energies and the distance from the electron to the barrier is decreased. Thus, the electrons 'see' a thinner and lower barrier as its energy is increased. Meanwhile, the number of excited electrons decreases very rapidly with increasing energy, and there will be a maximum

contribution to the current from the electrons, which have an energy E_M above the bottom of the conduction band. This is the second possible tunnelling process known as *thermionic-field emission*. Ultimately, if the temperature is raised further, a point is eventually reached in which almost all electrons have an energy greater than the barrier maximum. At this point, tunnelling effect is negligible and pure thermionic emission will occur.

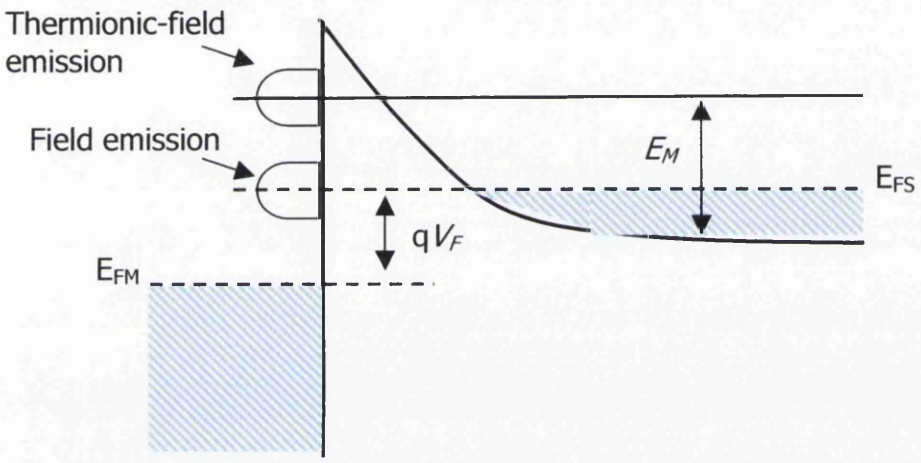

Figure 2.7: Two possible tunnelling mechanisms (field and thermionic-field emission) allowed for a Schottky barrier under forward bias of V_F.

The concept of tunnelling can be further explained by applying the WKB approximation to a triangular barrier [4]. The probability, P, of a triangular barrier being tunnelled through by an electron with energy ΔE less than the height of the barrier is given as

$$P = \exp\left\{-\frac{4}{3}(2qm^*)^{\frac{1}{2}}(\Delta E)^{\frac{3}{2}} / \hbar\varepsilon\right\} \qquad [2.19]$$

where ε is the electric field in the barrier. This can be applied to a Schottky barrier with a diffusion potential of V_D and if ΔE is small enough for the barrier to be consider as triangular. Based on the depletion approximation, the maximum field in the barrier, ε_{max} is given by

$$\varepsilon_{max} = (2q N_d V_D/\varepsilon_s)^{1/2} \quad [2.20]$$

Substituting equation [2.20] into [2.19] yields:

$$P = \exp\left\{-\frac{2}{3}(\Delta E)^{\frac{3}{2}} / E_{00} V_D^{\frac{1}{2}}\right\} \quad [2.21]$$

with

$$E_{00} = \frac{\hbar}{2}\left[\frac{N_d}{m^* \varepsilon_s}\right]^{\frac{1}{2}} \quad [2.22]$$

where N_d is the donor concentration (m^{-3}) and ε_s is the permittivity in the semiconductor. Note that E_{00} is an important parameter in tunnelling theory [13], the ratio (kT/qE_{00}) determines the relative importance of thermionic field emission and field emission. If $kT << qE_{00}$, field emission is likely to occur and if $kT >> qE_{00}$, thermionic emission should be expected. However, if $kT \sim qE_{00}$, then a combination of thermionic-field emission will arise. Since this work often involves the formation of an Ohmic contact, which requires a low contact resistance, it is essential to note that field emission only occurs in degenerate semiconductors. The main concern in this case is the specific contact resistance, R_c, around zero bias (i.e. $dV/dJ)_{V=0}$. For low doping (thermionic-emission regime), R_c is independent of N_d. Meanwhile, for high doping (field emission regime), R_c is inversely proportional to the square root of N_d. Thus, for Ohmic contacts formed in degenerate semiconductors, the high resistivity of the barrier has been overcome by the tunnelling of electrons from semiconductor to metal via field emission.

The current-voltage relationship can be written in a similar manner as in the thermionic emission theory and is given as

$$J = J_S \exp\left(\frac{V}{E_0}\right)\left\{1 - \exp\left(\frac{-qV}{kT}\right)\right\} \quad [2.23]$$

where $E_0 = E_{00}$ for field emission and $E_0 = E_{00}\ coth(qE_{00}/kT)$ for thermionic field emission. For thermionic-field emission, the pre-exponential term, J_S is given by [13],

$$J_S = A^* T^2 \exp\left(\frac{-q\xi}{kT}\right)\frac{q}{kT}\frac{\left\{\pi E_{00}\left(\phi_b - V - \xi\right)\right\}^{\frac{1}{2}}}{\cosh\left(qE_{00}/kT\right)}\exp\left(\frac{-\phi_b - \xi}{E_0}\right) \quad [2.24]$$

A more exact and detailed description on the effect of temperature, barrier height and other semiconductor parameters can be found elsewhere [4].

2.8.3 Recombination

Among all transport mechanism discussed previously, recombination currents are comparatively small but their effect are often apparent especially in low forward current regime. Although small in magnitude, these currents are generated by the electrons that are transported across the interface via a series of recombination-generation steps, which can occur in either the depletion region through localised states or in the bulk of the semiconductor by hole injection. For an n-type semiconductor, hole injection recombination occurs when the height of the Schottky barrier is greater than half the band gap, in which the semiconductor region adjacent to the metal becomes p-type and consists of a high density of holes.

For a low forward bias, the recombination current density, J_R, is given by:

$$J_R = J_{RO}\exp\left(\frac{qV}{2kT}\right)\left\{1 - \exp\left(\frac{-qV}{kT}\right)\right\} \quad [2.25]$$

and

$$J_{RO} = qn_i\frac{w}{2\tau_R} \quad [2.26]$$

where n_i is the intrinsic electron concentration, w is the width of the depletion region and τ_R is the lifetime in the depletion region.

2.9 Extraction of Schottky Barrier Height

Upon understanding the mechanism of metal-semiconductor contacts formation, it is essential to recognize the value of the Schottky parameters (i.e. Schottky barrier height, ϕ_b and ideality factor, n) in order to determine the quality of the contact. As mentioned previously, it is the height of this barrier

that determines the rectifying properties of the contact, thus how good is the contact in preventing unnecessary voltage flow before breakdown. Meanwhile, the ideality factor is a parameter that relates the closeness of the extracted value of ϕ_b in obeying the thermionic emission theory. To date, there are several techniques being implemented to extract ϕ_b and n. The most common used techniques are the current-voltage (I-V), capacitance-voltage (C-V), photo response and photoelectron spectroscopy. In this work, the early stages of the metal-semiconductor contact formation is investigated using the surface sensitive technique of photoelectron spectroscopy (i.e. X-ray photoelectron spectroscopy, XPS) and the fully formed contact are assessed using the I-V technique. Hence, this section only concentrates on these two techniques and all other methods can be found elsewhere [4, 7, 12].

2.9.1 Current-Voltage Technique

As suggested from its name, this technique measures the I-V characteristics of the Schottky diode. However, for all materials, it is often that the current is expressed as current density, J, (i.e. current per unit area) as a function of applied voltage, V, giving a J-V characteristic curve as illustrated in Figure 2.8.

This technique is based on the thermionic emission theory as discussed previously in section 2.8.1.1. From the theory, the total current density is given by;

$$J = J_0\left[\exp\left(qV/kT\right) - 1\right] \qquad [2.27]$$

where $J_0 = A^{**}T^2 \exp\left[-q(\phi_b - \Delta\phi_{bi})/kT\right]$. Here, A^{**} is the modified Richardson constant taking into account the effective mass of electrons in the semiconductor, quantum-mechanical reflection of those electrons which are unable to negotiate the barrier and phonon scattering of electrons between the top of the barrier and the surface of the metal. Also, for ease of discussion, ϕ_b - $\Delta\phi_{bi}$ is taken to be the effective barrier height, ϕ_e.

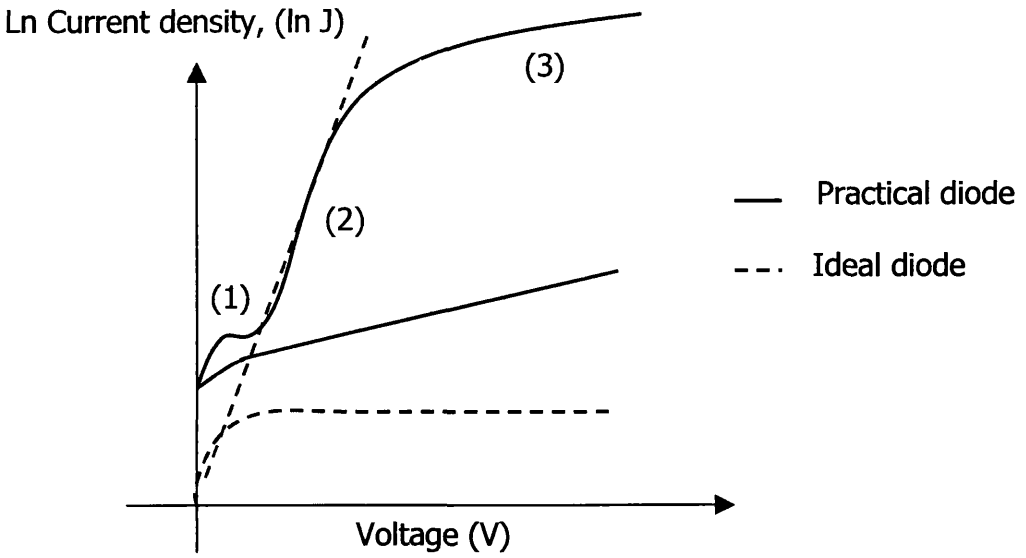

Figure 2.8: J – V characteristic of an ideal Schottky diode and a practical fabricated Schottky diode. Region (1) corresponds to recombination, (2) thermionic emission and (3) series resistance (see section 2.8).

However, as illustrated from Figure 2.6, the practical diodes never satisfy the ideal equation [2.27] precisely, but are more closely described by the modified equation,

$$J = J_0 \exp(qV / nkT)[1 - \exp(-qV / kT)] \qquad [2.28]$$

where n is the ideality factor that might be dependent on temperature and is approximately independent of V and is greater than unity. For values of $V > 3kT/q$, equation [2.27] can be further simplified as:

$$J = J_0 \exp(qV / nkT) \qquad [2.29]$$

For the plot of ln J against V in the forward direction (Figure 2.8), the dotted line represents the ideal Schottky characteristic (i.e. equation [2.27]), which is a straight linear line for region of $V > 3kT/q$. Meanwhile, the solid line represents the characteristic of practical diode. The initial 'bump' in region (1) corresponds to recombination effect, the linear region (2) originates from the thermionic

emission and the saturated region (3) relates to the series resistance of the metal-semiconductor contact.

In the extraction of the Schottky parameters (i.e. ϕ_b and n), the measured forward characteristic of the fabricated diode is the curve fitted with a first order linear function, $y = mx+c$. Rearranging equation [2.28] by taking the natural log of both sides we now have;

$$Ln\, J = Ln\, J_0 + (qV/nKT) \qquad [2.30]$$

or

$$Ln\, J = (qV/nKT) + Ln\, J_0 \qquad [2.31]$$

Comparing the above equation with the basic linear equation y = mx+c, we can determine n from the slope of the graph, m, and ϕ_b from the intercept point, c, in the Y-axis. Therefore, the ideality factor n is given by

$$n = q / mKT \qquad [2.32]$$

and by evaluating J_o, we have ϕ_b

$$\phi_b = \{Ln\,(A^*T^2) - Ln\, J_o\} /(q/KT) \qquad [2.33]$$

The determination of barrier height from this technique is only reliable if one can be confident that the current is determined by thermionic emission theory, i.e. the approximation of the obtained values compared to the theory and this corresponds to the ideality factor n. For an ideal diode, n is equal to unity, which corresponds to a linear straight line in the forward characteristic as shown in Figure 2.8. Therefore, all fabricated diodes are aimed to have a low value of n. For large values of n or non-linear characteristics, the diode is far from ideal, probably due to the presence of a thick interfacial layer or due to the recombination in the depletion region [4]. In this case, the current will not be determined by the theory. By obtaining the values of these parameters, the quality of the Schottky contact fabricated can be easily analysed.

2.9.2 Photoelectron Spectroscopy

Apart from practical I-V measurements, ϕ_b can also be evaluated by photoelectron spectroscopy. Based on the classical theory of 'photoelectric effect'

(see Chapter 3), photoelectron spectroscopy offers a wide range of information through the energy distribution curve, (EDC) as illustrated in Figure 2.9. The EDC is a measure of the number of electrons emitted at each value of the kinetic energy from zero up to some maximum value, which is determined by the energy of the incident photons. In this work, we have utilized the X-ray photoelectron spectroscopy (XPS) to measure the value of ϕ_b at the initial stage of metal-semiconductor interface formation. The reason for this is that the operation of XPS is limited to the surface level by inelastic scattering from the photoemission process occurring at depths of approximately 20Å to 40Å from the surface.

To extract the value of ϕ_b from the EDC, it is necessary to establish a reference level in the emitted photoemission spectrum. A rule of thumb is applied for the photoelectron spectroscopy technique, where the Fermi level is taken as the reference point. This is achieved by obtaining the Fermi level position with respect to the valence band maximum by measuring a spectrum for a metal in contact with the semiconductor or by simply measuring the emission spectrum from the metal sample holder [34]. Hence, those electrons emerging with the largest kinetic energies originate at the Fermi level of the metal, which is the same as the Fermi level of the semiconductor (see Figure 2.9). Upon establishing the reference level, ϕ_b can be easily obtained by deducting the difference between the maximum energies of the semiconductor and metal respectively given by the relationship;

$$\phi_b = E_g - (E_F - E_{VS}) \qquad [2.34]$$

where E_g is the energy gap, E_F is the Fermi level and E_{VS} is the valence band maximum. However, this only implies on a monochromatic X-rays. In this work, the formation of Schottky barriers is investigated by observing the shifts in kinetic energies of peaks originating from the core levels. The kinetic energy at the final deposition (i.e. fully formed barrier) is subtracted from the kinetic energy at the initial condition (i.e. clean surface before metal contact deposition)

giving the value of ϕ_b or $\Delta\phi_b$ (if the surface is originally pinned) of the examined metal-semiconductor contact.

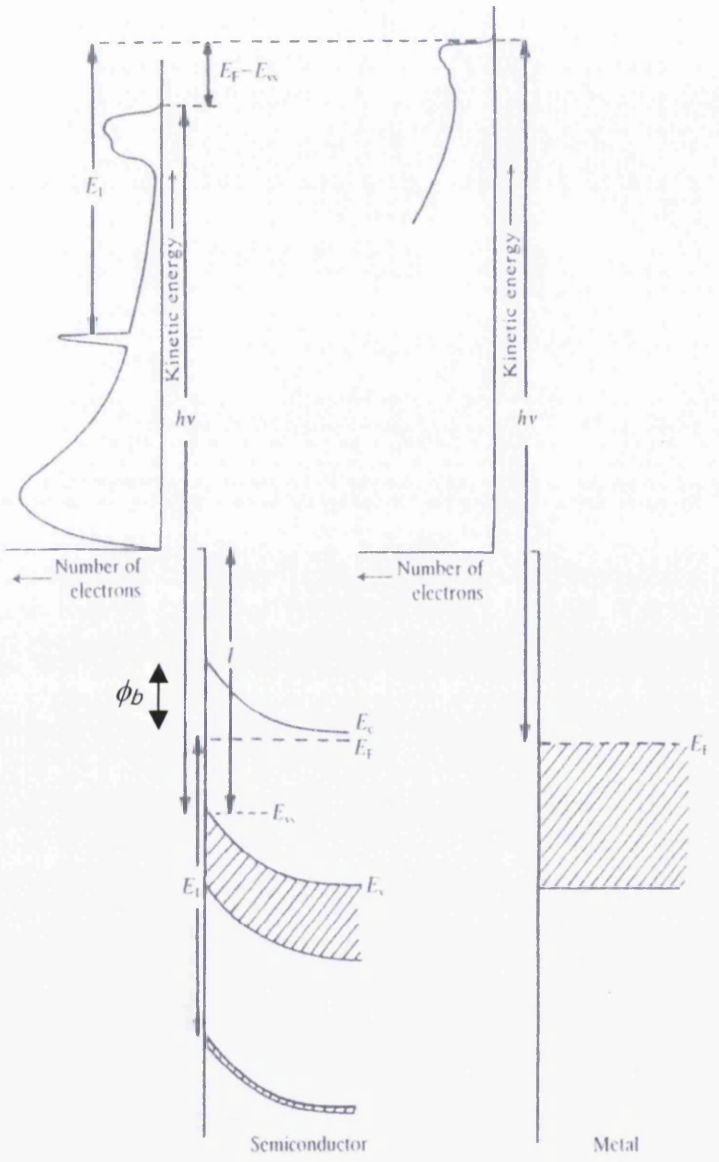

Figure 2.9: Energy relationship in photoelectron emission spectroscopy [4].

One of the drawbacks in photoelectron spectroscopy is that the technique is only valid for very small surface coverage (less than a monolayer). In addition, the analysis assumes that photoemission from the metal coverage itself has been

ignored for simplicity in the measurement of ϕ_b. Hence, for thicker metal coverages (a few Å), the photoemission from the metal overlayer tends to mask that from the substrate resulting in difficulty in determining $E_F - E_{VS}$. Since this technique essentially measures E_{VS} at the surface as a reference point, therefore, the true barrier height can only be determined if the energy gap, E_g has the same value at the surface as in the bulk. This might not be the case if there is considerable metal silicide formation or intermixing at the interface. Thus, these conditions have to be taken into consideration when measuring ϕ_b using XPS.

2.10 References

[1] F. Braun, Pogg. Ann., **153**, 556 (1874).

[2] W. Schottky, Naturwissenschaften, **26**, 843 (1938).

[3] N. F. Mott, Proc. Cambr. Phil. Soc., **34**, 568 (1938).

[4] E. H. Rhoderick and R. H. Williams, 'Metal- Semiconductor Contacts', Oxford University Press, (1988).

[5] S. P. Wilks, PhD Thesis, University of Wales Cardiff, (1992).

[6] J. Bardeen, Phys. Rev. Lett., **71**, 717-727 (1947).

[7] Gary Y. Robinson, Chapter 2, 'Schottky Diodes and Ohmic Contacts for the III-V Semiconductors', Edit. C. W. Wilmsen, Plenum Press (1985).

[8] R. I. G. Uhrberg, G. V. Hansson, J. M. Nicholls and S. A. Flodstom, Phys. Rev. Lett. **48**, 1032 (1982).

[9] I. E. Tamm, Phys. Z. Sowjet., **1**, 733, (1932).

[10] W. Shockley, Phys. Rev., **56**, 317 (1939).

[11] H. A. Bethe, M.I.T. Radiation Lab., Rep. 43-12, (1942).

[12] K. N. Tu, J. W. Mayer and L. C. Feldman, 'Electronic Thin Film Science for Electrical Engineers and Materials Scientist', Macmillan Publishing Company, (1992).

[13] F. A. Padovani and R. Stratton, Solid State Electronics, **9**, 695 (1966).

[14] V. Heine, Phys. Rev., **A138**, 1689, (1965).

[15] S. G. Louie and M. L. Cohen, Phys. Rev., **B13**, 4172, (1976).

[16] S. G. Louie, J. R. Chelikowsky and M. L. Cohen, Phys. Rev., **B15**, 2154, (1977).

[17] J. Ihm, S. J. Louie and M. L. Cohen, Phys. Rev., **B18**, 4172, (1978).

[18] C.Tejedor, F. Flores and E. Louis, J. Phys. C: Solid State Phys., **10**, 2163, (1977).

[19] J. Tersoff, Phys. Rev. Lett., **52**, 465 (1984).

[20] J. Tersoff, Phys. Rev. Lett., **B32**, 6968 (1985).

[21] W. E. Spicer, I. Lindau, P. Skeath and C. Y. Su, J. Vac. Tech., **17**, 1019, (1980).

[22] W. E. Spicer, I. Lindau, P. Skeath, C. Y. Su and P. W. Chye, Phys. Rev. Lett., **44**, 420, (1980).

[23] A. Zur, T. C. McGill and D. L. Smith, Phys. Rev. B, **28**, 2060, (1983).

[24] M. Hecht, J. Vac. Sci. Technol. B, **8**, 1018, (1990).

[25] J. L. Freeouf and J. M. Woodall, J. Vac. Sci. Tech., **21**, 574 (1982).

[26] J. M. Andrews and J. C. Philips, Phys. Rev. Lett., **35**, 56 (1975).

[27] S. Kurtin, T. C. McGill and C. A. Mead, Phys. Rev. Lett., **22**, 3212 (1969).

[28] L. J. Brillson, C. F. Brucker, A. D. Katnani, N. G. Stoffel, R. Daniels and G. Margaritondo, J. Vac. Sci. Tech., **21**, 564 (1982).

[29] L. N. Pauling, 'The nature of the chemical bond', 2nd edition, Cornell University Press, Ithaca, New York (1960).

[30] M. J. Bozack, Phys. Stat. Sol. B, **202**, 549 (1997).

[31] C. A. Mead, Appl. Phys. Lett., **6**, 103 (1965).

[32] C. A. Mead, Solid State Electronics, **9**, 1023 (1966).

[33] A. M. Cowley and S. M. Sze, J. Appl. Phys., **36**, 3212 (1965).

[34] M. P. Seah and W. A. Dench, 'Surface and Interface Analysis, Vol 1- Auger and X-ray Photoelectron Spectroscopy', Edition 2 (1990).

Chapter 3

X-Ray Photoelectron Spectroscopy

3.1 Introduction

X-ray Photoelectron Spectroscopy (XPS) is one of the most powerful non-destructive surface science technique applied to study chemical, electrical and structural properties of surfaces and interfaces. In this research, XPS has been implemented as the main characterisation technique. Hence, in order to further elucidate the interpretation of the experimental results; it is essential to understand the theoretical background of this useful technique. This chapter presents an outline of the basic concepts and underlying principles of the physical phenomena involved within the technique. In addition, brief introductions to low electron energy diffraction (LEED) and Scanning Tunnelling Microscopy (STM) techniques, which were used occasionally, are included at the end of the chapter.

3.2 Basic Principles

In essence, photoelectron spectroscopy is based on the photoelectric effect, which is the primary interaction of photons with solid and the occurring phenomena is known as the photoemission process. This technique is widely used in surface science and material characterisation as it offers quantitative and

qualitative information at a surface-sensitive scale. Operating in an UHV environment, photoelectron spectrometer consists of a source (an X-ray source for the case of XPS), an electron energy analyser and a data recording, processing and output system. In the system, the sample surface is irradiated by photons with energy $h\nu$, emitted by the X-ray source. An electron then absorbs the photon energy and provided that this photon energy is greater than the sum of the binding energy E_B of the electron and the work function ϕ of the instrument, the excited electron, also known as photoelectron will then be ejected from the surface with a kinetic energy E_K. Assuming the photoemission process is elastic, Einstein conservation law [1] of energy yields:

$$E_K = h\nu - \phi - E_i \qquad [3.1]$$

where E_i is the initial state energy of the electron in the solid. The initial state energy, as proposed by Koopman's theorem [2, 13] can be approximated by the binding energy of the electron in the solid. However, this approximation has neglected the effects of the core hole created by photoionisation. The remaining electrons in the atom will tend to relax to a lower energy states in order to screen the recently created hole from the nucleus. Hence, an excess energy is added to the kinetic energy of the ejected photoelectron. Upon detection, this effect results in inaccuracy as it gave the appearance that the photoelectron originated from a lower binding energy. Nevertheless, this approximation has been widely applied to demonstrate the photoemission process.

After escaping from the surface of the solid, the photoelectrons are collected by an electron detector where their energies are measured by an electron energy analyser. The result from the analyser is displayed in terms of an energy distribution curve (EDC) representing the initial states of the electrons or the density of states of the solid [3] as illustrated in Figure 3.1. Essentially, the distinctive features of the EDC are the sharp discrete peaks representing the core level electron emission and the broad valence band features at higher kinetic energy. Apart from the discrete peaks, the EDC also consists of an attenuating featureless background corresponding to the emission of electrons, which have

suffered inelastic scattering during the propagation through the solid to the surface. Thus, the EDC cannot directly represent the density of the filled state. Meanwhile, since each element has a unique set of core level energies; the sharp discrete peaks in the EDC spectrum can be mathematically deconvoluted using equation [3.1] to represent the binding energies associated with the elements present within the sample. This feature allows the chemical composition near the surface of the sample to be ascertained and thus XPS is also known as electron spectroscopy for chemical analysis (ESCA). Elegantly, additional information on structural, electrical and chemical properties can be extracted from the spectrum by further analysis as discussed in section 3.4.2.

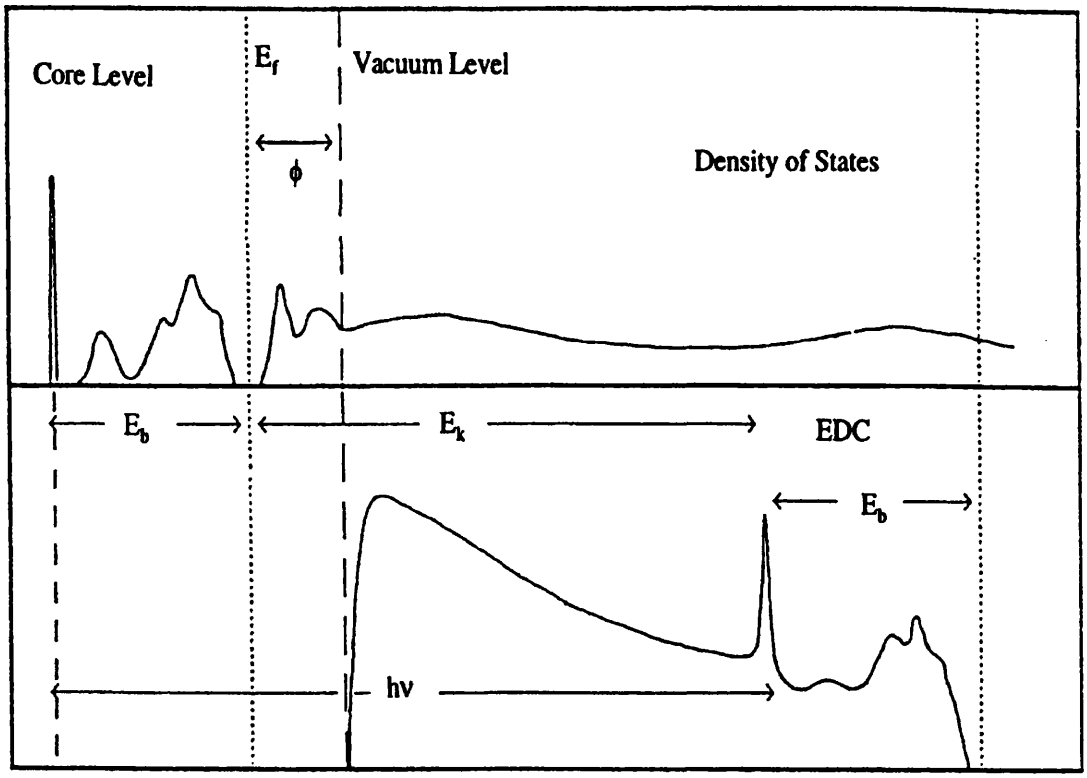

Figure 3.1: Schematic diagram of the relationship between the initial density of states in a solid and the photoelectron energy distribution curve (EDC) via photoemission process.

3.3 Photoemission Theory

Various theories and models have been proposed in order to describe the photoemission process. Among these theories, the most accurate ones are those based on a single quantum mechanical event [4], from the initial absorption of a photon to the emission and finally the detection of a photoelectron. Although these theories do give an accurate account of the process, they are extremely complex and lead towards complicated formulations. However, the photoemission process can be most simply described by 'The Three Step Model' [5,6]. In its simplest description, this model describes the basic concepts of the photoemission process neglecting many body effects, such as electron-electron interactions and inelastic scattering of the electrons and mainly concentrate on the elastically scattered electrons. Even in its simplest form, this model can smartly explain the experimental observations presented in this work. Therefore, this 'Three Step Model' will be described in the following section as the basis of understanding the physical principles beneath the photoemission process. Additional aspects such as the wave function properties at the interface and cross sections will also be discussed.

3.3.1 The Three Step Model

According to this model, the photoemission process can be viewed as a three-step process, as follows:

- Photoexcitation of an electron, P (E, $h\nu$)
- Transport and propagation of the electron through the solid, T (E, $h\nu$)
- Escape of the electron from the solid surface into vacuum, D (E, $h\nu$)

In all steps, the probability (P, T and D) is assumed to be dependent on the initial electron energy, E_i, and the incident photon energy, $h\nu$. In other words, only elastically scattered electrons are taken into account. The resultant photocurrent (J), is expressed as the product of these three steps:

$$J(E, h\nu) = P(E, h\nu)\, T(E, h\nu)\, D(E, h\nu) \qquad [3.2]$$

Step One: Photoexcitation

As the model is concentrating only on unscattered electrons, an independent particle approach in the photoexcitation process is assumed. Therefore, the system can be approximated by the single-particle Hamiltonian [6]

$$\hat{H}_0 = \frac{\hat{p}^2}{2m} + V(r) \qquad [3.3]$$

where $\hat{p}$ is the momentum operator, m is the mass of the electron and V(r) is a self-consistent screened potential energy operator which describes the effects of the other electrons on the independent electron including surface effects.

The quantum mechanical interaction with a photon is described by an electromagnetic wave vector potential **A**, which modifies the momentum operator, thus the momentum operator becomes:

$$\hat{p} + \frac{e}{c}A \qquad [3.4]$$

By substituting equation [3.4] into [3.3], the new perturbed energy Hamiltonian can then be represented as:

$$\hat{H} = \frac{1}{2m}\left(\hat{p} + \frac{e}{c}A\right)^2 + V(\mathbf{r}) \qquad [3.5]$$

Expanding the above equation we have:

$$\hat{H} = \frac{\hat{p}^2}{2m} + V(\mathbf{r}) + \frac{e}{2mc}(\hat{p}.\mathbf{A} + \mathbf{A}.\hat{p}) + \frac{e^2\mathbf{A}^2}{2mc^2} \qquad [3.6]$$

Rewrite the equation again substituting equation [3.3] yields:

$$\hat{H} = \hat{H}_0 + \hat{W} \qquad [3.7]$$

where $\hat{W}$ is termed as the electron-radiation interaction Hamiltonian. Applying the dipole approximation [7], which includes only linear terms in **A** neglecting its spatial variation to ensure $\nabla . \mathbf{A} = 0$, the electron-radiation interaction Hamiltonian can be simplified as

$$\hat{W} = \frac{e}{mc}(\mathbf{A}.\hat{p}) \qquad [3.8]$$

Hence, the Hamiltonian can now be written as:

$$\hat{H} = \hat{H}_0 + \frac{e}{mc}(\mathbf{A}.\hat{p}) \qquad [3.9]$$

Nevertheless, the actual probability of the transition must be taken into account. According to the Fermi's Golden Rule [8], the probability of transition P_{fi} from the initial state $|\psi_i\rangle$ at energy E_i to the final state $|\psi_f\rangle$ at energy E_f is proportional to the square of the matrix element between the two states such that

$$P_{fi} = \frac{2\pi}{\hbar}\left|\langle\psi_f \mid \hat{W} \mid \psi_i\rangle\right|^2 \delta(E_f - E_i - h\nu) \qquad [3.10]$$

where the energy δ-function ensures that the transitions between initial and final states are consistent with the conservation of energy. The resulting photocurrent in the photoexcitation process can be written as:

$$P(E,h\nu) = \frac{2\pi}{\hbar}\sum_i \left|\langle\psi_f \mid \hat{W} \mid \psi_i\rangle\right|^2 \delta(E_f - E_i - h\nu) \qquad [3.11]$$

The photocurrent in equation [3.11] is the sum over all initial states. This is based on an approximation that if the final state energy is high enough (e.g. $\geq$ 20eV) then the density of final states will be great enough to prevent modulation of the photoexcitation current. However, if the final state energy is very low then the final state density would have an influence on the observed photocurrent. This approximation is valid for the case of XPS. Hence, the measured photocurrent is therefore the characteristic of the initial density of states.

Step Two: Transport and Propagation of Electron Through the Solid

Subsequent to the absorption of photon energy, the excited electrons must travel through the solid to reach the surface in order to be emitted and detected by a spectrometer. On the way through the solid, these electrons are more likely to be scattered, thus the resulting photocurrent will be attenuated by the propagation probability T (E, $h\nu$). This probability can be expressed as a function of the travelling distance, d of the electron within the solid and the

inelastic mean free path of the electron λ(E) (see section 3.4.1.1) and is written as:

$$T(E, h\nu) = \exp\left(-\frac{d}{\lambda(E)}\right) \qquad [3.12]$$

From the equation, the probability will be a constant if the travelling distance d is much greater than the inelastic mean free path λ(E).

Step Three: Escape of the electron from the solid surface into vacuum

Upon reaching the surface, the possibility of the electrons to escape into the vacuum is determined by its final state energy relative to the work function ϕ of the solid. In order to escape, the electrons must have a momentum component and enough energy to overcome the work function of the solid. This probability can be represented by a step function probability known as the escaping probability D (E). This probability is equal to unity if the photoelectron has enough energy and momentum normal to the surface; and it is simply zero if the photoelectron does not meet the requirements. This criterion can easily be expressed as:

$$D(E) = 0 \qquad \text{if } E_{norm} - E_{vac} < \phi \qquad [3.13]$$

$$D(E) = 1 \qquad \text{if } E_{norm} - E_{vac} \geq \phi \qquad [3.14]$$

where E_{norm} is the component of the final state energy normal to the surface and E_{vac} is the vacuum level of the solid.

Finally, by combining these three steps, the overall expression for the photocurrent J (E, $h\nu$) is simply the product of the probabilities

$$J(E,h\upsilon) = \frac{2\pi}{\hbar}\sum_i \left|\langle\psi_f \mid \hat{W} \mid \psi_i\rangle\right|^2 \delta(E_f - E_i - h\nu)\exp\left(-\frac{d}{\lambda(E)}\right)D(E) \qquad [3.15]$$

3.3.2 Wavefunction Matching: Surface Localisation

Quantum mechanics dictates that it is compulsory to have wave matching between the initial state and final state wave functions at the solid surface for a successful emission of a photoelectron from the solid surface into vacuum. The initial state wave function describes the bound electron before excitation whereas the final state has a free electron-like wave function in the vacuum, which is non-vanishing representing the electron arriving at the detector. The wave function describing the entire system are said to be matched if the conditions in both vacuum and solid are fulfilled. To further elucidate the wave matching theory, Figure 3.2 illustrates several possible initial state and final state wave functions.

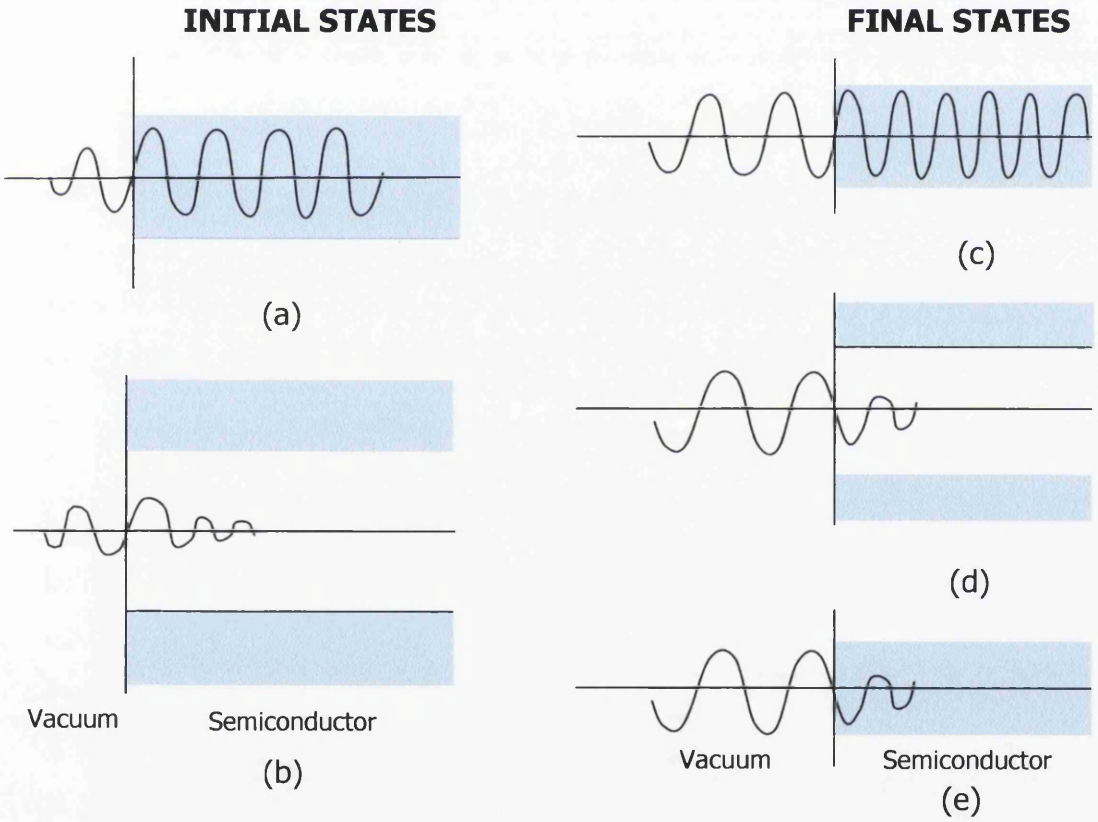

Figure 3.2: Schematic diagrams illustrating the possible initial state wave functions (a and b) and final state wave functions (c, d and e). The shaded areas correspond to allowed energy bands, which are separated by band gaps.

As shown in Figure 3.2, there are two possible initial states (a and b) and three possible final state wave functions (c, d and e). The first possible initial state (Figure 3.2(a)) corresponds to an electron state that exists within an allowed energy band in the solid, which can be described as a delocalised Bloch function [6] propagating through the solid and is matched at the surface to an exponentially decaying (also known as evanescent) wave function in the vacuum. The second possible initial state wave function is shown in Figure 3.2(b). For this wave function, an electron state exists within the band gap in the solid. Such states can only exist at or near the surface (i.e. localised surface state) and its wave function decays exponentially into the solid and matches to an evanescent wave function in the vacuum.

Generally, the possible final state wave functions have free electron-like wave functions in the vacuum and they are matched at the interface to wave functions that are dependant on the band structure of the solid. Some of the extreme cases are illustrated in Figure 3.2(c) to (e). The first extreme case of the final state wave function is shown in Figure 3.2(c), where the free electron-like wave function couples with a state within an allowed band in the solid, which is only lightly damped. Therefore, the detected electron is the characteristic of the bulk core levels. Another extreme case is illustrated in Figure 3.2(d), where the free electron wave couples to a state within the band gap of the solid. This state is originated from the surface region, as only surface state can exist within the band gap. Hence, the detected electron will be the characteristic of the surface state. So far, we have discussed on the extreme case where the wave function is lightly damped. Nevertheless, the case of strong damping is illustrated in Figure 3.2(e). In this case, the free electron wave function couples to an allowed band in the solid, which is strongly damped and therefore causing the state to decay evanescently. Hence, the detected electron is the characteristic of the surface band structure due to the short mean free path of the electron.

From the discussion, we observed that five out of six possible variation of the wave functions from the initial state to the final state shows surface probing.

Only one bulk sensitive case was observed and this case is never achieved practically due to the limited escape depth of electrons in XPS. Therefore, it is clearly seen that the photoemission technique is a surface sensitive technique.

3.4 The Aspects of Photoelectron Spectroscopy

The usefulness of XPS is based on its ability to probe and to provide maximum information on the investigated surface. Therefore, the primary factors of surface sensitivity and quantitative issue of the technique had become the main consideration in order to provide maximum information as required. This section will detail on some of the important aspect of photoelectron spectroscopy applications in terms of practical considerations and spectrum features with the aim of maximising and enhancing the generated spectra. The spectral interpretation of the photoemission spectra will also be discussed.

3.4.1 Surface Sensitivity

3.4.1.1 Inelastic mean free path, λ

Upon excitation, the photoelectrons propagating through the solid may experience elastic and inelastic scattering. When elastically scattered, the electron suffers no loss of energy but a change in direction. These electrons are the main interest as they contribute to the distinguishable core level peaks in the EDC. Meanwhile, the inelastically scattered electron suffers energy loss in the range of a few eV and they may also experience change in direction. Although they suffer a loss in energy, these electron still have sufficient energy to leave the solid surface, thus they contribute to the featureless background of the EDC. Other scattering such as phonon scattering results in energy loss of a few meV and is normally negligible compared to the resolution of the spectrometer. Inelastic scattering can also occur due to the creation of electron-hole pairs by plasmon formation, which involves a collective oscillation of electrons (conduction, valence or shallow core level electrons). Plasmon loss features are

not random and they produce distinguishable small peaks in EDC. Typical plasmon loss energies are 10-30eV and the corresponding features situated on the lower kinetic energy side of the elastically scattered peak.

As revealed previously, an important quantity describing the inelastic scattering of the electrons in photoemission studies is the inelastic mean free path, λ. By definition, it is the average distance that an electron of energy, E, can propagate through the solid before being inelastically scattered [9]. The value of λ is mainly dependent on the kinetic energy of the electron and the correlation between these two parameters can be shown in the 'universal curve' derived from experimental values by Seah and Dench [9] as illustrated in Figure 3.3 below.

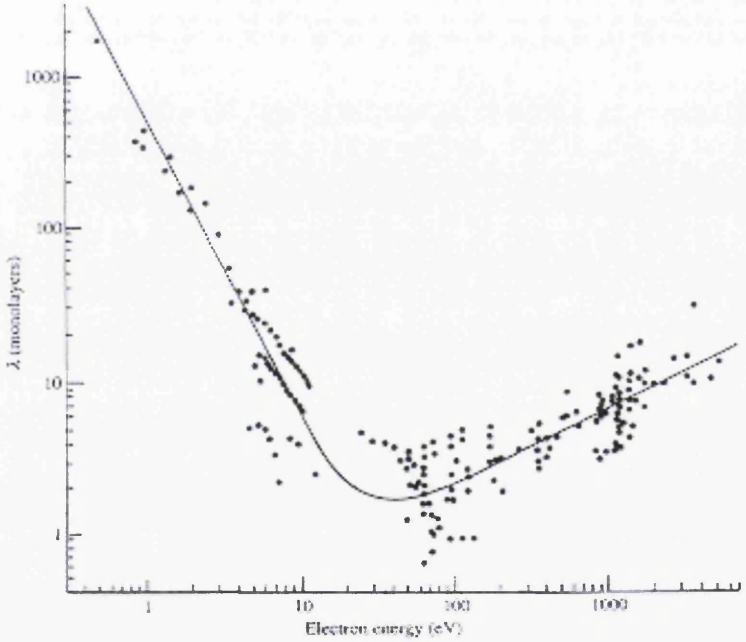

Figure 3.3: Dependence of the inelastic mean free path, λ and the kinetic energy of the photoelectrons (eV) from [9].

An important feature in this curve is the presence of a minimum mean free path in the energy range between 20-100eV. At low energies (below the plasmon energy) the scattering is dictated by single-particle excitations involving valence electrons and the ionisation of core levels [7], which have small cross sections.

Thus, the mean free path for such a collision is generally at least two orders of magnitude longer than those for plasmon scattering. Conversely, at energies above the plasmon energy, the plasmon scattering cross-section rises sharply, which increases the probability of inelastic scattering. The scattering at high energy is dominated by plasmon scattering, which is inversely proportional to the energy. This reduces the mean free path to about a few Å. Therefore, if the value of the mean free path is small; the detected electrons at this energy are associated with the first few monolayers of the solid. Evidently, surface sensitivity can be achieved by implementing a tuneable radiation source to select a suitable radiation energy and hence kinetic energy, E_k, (as related in equation [3.1]) to obtain maximum surface sensitivity.

3.1.4.2 Photoionisation cross sections, σ

The number of photoelectrons produced from any given core level of an element is determined by the photoionisation cross section, σ, of that core level for the photon energy used. By definition, σ is the transition probability per unit time of excitation of a single photoelectron from the core level of interest under an incident photon flux of $1cm^{-2}s^{-1}$. The cross sections are directly related and are proportional to the square of the matrix element $\left|\langle\psi_f \mid \hat{W} \mid \psi_i\rangle\right|$ (as described in section 3.3.1). Therefore, σ is dependent on the energy levels and photon energies [7]. The values of σ for different orbitals of most elements has been tabulated as a function of photon energy by Yeh and Lindau [10]. Hence, by selecting an appropriate photon energy using a synchrotron radiation source, the cross section of the photoelectron can be maximised and thus the observed photocurrent. However, there is usually a compromise between the surface sensitivity and the maximum cross section as it is often difficult to achieve both criteria at the same time with the same photon energy. Therefore, one needs to take a careful consideration before selecting a suitable value of photon energy in order to achieve the best results.

3.4.2 Spectrum Features

As seen in the previous section, the data obtained from the photoemission spectroscopy is displayed as an EDC. Therefore, it is essential to fully understand the spectrum features in order to precisely interpret the displayed photoelectron spectra. In this section, the spectrum features and its associated characteristics will be discussed and highlighted.

3.4.2.1 Broadening Effects

In photoelectron spectroscopy, a direct emission of a high X-ray flux from an anode to the sample may have several disadvantages [11]. One of the brutal disadvantages is that the energy resolution of the X-ray source is determined by the natural line width of the fluorescence line (typically less than 1eV). Therefore, the observed lineshape of the photoemission peaks in the EDC are limited by the natural line width. However, this narrow line will eventually be broadened and exhibits finite width, which is characterised by the full-width-half-maximum (FWHM) of the EDC. The corresponding broadening process can be classified into two groups, intrinsic broadening and extrinsic broadening.

Intrinsic broadening is inherent to the sample; it includes momentum broadening and lifetime broadening. Momentum broadening is due to the uncertainty in the final state momentum of the electron, whereas lifetime broadening is the effect of the finite lifetime of the core hole after photoexcitation of an electron [3].

Extrinsic broadening is often known as instrumental broadening. As suggested from its name, it includes instrumental broadening contributions from the photon source and the analyser. The emission linewidths and the characteristics energy for common anodes are listed in Table 3.1.

Anode Material	Emission Line	Energy (eV)	Width (eV)
Mg	Kα	1253.6	0.7
Al	Kα	1486.6	0.85
Si	Kα	1739.5	1.0
Zr	Lα	2042.4	1.7
Ag	Lα	2948	2.6
Ti	Kα	4510	2.0
Cr	Kα	5415	2.1

Table 3.1: Characteristic energies and linewidths for common ESCA anode materials from ref [11].

The linewidth of the X-ray source places a minimum line width on the photoelectron spectra features, which often adds difficulty in detection of changes in width and position of the photoelectron peaks. By implementing an X-ray monochromator, the linewidth can be significantly reduced (e.g. ~ 0.4eV for an Al Kα radiation). However, a disadvantage of using of a monochromatised source is that it decreases the X-ray intensity towards the sample and so that efficient collection lens, energy analyser and a multi-channel detection system are needed to compensate. Another alternative is to use a synchrotron radiation source, which provide the best resolution with broadening in the range of 0.1-0.6eV.

3.4.2.2 Spin Orbit Splitting Effect

Core levels with an angular momentum number $\ell > 0$ (i.e. *p, d, f* etc except *s*) form doublets due to the coupling of their orbital and spin angular momenta of the electrons. The coupling results in a new total angular momentum, *j*, given by

$$j = \ell + s \qquad [3.16]$$

where ℓ is the orbital momentum and s is the spin quantum number with the value of ±½. Thus, the total angular momentum is then ℓ+½ or ℓ-½. The resulting energy difference is known as spin orbit splitting. Electrons with $j=\ell+½$ will be shifted to a higher binding energy than those with $j=\ell-½$. The total angular momentum also determines the degeneracy of the electron state, given by $(2j+1)$. The relative intensities of the photoemission peak for core level with doublets are simply the ratio R of their respective degeneracies and are written as;

$$R = \frac{2(\ell - s)+1}{2(\ell + s)+1} \qquad [3.17]$$

As an example, for a *d* orbital where $\ell = 2$, the intensity ratio of the $^3/_2$ spin orbit split component to the $^5/_2$ component is 2:3.

3.4.3 Core Level Spectroscopy and Data Analysis

Based on the photoemission process, photoelectron spectroscopy is capable of providing information on surfaces and interfaces. This ability is a result of the dependence of the binding energy of the core levels to the change in its environment electronically and chemically. As a consequence of the change in binding energy, shifts are observed in the detected core level photoemission spectra. Therefore, it is vital that these shifts are interpreted correctly in order to analyse the effect of external agents on the properties of the sample. This section will discuss on the factors that contributes towards such shifts in the photoemission spectra. In addition, the processing of photoemission data will be highlighted at the end of the section.

3.4.3.1 Band Bending

Generally, band bending occurs when the position of the Fermi level in a semiconductor shifts due to the presence of surface states within the band gap or during the formation of metal-semiconductor interfaces [12] (see chapter 2).

For the case of surface states, they create a potential barrier at the surface. This barrier causes the position of the Fermi level at the surface to differ compared to its position relative to valence and conduction band edges within the bulk. Hence, band bending occurs, which is an electronic effect due to the charge transfer at the surface or interface. In a semiconductor, the direction of band bending would depend on the position of the Fermi level or the doping of the semiconductor (i.e. upward bending for n-type and downward bending for p-type). Meanwhile, band bending can also extent into the bulk in a scale that depends on the doping of the bulk semiconductor [12]. Although band bending occurs within the depletion region, it also affects the core levels, which cause them to move towards the same direction as the Fermi level. In photoemission spectroscopy, the sampling depth of the photoelectron is small; therefore only bands near the surface can be probed. The effect of band bending is observed as shifts in the photoemission peaks in the EDC. Note that all photoemission peaks will be shifted by the same amount as the band bending process affects all core levels equally.

3.4.3.2 Core Level Shifts

Apart from band bending, the shifts in the photoemission peaks can also be associated with the change in binding energy of a core level electron. These correlated shifts can be subdivided into two types; surface or structural induced shifts and chemical shifts.

From the basic of solid-state physics, the electrical and structural properties of the surface structure are different from the bulk structure as the bulk periodicity is abruptly terminated. At the surface, the top-most layer of atoms may share bonds with one another, a process generally known as reconstruction, and they may also find new equilibrium position, i.e. relaxation in order to minimise the surface energy [14]. Therefore, the binding energies of the electrons at the surface is slightly different than those associated with the bulk. Consequently, the observed core level photoemission peak would consist of both

bulk and surface components. Therefore, in order to investigate the individual components from different surface environments within the spectra, it is necessary to resolve the components from the spectra. In this case, a highly surface sensitive photoemission is required, which is easily achieved by using a tuneable synchrotron radiation source. By choosing different energies of the photon source, the sensitivity of the photon source can then be varied to observe these surface components.

When an atom of a particular element interacts with an external agent, it experiences a change in its chemical environment. This involves charge transfer between these atoms as determined by their relative electronegativities, and also the formation of new atomic bonding to form new species, for example, silicides [14]. These reaction processes involve the valence electrons, which causes a redistribution of the valence charge. The phenomenon alters the electronic properties of the bonded atom and is observed in the EDC by shifts in binding energy of the core levels. These shifts are known as 'chemical shifts', which provide information on the chemical composition and the extent of the reaction at the surface. However, this chemical shifts are usually very small in magnitude (~ a few eV), therefore high energy resolution is often required to resolve such shifts.

3.4.3.3 Core Level Intensities

So far, the analysis of the core levels we have dealt with is associated with the changes in binding energy, which contributes to the shifts related to band bending and surface induced shifts. In addition to these shifts, the intensities of the core level peaks can also provide useful structural information of surface and interfaces. To further illustrate, we take an example of interface formation experiment where overlayers of a material are deposited onto a clean semiconductor surface. During the interface formation, the emission from the substrate will be attenuated by the growth of the overlayer. These attenuation patterns can reveal the growth mode of the overlayers. Conventionally, there are

three types of growth modes as illustrated in Figure 3.4. If the deposited material grows in a layer-by-layer mode, also known as Franck-van der Merwe mode, the substrate core level intensity will decay exponentially as a function of the overlayer thickness given by;

$$I_d = I_o \exp\left(\frac{-d}{\lambda}\right) \qquad [3.18]$$

where I_d is the substrate core level intensity at the overlayer thickness of d, I_o is the core level intensity of the clean substrate and λ is inelastic mean free path of the substrate photoelectrons.

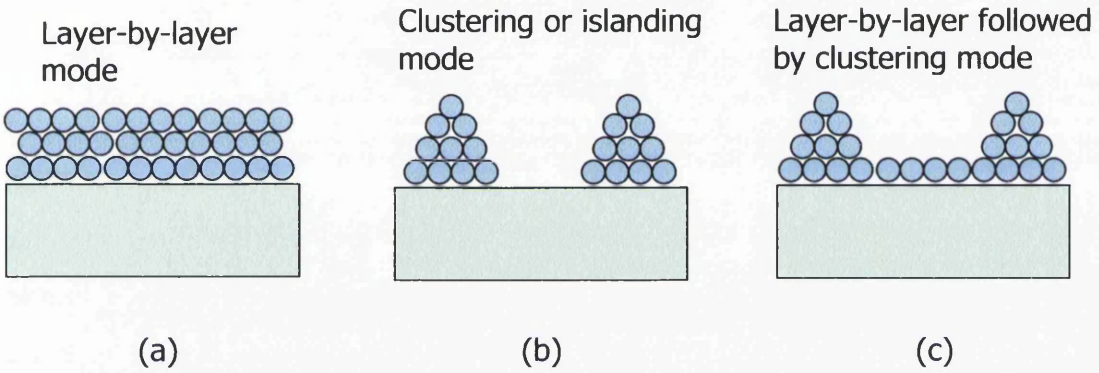

Figure 3.4: Various growth modes (a) Franck-van Der Merwe (b) Volmer-Weber (c) Stranski-Krastanov

Deviations from the exponential decay would suggest non-uniform growth, such as clustering or island formation of the overlayer and also out-diffusion of the substrate elements due to chemical reactions at the interface. Hence, the analysis of the core level attenuation behaviour could provide useful information on the formation of interfaces.

3.4.3.4 Curve Fitting Core Level Spectra

From the above discussion, we can see that a core level spectrum consists of useful electronic, structural and chemical information about the atoms within the material surface. Hence, it is essential to perform detailed analysis of the individual components in order to understand the changes of their properties

corresponding to the process involved. However, it is quite often that different components arising from different environments overlapping each other that cannot be clearly resolved in a spectrum. Although limited by the equipment resolution, it is possible to deconvolute the raw spectra of a core level into all its separate individual components mathematically, a process known as curve fitting.

In a curve fitting process, several 'pre-treatment' steps are performed to the raw spectra to minimise distortion. This includes the subtraction of unnecessary satellites, spikes and background (linear, Shirley or slope) removal. The process is followed by fitting the peaks using various parameters. In the curve-fitting programme, each individual component is represented by a Voight function, which is a mixture of a Gaussian and Lorentzian function. There are seven parameters associated with these functions, which includes the peak position, height, width, Gaussian-Lorentzian mix, tail height, exponential tail slope and tail mixing ratio [7]. During the fitting, several parameters (such as peak width, tail height, mixing ratio) were often restricted so that the number of variables is kept to the minimum. In addition, the number of components should also be kept to the minimum to avoid confusion. Additional components are only introduced provided there is a realistic physical explanation behind it. To date, the curve-fitting programme allows a maximum of eight components within a spectrum. Also, there is a possibility of having considerable deviations from the correct fit. Hence, the square of the residual is taken into account rather than the actual value. This square value can be weighted by a weighting function known as chi-square, χ^2. A chi-square value represents the accuracy of the fit to the actual spectrum; hence, the least-chi-square approach [9] is employed in the fitting procedure. By implementing this useful curve fitting method, valuable information from the core level spectra can be revealed, giving a better understanding towards the chemical and structural properties of the components.

3.5 Low Energy Electron Diffraction

Electron diffraction technique, in particular low energy electron diffraction (LEED) play a dominant role in the study of bulk and surface crystallographic structure [7,15]. This technique is non-destructive and fairly simple but powerful in providing rather direct information on the periodicity or translation symmetry of a surface structure [7]. The schematic diagram of the LEED optics is illustrated in Figure 3.5 below.

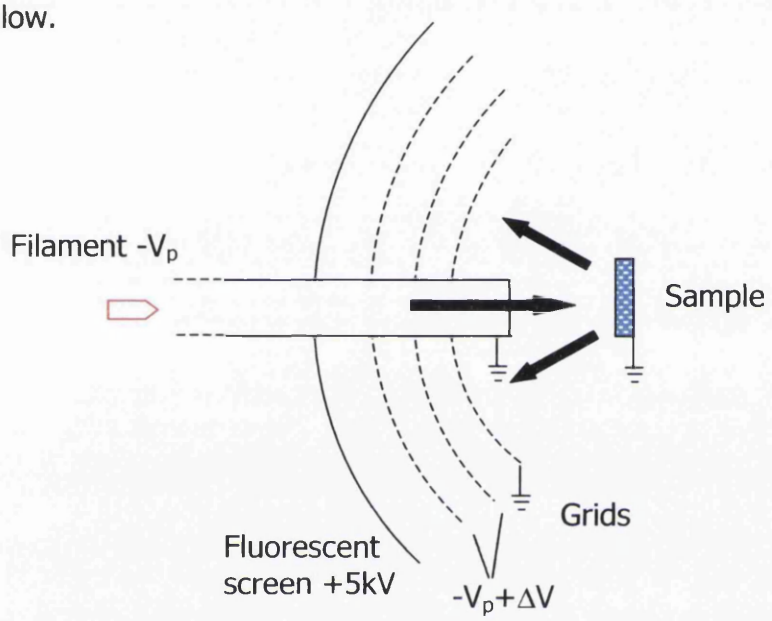

Figure 3.5: Schematic diagram of LEED optics for displaying diffraction pattern.

As illustrated, a beam of low energy electrons (in the range of 20-300eV) is incident perpendicular to the sample surface, with the sample at ground potential. Electrons scattered or emitted from the sample travel in the field free region towards the spherical grids. Note that the first set of these grids is at ground potential (same to that of the sample) and the following second and third grid are set using a potential (V_p+ΔV) close to that of the original electron source filament (V_p) so that it retard all electrons other than those which have been elastically scattered. These elastically scattered electrons are then accelerated towards a fluorescent screen, where the diffraction pattern is displayed and

viewed or photographed. A 5kV potential is applied to the fluorescent screen in order to ensure the diffraction pattern is projected onto the screen. The low energy diffraction pattern is attributed to the surface geometry because of the short inelastic mean free path of the low energy electrons. The electrons underneath the surface would experience strong inelastic scattering so that they do not contribute to the observed pattern. Hence, the diffraction pattern is simply the projection of the surface reciprocal mesh and it can be explained using a two-dimensional map of the reciprocal space of the surface. If the incident wave vector is represented by **k** and the diffracted wave vector is **k'**, then conservation of energy gives

$$k^2 = k'^2 \qquad [3.19]$$

and the conservation of momentum parallel to the surface gives

$$k'_{\parallel} = k_{\parallel} + g \qquad [3.20]$$

where **g** is a reciprocal lattice vector given by;

$$g = ha^* + kb^* \qquad [3.21]$$

h and *k* are integers referred to as Miller indices [7] and a^* and b^* are the primitive translation vectors of the reciprocal lattice. They are related to those of the real lattice by;

$$a^* = 2\pi \frac{b \times n}{A}, b^* = 2\pi \frac{a \times n}{A}, A = a.b \times n \qquad [3.22]$$

where **n** is the unit vector normal to the surface. As the diffraction condition is dictated by the reciprocal net vectors that consist of two components, thus the diffracted beams are denoted by a two number index, *(hk).*

The most effective graphical way of representing the diffraction conditions is the construction of an Ewald sphere as illustrated in Figure 3.6 [7]. The main feature of the Ewald sphere construction is that it is built on the reciprocal lattice. Due to the two-dimension nature of the surface, there is loss of constructive interference of the scattered waves in the direction perpendicular to the surface.

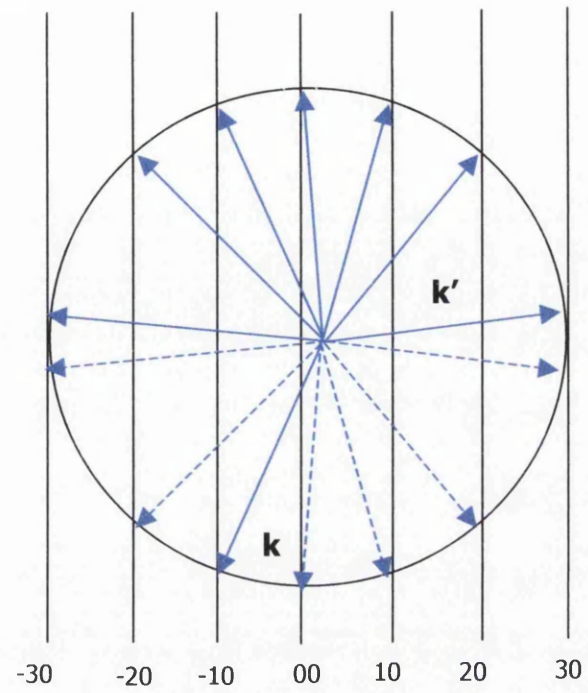

Figure 3.6: Two-dimensional Ewald sphere construction in LEED. Several cases of the incident wave vector **k** are shown in dotted lines that propagate into the solid and will not be observed. The corresponding backscattered wave vector **k'** shown in solid line is accelerated towards the fluorescent screen displaying the diffracted pattern.

Hence, the two-dimensional case is represented by a series of infinite rods (i.e. infinite reciprocal lattice rods in the Ewald sphere). The diffraction occurs every time the Ewald sphere intersects a reciprocal rod. Each diffracted beam produces a spot in the resulting LEED pattern and is indexed according to the reciprocal lattice vector that produces the diffraction. Hence, in principle, the real space lattice and symmetry can be deduced from the LEED pattern using equation [3.22]. By altering the energy of the incident electrons, the radius of the sphere changes, varying the number of reciprocal lattice rods that are intersected and consequently the number of diffracted beams. If the surface has a larger unit mesh than the bulk, as in the case of reconstruction, the reciprocal unit mesh of

the surface will be smaller than the reciprocal unit mesh of the bulk. As a result, the reconstruction spots then appear as fractional in the observed LEED pattern. In addition to structural information, LEED can also provide immediate information on surface ordering. A well ordered surface would give rise to a very sharp LEED pattern whereas a disordered and contaminated surface will generate a blurring or no LEED pattern at all. Other application of LEED includes qualitative analysis, which involves the study of the diffracted beam intensities and a more complicated quantitative scattering theory. However, this aspect is beyond the scope of this thesis and hence will not be discussed.

3.6 Scanning Tunnelling Microscopy (STM)

Scanning tunnelling microscopy (STM) is one of the most popular and widely used surface science techniques as it has the ability to provide three-dimensional, real space images of surfaces down to the atomic scale. The schematic diagram of a typical STM system is illustrated in Figure 3.7.

The basic principle of STM is based on the quantum mechanical tunnelling effect. The STM operation involves a sharp metal tip to be brought into close proximity with a electrically biased conducting sample. If the distance between the metal tip and the sample is close enough, (e.g. in order of Angstroms, Å), significant overlap of the wavefunctions will occur and thus, a tunnelling current is established across the vacuum barrier between the tip and the sample. This tunnelling current, I, is of a very small magnitude, normally in pico (10^{-12}) or nano (10^{-9}) amps and is extremely sensitive to the distance between the tip and the sample [16]. The relationship between the tip-sample distance, Z, and I is given by

$$I \propto e^{-2kZ} \qquad [3.23]$$

where k is the wave vector, which is a function of energy and applied voltage. Due to the exponential dependence of the tunnelling current with Z, STM is extremely sensitive to the height variations of the sample [17]. For example, a

decrease of 1Å in Z will cause an increase of current by an order of magnitude. It is this sensitivity that gives STM its extremely high Z resolution, in the order of 0.1Å. Lateral resolution can be as good as 1Å, provided that the tip used is sharp enough and consists of only one atom located at its apex.

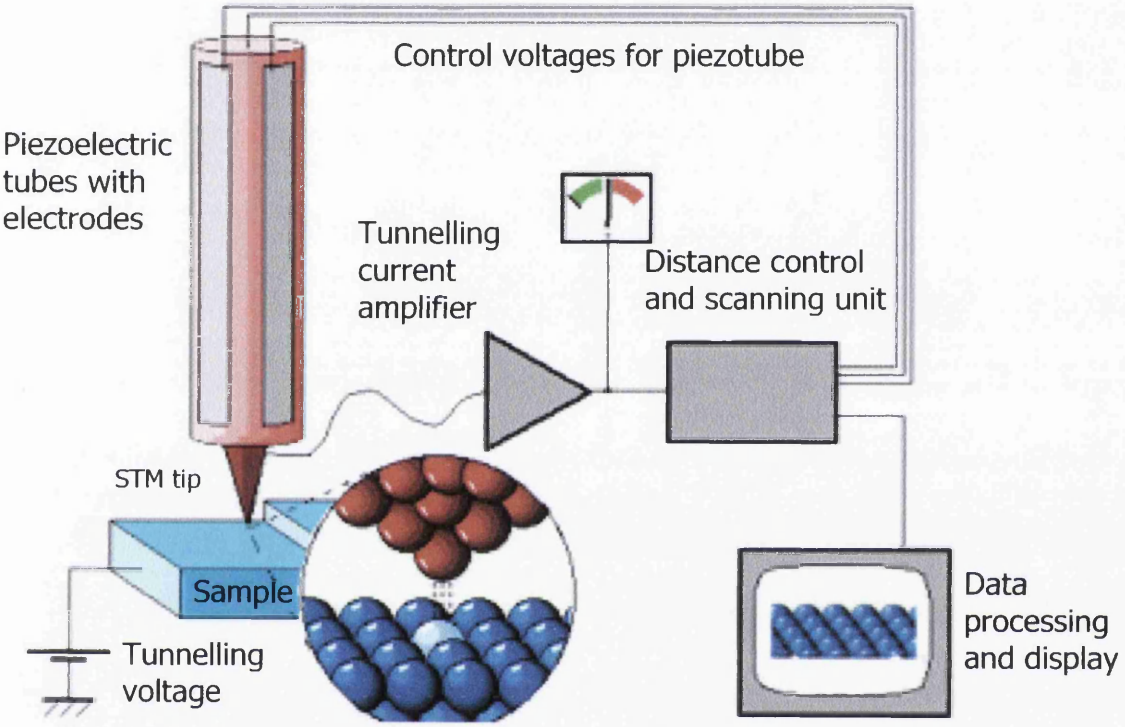

Figure 3.7: Schematic diagram of a STM system.

A piezoelectric driver attached to the tip accurately controls the position of the tip, which the tip can be scanned in two lateral directions parallel to the sample surface. The tunnelling current is monitored and constantly regulated by a feedback system through the adjustment of vertical sample-tip separation. The STM can operate in two-operation modes, the *constant current mode* and the *constant height mode*. For the case of *constant current mode*, a feedback circuit is enabled to constantly alter the tip height so that the tunnelling current remains constant. The topographical image is obtained by recording the height of the tip

as the function of the lateral location, which can be derived from the applied voltage of the piezoelectric driver. For the second mode of operation, the *constant height mode*, the tip height is kept constant while scanning via a slow feedback. In this case, the topographical information is extracted from the variations of the tunnelling current. Regardless of the operation mode, valuable topographical information of the structure of the sample surface can be obtained through STM.

3.7 References

[1] A. Einstein, Ann. Physik, **17**,132 (1905).

[2] T. Koopmans, Physica, **1**, 104 (1933).

[3] R.H. Williams, G.P. Strivastava, and I. T. McGovern, Rep. Prog. Phys., **43** 1357 (1980).

[4] C.S. Fadley in 'Electron Spectroscopy: Theory, Techniques and Applications, Vol.2', Edit. By C.R. Brundle and A.D. Baker, Academis Press (1978).

[5] C.N. Berglund and W.E. Spicer, Phys. Rev., **136** (4A), A 1030 (1964).

[6] B. Feuerbacher and R.F. Willis, J. Phys. C: Solid State Phys., **9**, 169 (1976).

[7] D. P. Woodruff and T. A. Delchar, 'Modern techniques of surface science', Cambridge University Press, Cambridge (1986).

[8] C. Cohen-Tannoudji, B.Dui and F. Laloë, 'Quantum Mechanics', Volume 2, J. Wiley and Sons (1977).

[9] M. P. Seah and W. A. Dench, 'Surface and Interface Analysis, Vol 1- Auger and X-ray Photoelectron Spectroscopy', Edition 2 (1990).

[10] J. J. Yeh and I. Lindau, Atomic data and nuclear tables, **32**, 1(1985).

[11] B. D. Rather and D. G. Castner in 'Surface Analysis- The Principle Techniques', Edit. By J. C. Vickerman, Wiley and Sons (1997).

[12] E. H. Rhoderick and R. H. Williams, 'Metal- Semiconductor Contacts', Oxford University Press, (1988).

[13] J. M. Hollas, 'Modern Spectroscopy', John Wiley and Sons, Second Edition (1992).

[14] K. N. Tu, J. W. Mayer and L. C. Feldman, 'Electronic Thin Film Science For Electrical Engineers and Material Scientist', Macmillan (1992).

[15] M. Prutton, 'Introduction to Surface Physics', Claredon Press (1994).

[16] J. A. Stroscio and N. D. Lang, Chapter 1, 'Methods of Experimental Physics: Scanning Tunnelling Microscopy', Edit. J. A. Stroscio and W. J. Kaiser, Academic Press (1993).

[17] G. F. A. van de Walle, E. J. van Loenen, H. B. Elswijk and A. J. Hoeven, Chapter 3.3, 'Analysis of Microelectronic Materials and Devices: Scanning Tunnelling Microscopy', Edit. M. Grasserbauer and H. W. Werner, John Wiley and Sons (1991).

Chapter 4

Experimental Techniques

4.1 Introduction

In this chapter, the practical aspects of the sample preparation, experimental set-up plus the procedure of the techniques employed in this research work will be addressed. In previous chapters, the theories and principles of X-ray photoelectron spectroscopy (XPS), Scanning Tunnelling Microscopy (STM) and low energy electron diffraction (LEED) have been presented. Within this work, the interface study experiments were performed *in-situ* in a multi-stage integrated ultra high vacuum (UHV) system and all fabrication experiments were conducted in a clean room environment under a high vacuum (HV) Edwards evaporation chamber. The UHV system consists of the above mentioned surface analysis techniques and a multi source evaporation stage consisting of silicon and a metal source. On the other hand, the Edwards evaporation chamber includes a single specimen evaporation stage plus annealing facilities. In order to extract a variety of information, it is essential to understand the practical aspects of each technique employed. Hence, the details of the experimental procedure and a brief description of the instrumentation will be addressed to aid the understanding and to ensure

the consistency of this work. Note that all materials and equipment have been originally tested and calibrated.

4.2 Sample Preparation

In this work, all sample used were Silicon Carbide (SiC) wafers obtained from CREE Research Inc. The samples used were n-type epilayers hexagonal SiC (4H-SiC) nitrogen doped ($10^{19}cm^{-3}$). The summary of the specifications of these wafers are listed in Table 4.1 below:

Conductivity	N-type
Dopant	Nitrogen
Doping Density	$1 \times 10^{19}/cm^3$
Epilayer thickness	10μm with tolerance of ±15%
Surface orientation	8° off-axis, Si faced
Wafer thickness	416.56μm
Surface finish	Polished
Resistivity	0.02Ωcm

Table 4.1: Wafer specification of the 4H-SiC wafers.

The 'as-received' samples generally contain man-made physical dirt (i.e. dust, fingerprints, oil, etc.) and also organic adsorbates (i.e. hydrous oxide, ionic traces). In addition, the surface of the sample is rough with a surface roughness of approximately 23.3Å RMS [1]. Hence, prior to any experiments, these samples were treated in order to obtain an atomically clean surface as a starting platform to all experiments to ensure consistency and reliability to the result obtained. The cleaning procedure is discussed in the following section.

4.2.1 Wafer Cleaning

Generally, the cleaning procedure implemented in this work can be divided into two stages. The first stage involves an *ex-situ* chemical clean and the second stage comprise of an *in-situ* annealing cycles. The objective of

such cleaning processes is as mentioned previously and the cleanliness of the sample is gauged by XPS and LEED. The detailed aspect of these processes will be addressed in the next section.

4.2.1.1 *Ex-situ* Chemical Clean

Artificial contamination such as fingerprints, dust and oil on the surface of the sample can be easily cleaned off using a wet chemical clean. This chemical cleaning procedure is conducted *ex-situ* in a clean room environment. Within this work, the chemical cleaning procedure can be divided into two main steps; solvent clean, which is a soft chemical clean and a modified RCA (Radio Corporation of America) clean developed by Werner Kern [8], which is a strong chemical clean involving organic removal, oxide strip and ionic clean. The summary of the cleaning procedure is listed below.

Solvent clean

The solvent clean process involves a three step chemical ultrasonic bath for 5 minutes each. The orders of the chemicals used are as follows:

1. Trichloroethylene ($CHCl = CCl_2$)
2. Acetone (CH_3COCH_3)
3. Isopropanol ($(CH_3)_2CHOH$)

The solvent cleaning technique is basically a starting point to remove oil, dust and fingerprint from the 'as-received' sample. After the solvent clean process, the sample is expected to be free from physical dirt and is ready for further adsorbate contaminants removal through the RCA clean.

RCA clean

The RCA clean has been adopted widely by the semiconductor industry as the major cleaning technique for wafers. However, we have slightly modified the cleaning procedure by adding an extra cleaning step, the Piranha clean, which is used as a resist strip process before the 1st stage if the RCA clean.

Piranha clean: Sulphuric acid (H_2SO_4) + Hydrogen Peroxide (H_2O_2)
Ratio 5:1 at 50°C for 5 minutes.

The RCA cleaning procedure has three major steps used sequentially. They are listed below.

1. Organic clean: For the removal of insoluble organic contaminants. Consists of Ammonium Hydroxide (NH_4OH) + Hydrogen Peroxide (H_2O_2) + Deionised Water (DI H_2O). Ratio 1:1:5 at 75°C for 5 minutes.
2. Ionic clean: For the removal of ionic and heavy metal atomic contaminants. Consists of Hydrochloric acid (HCl) + Hydrogen Peroxide ((H_2O_2) + Deionised water (DI H_2O). Ratio 1:1:5 at 75°C for 5 minutes.
3. Oxide Strip: For removal of the thin silicon oxide layer (also present on SiC wafers) where metallic contaminants may have accumulated as a result of cleaning step (1). Consists of Hydrofluoric acid (HF) + Deionised water (DI H_2O). Ratio 1:10 at room temperature for 15 seconds followed by rinsing in 40 millilitres of deionised water for another 20 seconds.

The cleaning process is completed by blow-drying the sample using nitrogen gas. The RCA cleaning technique does not attack Si, and only a very thin layer of silicon dioxide is removed. The process is also designed to prevent re-plating of metal contaminants from the solution back to the sample's surface. After completing the cleaning process, the sample's surface should be free from any residue and contaminants.

4.2.1.2 *In-Situ* UHV clean

Once exposed to air, there is a high possibility that water molecules and oxygen molecules within the air ambient could attach on the sample surface. For metal-semiconductor contacts, these residues from the air would alter the performance of the fabricated devices. Hence, it is vital that these residues are removed completely. This is conducted by annealing the sample

in-situ by electron bombardment (e-beam) at temperatures between 980°C and 1050°C.

Subsequent to the *ex-situ* wet chemical clean mentioned previously, the sample is mounted to a well out-gassed e-beam stub (see section 4.6.3) and is admitted immediately into the ESCAlab (see section 4.6) via the load lock to minimise the contamination from the air ambient. Once in the system, the sample is gradually heated to ~850°C keeping the pressure below 10^{-9} mbar for a duration of at least 20 hours to evaporate the water vapour. Next, the sample is flashed up to a temperature of 1050°C, several times in short duration maintaining the pressure within the range of 10^{-9} mbar. This step is taken with caution as prolonged anneal at such a high temperature will result in Si being depleted from the SiC surface leaving a carbon-rich surface [5].

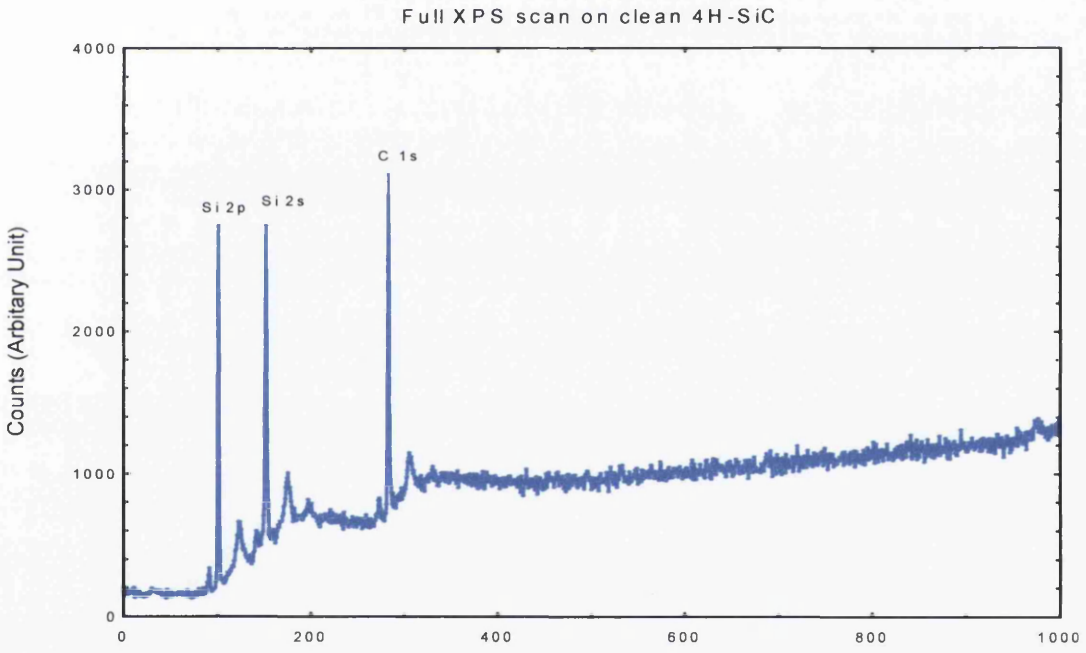

Figure 4.1: A full scan XPS spectrum of a clean 4H-SiC sample after wet chemical clean and *in-situ* annealing cycles. In the spectrum, only Si and C peaks are visible, indicating that all contaminations have fallen below the detection limit.

Also, long anneal at such high temperatures will also heat up the residual gas within the system causing an increase in pressure. Even so, this stage cannot be omitted, as a temperature of approximately 1000°C is required to remove oxygen contaminants [6]. Hence, there is a compromise between the cleanliness of sample and the operating pressure. In this work, the operating pressure throughout the *in-situ* cleaning procedure is maintained within the range 10^{-9} mbar and the flashing process is repeated until a satisfactory clean surface is obtained. The cleanliness of the sample is assessed by XPS and LEED.

Figure 4.1 illustrates a full scan XPS spectrum of a 4H-SiC sample after the completed wafer cleaning procedure (i.e. both *ex-situ* and *in-situ*). The spectrum shows no other elements other than the primary elements of SiC (i.e. Si and C components). This indicates that the amount of surface contaminants has fallen below the XPS detection limit. The cleanliness of this surface is confirmed by LEED, which the surface will exhibit a sharp (1 x 1) pattern [6,7]. Upon obtaining this clean surface, the sample is now ready for experimental use. However, in order to obtain a clean surface at the atomic scale, further treatments are required and this will be discussed in Chapter 5.

4.3 Thin Film Deposition

The formation of metal-semiconductor contacts is central to this work, thus the metalisation process cannot be omitted. In order to investigate the effect of Schottky barrier formation, it is necessary to deposit the metal overlayer sequentially so as to observe the initial stages of the barrier formation. Nevertheless, it is important to note that fully metallic behaviour only arises when the metal overlayer is thick enough (>1000Å). Thus, a thick layer of metal is also required in the fabrication of Schottky contacts. In this work, we have implemented two methods of metal deposition in order to meet the requirements mentioned above. The UHV evaporator for metal and Si source is used for thin film deposition (0Å to 60Å) whereas the HV Edwards

evaporation chamber is used for thick overlayer coverage (μm). The practical aspects of these equipments are introduced individually in the next section.

4.3.1 UHV Evaporation Sources

In this work, two UHV evaporation sources were employed, namely a Si evaporation source and a mini e-beam evaporator for metals. Their principles of operation and set-up are addressed in the following sections.

4.3.1.1 The Silicon Evaporation Source

The Si evaporator used to grow Si throughout this work is a commercial EFM 3 evaporator fitted with an integral flux monitor, manufactured by Omicron. The schematic diagram of the design of the evaporator [2] is illustrated in Figure 4.2.

The principle of operation is based on e-beam heating, where a wide range of material other than Si can be evaporated using the evaporator [2]. The evaporant used is a square shaped Si rod having a cross section of 2mm x 2mm. This rod is slotted into the end of a high voltage (HV) feed through. The electron beam generated from the adjacent filament is accelerated towards the high voltage rod, aiming at the tip of the rod. Hence, the tip of the rod is melted by the enormous heat generated by the electron bombardment thereby producing a flux of Si atoms. Note that only the tip of the rod heats up as the remaining part of the rod stays in ambient temperature through the water-cooled copper shroud in the evaporator. The generated flux is directed to the sample through the exit tube. At the end of the evaporator exit column, there is an ion collector used to detect the amount of flux leaving the exit tube, which is being monitored via a flux monitor. The amount of flux of the evaporated material can be varied by varying the emission current. However, the maximum flux is limited by the geometry of the molten 'ball' formed at the end of the rod as too high emission current increases the size and weight of the molten 'ball', which will

eventually drip off from the rod, causing a loss of flux. Therefore, it is vital to choose for a suitable emission current in order to maintain an optimum and yet stable flux.

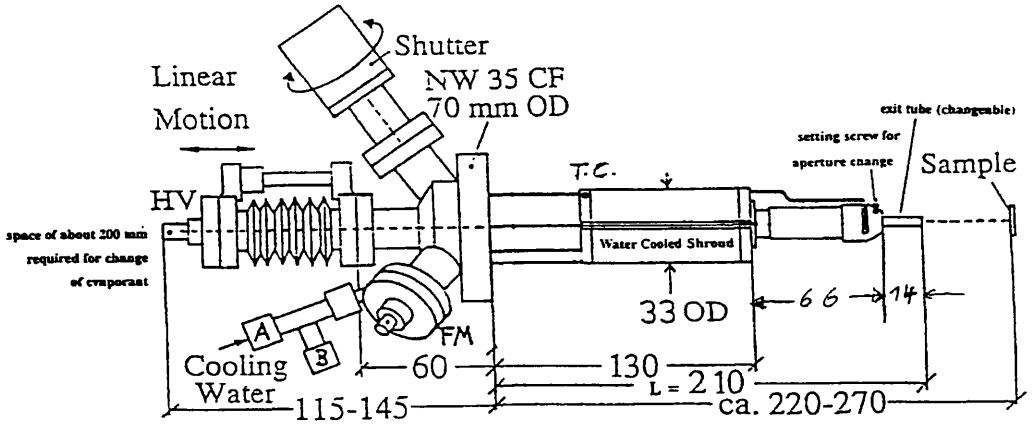

Figure 4.2: The Omicron EFM 3 UHV evaporator. HV: high voltage feed through, TC: thermocouple and FM: socket for flux monitor. Note that the linear motion is the movement of the evaporant and not the entire evaporator [2].

After several depositions, the rod will become shorter as indicated by a low flux evaporation. When this happens, the rod can be further brought forward towards the filament to resume the required flux. Nevertheless, when the rod is too short, it has to be replaced.

The vacuum has to be broken to install a new rod. Therefore, all new rods have to be thoroughly degassed to remove any possible contaminants on the rod and inside the chamber. This is performed by heating the rod and the source via filament current without applying any HV. Also, the water-cooling has to be removed to ensure the source can exceed its normal operating temperature up to 300°C, as monitored by the thermocouple integrated in the evaporator. The degassing process normally takes several hours, but it enables the evaporator to operate in a pressure of $\sim 10^{-10}$ mbar producing a clean and uncontaminated Si source.

The deposition rate of the evaporator is inversely proportional to the square distance (L) between the tip of the rod and the sample surface and is given by the relationship:

$$Deposition\ rate \propto \frac{1}{L^2} \qquad [4.1]$$

The deposition rate has been calibrated using XPS and MBE grown samples [3]. The calibration was later confirmed by Scanning Tunnelling Microscopy (STM) measurements. When the evaporator is employed in other systems, the corresponding deposition rate can be obtained by applying equation [4.1] at a constant flux rate.

4.3.1.2 The Metal Evaporation Source

Similar to Si deposition, the growth of metal within this work is carried out using a commercial mini e-beam UHV evaporator, EGN 4, manufactured by Oxford Research. The principle of operation is again similar to the Si source described previously (i.e. based on electron bombardment). Figure 4.3 shows the schematic diagram of the EGN 4 evaporator [4].

The evaporator has the capability of evaporating high melting-point materials including tungsten (W), the highest melting point element in the periodic table [4]. The evaporator consists of four hearths, in which four different evaporants can be loaded at the same time. The evaporator has an integrated electronic switching control that enables rapid and simple switching between alternate evaporant. The evaporants used in this work are 99.99% purified nickel (Ni) rods with a dimension of 2cm in length and 0.08 inch in diameter. The rod is slotted into one of the hearths, which has its own individual filament. The rod is held in at high potential (2kV) and electrons generated from the dedicated filament are accelerated towards the end of the rod. Thus, the tip of the rod is melted by e-beam, generating a metal flux gauged by the ion current collector. Like the Si source, the EGN 4 evaporator also comprises of a direct water-cooling system of the turret, keeping an

ambient temperature to the adjacent hearths. In addition, the hearths are shielded from the evaporant contamination by the neighbouring hearths through the means of extensive cross-contamination shielding (see Figure 4.3).

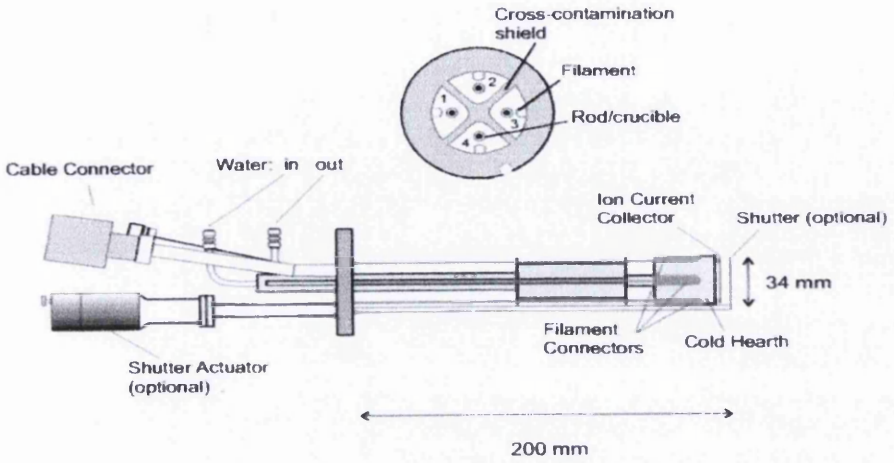

Figure 4.3: Schematic diagram of the EGN 4 mini e-beam evaporator [4].

The emitted flux is also controlled via the emission current and the rate of deposition is measured by the ion current. Note that the increase in the ionised background gas may contribute to the measured the ion current, which also includes the emitted flux and residual gas in the vacuum chamber. Hence, the pressure within the chamber plays an important role and therefore the rods and filament needs to be thoroughly degassed after venting the chamber. The degassing procedure is as described previously in section 4.3.1.1 and subsequent to the degassing process; the evaporator would be expected to operate within the pressure of 10^{-10} mbar.

The deposition rate can be calibrated using a quartz crystal monitor. Figure 4.4 show the manufacturing data sheet of the calibration of a 2mm Ni rod with a distance of 100mm from the sample. From the graph, the calibrated deposition rate is approximately 1Å per 9.2 seconds. However, we have re-calibrated the deposition rate using XPS and the rate of deposition employed in this work is approximately 1Å per 7 seconds.

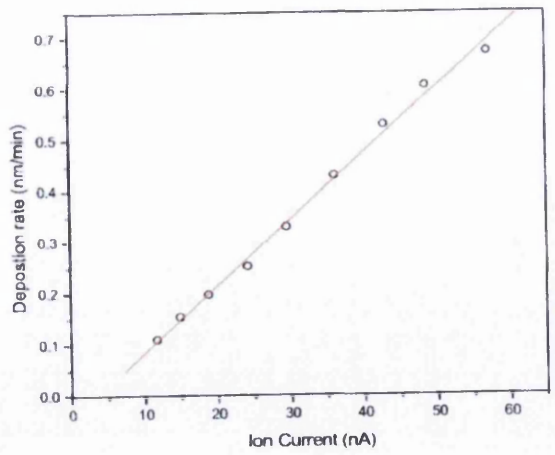

Ion current vs deposition rate – Ni

Figure 4.4: Calibration data of the EGN 4 evaporator using a quartz crystal monitor: Ni deposition rate (nm/min) versus ion current (nA) [4].

4.3.2 High Vacuum Edwards Evaporation Chamber

The UHV sources described previously are more appropriate for experiments that require low overlayer coverages. However, in terms of fabrication of practical Schottky diodes, a thick metal overlayer is compulsory to ensure proper contact between the metal and the semiconductor. In this case, the Edwards E306A Thermal Evaporator was used. The instrument layout of the Edwards Evaporator is illustrated in Figure 4.5.

Operating in a HV environment, the Edwards evaporator also belongs to the electron beam instruments family, where the working principle is based on e-beam heating. From Figure 4.5, the main component of the evaporator consists of a chamber where the multi-crucible terminal, target plate and crystal monitor are held, the pressure gauge and the voltage - current control box. The HV environment within the chamber is maintained via a rotary pump and a nitrogen cooled diffusion pump. During evaporation, the target plate is held upside down with the sample facing downwards to the crucible. The desired evaporant material (usually metal) is cut into small pieces and placed into one of the crucible. The e-beam current generated at the coil filament

situated above the crucible then heats the crucible. Note that the evaporator system can be used to evaporate various materials depending on the melting point of the material itself. The amount of current and voltage used to melt the desired material is controlled through the voltage – current control box. The crucible becomes very hot and thus the small pieces of metal are melted and evaporated onto the sample surface. The thickness of the evaporated material can be monitored via a crystal monitor adjacent to the target plate.

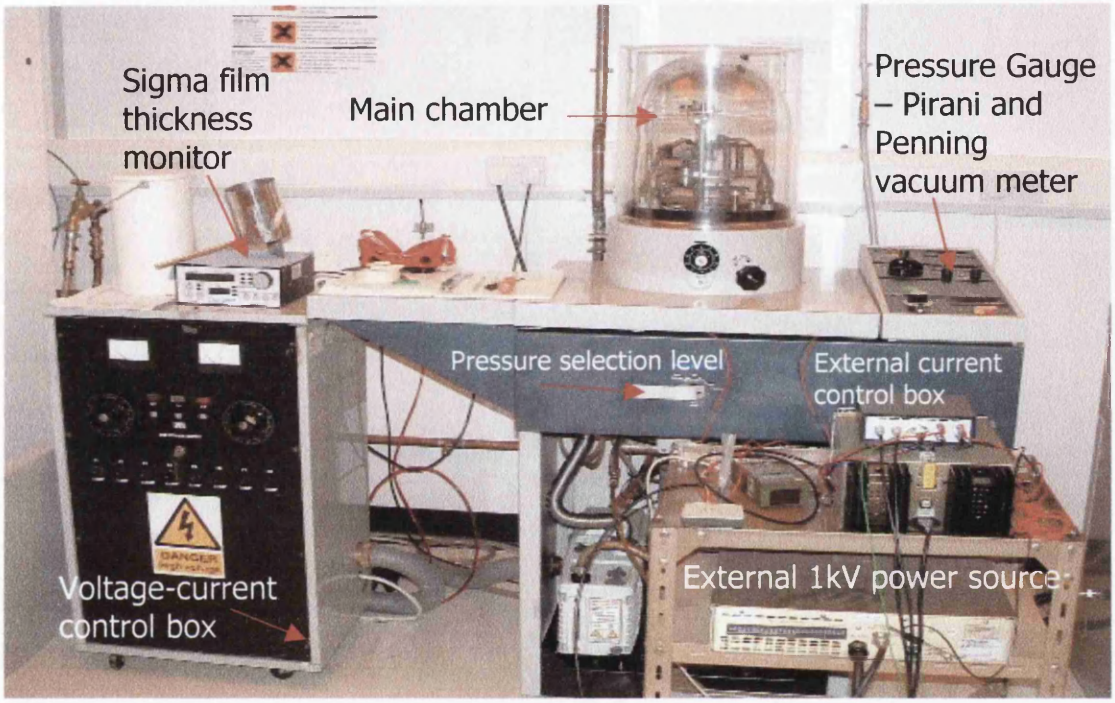

Figure 4.5: Photograph of the Edwards E306A Thermal Evaporator equipment.

Apart from metal evaporation, the Edwards E306A evaporator also provides an annealing facility for temperatures up to 1000°C. In this case, the modified e-beam stub holds the sample replacing target plate and is connected to an external power source. This external source consists of a high voltage source (1kV) and a current control box. The calibration of the temperature versus current for the Edwards evaporator is illustrated in Figure 4.6.

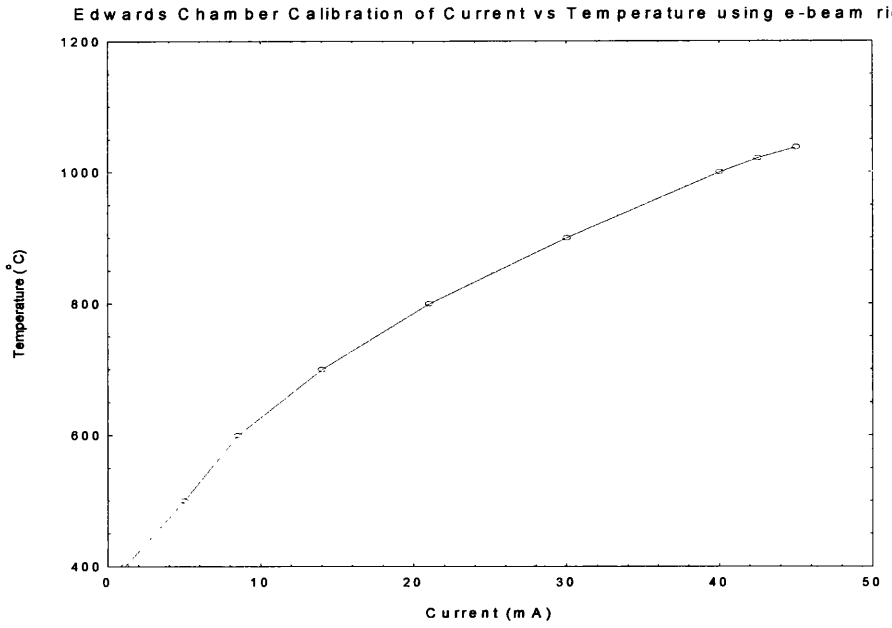

Figure 4.6: Temperature vs current calibration plots for annealing operation of the Edwards evaporator.

4.4 Photolithography

The Schottky diodes fabricated in this work are 650μm diameter dots, developed via photolithography on a shadow mask film. The samples, after all necessary overlayer growth (i.e. both Si and metal) for both back Ohmic contact and top overlayer are coated with positive photo resist. The photo resist is spur at 6000rpm to produce an even layer. This is followed by a 15 minutes soft bake (at 85°C) to ensure a proper adhesion of the photo resist to the sample. Next, the shadow mask is carefully aligned on top of the sample, maximising the number of dots (diodes) within the sample surface. Once a satisfying position is achieved, the mask is exposed to ultra violet (UV) light.

Subsequently, the samples are developed in a diluted solution of photo resist developer and DI water (ratio 2:1) until the dots becomes visible. Next, the sample undergoes a hard bake process (at 100°C) for 5 minutes to protect the already developed dots before stripping off the photo resist. The unwanted metal on the side of the dots is etched off using HCl where as the

Si interlayer is etched off using a standard 2N KOH solution. Finally, the photo resist on top of the dots is stripped off using Acetone until a satisfactory clean photo resist free diodes is obtained. The fully developed structure of the diode is illustrated in Figure 4.7.

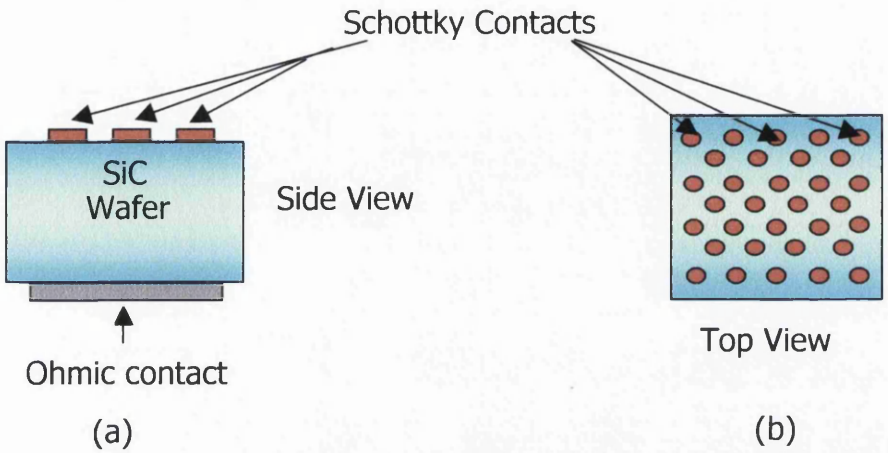

Figure 4.7: The fabricated 4H-SiC Schottky diode structure. (a) Side view (b) top view

4.5 I-V Measurement

After the fabrication of Schottky diodes, the current-voltage (I-V) performance of the diode has to be gauged in order to determine the behaviour and the quality of the metal-semiconductor contact. The Hewlett Packard 4142B measurement rig, is a widely used commercial instrument that is capable of performing both I-V and C-V measurement. However, since we are only interested in the I-V performance, the rig was set-up for I-V assessment mode only. The schematic diagram of the settings for I-V measurement is illustrated in Figure 4.8.

Initially, the processed sample is placed onto a copper made stage inside the measurement black box. The measurement box is usually tinted black as any source of light might distort the measurement results.

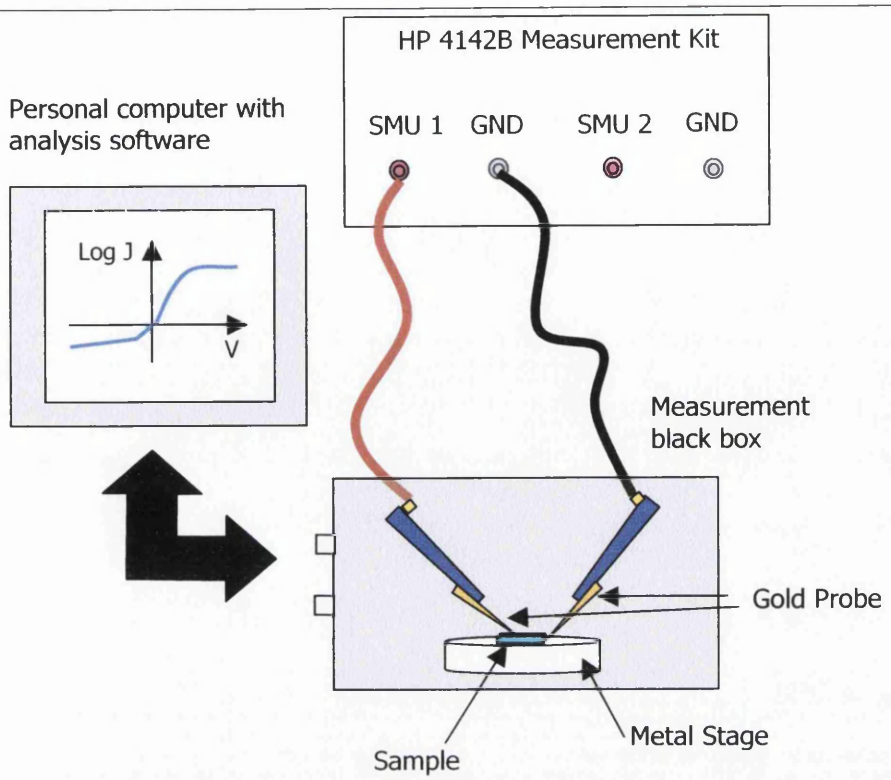

Figure 4.8: Schematic diagram of the HP 4142B instrument set-up for I-V measurements.

The sample is placed in such a way that the back Ohmic contact is facing down, touching the metal stage and the Schottky contacts are facing upwards. Subsequently, two sharp metal probes are placed into contact with the sample, with one probe on the diode to be measured and the other at the edge of the sample on the metal stage, which is used as an Ohmic contact. In this case, gold probes are used to minimise surface scratches on the diodes. The probes are positioned by micrometric verniers and are placed accurately on top of the 650μm diodes using a microscope. A bias is applied across the probes and the current passing through the diode and the Ohmic contact is measured. The I-V characteristic curve (see Figure 2.8) is then displayed on the computer connected to the instrument. The parameters such as step size, voltage range, acquisition time and noise filters can be adjusted by software

pre-loaded on the computer. The I-V plots are then saved as ASCII file and further processed using EXCEL in order to extract ϕ_b and the ideality factor, n.

4.6 The VG ESCAlab MKII

The Vacuum Generators (VG) electron spectroscopy for chemical analysis laboratory (ESCAlab) was manufactured using non-magnetic stainless steel. The system consists of three main chambers; namely the analysis, preparation and the evaporation chamber. The instrument layout of the system is illustrated in Figure 4.9. Although these three chambers are built-in together, they can be individually sealed off by UHV gate valves, enabling them to operate separately. Two liquid nitrogen trapped diffusion pumps, attached to the analysis and preparation chambers respectively, maintained the UHV environment in the system. Subsequent to baking, pressures of $\sim 6 \times 10^{-10}$ mbar in the analysis chamber and $\sim 8 \times 10^{-10}$ mbar in the preparation chamber were usually attained.

The heart of the system is the analysis chamber, which consists of all essential components for XPS operation, an electron gun for both Auger Electron Spectroscopy (AES) and Scanning Electron Microscopy (SEM), a scintillator, a high precision sample manipulator and an ion gun.

On the other side, the preparation chamber comprises of a fast entry load lock, which can be isolated from the system via a valve. The vacuum within the load lock is maintained by a rotary pump at pressure of $\sim 10^{-2}$ mbar. Samples were mounted onto custom-made stubs (see section 4.6.3) and were introduced into the main system through the load lock. Once in the system, the load lock valve has to be shut immediately in order for the pressure to recover in the main system. Within the system, the sample can be transferred between the analysis or preparation chamber using a transfer mechanism referred to as 'railway track'. The LEED optics are situated at the end of the preparation chamber, which can be used for crystallography study.

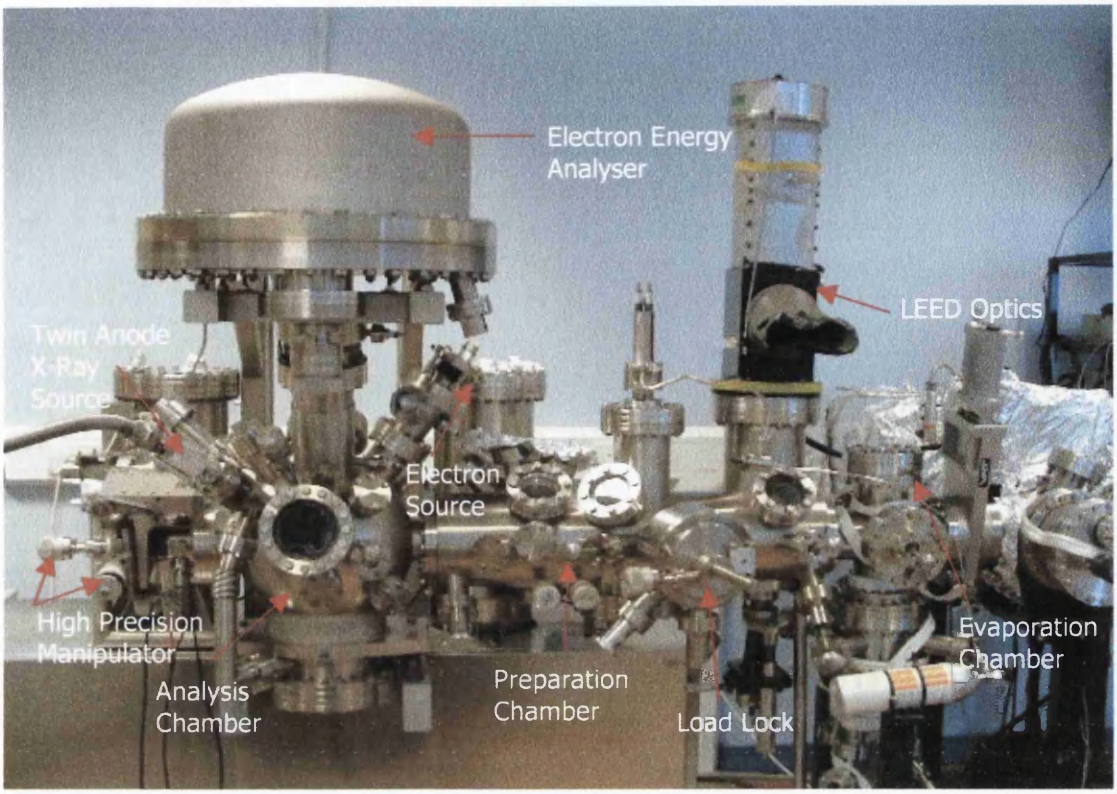

Figure 4.9: Front view photograph of the VG ESCAlab MKII surface analysis instrument.

The third part of the system is the evaporation chamber, which is mainly used for deposition or growth of materials. The evaporation chamber can be fitted with four different sources and is also equipped with electrical connections, allowing annealing of the sample via an external power source. During deposition, the sample is held upside down in the evaporation chamber by a tailor-made manipulator stage attached to a rotary drive enabling mechanical adjustments to the position of the sample. Thus, the facility within the evaporation chamber has the capability of depositing materials onto a sample held at either room temperature or elevated temperature.

4.6.1 X-ray Source

As suggested from its name, the operation of XPS requires an X-ray source as a photon source. The ESCAlab system is equipped with a twin anode (Al and Mg) X-ray source, which provides two different photon energies of 1486.6eV for Al Kα and 1253.6eV for Mg Kα. Depending on the experiment requirements, one could easily swap between these two anodes. There are two main considerations on the choice of material used for the X-ray source. Firstly, the characteristic X-ray energy must be sufficiently high to excite electrons from the most core levels in the sample and secondly, the line width of the characteristic X-ray energy must not limit the energy resolution required in the technique. In order to avoid such limitation, it is essential to use materials that have a characteristic line width of less than 1eV [9]. Al and Mg have the line width of ~ 0.85eV and 0.7eV respectively, making them the best candidates for X-ray sources (see Table 3.1). However, since the system is not fitted with a monochromator, the spectra were generally broadened by ~ 1eV resulting in poorer resolution as compared to system with fitted monochromator and SXPS system.

4.6.2 Electron Energy Analysis

The photoelectrons emitted from the sample enter an energy analyser via a set of transfer lens. The analyser is a μ-metal concentric hemispherical analyser (CHA) and is illustrated schematically in Figure 4.10.

The analyser mainly consists of two hemispherical surface (inner and outer) of radius R_1 and R_2 positioned concentrically on a circular flat metal plate known as the Herzog plate. There are slits on the Herzog plate, centred on an equipotential surface between the two hemispheres, which provides the entrance and the exit path for the electrons. A potential of V_1 and V_2 is applied to the two hemispheres such that V_1 is positive with respect to V_2. The median equipotential surface between the two plates has a radius of R_0 and a potential of V_0 given by [9]

$$R_0 = \frac{R_1 + R_2}{2} \qquad [4.2]$$

$$V_0 = \frac{V_1 R_1 + V_2 R_2}{2R_0} \qquad [4.3]$$

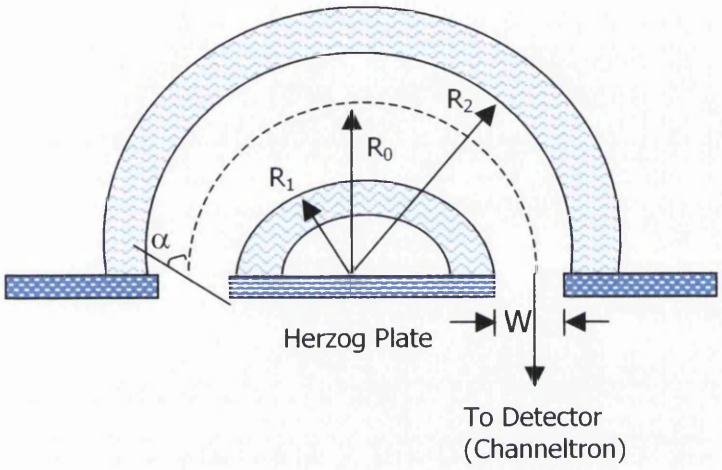

Figure 4.10: Schematic diagram of the concentric hemispherical analyser (CHA) used in ESCAlab. Dotted lines represents the electrons path.

The slits of the Herzog plate have a width W and a retarding potential of V_r is applied to the plate. Photoelectrons entering the analyser via the slit are focused with an electrostatic lens and they are either retarded or accelerated to the pass energy of E_p by the plate. For electron with an initial kinetic energy E_k, the relationship between pass energy and retarding potential can be written as

$$E_k = E_p + eV_r \qquad [4.4]$$

Upon entering the analyser, the photoelectrons come under the influence of the electrostatic field between the hemispheres. Therefore, the photoelectrons will travel in the curved path in the centre as illustrated by the dotted line in Figure 4.10. Only electrons with the correct E_p will be effectively deflected to travel between the hemispheres until they emerge from the exit

slit to be detected by the channel electron multiplier (channeltron). The relationship of the pass energy and the potential difference (ΔV) across the hemisphere is given by

$$E_p = eV_0 = e(V_1 - V_2)\left(\frac{R_1 R_2}{R_1^2 - R_2^2}\right) \qquad [4.5]$$

A constant pass energy is required during the recording of a spectrum to maintain a constant absolute resolution (ΔE) . This is achieved by operating the analyser in constant analyser energy (CAE) mode. In this mode, the retarding potential V_r applied to the Herzog plate is swept to produce the correct spectrum. For example, if the scanning range is 35-45eV with a pass energy is 20eV, the retarding voltage would have to vary between 15-25eV as related by equation [4.4]. The absolute resolution of the analyser can then be expressed as

$$\Delta E = E_p\left(\frac{W}{2R_0} + \frac{\alpha^2}{4}\right) \qquad [4.6]$$

where α is the acceptance angle of the analyser. The resolution can be further improved by reducing the value of pass energy or the width of the entrance slit. However, this will also reduces the signal intensity, thus a compromise between the resolution and the intensity must be made. The signals leaving the analyser will be collected and amplified by a multiple channel detector (MCD) which consists of five channels. These amplified signals are then sent to a computer for further analysis.

4.6.3 Sample Mounting and Temperature Calibration

Within this work, all samples are held in a modified e-beam stub, which enables e-beam heating for annealing purposes. In addition, the stub is designed in such a way that it securely holds the sample while performing all the necessary experiments within the UHV system, including overlayer

deposition, annealing, XPS scans and LEED investigation. The geometry of the e-beam stub is shown in Figure 4.11.

Generally, the main structure of the stub is commercially available from Vacuum Generators (VG). However, the top plate is specially designed to suit the experimental requirements of this work. The plate is made of metal, and a hole is cut in the centre of the plate. Note that the 'eyelet' feature on the top plate is designed for connections purposes. The sample is held on the top plate by a pair of isolated tantalum clips, secured by molybdenum screws. These clips are located on side of the plate, which accords with the sample size such that the pressure is distributed evenly to avoid damage to the sample.

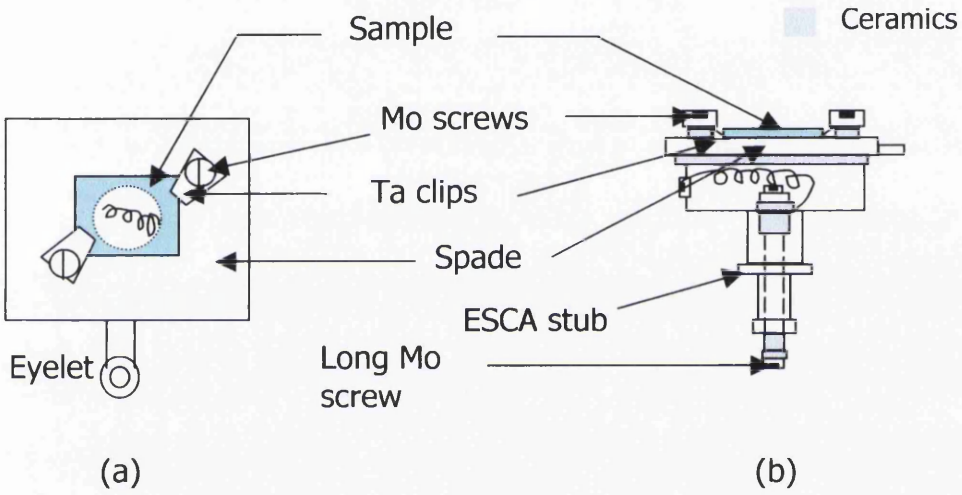

Figure 4.11: E-beam heating stub for ESCAlab. (a) Top view (b) Cross-sectional side view.

Underneath the plate, there is a tungsten filament held securely by a long molybdenum screw. Electrically isolated by suitable ceramics, the stub can be used for high temperature e-beam heating with a high voltage being applied on the top plate, thus heating the sample indirectly from below. Figure 4.12 shows the annealing process on the e-beam stub at high temperature. A careful calibration of the annealing temperature (running at 1kV) is conducted using thermocouples to produce a stable temperature. The plot of

temperature versus emission current for e-beam heating is plotted in Figure 4.13. The temperature obtained is expected to have a percentage error of ±15%.

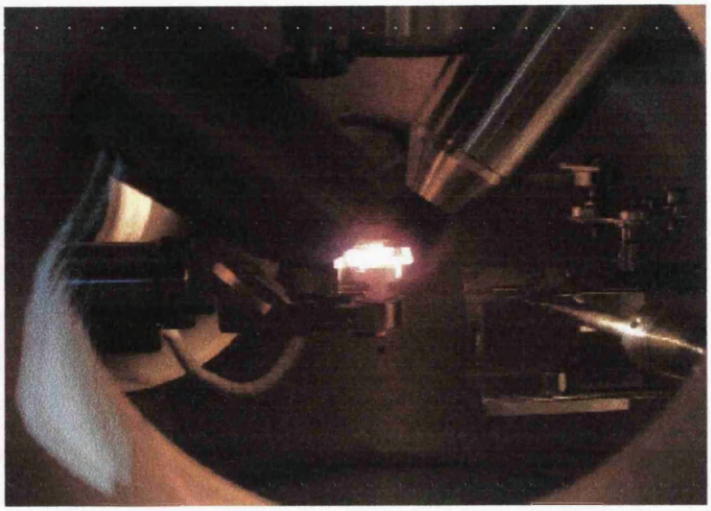

Figure 4.12: Annealing process using the e-beam stub under UHV conditions.

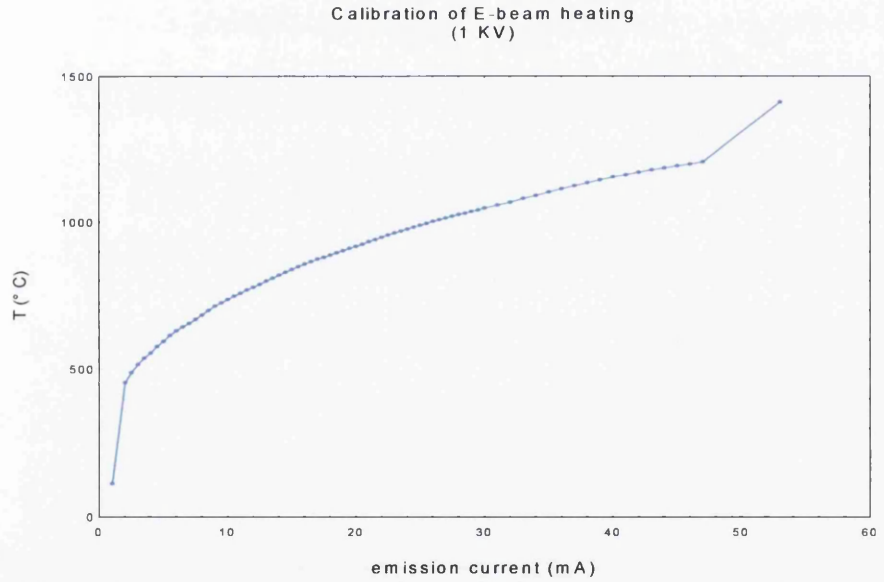

Figure 4.13: The plot of calibrated temperature versus emission current (mA) for e-beam heating in the ESCAlab.

4.7 References

[1] A. Koh, A. Kestle, C. Wright, S. P. Wilks, P. A. Mawby and W. R. Bowen, Appl. Surf. Sci., **174**, 210-216 (2001).

[2] Omicron Vakuumphysik Gmbh, *Instruction manual for the Omicron UHV evaporator EFM 3*, Version 1.7, (1993).

[3] P. R. Dunstan, PhD Thesis, University of Wales, 1997.

[4] Oxford Applied Research, *Operating and service manual for the mini e-beam evaporator EGN 4*.

[5] J .J. Bellina Jr., J. Ferrante and M. V. Zeller, J. Vac. Sci. Technol., **A4**, 1692 (1984).

[6] V. Van Elsbergen, T. U. Kampen and W. Mönch, Surf. Sci., **365**, 443-452 (1996).

[7] U. Starke, Ch. Bram, P. R.Steiner, W. Hartner, L. Hammer, K. Heinz and K. Muller, Appl. Surf. Sci., **89**, 175 (1994).

[8] W. Kern, D. A. Puotinen, RCA Rev., **31**, 187 (1970).

[9] M. P. Seah and W. A. Dench, 'Surface and Interface Analysis, Vol 1-Auger and X-ray Photoelectron Spectroscopy', Edition 2 (1990).

Chapter 5

Cleaning of Silicon Carbide

5.1 Introduction

The ultimate triumph in fabrication of devices is to be able to produce devices with excellent performance, long lifetimes and lastly, high reliability. The initial cleaning step or surface preparation of the wafer plays a crucial role in achieving these goals, as to determine the quality of the final device produced. Hence, it is essential that this phase be carried out with extreme care and caution before proceeding to any other fabrication procedure. Although SiC has been identified as a potential material for high power electronics [1], the difficulties in achieving good metal contacts have so far prevented wide commercial development. Thus, it is apparent that a clean surface is compulsory, as a starting platform prior to metalisation as it plays an important role in controlling the behaviour of metal contacts.

Up to date, various techniques have been adopted to prepare chemically clean, atomically ordered SiC surfaces. The first approach is via wet chemical etch. Although it may sound simple, this technique has been widely investigated and it has been proven that chemical treatments can be used to control surface termination, which is directly related to the mechanism of Fermi level pinning [2, 3]. Commercially grown wafer surfaces are far from atomically clean. Thus, as the

rule of thumb in semiconductor industry, all wafers (also applicable to SiC wafers) are chemically etched using the standard RCA clean [4], which includes a HF dip to remove organic, ionic and oxide substances. Although these chemical solutions are able to remove most of the native oxide, the possibilities of the surface being re-oxidised are very high as the SiC surface has to be exposed to air before metal deposition. However, it is possible to obtain atomically clean surface via UHV treatments. Generally, this is a follow-up on the RCA clean and consists of UHV preparation techniques such as annealing cycles, oxide-strip and heating the sample under Si-flux or hydrogen plasma [5 – 8] environment.

In this chapter, an investigation on a new procedure for obtaining an atomically clean surface in SiC will be presented. This technique is based on a layer of Si, which is evaporated onto the SiC surface followed by an immediate re-evaporation. Note that this technique is optimised to our laboratory equipment calibration and might be slightly different if applied to other systems. The analysis of data obtained from XPS, STM and LEED will be appraised and discussed. In addition, the result from the interface study on Si-SiC will also be presented to aid the understanding of the effect of Si interlayer onto the atomically clean SiC surface.

5.2 Experimental Procedures

All XPS experiments were conducted on the VG ESCAlab MKII system as described in section 4.6. Core levels spectra were recorded on the surface before and after the investigated preparation techniques, emphasising the *Si 2p* and *C 1s* core level. In addition, spectra from the surface at different Si overlayer thickness and after annealing were recorded in order to gain more information about the cleaning process. In order to observe the surface structure of the final atomically clean surface, STM images were also recorded. Surface crystallography and reconstructions were investigated using LEED.

5.2.1 Silicon Carbide Starting Surface

The SiC samples used were obtained from CREE Research Inc. and the specifications of the wafer are listed in Table 4.1. The 'as-received' samples are far from clean and exhibit screw defects, planar defects plus a surface roughness of 23.3Å RMS over a 50μm x 50μm surface [9]. An STM image (5nm x 5nm) of such rough surface is shown in Figure 5.1. From the image, wide trenches and a high degree of surface roughness is clearly observed. In addition, the sample exhibits a blur undetermined LEED pattern at very high energy (above 180eV), which clearly indicates the heavy contamination on the surface.

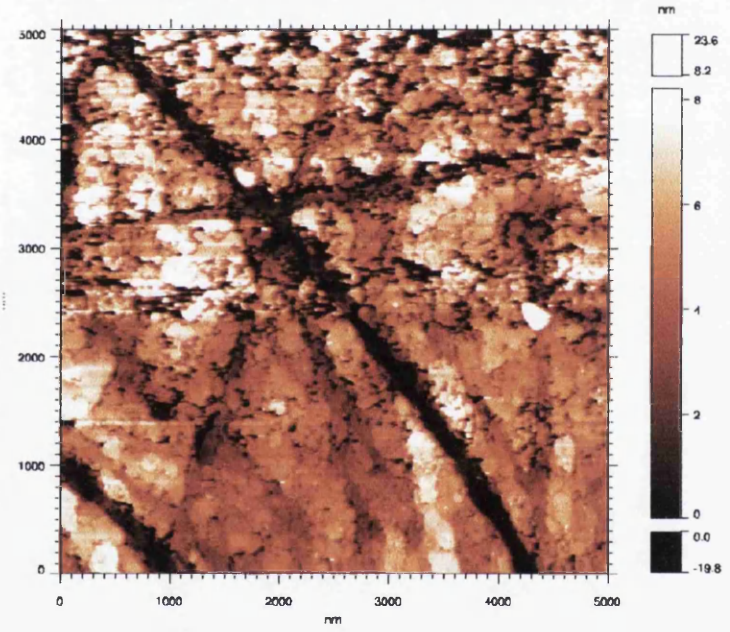

Figure 5.1: A (5μm x 5μm) STM image of the SiC substrate surface taken at –2.056V, 0.5nA. Wide trenches and a high degree of surface roughness can be visibly observed.

Hence, the preparation of a clean semiconductor (in our case SiC) surface is critically important to produce good contact properties. To achieve an atomically clean surface, the preparation techniques and the resulting surface from the associated cleaning procedure used in this work are discussed in detail in the

following sections.

5.2.2 Wet Chemical Etch

Before any experimental procedure, the 'as-received' sample has to be cleaned to remove unwanted contaminants and substances. The sample preparation and initial cleaning procedure are as described in section 4.2.1.1. A wide XPS scan spectrum of such surface is shown in Figure 5.2. After the *ex-situ* RCA clean, the sample is expected to be free from any residues and contaminants. Even so, it is clearly seen that oxygen elements or possibly water molecules from the air are still present on the surface. The blurred and faded (1 x1) LEED pattern at high energy (above 100eV) confirms the presence of these surface contaminants. Hence, further cleaning is required to remove these air contaminants.

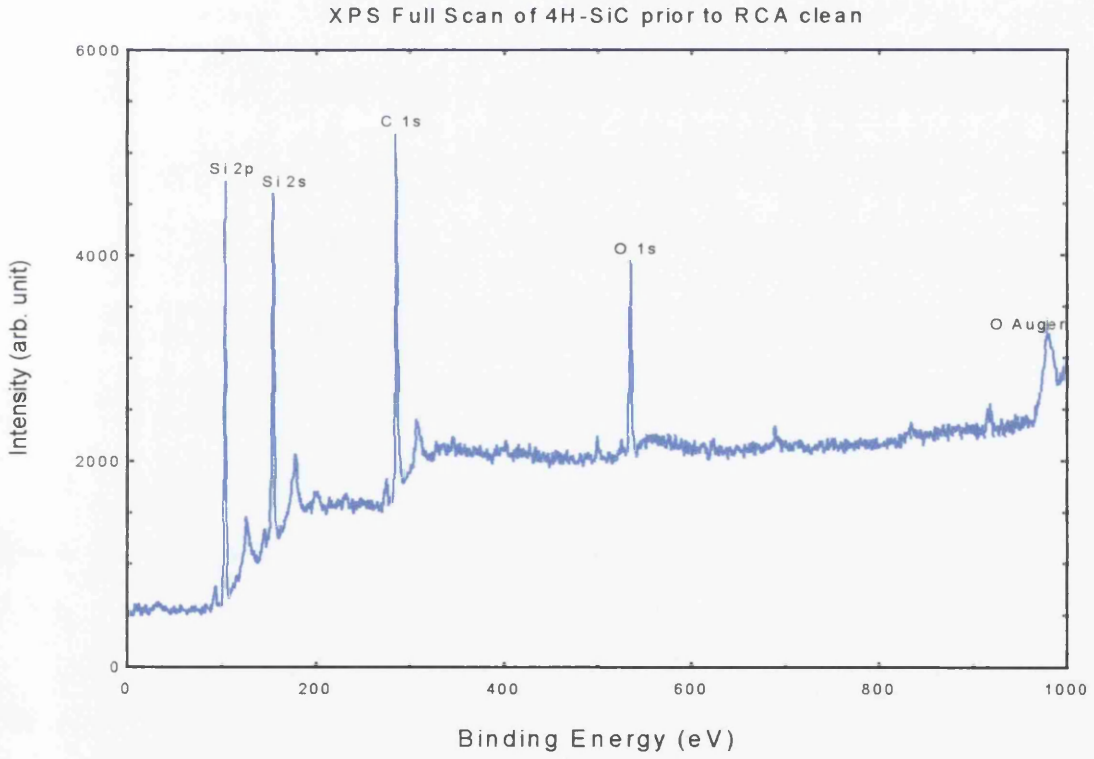

Figure 5.2: Full scan XPS spectrum of 4H-SiC sample after RCA clean. The *O 1s* core level is clearly seen.

5.2.3 *In-situ* UHV Annealing

In order to completely remove any possible surface contaminants including water vapour and oxygen, an *in-situ* clean, involving annealing cycles was implemented (described in section 4.2.1.2). The objective of the UHV annealing cycles is to remove oxygen and water molecules from the surface, yet to prevent over heating, which could produce graphite on the surface [10]. Therefore, a long overnight mid-temperature anneal and high temperature flashes is employed for this purpose.

After this cleaning procedure, the sample is expected to be free from any surface contaminants including oxygen as indicated by the XPS spectra (see Figure 4.1). In addition, LEED was used to check the surface cleanliness, and exhibited a sharp (1 x 1) pattern at a low energy of 45eV.

Figure 5.3: Sharp (1 X 1) LEED pattern of the UHV cleaned 4H-SiC sample, taken at 45eV.

The sharp (1 x 1) LEED pattern shows that the surface is cleaner than after the chemical clean but not yet atomically clean as no reconstruction was observed. This is confirmed by the curve fitting of the XPS *C 1s* spectrum, which shows other components than the bulk C component (see Figure 5.4(b)). These

additional components are proposed to be either carbonyl groups or hydrocarbons at the surface. Therefore, further cleaning is required to remove these unwanted C components.

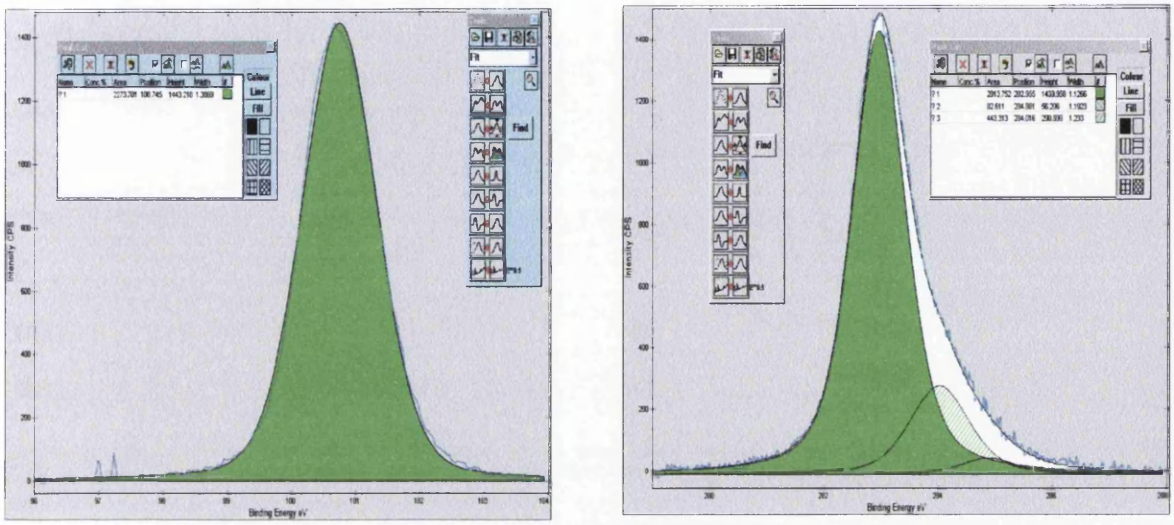

Figure 5.4: Deconvoluted core level spectra (a) *Si 2p*, consisting of bulk component only (b) *C 1s*, consists of bulk component plus additional hydrocarbon or carbonyl groups.

5.2.4 Si Evaporation/re-evaporation Clean

In order to remove the unwanted carbon components as described previously in section 5.2.3, a thin layer of Si is deposited onto the (1 x 1) SiC surface at room temperature followed by a re-evaporation of the deposited layer at 1000°C. The idea of this cleaning procedure is shown schematically in Figure 5.5. Nevertheless, the thickness of the Si has to be optimised in order to ensure the consistency of the cleaning procedure and this will be discussed in the next section.

5.3 Optimisation of Si Evaporation/re – evaporation Clean

The optimisation process is fairly straightforward. The procedure involves

depositing different thickness of Si, starting a 15Å, followed by annealing at 1000°C for several minutes in order to re-evaporate the Si. The resulting *C 1s* spectrum is the examined for every Si thickness in order to determine which thickness yields the cleanest surface. The Si thickness was increased in incremental steps of 5Å until a satisfactory clean surface was obtained. The deconvoluted spectra of the *Si 2p* core level after Si deposition and the resulting *C 1s* core level subsequent to an immediate anneal is illustrated in Figure 5.6 (a) and (b) respectively. The atomically clean surface, consisting of only bulk Si and C was obtained for 40Å Si and with a re-evaporation anneal at 1000°C for 8 minutes. The general properties of this atomically clean surface will be further discussed in the next section.

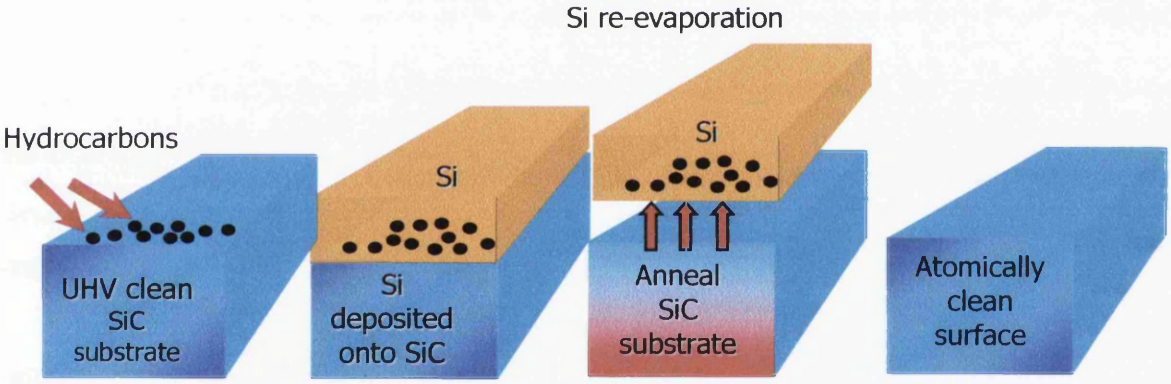

Figure 5.5: Schematic diagram of the Si evaporation/ re-evaporation cleaning technique.

5.4 The Atomically Clean Silicon Carbide Surface

Subsequent to the cleaning procedures (discussed in the last section), the surface appears free from any contaminants and consists of only bulk components as indicated by the *Si 2p* and *C 1s* spectra in Figure 5.7. Again, the surface cleanliness was checked with LEED. It was observed that the clean surface exhibits a ($\sqrt{3}$ x $\sqrt{3}$) LEED pattern at 56eV as illustrated in Figure 5.8.

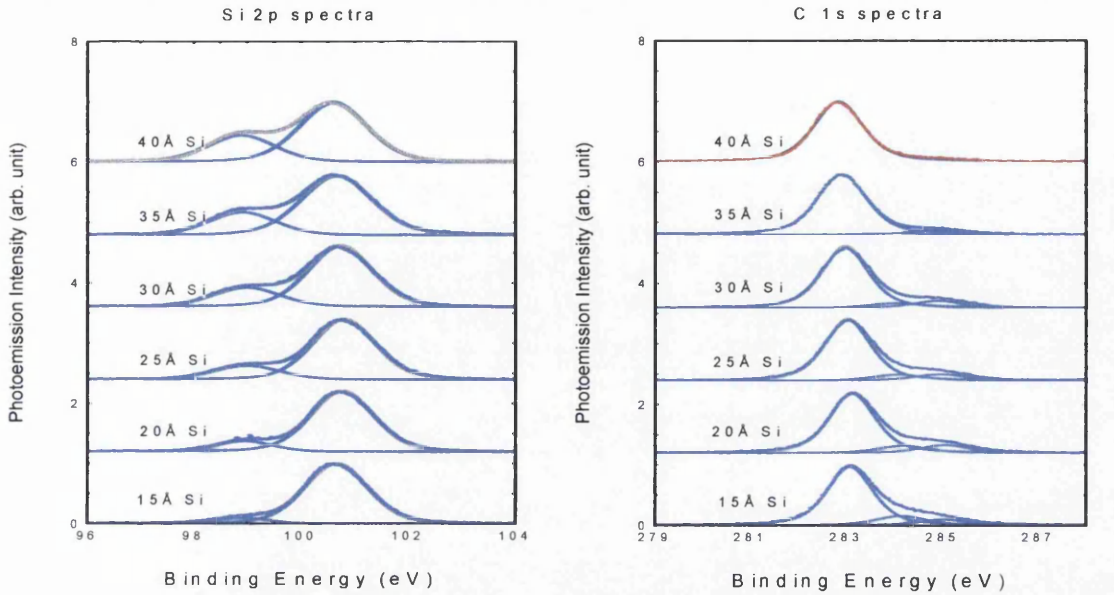

Figure 5.6: Core level spectra for the optimisation of the Si evaporation/re-evaporation cleaning process (a) *Si 2p* spectra after deposition of Si with various thickness (b) *C 1s* spectra annealed at 1000°C subsequent to the deposition of Si. An atomically clean surface is obtained at 40Å illustrated in the red spectra.

Si 2p core level

C 1s core level

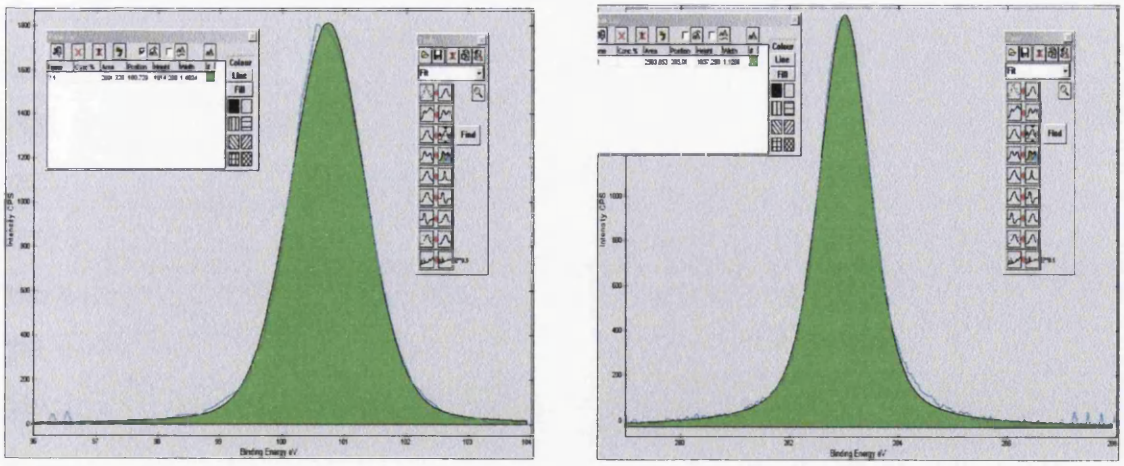

Figure 5.7: Core level spectra of the atomically clean surface consisting of only bulk Si and C.

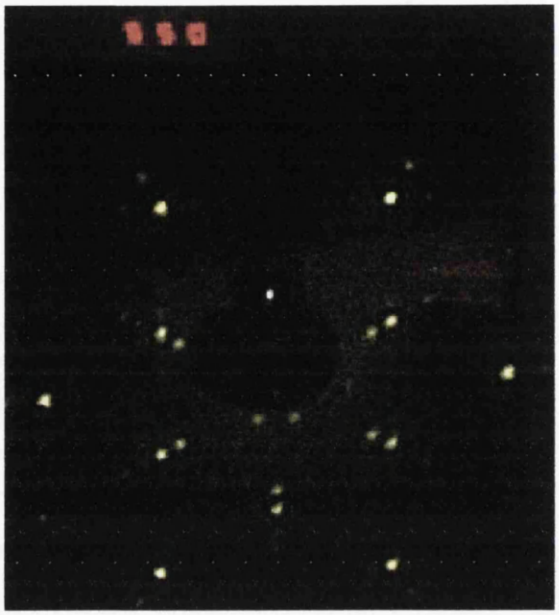

Figure 5.8: ($\sqrt{3}$ x $\sqrt{3}$) LEED pattern of the atomically clean surface taken at 56eV.

The ($\sqrt{3}$ x $\sqrt{3}$) surface reconstruction can be translated as a bulk terminated reconstruction [8]. Hence, this surface reconstruction again confirms the surface cleanliness. In order to further characterise this clean surface, STM images were taken and are shown in Figure 5.9 (a) to (d). From these images, it can be seen that the surface still consists of atomic steps, atomic defects, which includes vacancy defects and site defects plus the well-known micro pipe defects [9,10] despite of the clean surface. Although these defects are undesirable, they are more likely associated with the nature of the wafer growing process. Therefore, the necessary work to reduce these defects is beyond the scope of this work and hence will not be further discussed. STM provides the ultimate evidence about the cleanliness of the surface as the atomic resolution can only be achieved on atomically clean surfaces.

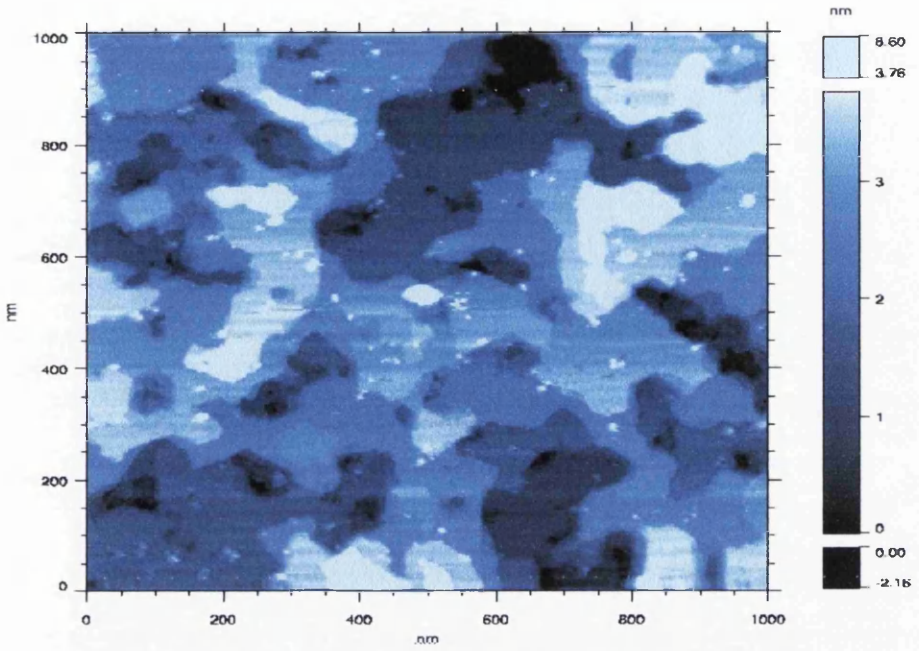

Figure 5.9(a): Wide area scans of the atomically clean surface. Steps of different height and left over Si (white spots) are clearly visible on the surface.

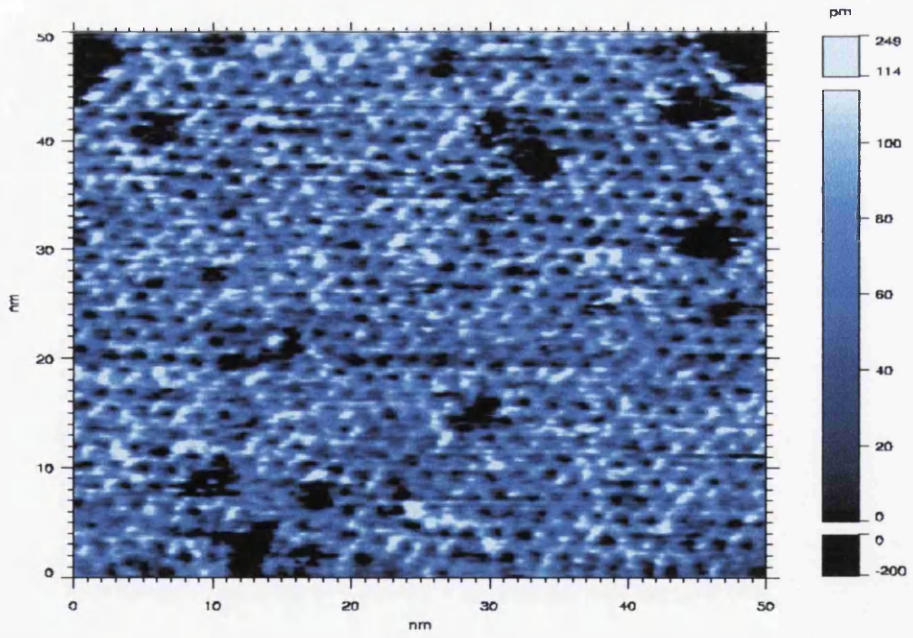

Figure 5.9(b): 50nm x 50nm scan of atomic rows of the clean surface. Surface defects are clearly visible.

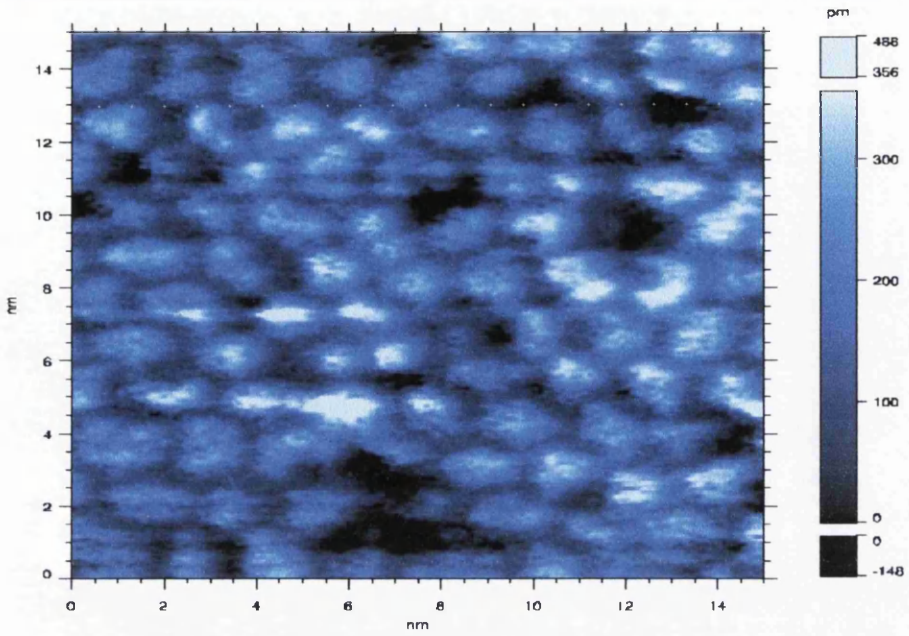

Figure 5.9(c): Small area scan (15nm) of the clean surface at atomic resolution. Atomic rows and missing atoms are clearly observed.

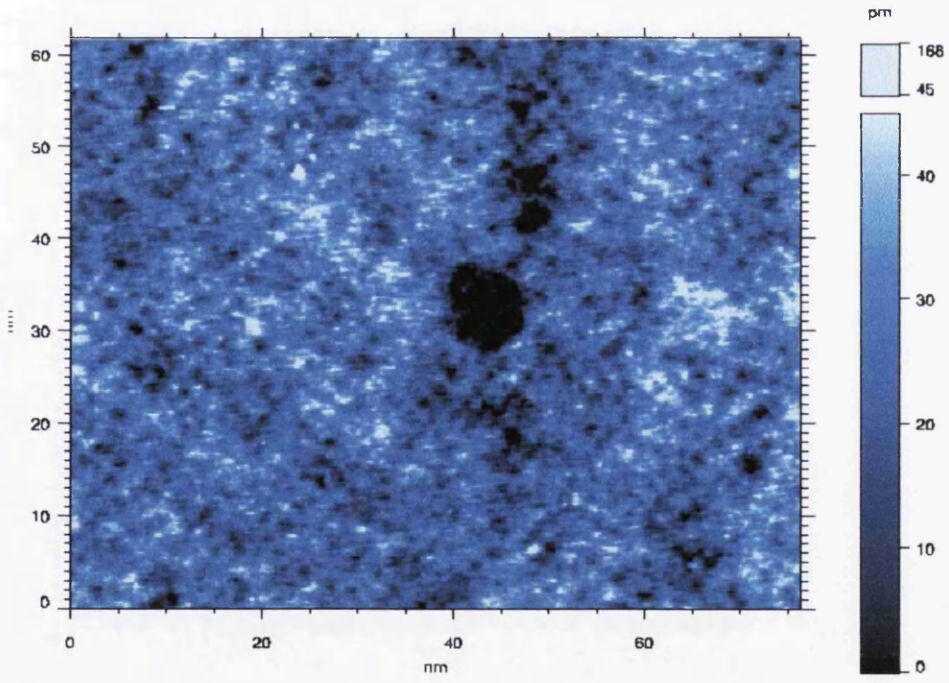

Figure 5.9(d): 80nm x 60nm scan of the clean surface showing a micro pipe defect at the surface.

The structure of an atomically clean SiC surface obtained via the Si-evaporation/re-evaporation cleaning process has now been elucidated. To ensure the consistency of this work, this atomically clean surface consisting of bulk only element is implemented as the starting surface for all experiments throughout this work.

5.5 The Si-SiC Interface Study

Previously, we have seen the usefulness of a thin layer of Si in producing an atomically clean surface. In addition, the main objective of this work is to investigate the effect of a thin Si interlayer in Ni-SiC contacts. Hence, it is essential to understand the basic reaction of the composite structure, prior to a more complex junction (i.e. Ni-Si-SiC) being formed to ease understanding at a later stage. The Si-SiC experiment is initiated by the obtaining the atomically clean surface (as discussed previously). This is followed by sequential deposition of Si with increasing thickness onto the atomically clean surface. The sample was then annealed from 250°C to 1050°C for 10 minutes. Throughout the process, the sample was constantly monitored by XPS to observe any changes in the interface properties. The results attained are presented as below.

- **Si – SiC interface formation**

Figure 5.10 shows the *Si 2p* and *C 1s* core level spectra during sequential deposition of Si onto an oxygen free surface (see section 5.2.3) after an *in-situ* anneal. The spectra clearly show that there is no shift in energy position for both *Si 2p* and *C 1s* peak throughout the interface formation. The 'shoulder' or the secondary peak located at the lower binding energy side of the *Si 2p* spectra is associated with the deposited Si. Hence, this secondary peak is observed to 'grow' with an increasing intensity with the deposition thickness. Generally, one would expect an increasing trend in Si intensity (deposited Si and bulk Si intensity) with additional Si overlayers onto the SiC surface. However, this is not

the case, as illustrated in the intensity plot shown in Figure 5.11(a). Note that the intensity used here refers to the area under whole spectrum (for both *Si 2p* and *C 1s*) and absolute values are employed. In the plot, the Si intensity (deposited Si and bulk Si) is observed to increase at initial deposition of very thin layer (< 1Å) followed by a sharp decrease until 5Å and finally, a linear increase. The occurrence of such behaviour indicates that overlayers are formed into islands or clusters of Si on the surface (i.e. Volmer-Weber mode, see section 3.4.3.3). Another reason for such behaviour is that the solid-state structure of additional Si atoms onto SiC surface had been altered.

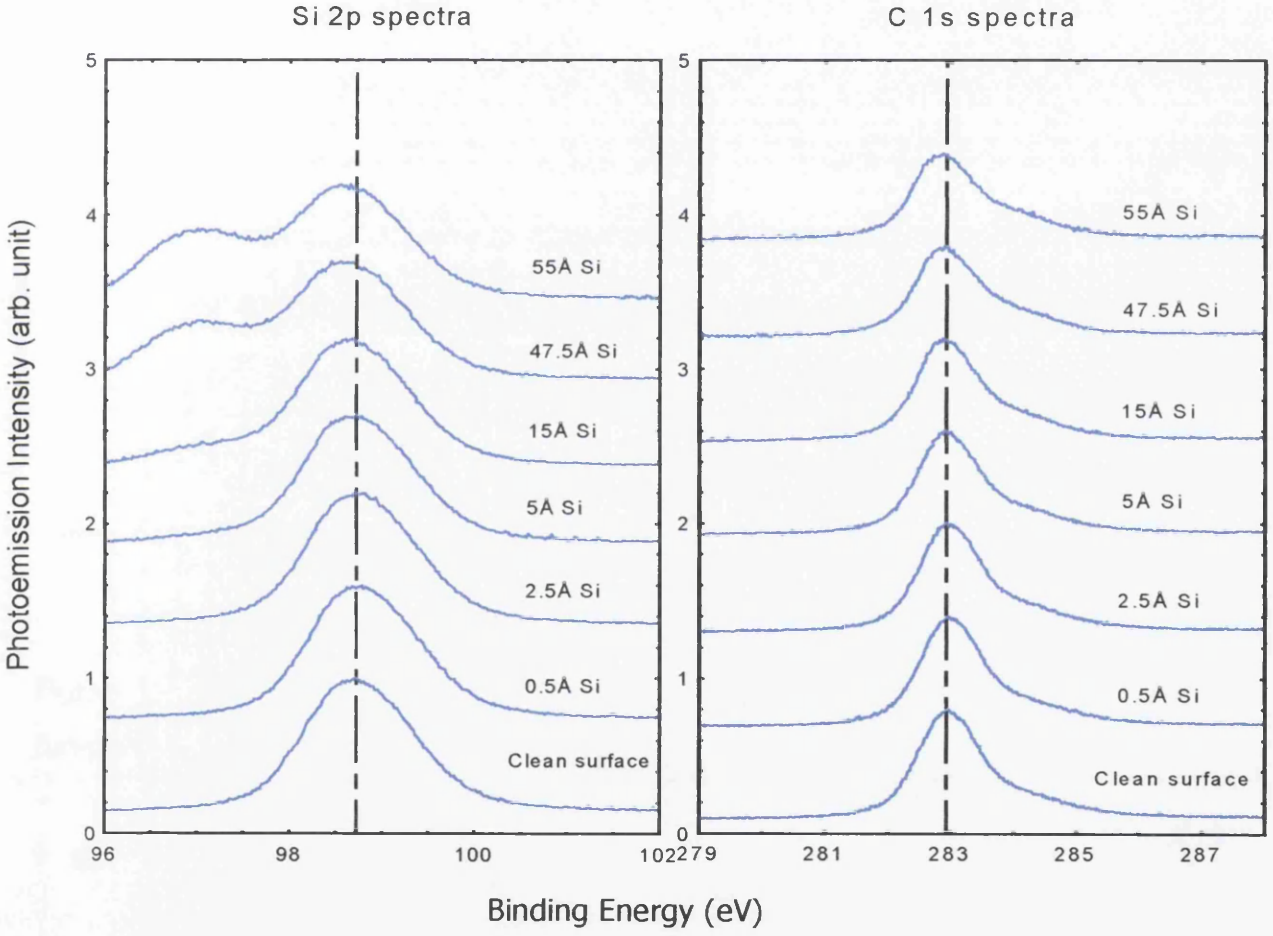

Figure 5.10 : Stacked *Si 2p* and *C 1s* core level spectra at sequential deposition of Si.

It is observed that the deposited Si atoms are likely to bond in the hexagonal structure of SiC at initial stages, but are changed into a cubic structure at later stage with thicker coverage. With reference to solid-state theory [11], the hexagonal closed-pack structure (SiC) has more atoms in a single primitive cell compared to the zinc-cubic structure (Si). This observation is in agreement with the work by *Starke et al* [8], which proposed that excess Si onto hexagonal SiC enhance in cubic stacking that could also lead to the formation of polytype heterojunctions. Meanwhile, the intensity of C is observed to be decreasing as expected with Si overlayers covering the bulk.

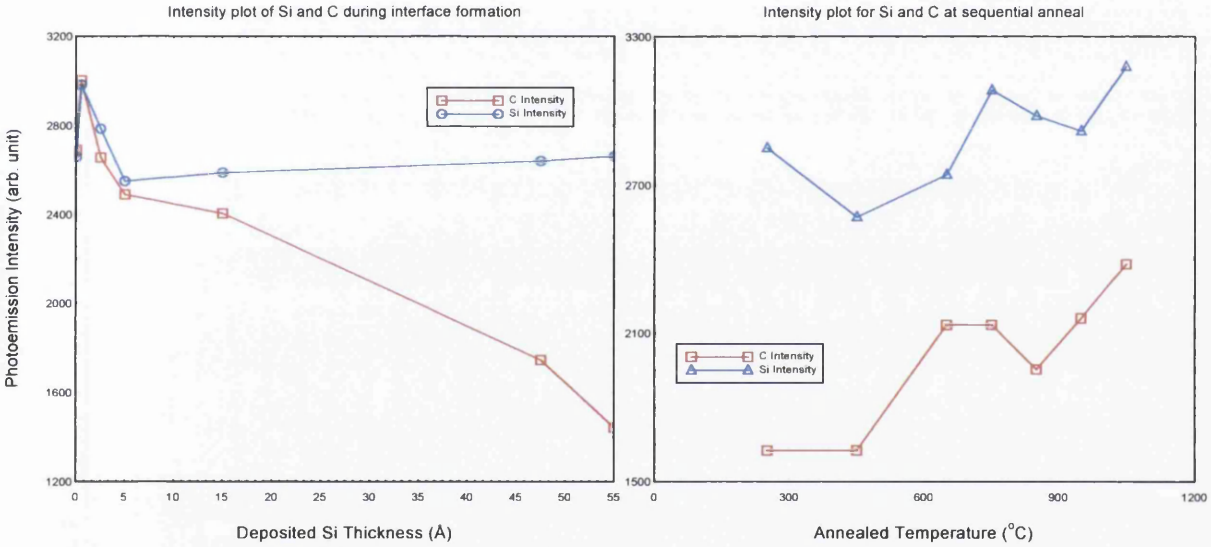

Figure 5.11: Intensity plot for Si and C (a) during interface formation (b) as a function of annealing temperature (°C).

- **Si – SiC interface annealed**

Subsequent to the interface formation, the interface is annealed sequentially starting from a low temperature up to a high temperature in incremental steps of 100°C. The *Si 2p* and *C 1s* core level spectra throughout the annealing stages is illustrated in Figure 5.12. Again, both core level spectra

show no sign of peak shifts. The main observation throughout the annealing process is the gradual disappearance of the 'shoulder' of the *Si 2p* core level spectra. This may correspond to the chemical reaction between Si and bulk SiC at low temperature anneal (250°C to 450°C) and finally re-evaporation of Si at higher temperature (above 650°C).

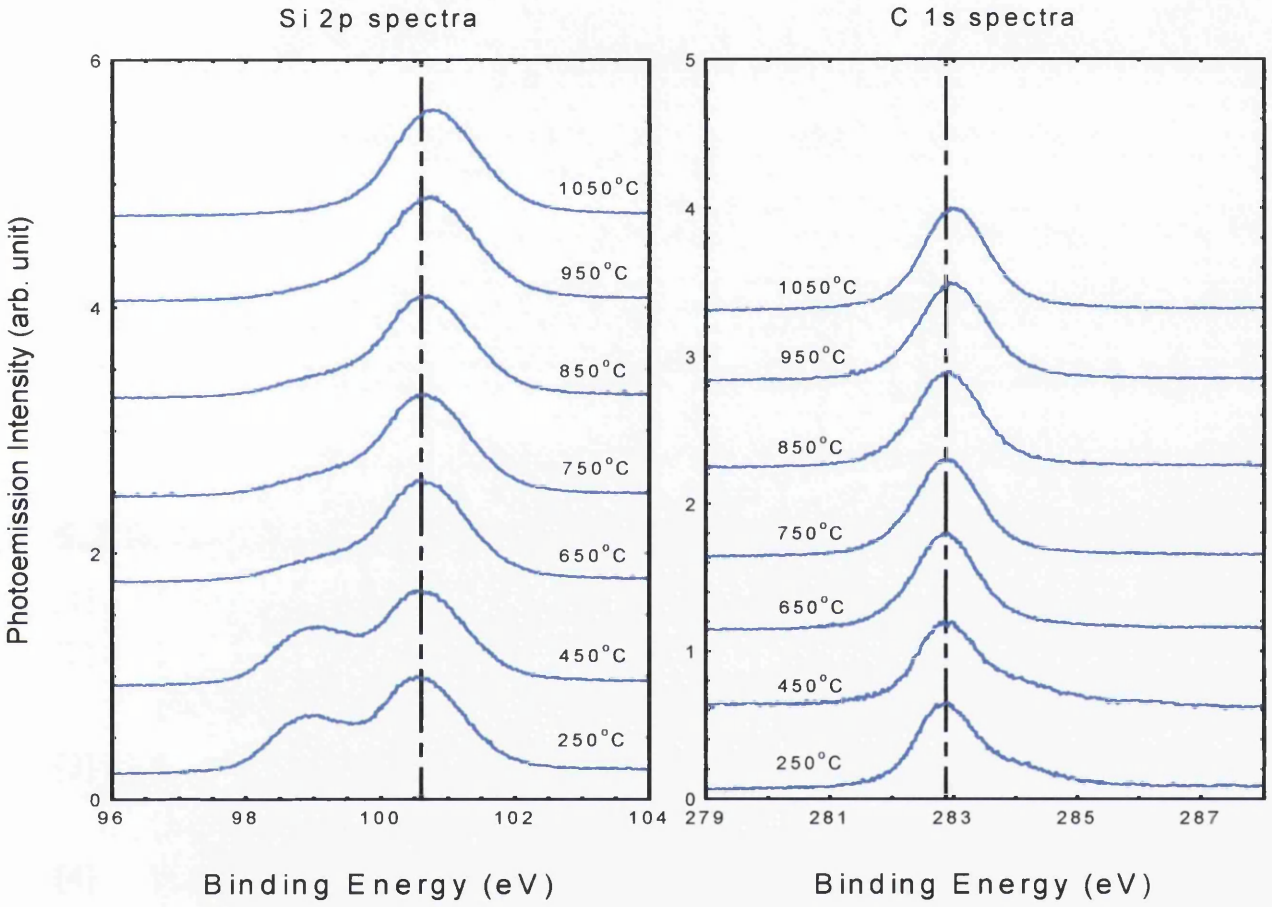

Figure 5.12 : Stacked *Si 2p* and *C 1s* core level spectra after sequential anneals.

This incident is confirmed by the intensity plot showed in Figure 5.11(b). Here, the overall intensity of both Si and C are observed to increase in a similar manner. The initial decrease in Si at low temperature is possibly due to surface re-ordering and further decrease at temperatures above 700°C as a result of re-evaporation of Si. Up to a temperature of 1050°C, almost all of the deposited Si

has been evaporated, hence revealing a strong bulk signal for both Si and C.

5.6 Conclusion

The ultimate objective of this work is to implement a layer of Si to improve the Ni-SiC contact conditions. In the past few sections, we have seen the merit of a Si interlayer in producing an atomically clean surface. Although the atomically clean surface still shows of defects, the surface conditions produced are adequate enough for metal contact purpose. In addition, the reaction between Si-SiC interfaces has also been studied; indicating that additional Si overlayers onto clean 4H-SiC do not form any barrier or any major chemical reactions. Hence, with the presence of a Si interlayer in any metal contacts will not cause any disturbance to the overall composition. However, the effect of such interface (Si-SiC) with additional layers of metal (in our case, Ni) is yet to be studied and will be further discussed in Chapter 6.

5.7 References

[1] J. B. Casady, R. W. Johnson, Solid State Electron., **39**, 1409 (1996).

[2] S. Hara, T. Teraji, H. Okushi, K. Kajimura, Appl. Surf. Sci., **117/118**, 394-399 (1997).

[3] S. Hara, T. Teraji, H. Okushi, K. Kajimura, Appl. Surf. Sci., **107**, 218-221 (1996).

[4] W. Kern, D. A. Puotinen, RCA Rev., **31**, 187 (1970).

[5] L. Li, Y. Hasegawa, T. Sakurai, I. S. T. Tsong, J. Appl. Phys., **80**, 2524 (1996).

[6] U. Starke, J. Schardt, M. Franke, Appl. Phys., **A65**, 578 (1997).

[7] J. Bernhardt, M. Nerding, U. Starke, K. Heinz, Mat. Sci. and Eng., **B61-62**, 207-211 (1999).

[8] K. Heinz, U. Starke, J. Bernhardt, J. Schardt, Appl. Surf. Sci., **162-163**, 9-18 (2000).

[9] A. Koh, A. Kestle, C. Wright, S. P. Wilks, P. A. Mawby and W. R. Bowen,

Appl. Surf. Sci., **174**, 210-216 (2001).

[10] M. J. Bozack, Phys. Stat. Sol. (B), **202**, 549 (1997).

[11] C. Kittel, 'Introduction to Solid State Physics', Wiley and Sons, 6th Edition (1986).

Chapter 6

X-Ray Photoemission Studies of Ni-Si-SiC Contact Formation

6.1 Introduction

Metal – semiconductor contacts play a crucial role in all electronic devices. Although they have been used for decades, the control the behaviour of such contacts remains a challenge especially for SiC, which is rather new in electronic industry. There is a demand for a detail study on the ways to control the metal – SiC contacts. Up to date, difficulties on controlling and problems associated with reaction between metal – SiC contacts have been reported [1-4].

The control of interface reactions between reinforcement materials and matrix is a significant issue and should be considered together with individual materials properties in a successful composite design [5]. The issues of chemical reactivity, thermal stability, electrical characteristic and Schottky barrier height, ϕ_b are among the areas of interest in this study. Within this work, a thin layer of Si is used as buffer layer between 4H-SiC and nickel (Ni). In terms of high power applications, 4H-SiC is the finest candidate due to its superior properties such as wide band gap, high thermal conductivity and

high breakdown field, enabling it to operate in harsh environments in which conventional Si devices could not adequately operate. On the other hand, Ni has attracted much attention due to its low resistivity properties. However, the combination of Ni-SiC contact often results in disassociation of Si and C and also C segregation to the surface [1,6,7]. Therefore, the contact exhibits a poor interface quality. Additionally, the presence of a layer of unwanted C in the contact layer is a potential of contact degradation at high temperature and hence reduces the device performance. The basic concept behind this work is that the presence of a Si buffer layer should reduce or even eliminate the unwanted free C at the interface. In this case, Si is chosen as a candidate as Si is often used as a passivating element in semiconductors. In addition, the presence of a Si interlayer between Ni-SiC does not affect the overall structure and Si and Ni has the smallest lattice mismatch of 0.4% [8], giving an advantage to the overall structure. Hence, it is envisaged that with the combination of all these three useful materials, the fabrication of a device that is capable in overcoming the conventional C segregation in metal – SiC contacts can be achieved.

In this chapter, a photoemission study of Ni-SiC contacts, in the absence and presence of three different thicknesses of Si interlayer is presented. The investigation is initiated with a study of the plain Ni-SiC contact. Subsequently, a study on 20Å, 40Å and 60Å of Si interlayers, implemented between the Ni-SiC junction is conducted. The experiment is divided into two parts, the initial contact interface formation and sequential heat treatment. The details on the experiment procedure are described in the next section. Finally, the comparison of all the experiment observations is presented at the end of this chapter.

6.2 Experimental Procedures

The *in-situ* interface study experiments were mainly performed using XPS and occasionally using the integrated LEED optics within the system. The

samples used were n-type 4H-SiC epilayer obtained from CREE Research Inc. The wafers specifications were as listed on Table 4.1. Subsequent to *ex-situ* and *in-situ* treatments (as discussed in Chapter 5), overlayers were grown onto the atomically clean sample with a ($\sqrt{3}$ x $\sqrt{3}$) surface reconstruction. The overlayers are grown using UHV evaporation sources (see section 4.3). After understanding the formation of Si-SiC interface (see section 5.5), the study continues with the investigation of Ni-Si-SiC interfaces. In this case, the Si layer will then act as a buffer layer and is deposited in a single evaporation. Meanwhile, the interaction between Ni and SiC with the presence of a Si interlayer is investigated by a sequential deposition of Ni onto SiC samples with different thickness of Si interlayer (in our case, 20Å, 40Å and 60Å). Spectra of the *Si 2p*, *C 1s* and *Ni 2p* core level are recorded from the atomically clean surface, during the sequential overlayer growth (for both Si and Ni) and during the sequential anneals. In addition, in order to clarify the sample cleanliness, a wide full scan spectrum was also recorded to detect any unwanted contaminants on the sample. LEED optics was also used to check the cleanliness (i.e. surface reconstruction) of the sample and also to ensure that overlayers are properly grown onto the sample and are thick enough to cover up the surface. Thermal stability studies of the interfaces were conducted by UHV anneals as discussed in section 4.6.3. The annealing process was performed sequentially starting at 400°C in increment steps of 100°C up to 1200°C for 10 minutes. XPS scans were recorded at each stage to gauge the thermal effect on these interfaces.

With the intention of discovering the effectiveness of the role of a Si interlayer in Ni-SiC contacts, it is essential to compare the results obtained from contacts with a Si interlayer, to the contacts without a buffer layer. Hence, a control experiment on Ni-SiC interface, performed by sequential deposition of Ni onto clean SiC surface has been conducted especially for this purpose. The experimental procedure for the thermal stability study is similar as the above experiment.

6.3 The Ni-SiC Interface Photoemission Study

Although investigations of Ni-SiC contacts can be widely found in the literature, the experimental techniques, conditions and the starting surface of such studies vary widely. Thus, it is essential to perform this study using the same technique and experimental conditions, in order to compare and demonstrate the effectiveness of the Si interlayer. In this study, the starting surface is the atomically cleaned surface described earlier (see Chapter 5). Ni is then deposited in incremental steps of thickness onto this clean surface, forming a Ni-SiC interface. The interface is then annealed sequentially. XPS scans were recorded before and after every step in order to observed any changes to the core level spectra and the C content of the interface. The experimental procedure is as described previously in section 6.2. The results attained are described below.

- **Ni – SiC interface formation**

The curve fitted *Si 2p* and *C* 1s core level spectra are illustrated in Figure 6.1 and 6.2 respectively. With an atomically clean surface as a starting surface, the spectrum consists of bulk components only (i.e. bulk Si and C) as shown in the stack plots for both Si and C (Figure 6.1 and 6.2). As soon as a thin layer of Ni (1Å) is deposited onto the surface, Ni silicides are formed, indicated by a small component at the lower side of the *Si 2p* spectra. The silicides formed are observed to grow with increasing deposition of Ni, clearly illustrated by the intensity plot showed in Figure 6.3. For the ease of understanding, note that the intensity used throughout the discussion refers to the area under the curve and is not normalised (absolute values). In addition, the cross-sections for *Si 2p* and *C 1s* are very close (0.25 and 0.27 respectively) and had been corrected using sensitivity factor [9]; hence their intensity can be compared directly. Meanwhile, the intensity of bulk Si is seen to decrease, as expected, as the overlayer tends to cover up the bulk signal. Simultaneously, the *C 1s* spectra display the formation of free C and another

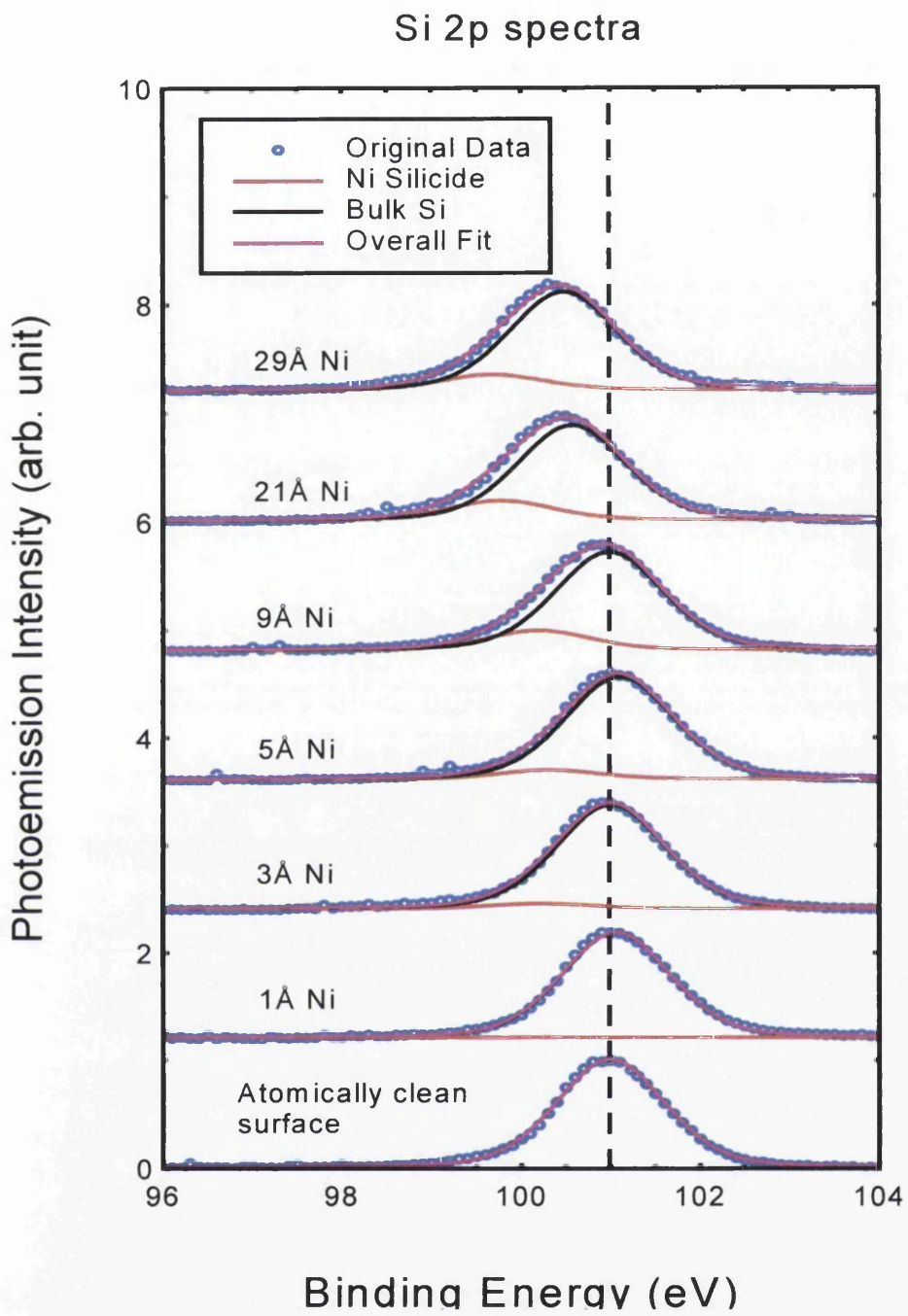

Figure 6.1: Curve fitted *Si 2p* core level spectra starting from the atomically clean surface followed by sequential deposition of Ni overlayers. The deconvoluted components including the original raw data are listed in coloured lines as described in the legend.

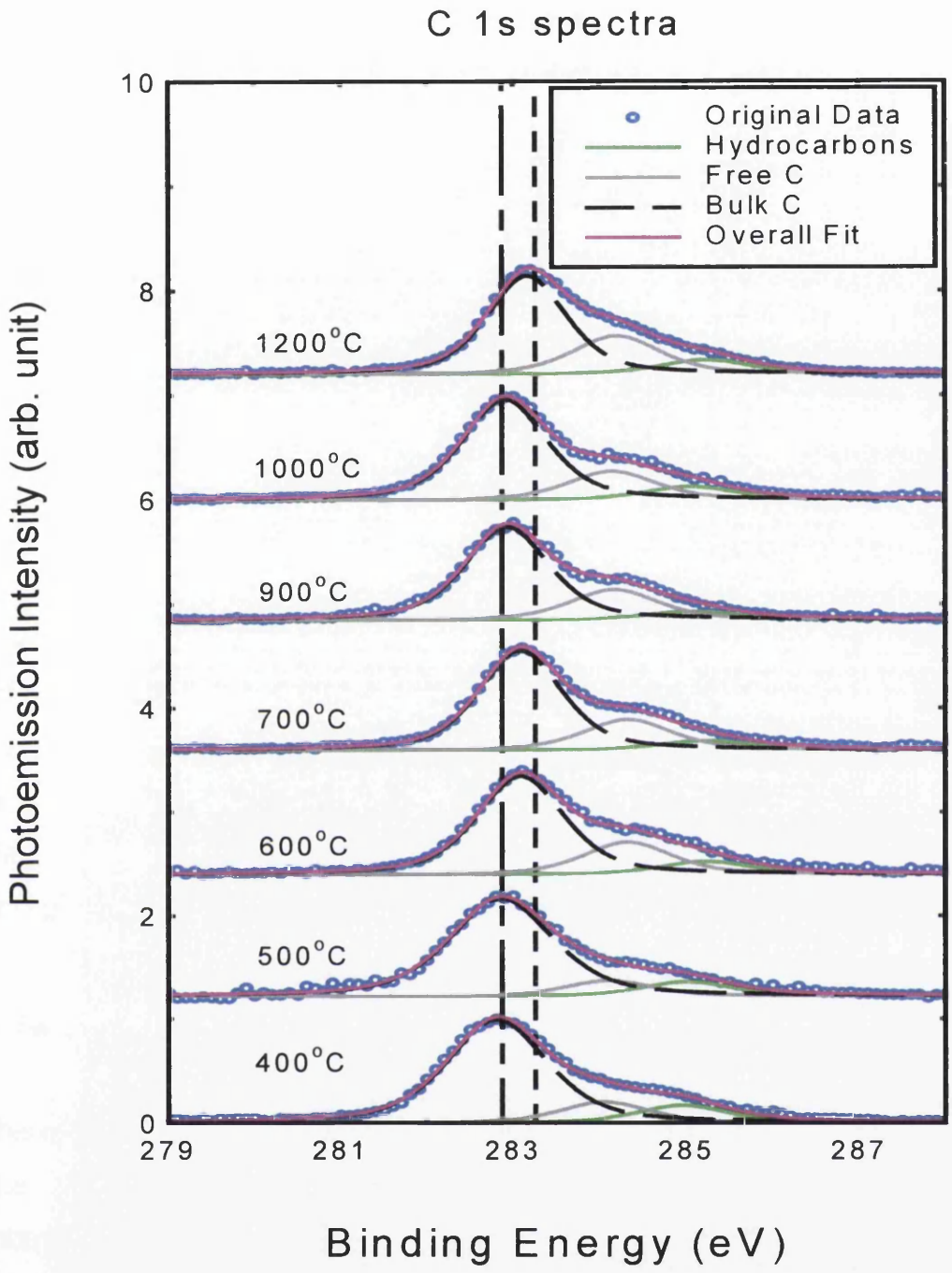

Figure 6.2: Curve fitted *C 1s* core level spectra starting from the atomically clean surface followed by sequential deposition of Ni overlayers. The deconvoluted components including the original raw data are listed in coloured lines as described in the legend.

component (proposed to be either carbon in carbonyl group or hydrocarbons), at the higher binding energy side of the spectra (see Figure 6.2). The intensity of these two newly formed components is also observed to grow together with the Ni silicides with increasing Ni thickness. However, the intensity of free C is seen to be slightly greater than the hydrocarbons. Similar to bulk Si, the intensity of the bulk C is also seen to decrease with increasing deposition of Ni. However, possible surface reconstruction might have occurred at the initial deposition of Ni, indicated by an increased in intensity for *Si 2p* and *C 1s* spectra between 3Å and 5Å of Ni. Obviously, the intensity of Ni increases with increasing deposition of Ni overlayers onto the surface (see Figure 6.3 (c)).

In addition, the interface formation is accompanied by a formation of barrier with the deposition of Ni overlayers. This event is indicated by the shift of the core levels (Si and C) towards low binding energy, which corresponds to a Fermi shift of approximately 0.5eV. Ni core level is also observed to shift in a same way, but in this case a much bigger shift of 1.3eV as a result of a Fermi shift superimposed to a chemical shift. The peak position plots of all three main components are shown in Figure 6.4 (a - c).

- **Ni – SiC annealed interface**

The study of the metal contacts would not be complete without a thermal stability study as it is vital to understand the effect of heat treatment (i.e. annealing process) to the interface, especially on the C content at the interface. The main objective of the sequential annealing process starting from a low to a high temperature is to analyse the effect of annealing to the interface in stages. The curve fitted *Si 2p* and *C 1s* spectra are illustrated in Figure 6.5 and 6.6 respectively.

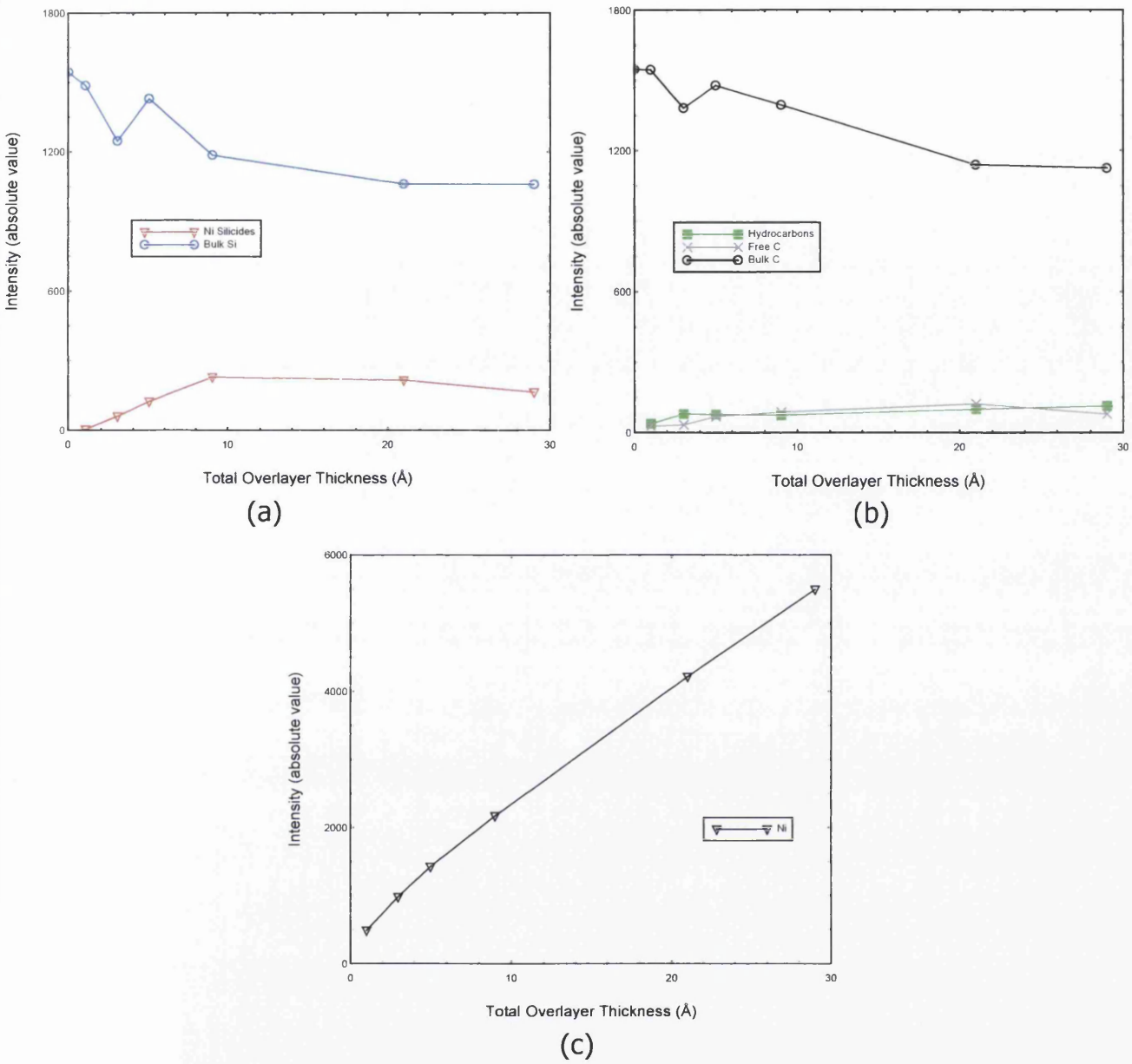

Figure 6.3: Intensity plot during interface formation for (a) *Si 2p* (b) *C 1s* (c) *Ni 2p*.

After annealing at low temperature, the first intermediate reaction is the immediate formation of additional Ni silicides, as a result of external energy input (i.e. from heat) [8]. The silicides formed are of a different species than the original silicide [5,16], indicated by the appearance of the second silicide

peak on higher binding energy side of the *Si 2p* spectra. With this additional silicide component, the intensity of the first silicide component is stable and is seen to remain almost constant throughout the annealing process up to 1000°C. Conversely, the secondary silicide is seen to be slightly decreased, possibly cause by interdiffusion towards the bulk.

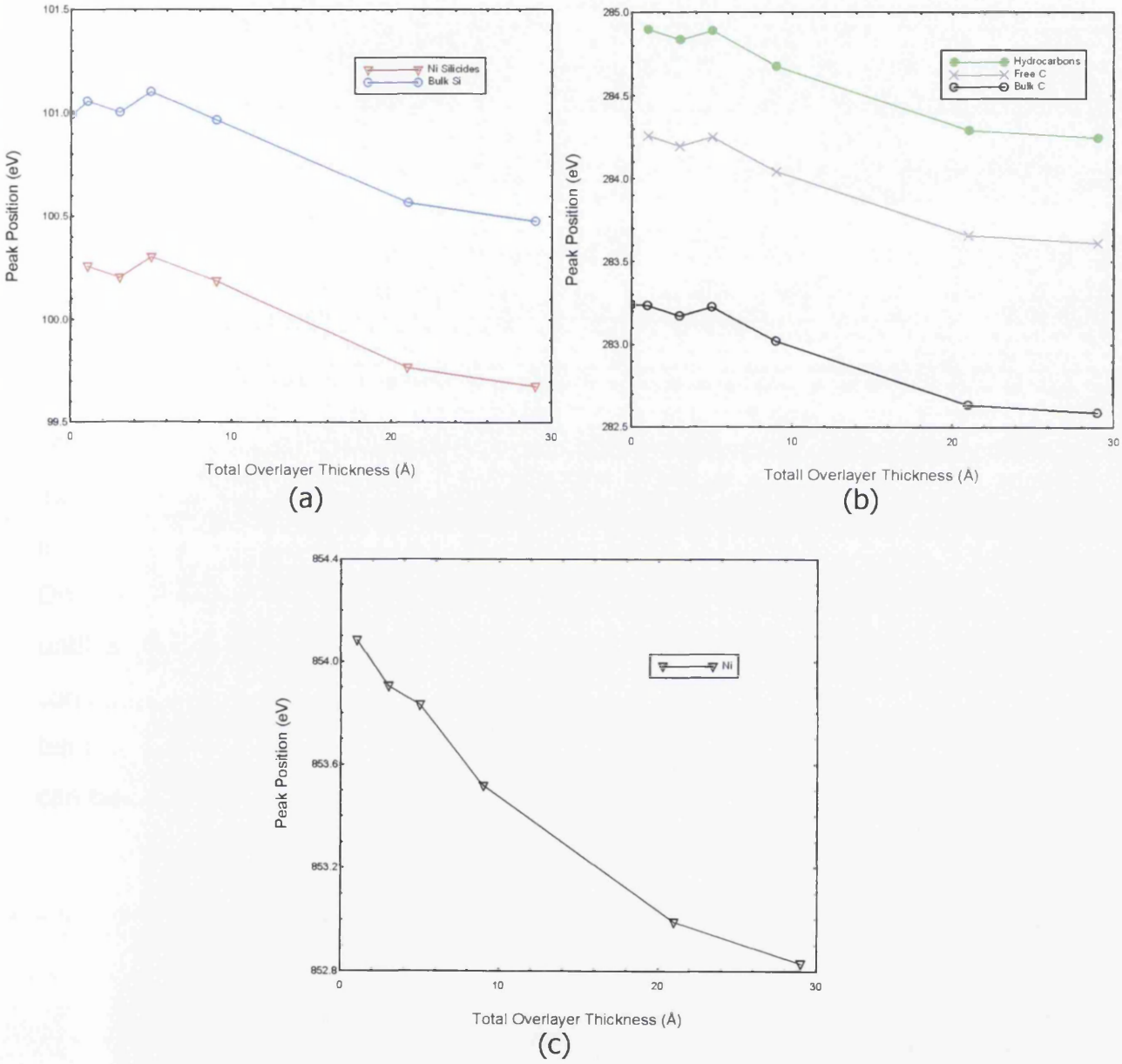

Figure 6.4: Peak position plots of the deconvoluted components during interface formation for (a) *Si 2p* (b) *C 1s* (c) *Ni 2p*.

Bulk Si is observed to gradually increased towards higher annealing temperature. These events can be translated as the interdiffusion of silicides towards the bulk at low temperature and the possibility of re-evaporation of Si and silicides at high temperature (above 1000°C), which results in a stronger bulk signal and the disappearance of silicides peak.

Correspondingly, the *C 1s* spectra showed an increase in free C. However, the hydrocarbons are seen to decrease gradually with increasing annealing temperature. The intensity of the bulk C is seen to decrease, which correspond to interdiffusion of silicides towards the bulk, that tends to cover up the bulk signal. An interesting point appeared at 900°C, where the intensity of bulk Si and bulk C are seen to increase and corresponds to a massive decrease of Ni. This incident can be associated with rapid re-evaporation of Ni silicides, which reveals stronger bulk signal. In addition, the hydrocarbons and free C is also seen to increased rapidly, again shows the C segregation towards the surface. Up to 1200°C, all C components are seen to increase, which is in agreement with the Si re-evaporation and C segregation event, and also the possible formation of graphite at such high temperature. On the other hand, the intensity of Ni showed a gradually decreasing trend until a finally reaches zero at 1200°C. This reaction can be translated as the consumption of Ni in the formation of silicide and interdiffusion in mid temperature and finally re-evaporation at high temperature. These reactions can be clearly illustrated in the intensity plot in Figure 6.7(a) to (c).

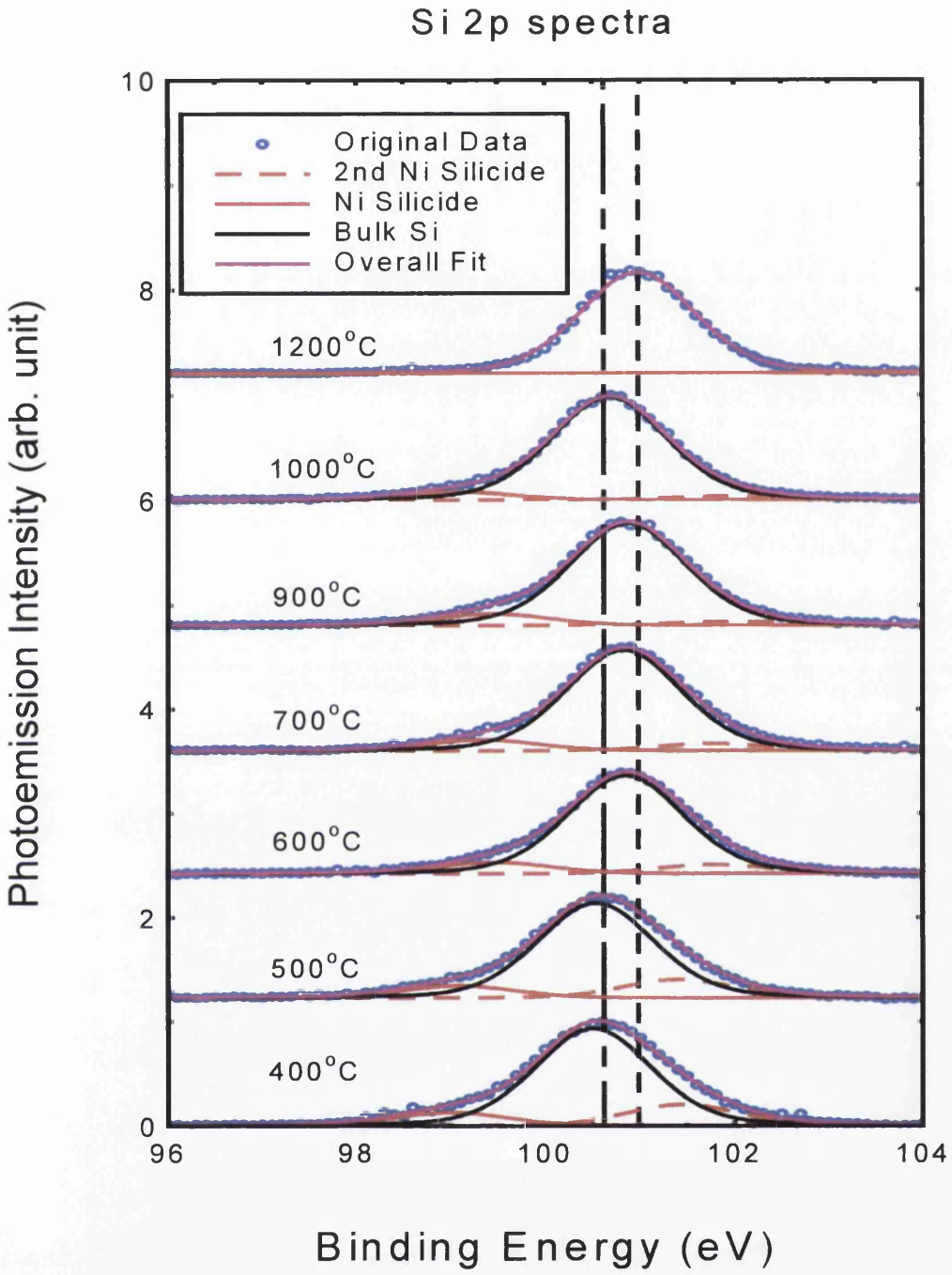

Figure 6.5: Curve fitted *Si 2p* core level spectra during sequential anneals starting from temperature of 400°C to 1200°C. The deconvoluted components including the original raw data are listed in coloured lines as described in the legend. The vertical dotted lines indicate peak movement in comparison to 400°C and the original clean surface.

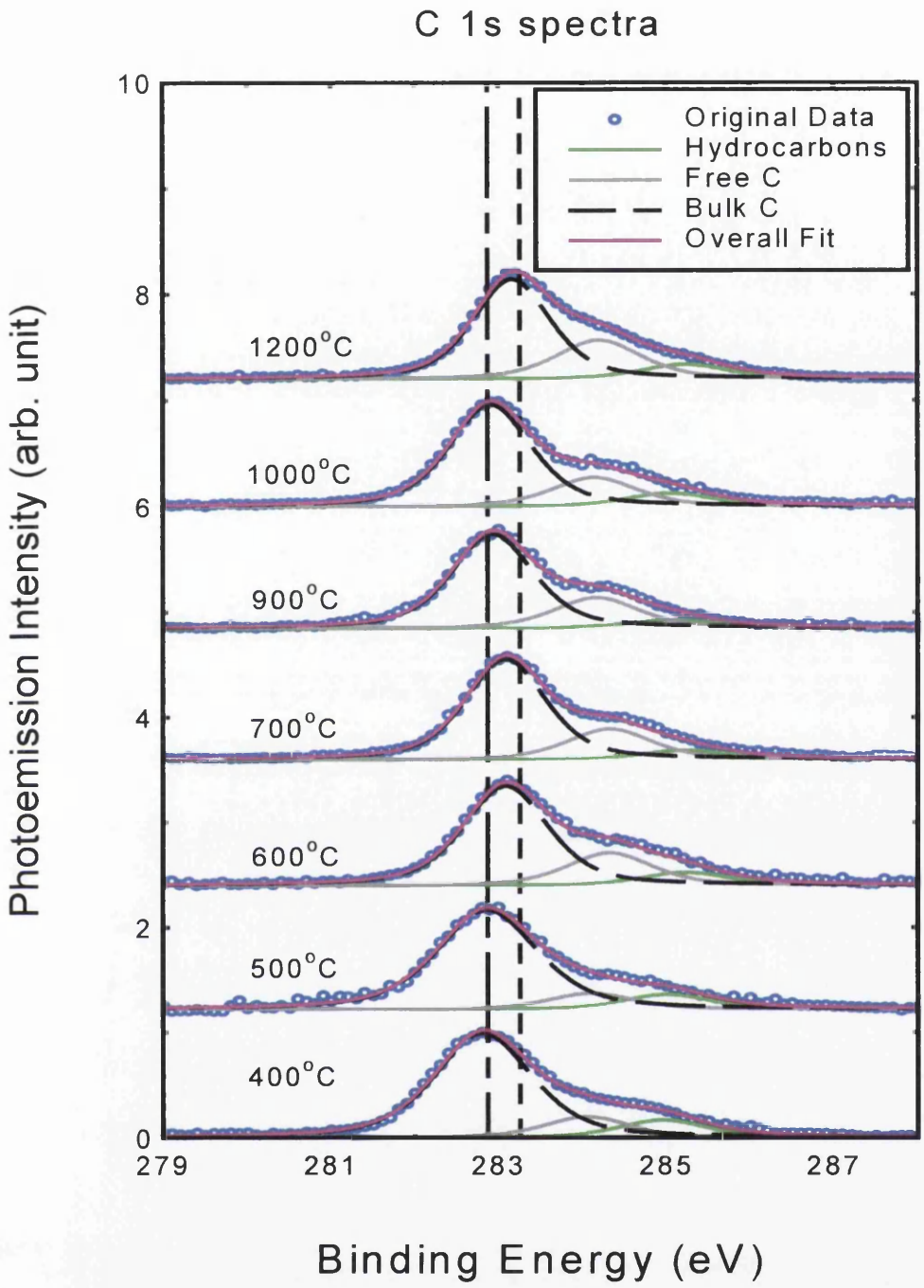

Figure 6.6: Curve fitted *C 1s* core level spectra during sequential anneals starting from temperature of 400°C to 1200°C. The deconvoluted components including the original raw data are listed in coloured lines as described in the legend. The vertical dotted lines indicate peak movement in comparison to 400°C and the original clean surface.

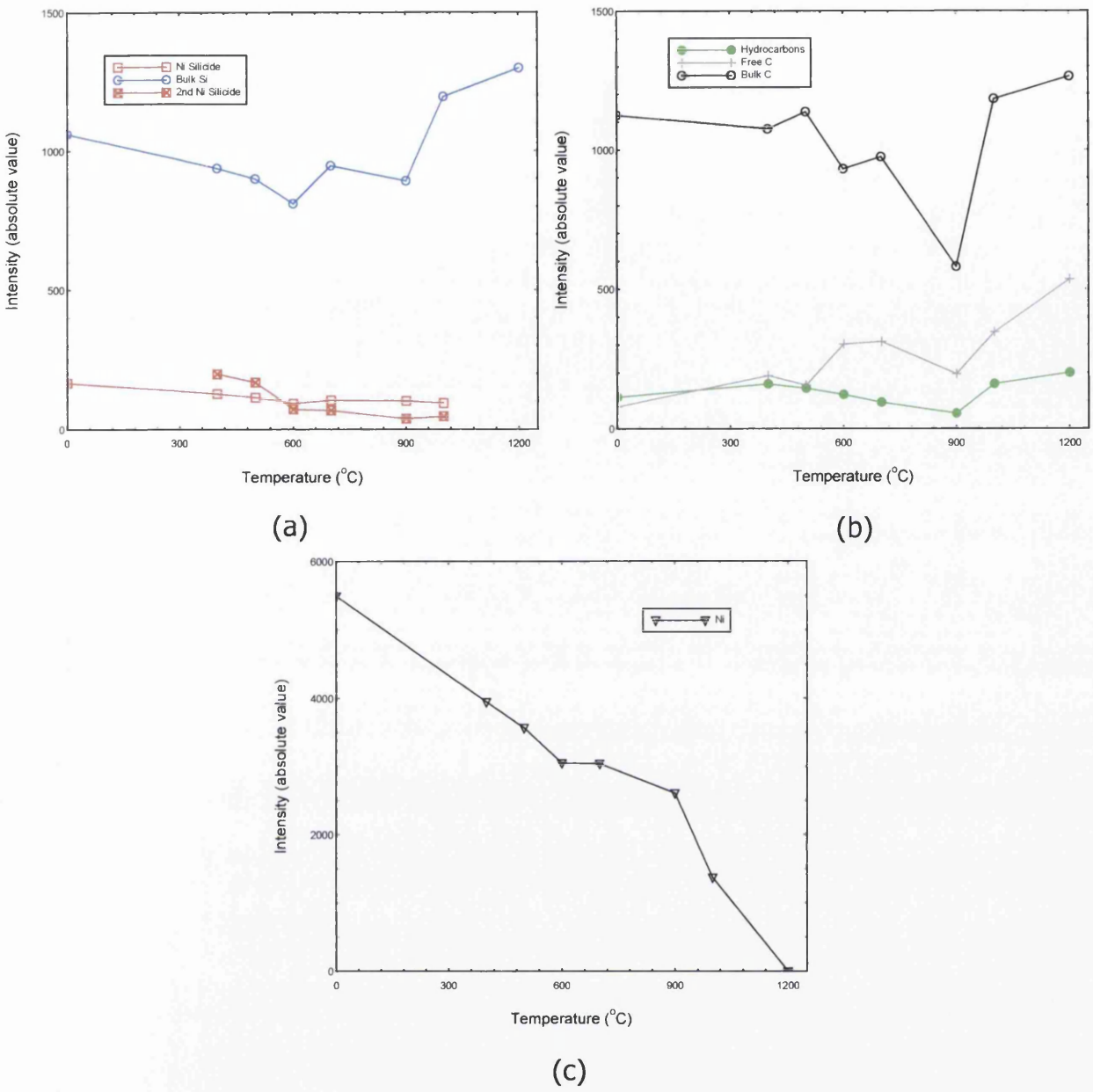

Figure 6.7: Intensity plot at sequential anneals for (a) *Si 2p* (b) *C 1s* (c) *Ni 2p*.

It is clearly seen that the *Si 2p* and *C 1s* core levels shift in an identical manner (see Figure 6.8(a) and (b)). Electrically, the interface exhibits a barrier lowering, indicated by a Fermi shifts (both *Si 2p* and *C 1s* core level) towards higher binding energy of approximately 0.4eV. However, the *Ni 2p* core level does not display a similar behaviour (see Figure 6.8(c)). This event

can be explained by the chemical reaction of Ni in forming silicides, interdiffusion of these silicides and re-evaporation at high temperature (as described previously), and therefore the peak shifts observed are more likely to associate to chemical shifts rather than a Fermi shifts. Note that the Fermi shifts can also be affected by the chemical reactions within the interface (e.g. the formation of Ni silicides). The peak position plots for all three main components is shown in Figure 6.8(a) to (c).

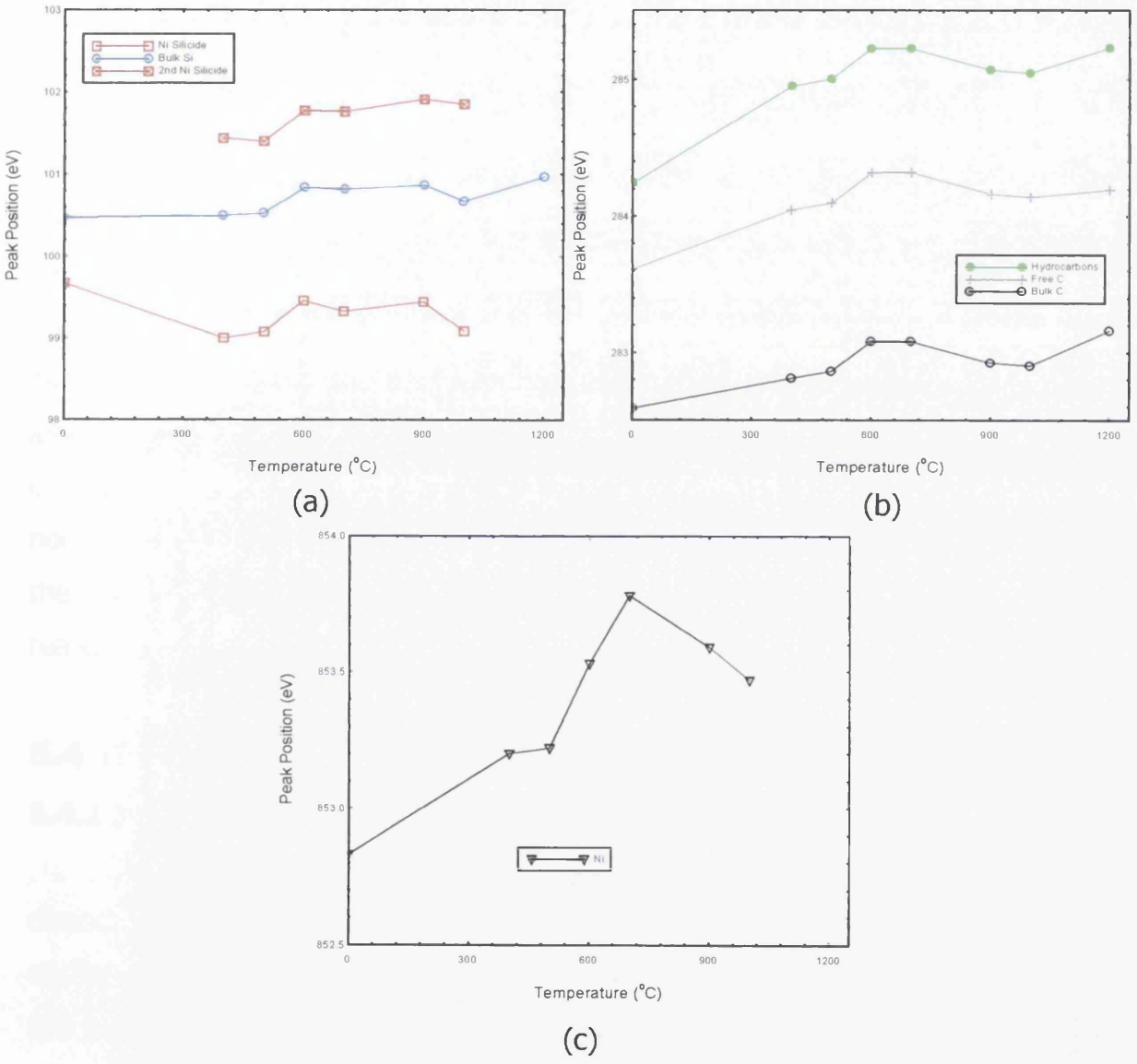

Figure 6.8: Peak position plots at sequential anneals for (a) *Si 2p* (b) *C 1s* (c) *Ni 2p*.

Summary

The main objective of the Ni-SiC photoemission study experiment is to act as a control experiment for comparison purpose at a later stage and to demonstrate the effect of Ni overlayers onto an atomically clean SiC surface (i.e. the conventional Ni-SiC contacts). Generally, the results show that deposition of Ni onto SiC results in formation of Ni silicides, free C and excess C in carbonyl group or hydrocarbons. All intermediate products of this Ni-SiC contact are observed to grow simultaneously with increasing deposition of Ni overlayers. When annealed, the initial reaction was the additional formation of a different phase of Ni silicides. The silicides are observed to intermix, diffuse into the bulk and finally being re-evaporated at high temperature (above 1000°C). Simultaneously for C, the free C at the interface is seen to increase and is suspected to be segregated towards the surface. The interdiffusion of silicides towards the bulk also results in the decrease in bulk C and hydrocarbons intensity. At high temperature, the interface exhibits a large amount of excess C (both free C and hydrocarbons). These additional groups of C at the interface are well known to induce electrical instability due to their non-conducting properties. Hence, a solution to this undesirable C content at the interface has to be put forward in order to produce a reliable contact with reasonable performance.

6.4 The Ni-Si-SiC Interface Photoemission Study

6.4.1 Introduction

As seen in the previous section, the formation of Ni-SiC results in the dissociation of bulk SiC into Si and C. This result is in agreement with various earlier works [1, 6, 7]. These dissociated components are expected to react with the metal overlayer (in our case, Ni) to form compounds or metal silicides. However, it is observed that Ni is more likely to form silicides with the disassociated Si, leaving a sufficient amount of free C at the interface. This free C, trapped between the junctions could cause undesirable effects in

terms of electrical stability and device reliability to the contact especially for high temperature operations. Hence, the maximum performance of the device is then inhibited. Therefore, immediate research and investigations had to be performed in order to provide possible remedies to the contact problem. Although it might sound simple, there are a few criteria that have to be met. Firstly, the solution proposed must be able to improve the contact properties while maintaining the properties and characteristics of SiC. Secondly, the solution must be adaptable commercially (i.e. low cost, re-producible) for the ease of production. With thoughtful consideration, the proposal has been made to implement a layer of Si to serve as a buffer layer, which will provide the source of Si atoms for Ni silicide formation without altering the bulk SiC. In the following section, the results of the investigation in the role of the Si interlayer are presented and discussed.

Until now, the advantages of a Si interlayer plus the formation mechanism of the Si-SiC interface has been revealed (see Chapter 5). Thus, the next stage is to consider the full matrix composition (i.e. Ni-Si-SiC) of the interface formation. In this case study, various thicknesses of Si interlayers are used in an attempt to determine the optimal thickness of the interlayer needed to prevent free C formation to minimise interface disruption. In the study, all core level spectra were recorded using the Al Kα (1486.6eV) X-ray source and were fitted using the least chi square approach described in section 3.4.3.4. The deposition rates of Si and Ni have been pre-calibrated and were maintained throughout the experiments. Some of the results presented have been normalised for ease of analysis and comparison purposes. The obtained results are presented and discussed.

6.4.2 20Å Si Interlayer

- **General Observation**

This section will present a general overview of the results obtained with an aim to clarify the trends of behaviour observed from the experimental

data. As mentioned previously, all experiments are performed on an atomically clean surface obtained via the Si evaporation/ re-evaporation technique (see Chapter 5), thus the surface of the sample consists of bulk SiC components (i.e. Si and C) and possibly a small left over Si component from the cleaning procedure described previously. Figure 6.9 shows the intensity plot of the three main components involved in the matrix composition formation (Si, C and Ni). Note that the intensity used here refers are the area under the un-fitted peak, therefore it corresponds to the total intensity of the peak. As soon as the 20Å Si interlayer is deposited onto the sample, the intensity of the bulk components is seen to be drastically reduced. This reaction is predictable, as the deposited overlayer covers up the substrate, hence reducing the signal from the bulk components. Similarly, subsequent to the sequential deposition of Ni overlayers, the bulk components have are reduced further. However, as observed from the plots, there is an increase in intensity of both Si and C components at early stages of Ni deposition. A possible explanation corresponding to this event is that the overlayers grown are likely to be in cluster mode (Franck-van Der Merwe mode) forming islands at the surface. Another possibility is that there are chemical reactions between the overlayers and the bulk component at the early stage. However, it is early to conclude at this stage, and this will be discussed later in this chapter. On the other hand, obviously, an increasing trend is observed for the intensity of the Ni component corresponding to Ni deposition of increasing thickness onto the surface.

In terms of electrical behaviour, the interface demonstrates the formation of a barrier of approximately 0.5eV following Ni deposition. This is indicated by the peak positions shift towards lower binding energy side of the spectra for all three components as illustrated in Figure 6.10 (a – c).

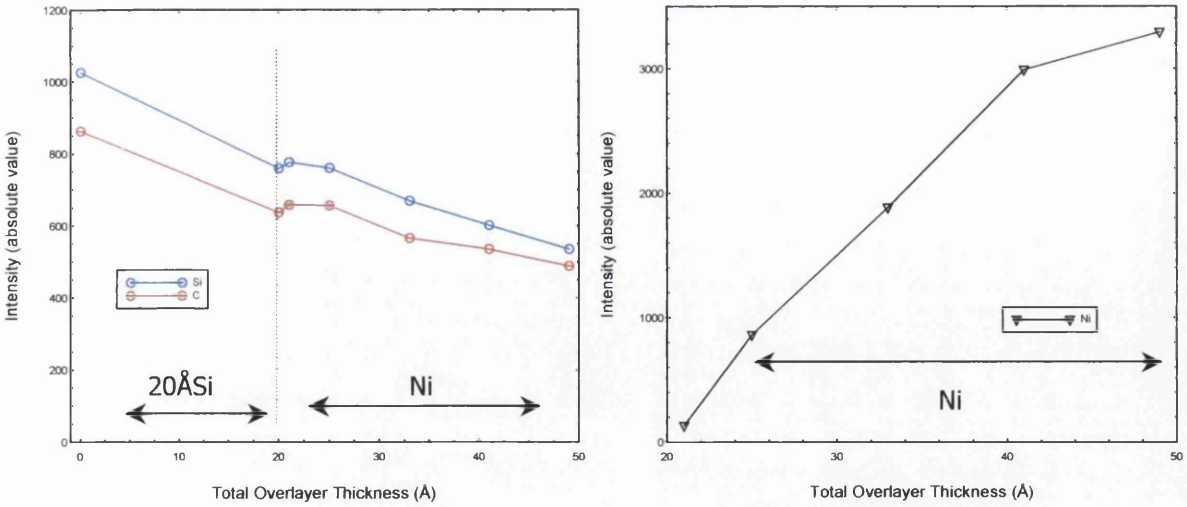

(a) (b)

Figure 6.9: Overall peak intensity plots during interface formation for (a) *Si 2p* and *C 1s* (b) *Ni 2p*.

Note that during initial deposition of 20Å Si interlayer onto the atomically clean surface, the core levels (for both *Si* 2p and *C 1s*) are seen to shifts towards high binding energy. However, from the previous case study of the Si-SiC interface, there is no sign of shifts for both *Si 2p* and *C 1s* core level spectra when Si is deposited onto the atomically clean surface. This peak shift can be explained by possible Si passivation, as the 20Å Si is deposited in a single deposition compared to sequential deposition as discussed in section 5.5. There is a point (at 25Å) where the peak position of the C spectra is increased while the other two components remains in the decreasing behaviour. This incident may be associated with the change in chemical environment of the C components within the bulk and will discussed in more detail later when the spectra are curve fitted. For *Ni 2p* spectra, the general trend of peak shift is similar to *Si 2p* and *C 1s* peak. However, with formation of Ni silicides, it is more likely that the peak shift observed here (0.65eV) is a combination of chemical shift and Fermi shift, hence a greater shift is observed compared to Si and C peaks.

When the interface is annealed, various behaviours are observed (see Figure 6.11). The most apparent behaviour was the increasing intensity of Si and C components with increasing temperature. However, at the initial stage (at temperature 400°C to 500°C), Si is observed to be slightly decreased, whereas C is slightly increased. This incident may be related to surface reconstruction or surface relaxation, where the overlayers (Ni silicides) tend to form a more laminar layer. Above 500°C, the increasing behaviour for Si and C is suspected to be associated with either interdiffusion of Ni silicides and bulk SiC or possible re-evaporation of the silicides in this temperature range. Hence, with the disappearance of the silicides, the bulk components are revealed more giving an increase in intensity. However, between 900°C and 1200°C, the Si and C behave in opposite ways. When C decreases, Si increases and vice-versa. This reaction might be caused be chemical reactions at such high temperature, and will be further discussed at a later stage in the next section. Conversely, the intensity of the Ni overlayer is seen to decrease with increasing annealing temperature as illustrated in Figure 6.11 (b)). Note that at the initial stage (400°C to 500°C), the Ni overlayer is suspected to experience surface reconstruction, similar to Si as discussed previously. Above 500°C, the gradual disappearance of Ni is likely to associate with the chemical reaction with bulk Si.

Generally, the composition of Ni-20ÅSi-SiC displayed a barrier lowering during the annealing sequence. This reaction can be further illustrated by considering the peak position plots of the Si, C and Ni components in Figure 6.12(a - c). From the plots, it is clearly seen that all three peaks shifts in a similar manner, indicative of a Fermi shift. From the starting temperature of 400°C to 500°C, it is observable that there are virtually no changes in the peak position for all three components. Next, the interface shows an increase in binding energy of approximately 0.3eV at 600°C, which corresponds to a lower barrier and stabilised at 700°C. Subsequently, at temperatures above 700°C, the interface shifts back to lower binding energy by approximately

0.5eV. Up to 1200°C, a massive shift of 0.8eV towards higher binding energy was observed. However, it was observed that the Ni peak displayed a much bigger shift. Again, the shift is suspected to be associated with chemical shift and Fermi shift superimposed together giving a larger peak shift. The exact reaction at this stage is yet to be known and will be further discussed in a later section.

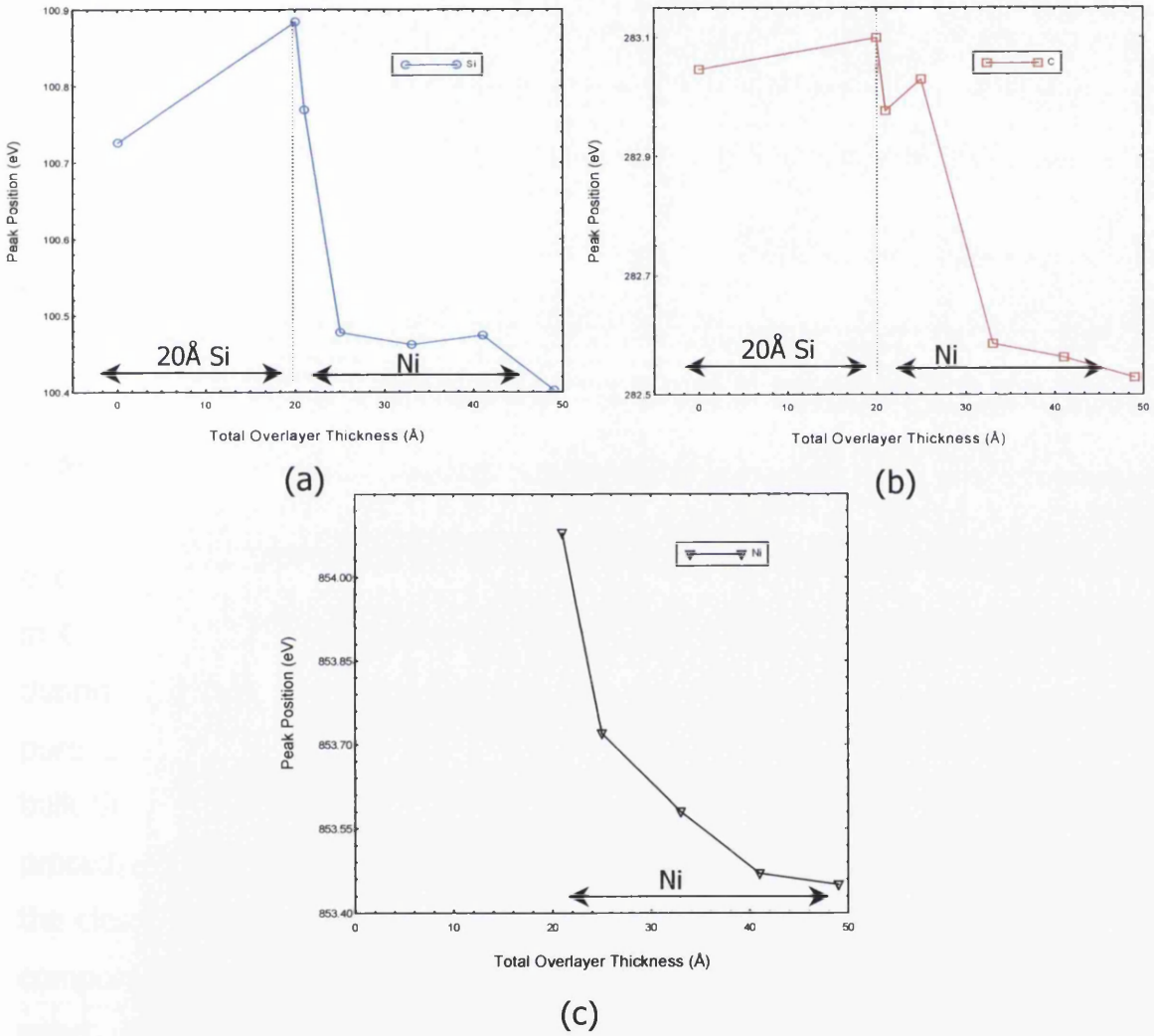

Figure 6.10: Peak position plots during interface formation for (a) *Si 2p* and *C 1s* (b) *Ni 2p*.

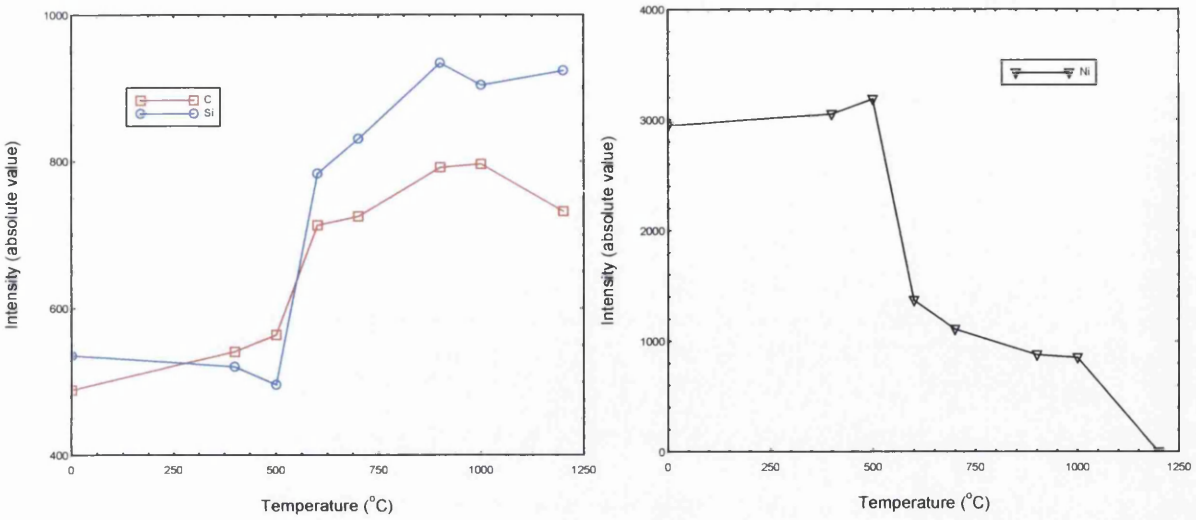

Figure 6.11: Overall peak intensity plot at sequential anneals (a) for *Si 2p* and *C 1s* (b) for *Ni 2p*.

- ***Si 2p* core level**

To further understand the interface reaction, all core level peaks have been curve fitted using the least-chi square [9] approach discussed previously in Chapter 3. Figure 6.13 shows the fitted spectra of the *Si 2p* core level during interface formation. The lowest spectrum in the stack plot is that of a pure atomically clean SiC surface. Evidently, this spectrum consists of only bulk Si component from the bulk SiC and the left over Si from the cleaning procedure. Subsequently, a Si interlayer with thickness of 20Å is grown onto the clean surface. Thus, the main features from this spectrum are the bulk Si component (black line) and the deposited Si (green line) separate by 1.55eV apart. Next, the Ni overlayers are grown sequentially on top of the Si interlayer. As a result of the deposited metal overlayer, a new component arises located 0.8eV with respect to the deposited Si component. This component, (red line), is believed to be metal silicides. The exact species is uncertain but proposed to be Ni silicides. The intensity plot of the individual Si components is illustrated in Figure 6.14(a) and (b).

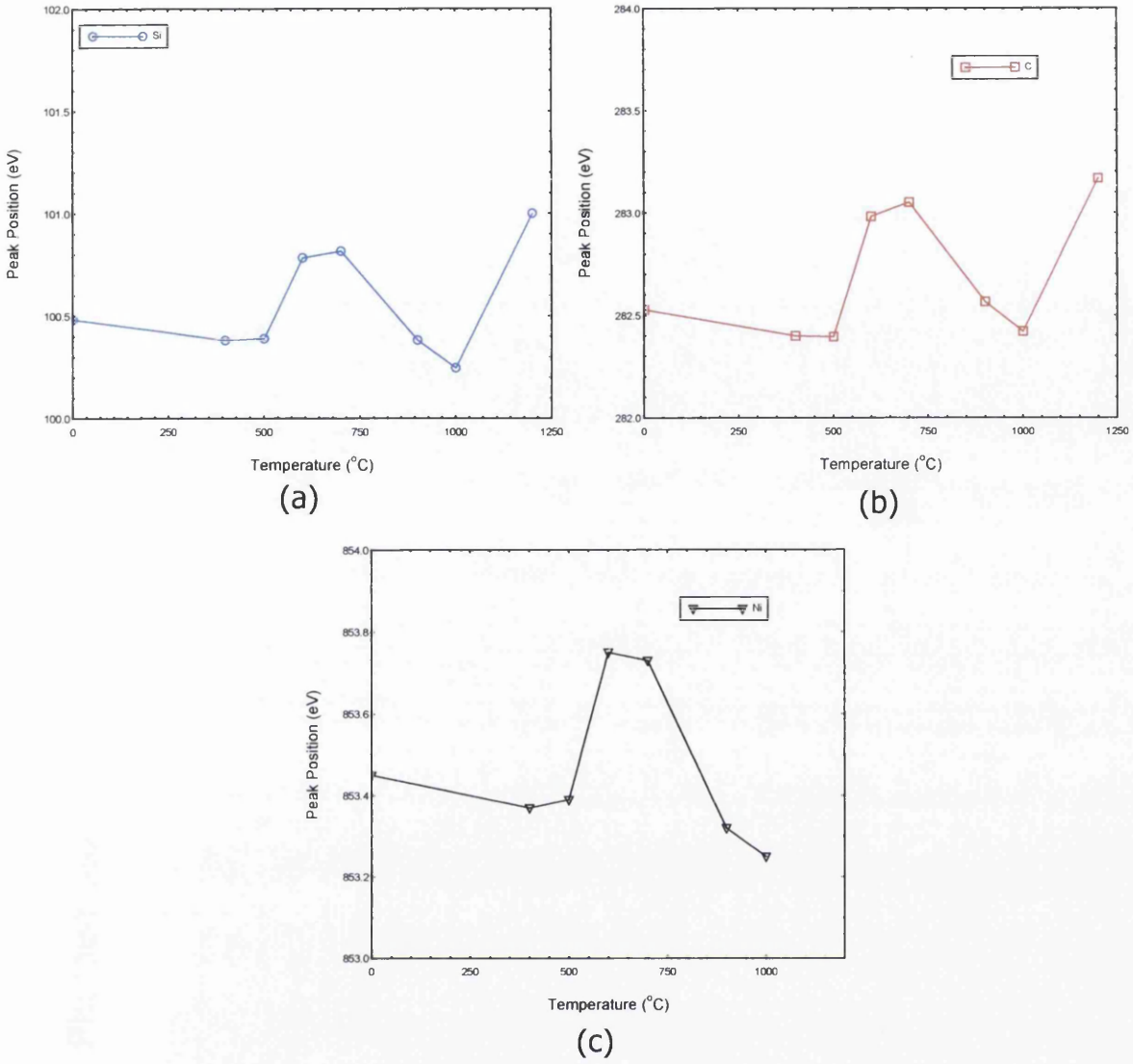

Figure 6.12: Peak position plots during sequential anneals for (a) *Si 2p* and *C 1s* (b) *Ni 2p*.

From Figure 6.14(a), the intensity of the bulk Si and the deposited Si interlayer is observed to be decreasing as the overlayer covers up the signal from the bulk. The rate of decay of the bulk Si is observed to be slightly faster than the deposited Si, indicating that the bulk is being buried and the deposited Si is consumed to form silicides, which remains near the surface. Conversely, the silicide component is seen to be growing with increasing thickness of Ni. While forming metal silicides, the interface is also seen to shift

towards low binding energy. As all the components shift by the same amount (Fermi shift), in agreement with result discussed in the general observation (section 6.4.1). The interface shows a formation of a barrier, with a height of approximately 0.4eV.

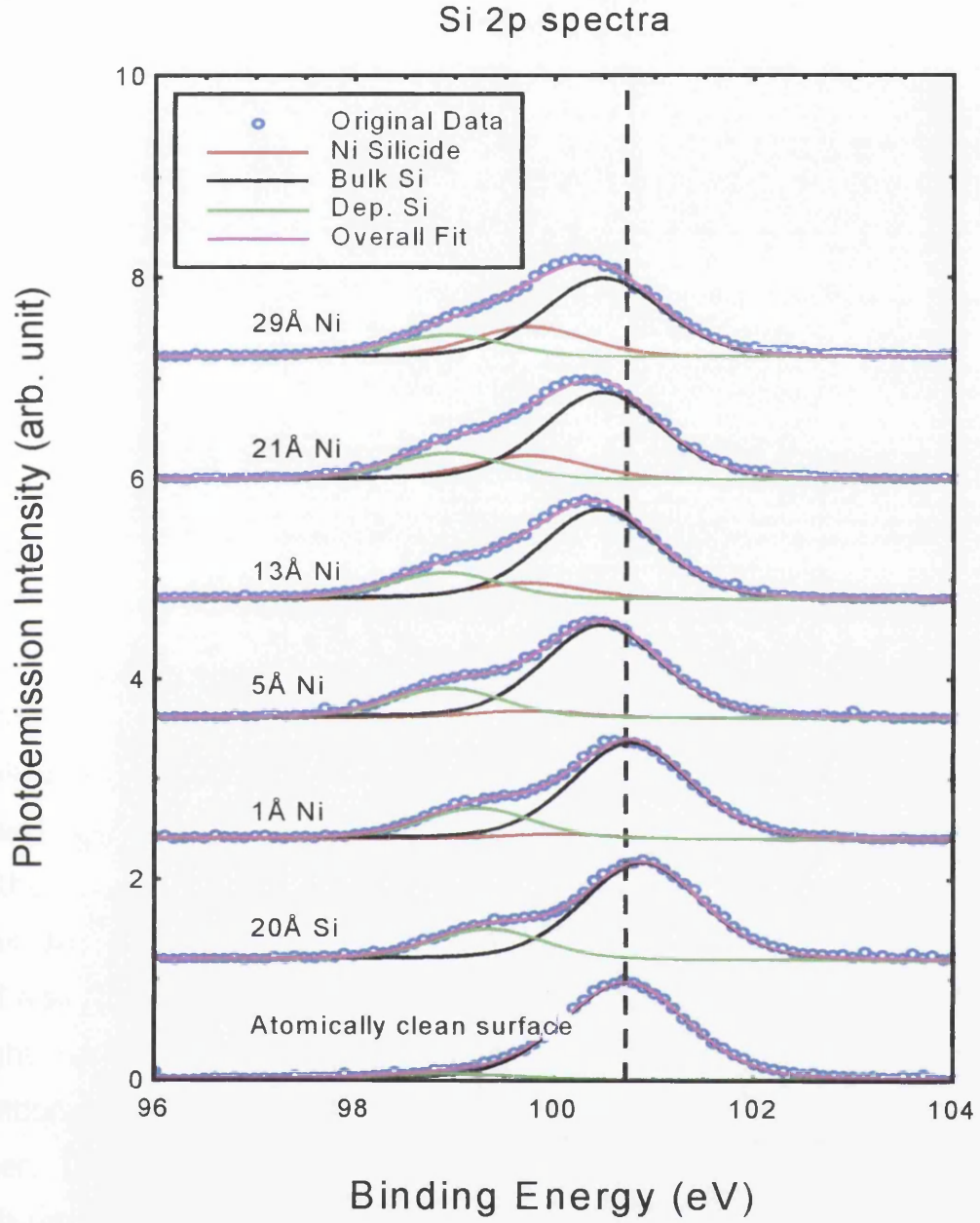

Figure 6.13: Curve fitted *Si 2p* core level spectra starting from the atomically clean surface to Si and sequential Ni overlayers deposition. The deconvoluted components including the original raw data are listed in coloured lines as described in the legend.

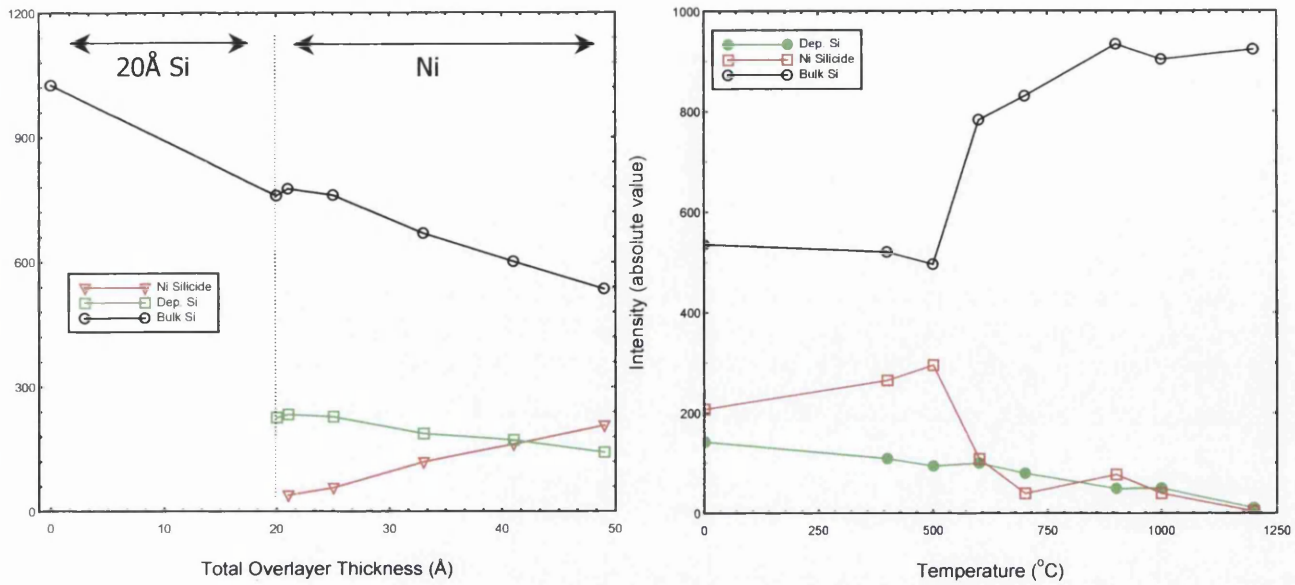

Figure 6.14: Intensity plots of the deconvoluted Si components (a) during interface formation (b) at sequential anneals.

Subsequent to interface formation, the investigation continues with a study of the effect of temperature on the interface. The curve fitted *Si 2p* peak at each annealing step is shown in Figure 6.15. At low temperature anneals (400°C to 500°C), the silicides are seen to form rapidly as indicated by the decrease in the bulk Si and deposited Si intensity and a bigger silicide peak. In other words, low temperature anneal encourages silicide formation and also surface ordering or reconstruction [8]. Here, several species of silicide might have formed (as observed in the Ni-SiC interface). However, these additional silicide peaks are small in intensity and located very close to each other. Therefore, it is hard to distinguish these peaks individually without high-resolution equipment. Hence, we consider these silicides peak as single peak for ease of analysis. Further annealing at higher temperatures could result in the interdiffusion of Ni silicides towards the bulk or even the re-evaporation of silicides.

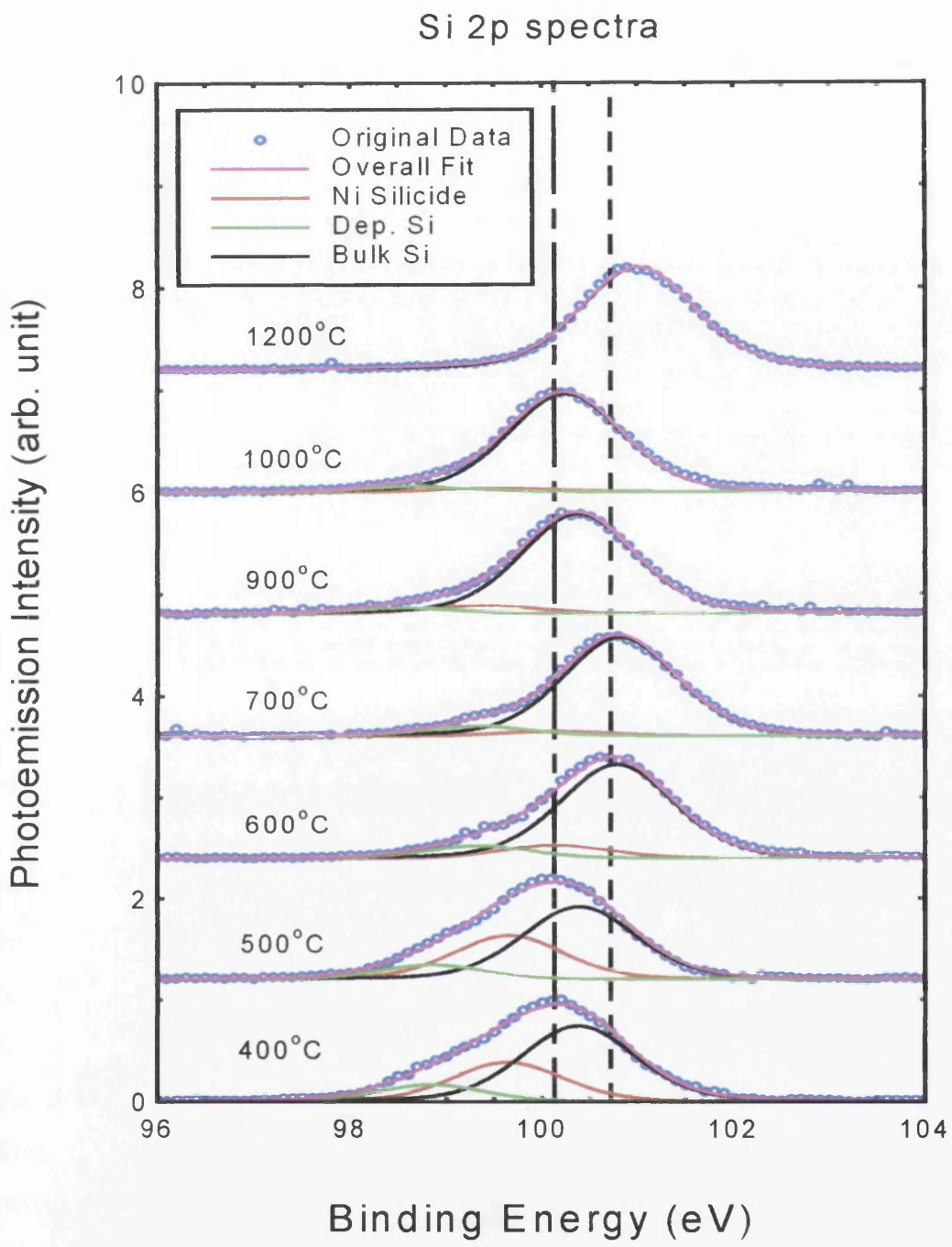

Figure 6.15: Curve fitted *Si 2p* core level spectra during sequential anneals starting from temperature of 400°C to 1200°C. The deconvoluted components including the original raw data are listed in coloured lines as described in the legend. The vertical dotted lines indicate peak movement in comparison to 400°C and the original clean surface.

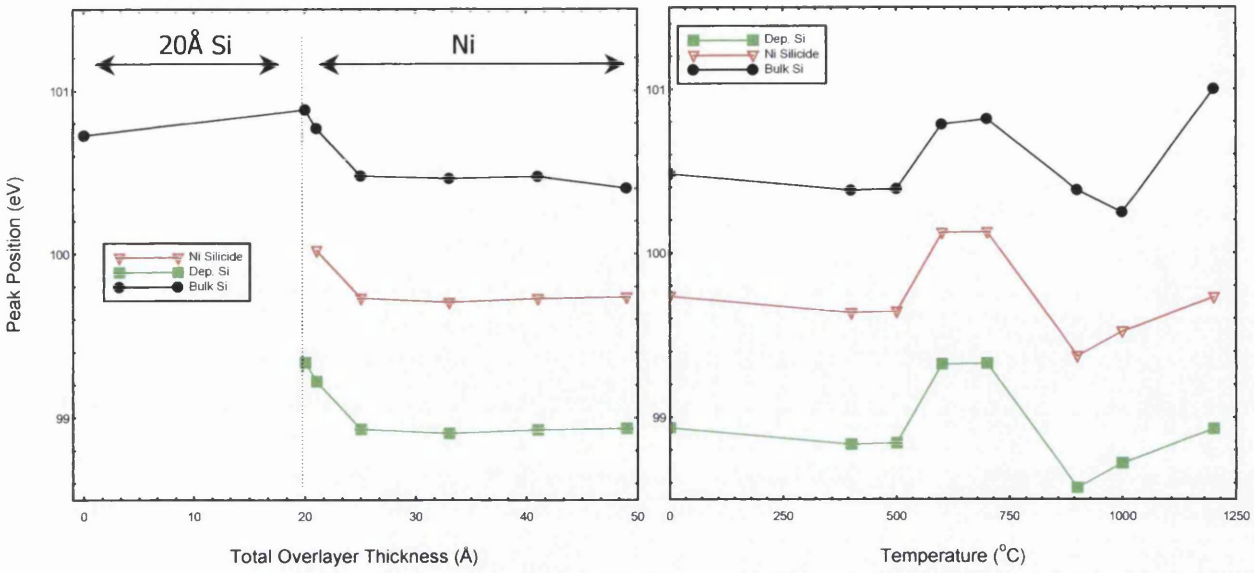

(a) (b)

Figure 6.16: Peak position plots of the deconvolved Si components (a) during interface formation (b) at sequential anneals.

This is indicated by the reducing intensity signal from both deposited Si and silicides, revealing a stronger bulk Si signal. Up to very high temperature (1000°C to 1200°C), this re-evaporation of silicides dominates, leaving only the bulk component indicated in the fitted spectra. All phenomena described previously can be clearly seen on the intensity plot shown in Figure 6.14(b). From the plots, the increasing behaviour of the bulk component and the opposite behaviour of the overlayer components is clearly visible. On the other hand, the barrier formed during interface formation (as observed previously) is seen to be gradually lowered, indicated via peak shifts towards higher binding energy. The peak position plot at sequential anneals is shown Figure 6.16(b).

- ***C 1s* core level**

The main interest within this work is on the role of the Si interlayer in preventing free C formation. Thus, the C spectrum provides vital information

on the reaction at the junction and the effect of the Si interlayer onto C elements within the bulk SiC. The curve fitted *C 1s* during interface formation and sequential anneal is illustrated in Figure 6.17 and 6.18. Starting with a single bulk C component on the atomically clean surface, the deposition of the 20Å Si interlayer results in a small amount of free C (grey line) on the higher binding energy side of the spectra (approximately 1.05eV from the bulk C). Note that the formation of free C is not observed previously with the Si-SiC interface study (see section 5.5). This might be due to the fact that the 20Å Si is deposited in a single deposition instead of a sequential deposition. Although it is not desirable, this free C formation at the interface is unavoidable, as the deposited Si tends to bond with the Si from the bulk SiC or with Si atoms at the surface (as the sample is Si-terminated or the left over Si atoms after the Si evaporation/ re-evaporation clean), thus breaking Si-C bonds leaving dangling free C bonds. Another possibility is that the deposition of the Si interlayer might also cause a change in the chemical environment of the C atoms in the bulk. With additional overlayers of Ni onto the sample, (apart from forming silicides with Si as described previously), it is observed that a third complementary phase arises within the C spectra (red line) located at the higher binding energy side, approximately 1.67eV from the bulk C component. The exact origin of this complementary phase is uncertain, but it is suspected to be related to the change in the chemical environment of the C, or could be a phase, which consists of a mixture of Ni silicide with C. This ternary phase silicide is not observable within the *Si 2p* spectra, probably due to the small energy separation between Ni silicides and the ternary phase. In addition, the intensity of the ternary phase is small compared to foremost Ni silicides formed at interface. Hence, the ternary phase falls below the detection limit within the *Si 2p* spectra.

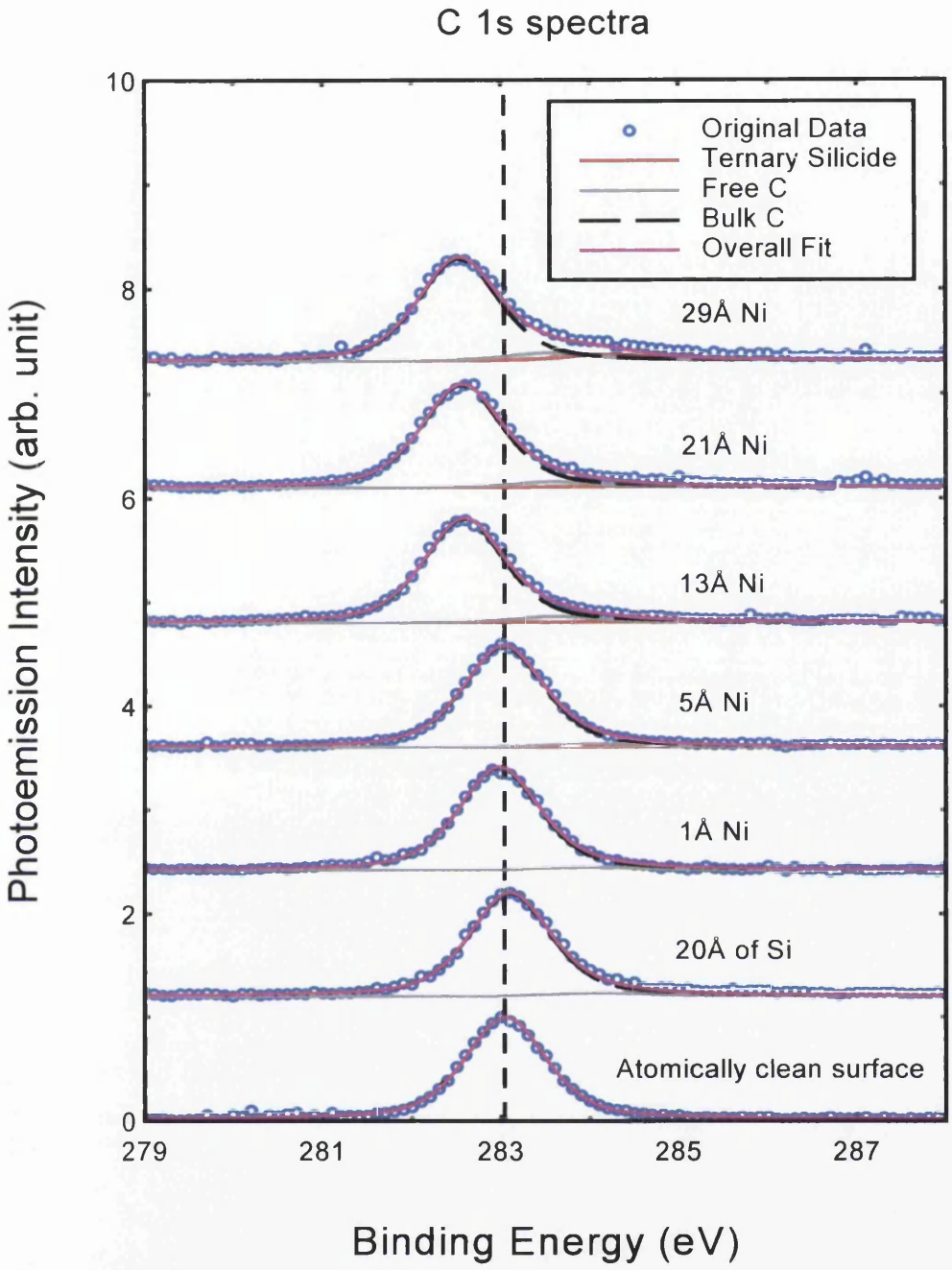

Figure 6.17: Curve fitted *C 1s* core level spectra starting from the atomically clean surface to Si and sequential Ni overlayers deposition. The deconvoluted components including the original raw data are listed in coloured lines as described in the legend.

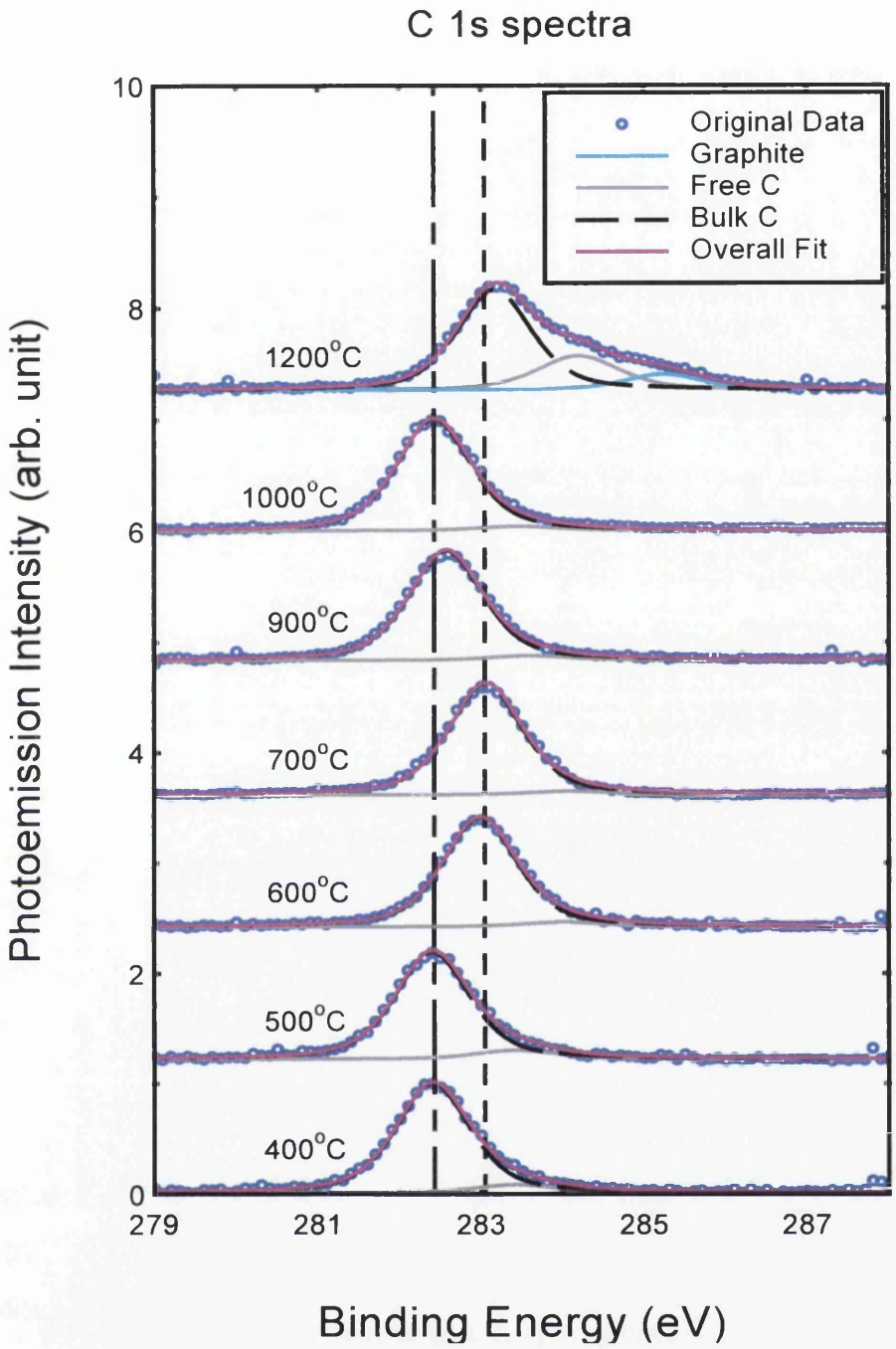

Figure 6.18: Curve fitted *C 1s* core level spectra during sequential anneals starting from temperature of 400°C to 1200°C. The deconvoluted components including the original raw data are listed in coloured lines as described in the legend. The vertical dotted lines indicate peak movement in comparison to 400°C and the original clean surface.

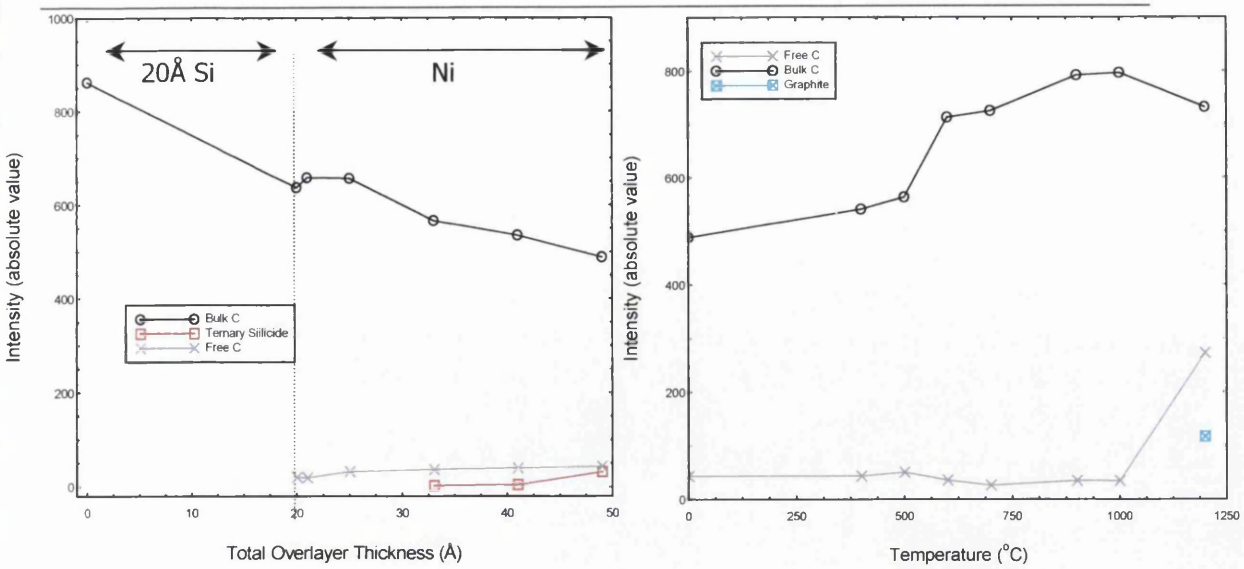

(a) (b)

Figure 6.19: Intensity plots of the deconvoluted C components (a) during interface formation (b) at sequential anneals.

The intensity plot of the C components is shown in Figure 6.19 above. Experimental observation shows that the bulk C signal decreases with increasing deposition of Ni, again indicating the buried bulk by the Ni overlayers. Meanwhile, the free C component remains virtually the same (see Figure 6.19(a)). This might suggest that the free C remains near or trapped at the junction between Si interlayer and Ni. The ternary phase is also seen to remain constant with increasing silicide formation. In addition, they are suspected to be localised near the free C. On the other hand, as a Fermi shift towards lower binding energy was observed on the Si spectra, a similar behaviour was also observed for C. From the data, a barrier height of approximately 0.5eV (a value slightly different to that of Si) was formed during interface formation. This bigger shift is likely due to the change in chemical properties of the C atoms, hence producing a chemical shift that is superimposed on the Fermi shift. Again, it is important to note that Fermi shifts of the core level spectra could be affected by the chemical reactions within the interface.

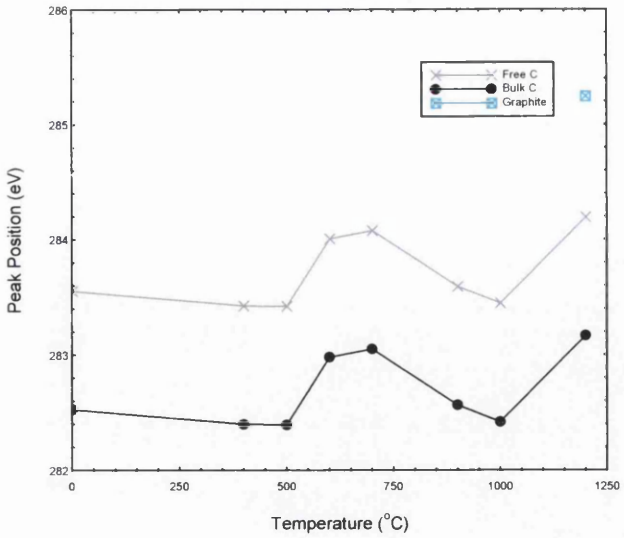

Figure 6.20: Peak position plots of the deconvoluted C components at sequential anneals.

As seen previously, low temperature anneals resulted in surface reconstruction and silicide growth. Similar properties have been observed for the bulk C component, where the bulk intensity is also seen to be increasing with the same pattern as bulk Si. Additionally, at temperature above 600°C, interdiffusion of overlayers into the bulk or re-evaporation of overlayer elements is also observed as indicated by the increasing intensity of the bulk component. Also, the disappearance of the ternary phase silicide might be associated with the change in chemical state of the ternary phase at elevated temperature. Although it is too early to conclude at this stage, nevertheless, this is not the case for the free C at the interface. From the intensity plots, the free C remains between the junctions, as indicated by the almost invariable intensity of the component. Yet, at the very high temperature of 1200°C, there is a massive amount of free C at the junction. In addition, at this temperature, graphite is also detected to be present at the interface. These reactions have been reported previously [6-7] and will be considered in more detail later in the discussion section. The electrical properties of the

junction are as described previously with the *Si 2p* core level spectra, which is associated with the identical peak position behaviour illustrated in Figure 6.20.

- ***Ni 2p* core level**

As well as analysing the behaviour of the bulk components of SiC, it is worth focussing on the behaviour of the Ni core level. Unlike the bulk Si and C components, this component has not been curve fitted due to the nature metallic behaviour, which results in an asymmetrical tail spectrum. This requires more complicated fitting procedures. Although the spectra are not fitted, the general trend of the Ni core level could still be observed. Obviously, sequential growing of Ni overlayers onto the sample will result in increasing core level intensity. Such spectra are shown in Figure 6.21.

On the other hand, upon annealing, the Ni spectra are expected to decrease in intensity with increasing annealing temperature as a result of interdiffusion of Ni silicides (as discussed previously in the 20Å Si section). The spectrum obtained is shown in Figure 6.22. At very high temperature, the Ni peak has completely disappeared as a result of either diffusion into the bulk or being re-evaporated as the final annealing temperature is almost high enough to reach the melting temperature of both Ni (1455 °C) and Si (1412 °C). In addition, as Fermi shift is observed with the *Si 2p* and *C 1s* core levels, the *Ni 2p* core level spectra are expected to show a similar trend. The peak position plots of the Ni peaks are shown in Figure 6.10(c) and 6.12(c). Although the peak shifts might be greater than that of the *Si 2p* and *C 1s* as result of the chemical shifts, it follow the same trend as the bulk components. This again proves that the shifts are true Fermi shifts corresponding to surface band bending. Especially during annealing stages, the gradual decrease in barrier height is clearly observed.

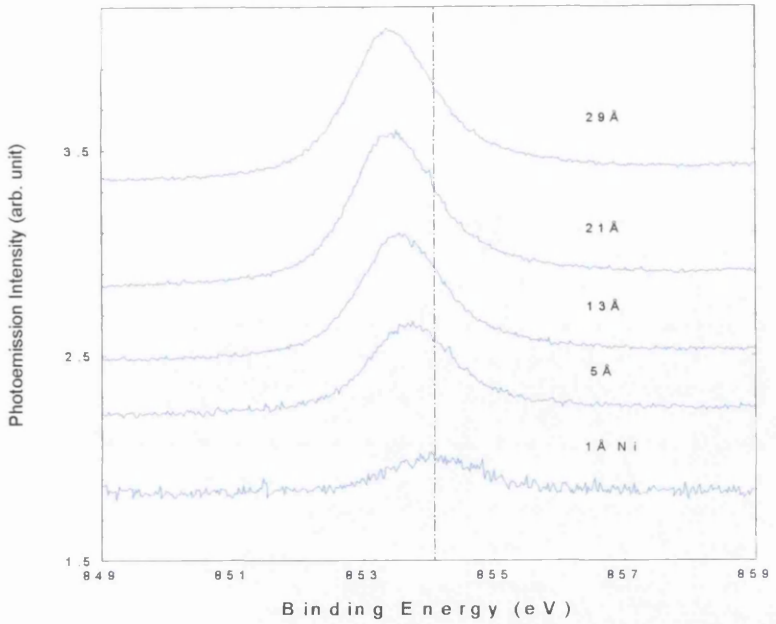

Figure 6.21: *Ni 2p* core level spectra during sequential Ni overlayers deposition.

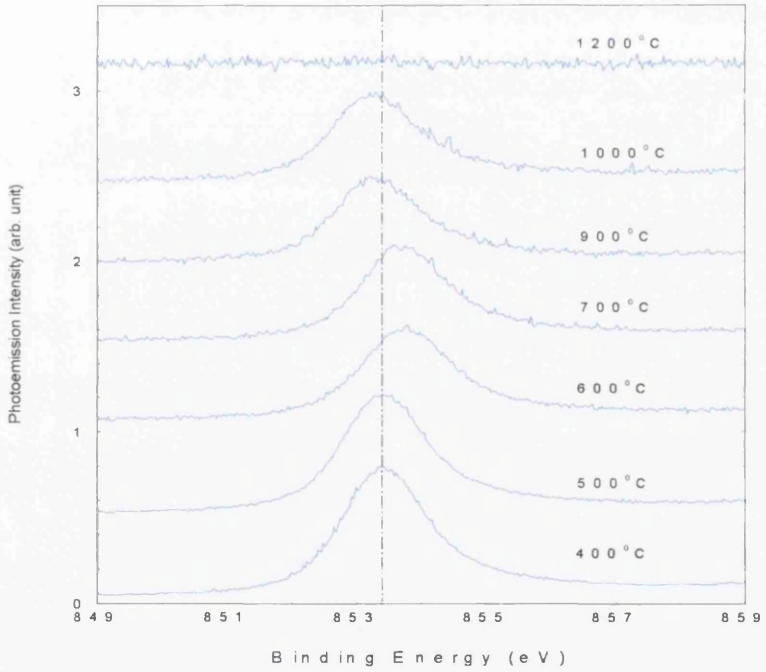

Figure 6.22: Ni 2p core level during sequential annealing temperatures.

Discussion

As seen in section 6.3, the formation of a Ni-SiC junction results in the presence of a significant amount of free C, which is detrimental to device

performance. Nevertheless, with the presence of a Si interlayer, the reactions at the junction have radically changed. Results obtained had so far showed that with a Si interlayer, the amount of C at the junction is greatly reduced. This result is in agreement with various previous works reported [10,18,19]. From the experimental observation, the free C at the junction between Ni and the Si interlayer is proposed to originate from the reaction of Ni with SiC. This phenomenon has been proven as metals may react with the SiC surface to form either silicide or carbide compounds [1-2] by solid-state transformation at elevated temperatures. As discussed previously in section 6.3, for the case of Ni, the reaction products of Ni-SiC mainly consists of Ni silicides and free C. However, with an additional Si interlayer into the matrix composition, this original reaction is then altered.

From the photoemission study, when a thin layer of Ni (1Å) is deposited onto the Si-SiC surface, an immediate interaction at the interface was observed. Clearly shown in the fitted *Si 2p* spectra, the interaction between the metal and the Si-SiC results in the formation of intermediate silicides. There is a possibility that several species of silicides phases being formed at the interface. However, these silicides are not observable within the *Si* 2p core level spectra as the binding energy of these silicides are very close together. Hence, is difficult to distinguish these silicides peaks individually. Nevertheless, the sign of the silicides formation could be predicted via increasing intensity of the silicide component and the decreasing intensity of the Si interlayer component within the *Si 2p* spectra, indicating the grow of Ni silicides via the consumption of Si atoms from either the bulk Si or the Si interlayer. These silicide formations are assumed to satisfy the mass balance and the standard entropy and enthalpy requirements [11].

While considering the reaction with Si, the interaction of Ni with C from the bulk SiC cannot be neglected. For our case, apart from interacting with Si, Ni also reacts with the free C originated from two sources. Firstly, the reaction between the Si atoms from the deposited Si (i.e. the Si interlayer) and the Si

atoms from the bulk SiC will give rise to broken bonds of C (i.e. free C) as the deposited Si atoms are more likely to bond with existing Si atoms on the surface, especially for a Si-terminated sample cleaned via Si evaporation/ re-evaporation procedure used in this experiment. This phenomenon is indicated by the appearance of a small peak on the high binding energy side of the curve fitted *C 1s* spectra right after the deposition of the 20Å of Si. The second source of free C arises from the Ni atoms grabbing Si atoms from the bulk in order to form metal silicides. The silicides formation mechanism often involve bonding between Ni and Si, thus again leaving some dangling C bonds as a result of the broken Si-C bonds. Although the role of the Si interlayer in this experiment is to prevent Ni from altering Si from the bulk, these results show that a 20Å Si interlayer is not adequate to protect the bulk Si. The amount of free C at the interface is observed to be increasing in intensity until a third compound arises and then remains almost constant at the interface. This third compound, is attributed to a ternary phase and can been seen in the fitted *C 1s* spectra on the higher binding energy side of the spectrum (indicated by the red line). This ternary phase is proposed to consist of Ni, Si and C (i.e. a Ni-Si-C compound) formed to meet the mass balance of the system. However, the exact composition of this compound is uncertain, and requires further investigation. As mentioned previously, the Ni-SiC system belongs to a reaction, in which the product of such system generally consists of Ni silicide and free C [5]. But in our case, with an additional source of Si atoms, there is a slight modification onto such system, thus the reaction is proposed to be altered. The generated free C is suspected to be trapped between the silicide layer and the bulk.

Apart from understanding the interface formation, it is also essential to investigate the effect of annealing onto such a matrix composition (in our case Ni-Si-SiC) in order to produce a metal-SiC system that is stable while operating at high temperature. Also, the compatibility of the Si interlayer reacting with the system composition during the annealing sequence is

among the points of interest in this study. In this experiment, drastic changes of both Si and C peaks have been observed. At low temperature, the initial observation was the growth of silicide formations. This reaction is predictable as the annealing process often changes the phase composition of the silicide and accelerates the silicide formation by altering the thermodynamic energy composition of the system (i.e. with external energy input from annealing). [12,13,17]. From the fitted *Si 2p* spectra, the silicide component is seen to increase at temperature of 400°C - 500°C. The sign of silicide enhancement can be clearly demonstrated in the intensity plot with an increase in silicide intensity and an opposite behaviour of the Si interlayer component and the bulk Si, indicating the consumption of Si in the further formation of silicides. However, at temperature above 600°C, the silicide component is observed to be decreasing rapidly, together with the Si interlayer. This can be explained by diffusion of the Ni silicides and Si interlayer towards the bulk or re-evaporation of Ni silicides, revealing a stronger bulk signal. The increase of the bulk components confirms this interpretation. This continues up to a very high temperature (1200°C), where all the silicides has either completely diffused into the bulk or re-evaporated.

On the other hand, the fitted *C 1s* shows that the free C formed during the interface formation remains trapped at the interface. Although the silicides are seen to diffuse into the bulk, the free C remains at the interface. This reaction is clearly illustrated by the intensity plot. From the plot, the intensity of the free C component almost remains unchanged throughout the annealing process. At 1200°C, there is a massive increase in free C and also graphite formation. This graphite component is indicated on the fitted *C 1s* spectra at approximately 285.2eV on the high binding energy side of the spectra (represented by the light blue line in Figure 6.18). The formation of graphite plus a huge amount of C are proposed to be originated from the dissociation of the bulk SiC into Si and C. Si is being re-evaporated at such high temperature, thus leaving C behind.

The electrical properties of this composition are quite straightforward and have been discussed previously. Band bending has been observed during interface formation, evidently illustrated in the peak position plots of both *Si 2p* and *C 1s* spectra. Hence, a barrier is formed at the Ni-Si-SiC junction, having a value of approximately 0.5eV. This reaction is expected and is in agreement with the theory of metal-semiconductor contact [14], in which deposition of metal onto semiconductor surface results in the formation of a surface barrier. However, when annealed, this barrier formed is observed to lower gradually, indicated by downward band bending. The performance of these contacts will be further discussed later in Chapter 7 where the Ni-Si-SiC diodes are tested.

6.4.3 40Å Si Interlayer

- **General Observation**

The study proceeded with a 100% thicker Si interlayer than the previous experiment (i.e. we now have 40Å instead of 20Å). The reaction between this thicker Si interlayer and Ni is investigated thoroughly using the identical methods applied previously to the 20Å study. The general trend of the experimental results is presented as follows.

With a thicker Si interlayer, the interface has demonstrated a general similarity but slightly different behaviour from the previous study. From the intensity plot showed in Figure 6.23 (a), the overall intensity of bulk Si and C are almost the same and their rate of decay subsequent to deposition of Ni overlayer is nearly identical. In addition, it is clearly seen that there is a slight deviation on the Si intensity compared to that of the C. This incident may be related to either chemical reaction of Si and Ni in forming silicides or the formation of silicides islands on the surface. We shall consider this incident in more detail in a later section when the spectra are curve fitted. Meanwhile, the Ni intensity is seen to rise sharply with increasing Ni deposition as expected. With similar electrical properties from the 20Å study (see section

6.4.2), the core levels display a barrier formation of approximately 0.3eV. Note that at initial deposition of the 40Å Si interlayer, both Si and C peaks shifts towards high binding energy, again indicating possible Si passivation as observed previously with the 20Å interface study. The trend of formation is clearly illustrated in Figure 6.24 (a - c).

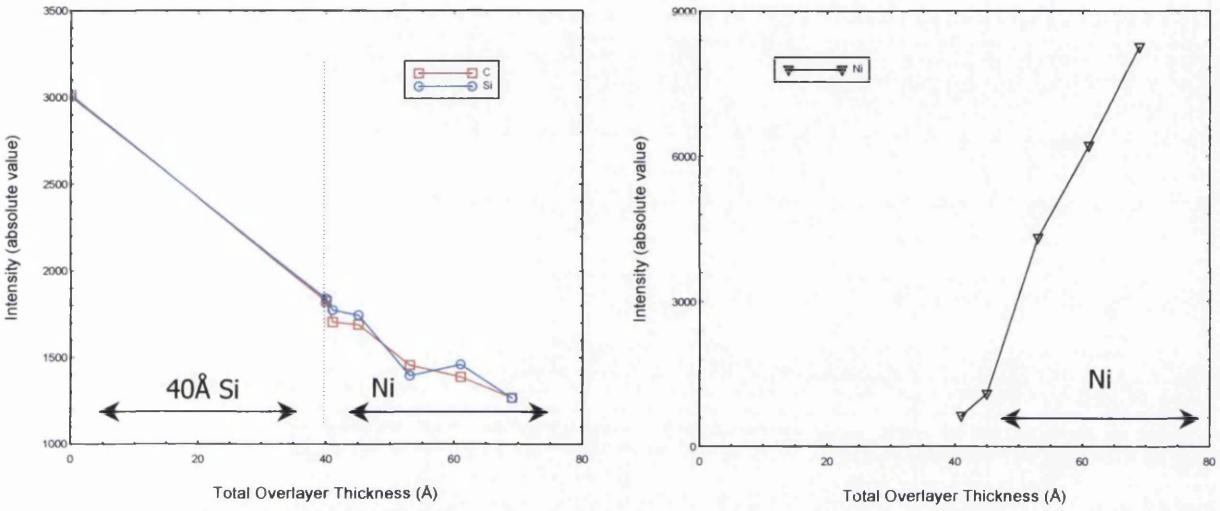

Figure 6.23: Overall peak intensity plots during interface formation (a) for *Si* 2p and *C 1s* (b) for *Ni 2p*.

At elevated temperature, the interface shows severe changes. The overall un-fitted peak intensity plot of the three main components is illustrated in Figure 6.25(a) and (b). In this case, the Si intensity is seen to react in an opposite behaviour to that of the C intensity. At low temperature (400°C to 500°C) anneal, there is a slight increase in Si intensity that may be cause by the growth of silicide, encouraged by the low temperature anneal or surface reconstruction as discussed in the previous section. At this stage, the C intensity remains almost constant. Above 500°C, the Si intensity is observed to decrease persistently up to 900°C, where the intensity is seen to increase again until it further decreases in the very high temperature range of 1000°C to 1200°C. While Si starts to decrease (at 500°C), C is increased at the same

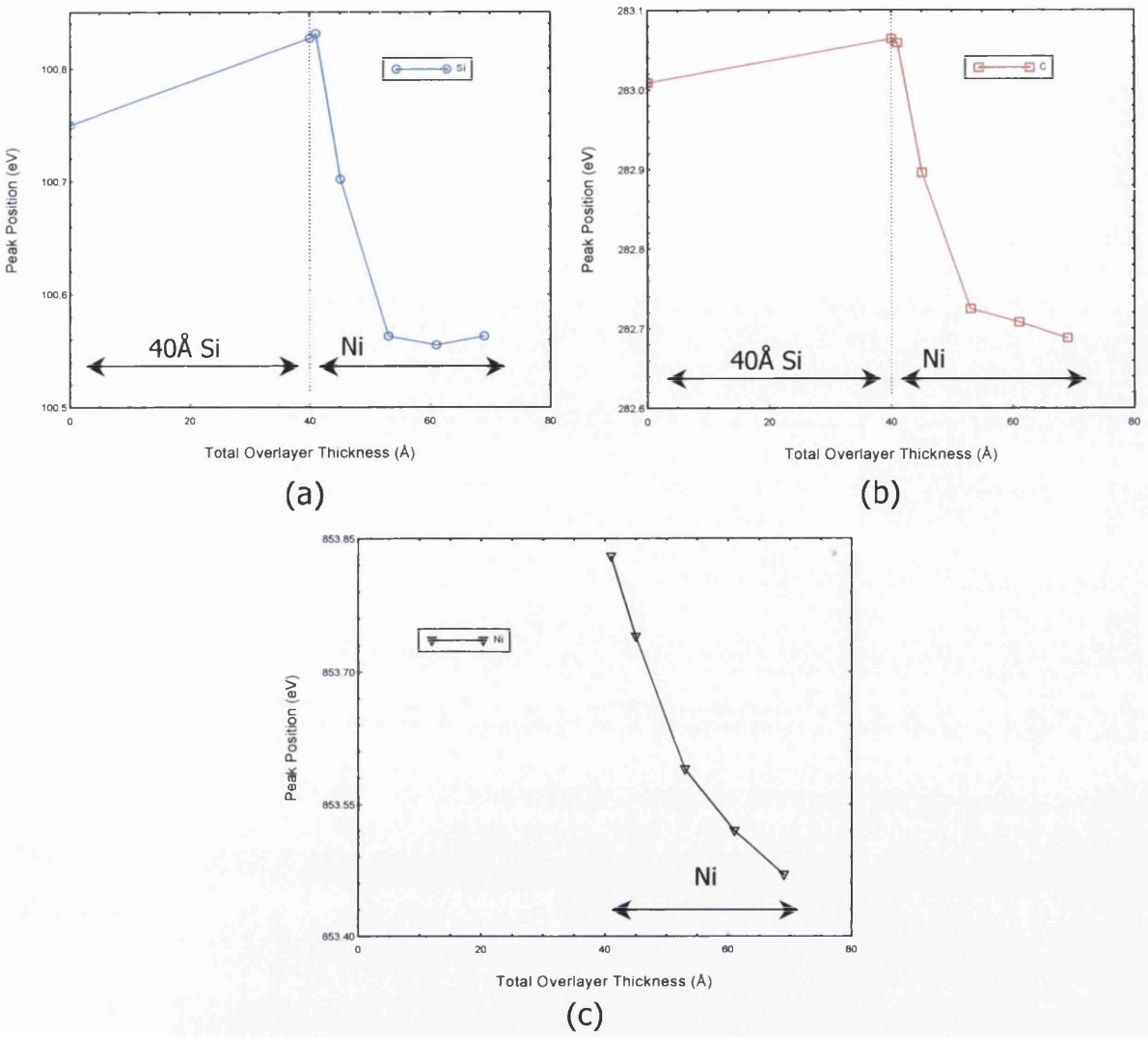

Figure 6.24: Peak position plots during interface formation for (a) *Si 2p* (b) *C 1s* (c) *Ni 2p*.

time and remains almost constant until the point where Si is seen to increase again (at 1000°C), where C rapidly increases up to 1200°C. These incidents might be the sign of C segregation onto the surface that covers up the bulk Si signal or the accumulation of C at the surface as a result of Si depletion via re-evaporation at such high temperature, hence the decrease in Si intensity. Another possibility is that the Ni silicides formation mechanism involves the consumption of the bulk Si. To date, the definite reason cannot yet be

established and will be discussed in more detail when reviewing the curve fitted spectra. On the other hand, Ni is seen to decrease in a similar manner as the 20Å Si interlayer interface study discussed in section 6.4.2.

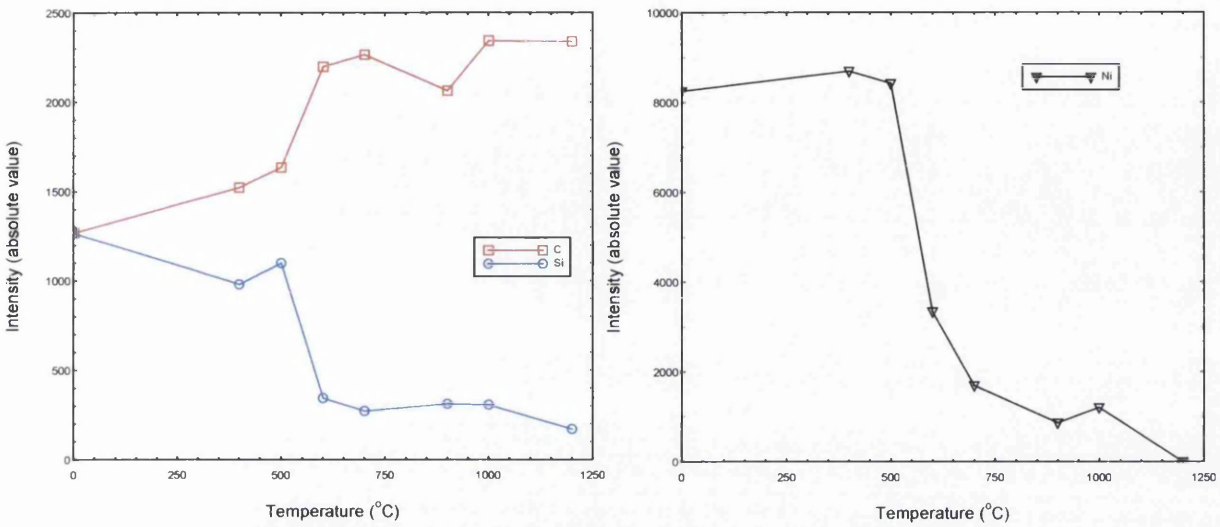

Figure 6.25: Overall peak intensity plot at sequential anneals (a) for *Si 2p* and *C 1s* (b) for *Ni 2p*.

Unlike the 20Å Si interlayer composition, the electrical behaviour of the 40Å Si interlayer composition has shows downward band bending throughout the annealing sequence. The peak position plots for the three main components is illustrated in Figure 6.26 (a – c). The core level of the bulk components (i.e. Si and C) are seen to shift in parallel towards higher binding energy, hence the barrier between the metal – semiconductor junction is lowered. Meanwhile, Ni spectra had displayed an opposite to that of the bulk components (Figure 6.26(c)). The difference in energy and behaviour between these components might be caused by chemical reactions or different in chemical environment and will be further discussed in the next section, where the spectra are analysed individually.

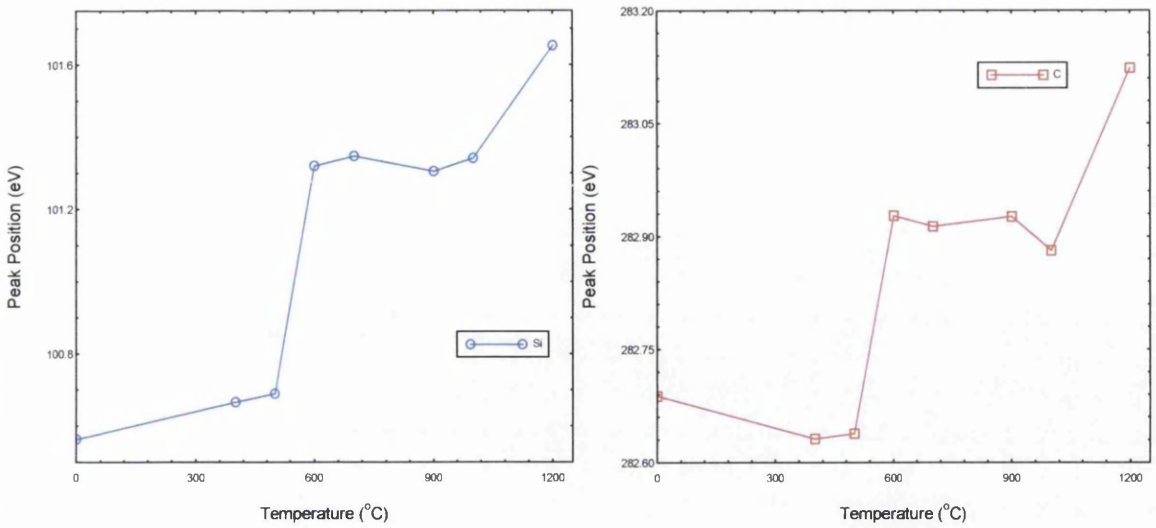

(a)

(b)

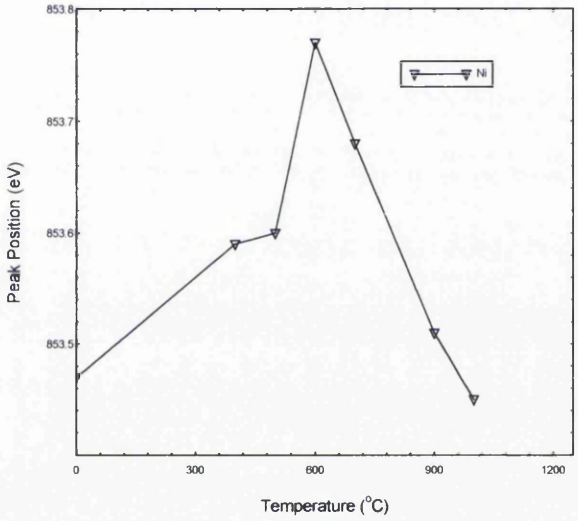

(c)

Figure 6.26: Peak position plots during sequential anneals for (a) *Si 2p* (b) *C 1s* (c) *Ni 2p*.

- ***Si 2p* core level**

Figure 6.27 reveals the curve fitted *Si 2p* spectra during the interface formation. Generally, the trend of all three components (bulk Si, deposited Si, silicides) is similar to the previous experiment where the silicide is observed to be growing while simultaneously consuming the Si interlayer (i.e. deposited Si) and the Ni overlayers.

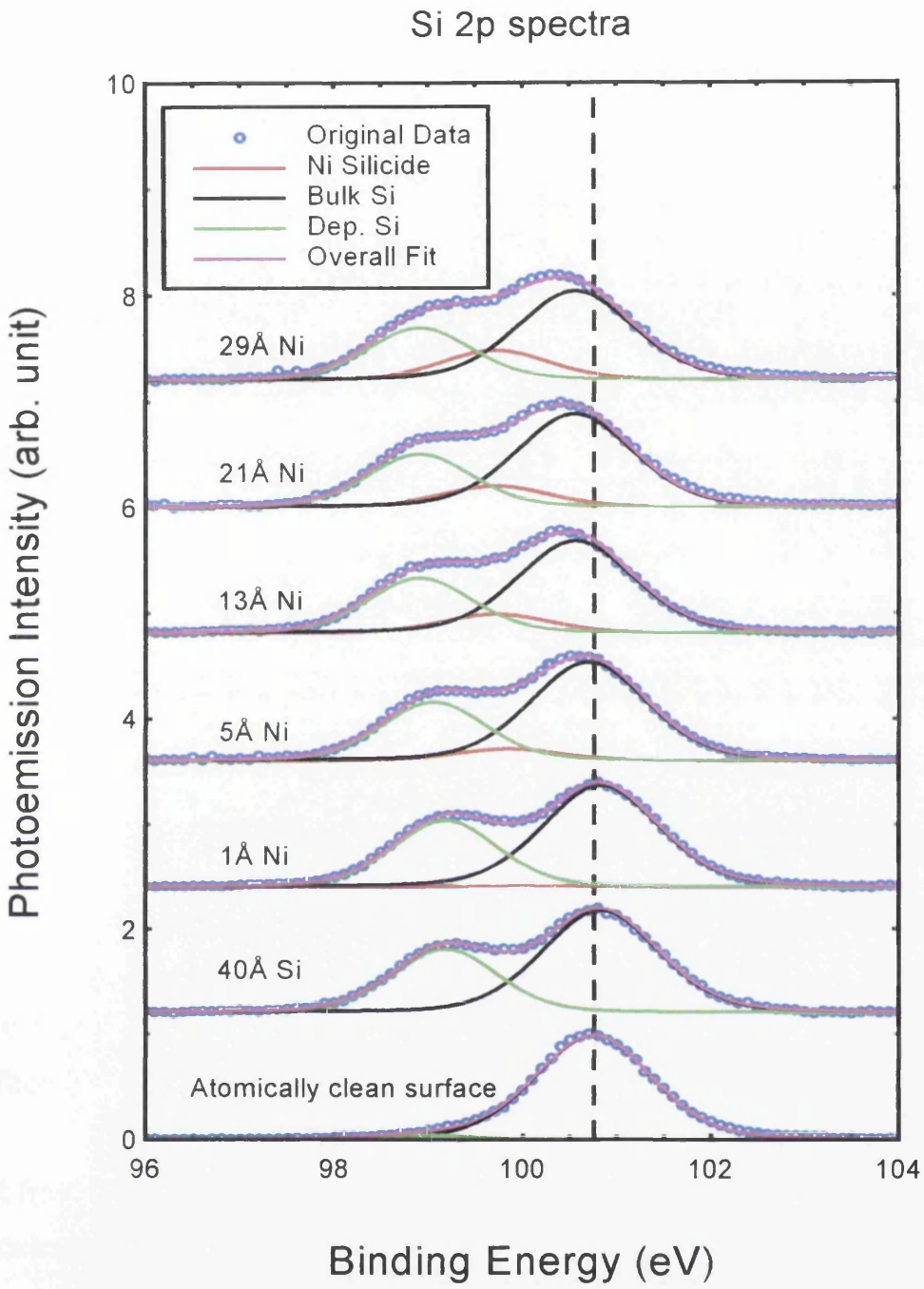

Figure 6.27: Curve fitted *Si 2p* core level spectra starting from the atomically clean surface to Si and sequential Ni overlayers deposition. The deconvoluted components including the original raw data are listed in coloured lines as described in the legend.

This incident can be clearly illustrated in the intensity plot of the three fitted components within the *Si 2p* spectra (see Figure 6.28 (a)). Here, the rate of decay of the Si interlayer (green line) and bulk Si (black line) is similar, which indicates that both components are consumed and buried at the same time via the formation of Ni silicides (red line) and is indicated by the increasing trend of Ni silicide intensity. The exact species of the Ni silicides is uncertain as described previously.

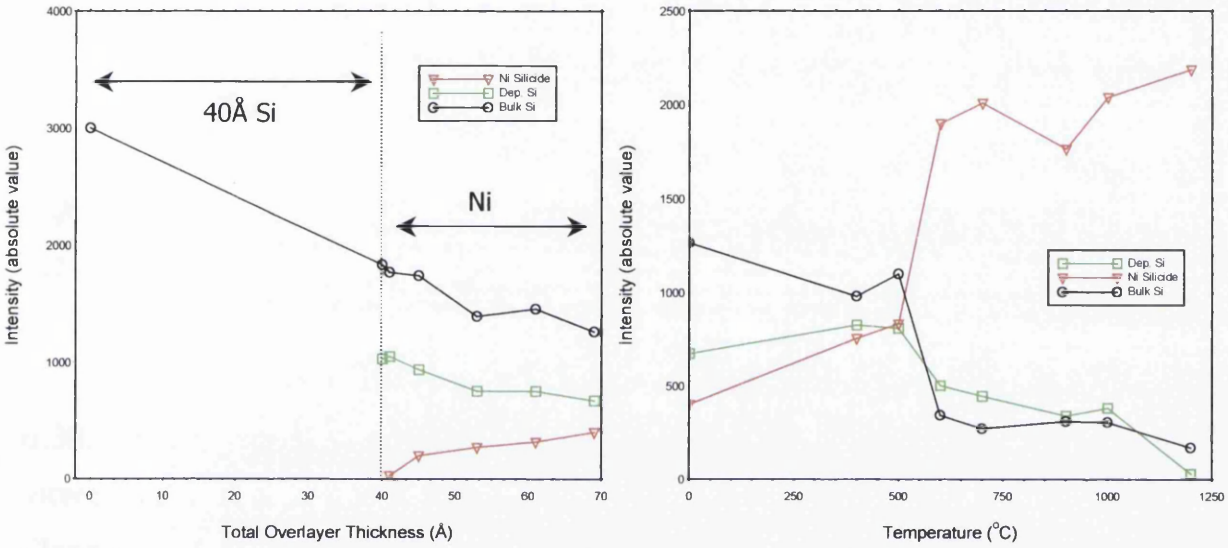

(a) (b)

Figure 6.28: Intensity plots of the deconvoluted Si components (a) during interface formation (b) at sequential anneals.

Apart from forming silicides, the interface is also observed to form a barrier of approximately 0.2eV. The sign of the barrier formation is indicated by the peak position shift of the *Si 2p* core level towards lower binding energy side of the spectra for all three fitted components, clearly illustrated in Figure 6.29 (a).

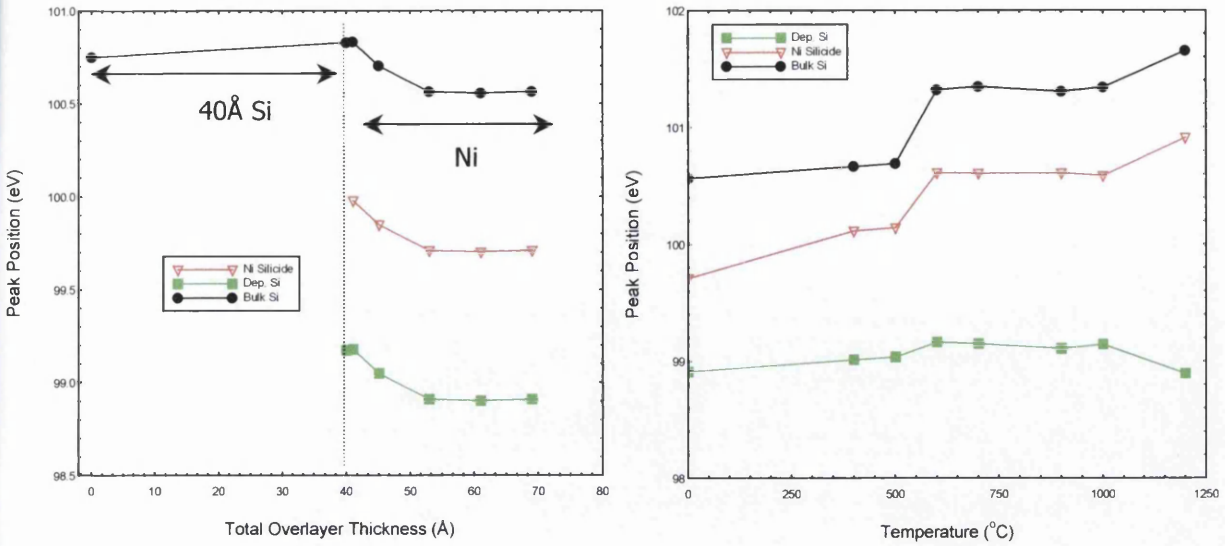

(a) (b)

Figure 6.29: Peak position plots of the deconvoluted Si components (a) during interface formation (b) at sequential anneals

The curve fitted *Si 2p* spectra at sequential anneals in shown in Figure 6.30. When annealed, the silicides are observed to grow rapidly while the intensity of bulk Si and Si interlayer is seen to decrease correspondingly. Clearly, this incident can be explained by the consumption of both bulk Si and Si interlayer in the silicide formation mechanism. The intensity plot shown in Figure 6.28(b) clearly shows the increase in silicide intensity, simultaneously a linear decrease of the intensity for bulk Si and Si interlayer. Here, the amounts of silicides formed are much greater than the 20Å Si interlayer interface, indicated by a huge silicide peak (red line) within the *Si 2p* spectra. Again, there is a possibility of several species of silicides being formed at this stage. However, as mentioned previously, these silicides peaks are hard to distinguish due to their small energy separation. The silicide peak is seen to grow with increasing annealing temperature and remains stable up to 1200°C. Meanwhile, the electrical properties show a similar trend to that of the 20Å

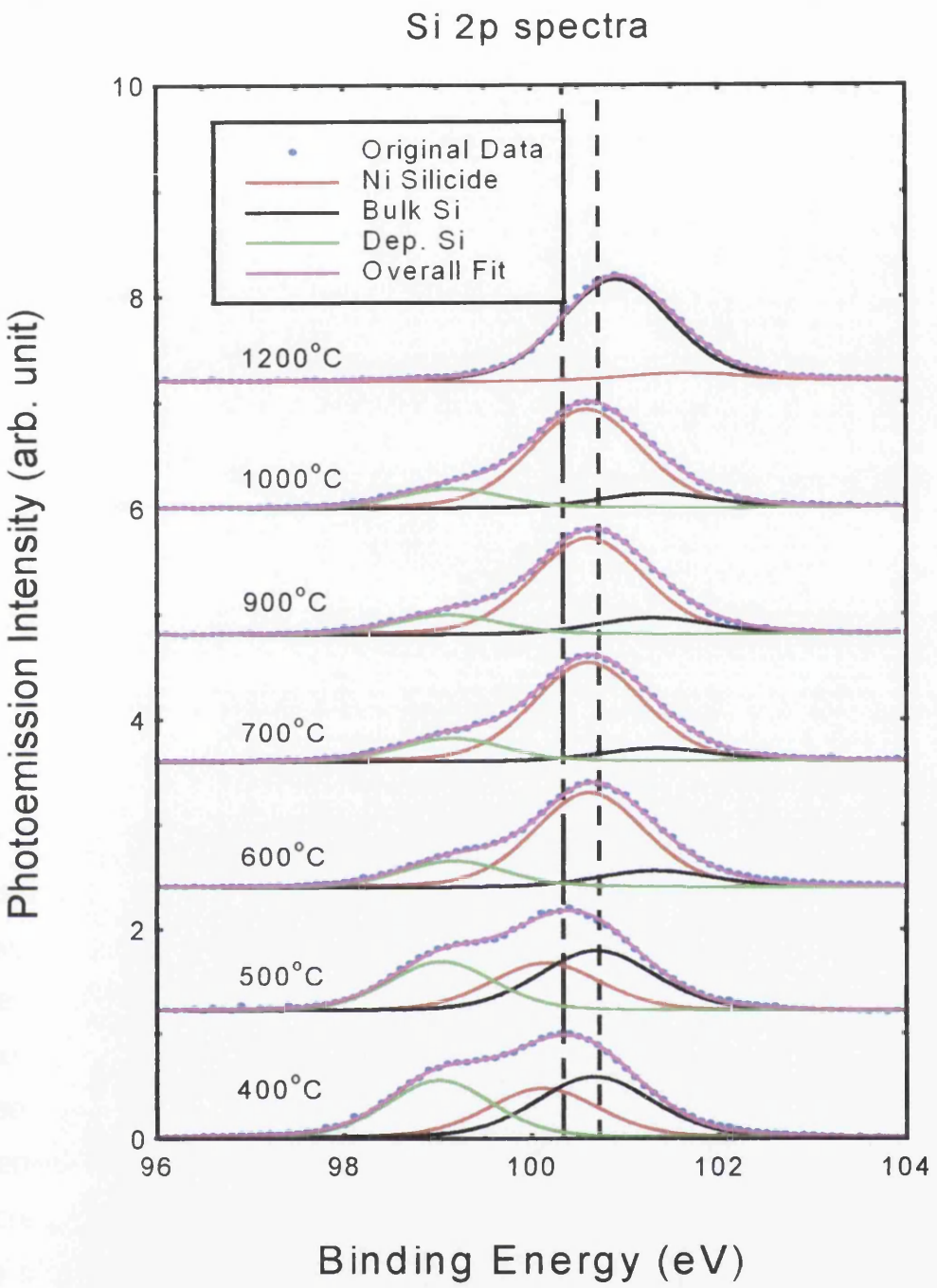

Figure 6.30: Curve fitted *Si 2p* core level spectra during sequential anneals starting from temperature of 400°C to 1200°C. The deconvoluted components including the original raw data are listed in coloured lines as described in the legend. The vertical dotted lines indicate peak movement in comparison to 400°C and the original clean surface.

experiment described in section 6.4.2. However, in this case, only the bulk Si and the formed silicide peak are seen to shift together, where as the Si interlayer are seen to remains almost constant throughout the annealing process. This event could be the sign of chemical reaction between Ni and Si interlayer or the sign of consumption of the Si interlayer in silicides formation at elevated temperatures. From the peak position plots in Figure 6.29(b), it is observed that the barrier is lowered to approximately 0.4eV at temperature range of 500°C to 600°C. Above 600°C, the peak position remains virtually stable up to 1000°C. At high temperature above 1000°C, there is clearly a further shift of approximately 0.3eV towards higher binding side of the spectra. The electrical properties of the interface associated with this downward band bending will be discussed in later Chapter 7.

- ***C 1s* core level**

From the general discussion section previously, it is demonstrated that the *C 1s* core level has a similar trend to that of the previous study discussed in section 6.4.2. The curve fitted *C 1s* core level spectra are illustrated in Figure 6.31 and Figure 6.32. Again, the spectra showed the occurrence of free C (grey line) immediately after the deposition of Si interlayer onto the atomically clean surface. The ternary phase silicide (red line) is also seen to arise after 5Å of Ni, exactly the same thickness as with the 20Å case. The intensity of the bulk C component (black dashed line) is observed to be decreasing with Ni overlayers covering the bulk signal, clearly illustrated from the intensity plot in Figure 6.33(a). Unlike the previous study described in section 6.4.2, the intensity of the free C component and ternary phase silicide does not increase with increasing thickness of Ni overlayers. In fact, they are seen to remain almost constant and are suspected to lie between the metal - Si interlayer junction. In addition, the *C 1s* core level also shift towards lower binding energy approximately 0.3eV (see Figure 6.34(a)), which indicates the

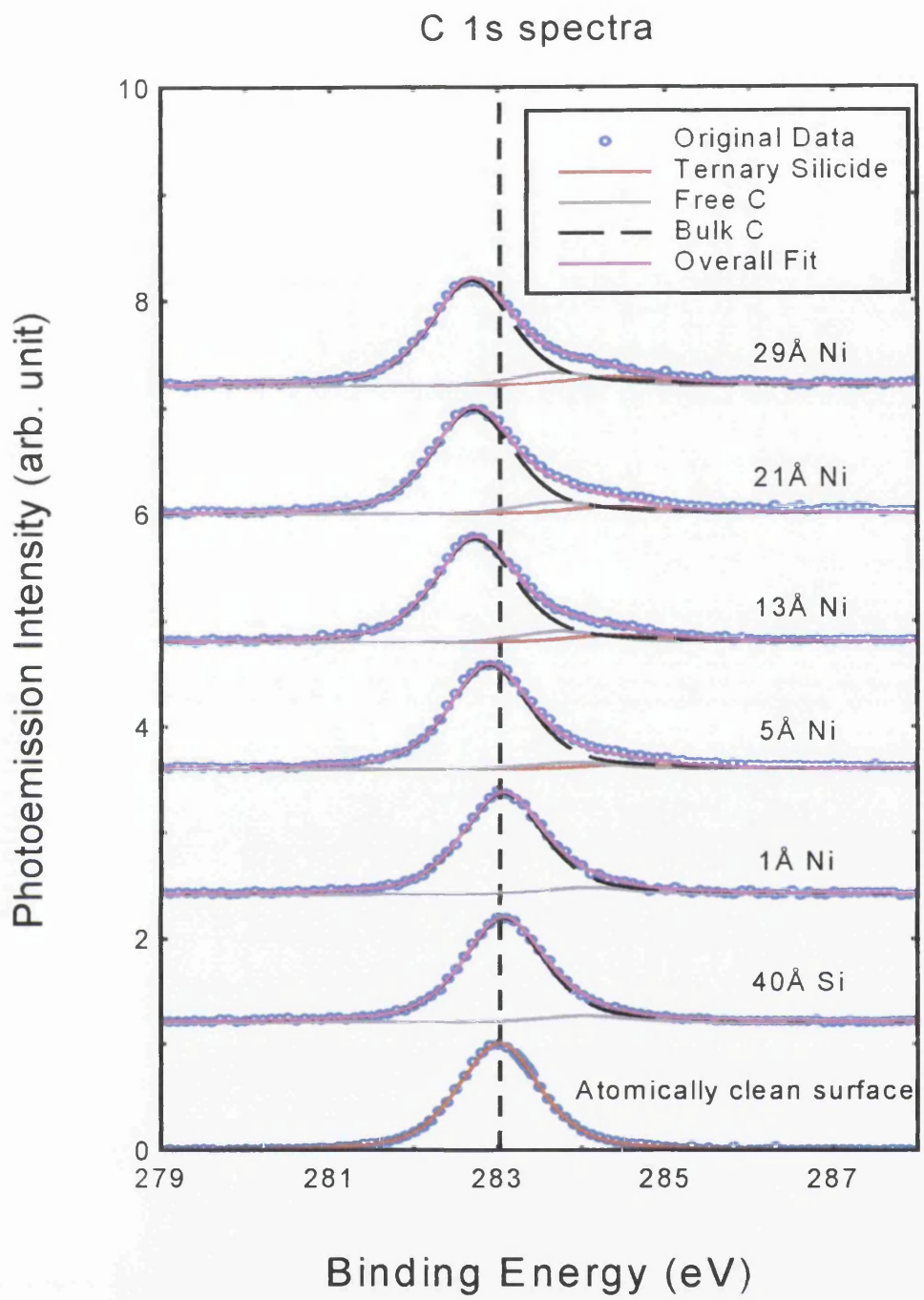

Figure 6.31: Curve fitted *C 1s* core level spectra starting from the atomically clean surface to Si and sequential Ni overlayers deposition. The deconvoluted components including the original raw data are listed in coloured lines as described in the legend.

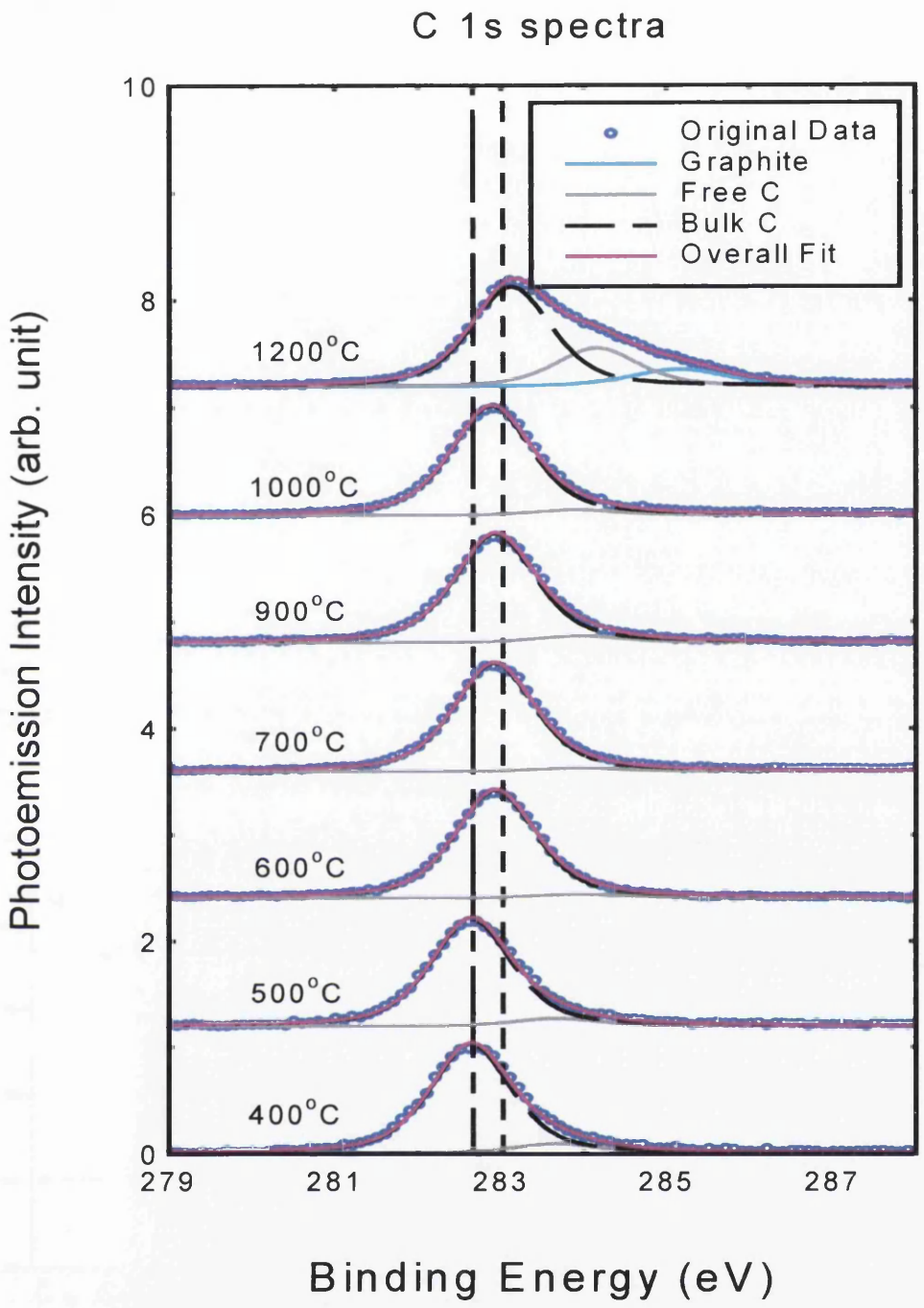

Figure 6.32: Curve fitted *C 1s* core level spectra during sequential anneals starting from temperature of 400°C to 1200°C. The deconvoluted components including the original raw data are listed in coloured lines as described in the legend. The vertical dotted lines indicate peak movement in comparison to 400°C and the original clean surface.

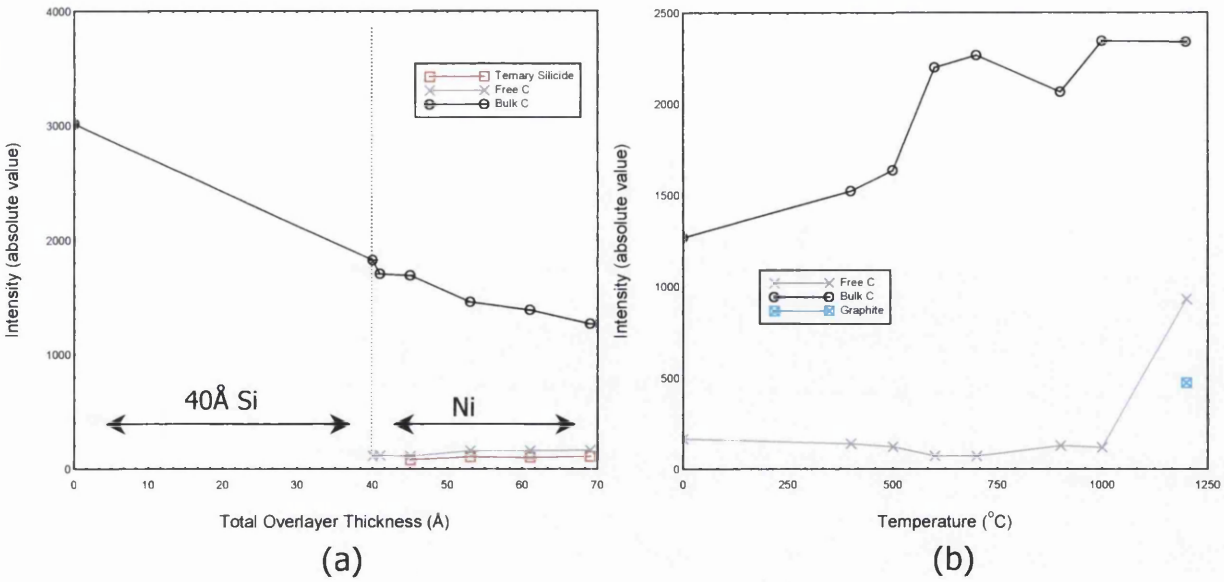

Figure 6.33: Intensity plots of the deconvoluted C components (a) during interface formation (b) at sequential anneals.

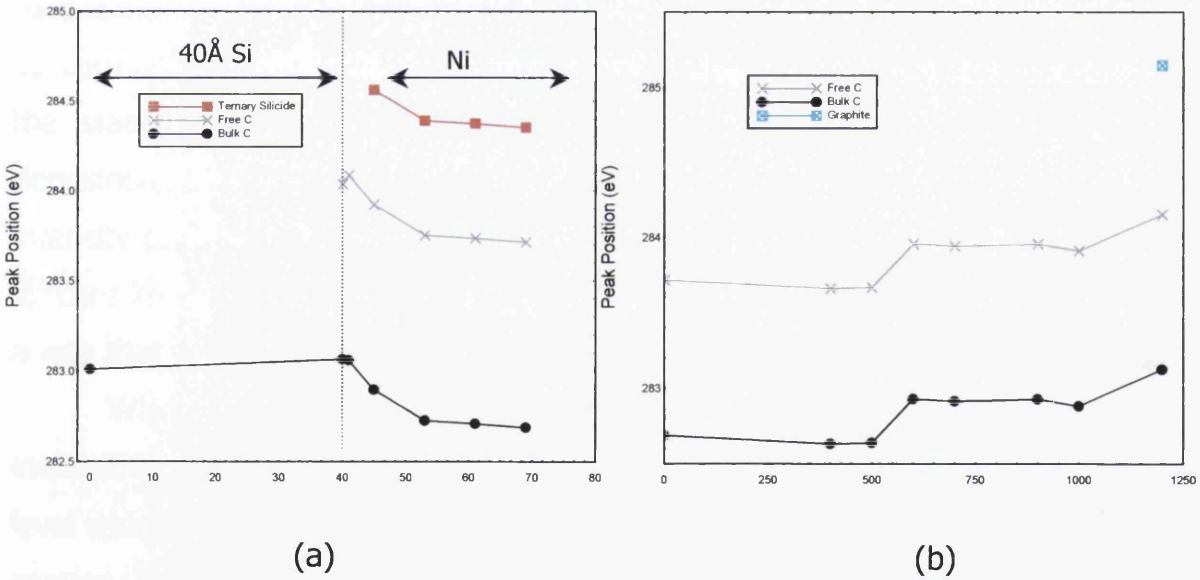

Figure 6.34: Peak position plots of the deconvoluted C components (a) during interface formation (b) at sequential anneals.

formation of a barrier, similar to the *Si 2p* core level discussed previously that shifts in the same way. Subsequent to annealing, the interface exhibits a similar behaviour with the previous study discussed in section 6.4.2 and is clearly indicated by the intensity plot in Figure 6.33(b).

Meanwhile, the electrical behaviour observed for the *C 1s* core level is the same as the *Si 2p* core level. However, the barrier was observed to be lowered by approximately 0.3eV at temperature of 500°C to 600°C and remains stable at temperature of 700°C to 900°C. The barrier was further shifts towards high binding energy by 0.25eV at high temperature of 1000°C to 1200°C (Figure 6.34(b)). The difference in binding energy shifts between *Si 2p* and *C 1s* core level are proposed to be originated from difference in chemical environment of the elements, thus creating a chemical shift superimposed on the Fermi shift.

- ***Ni 2p* core level**

As discussed previously on the general observation section (section 6.4.3), *Ni 2p* core level had a similar behaviour to 20Å Si interface. Figure 6.35 shows the stack plot of curve fitted *Ni 2p* core level spectra with increasing deposition of Ni overlayers. The increasing trend is clearly shown in the intensity plot of the Ni spectra shown in Figure 6.23. At the same time, the *Ni 2p* core level spectra have also demonstrated a shift (see Figure 6.24) in such a way that is similar to that of the bulk components.

When annealed, the gradual disappearance of Ni at the surface with increasing annealing temperature is clearly demonstrated in the *Ni 2p* core level spectra (Figure 6.36) and the intensity plot in Figure 6.25 in the previous section. This is probably due to Ni diffusion into Si or re-evaporation of Ni silicides, as discussed in section 6.4.2 for the 20Å Si interlayer. However, unlike the 20Å Si interlayer, the *Ni 2p* binding energy does not shift in the same way as the bulk core levels. This could be associated with chemical reaction between Ni and the Si interlayer.

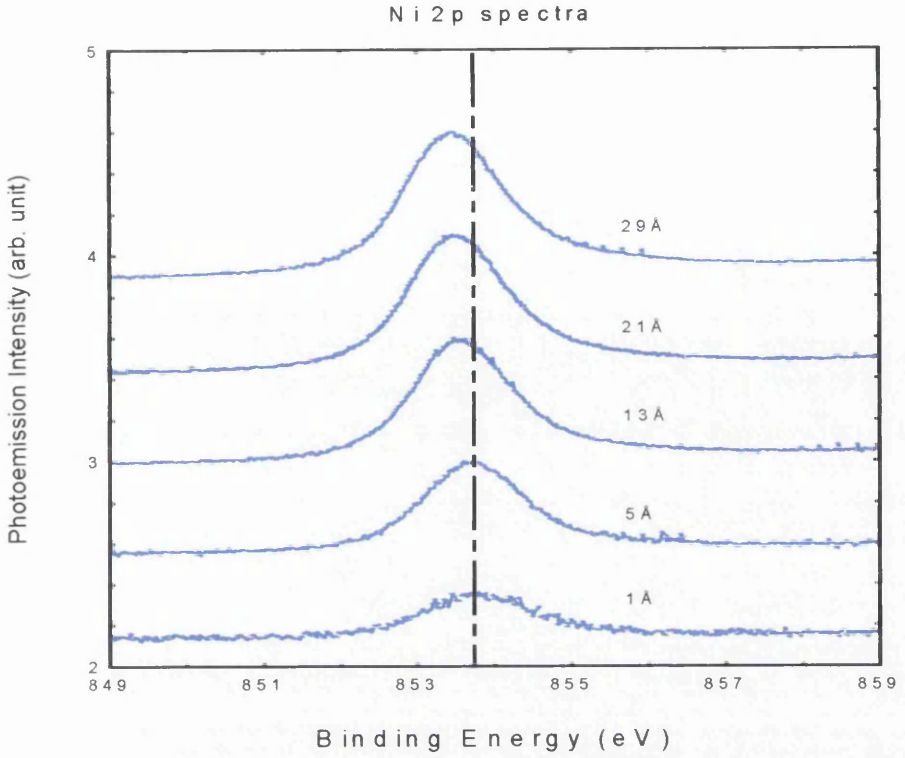

Figure 6.35: *Ni 2p* core level spectra during sequential Ni overlayers deposition.

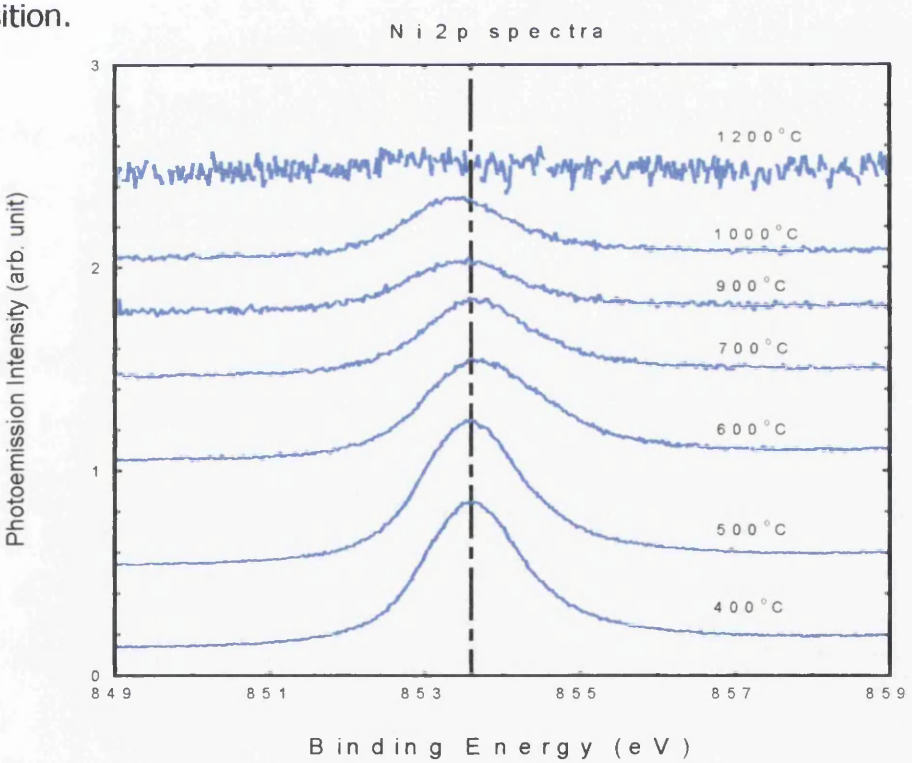

Figure 6.36: *Ni 2p* core level during sequential annealing temperatures.

Discussion

So far, the analysed experimental results of the 40Å Si interlayer study have shown similarities and also dissimilarities to that of the 20Å composition. The similarities between these two cases include the formation of free C, Ni silicides, the additional C ternary phase silicide and barrier formation. Each of these incidents has been discussed in detail previously in section 6.4.2. However, for the case of silicide formation, there is a slight difference as the Si interlayer is thicker than the previous case. The intensity plot (see Figure 6.28(a)) can further explain the reaction between the Si interlayer and bulk SiC. In the plot, the rate of decay of bulk Si (black line) and the Si interlayer (green line) is almost identical. However, if only the Si interlayer was consumed in the silicide formation mechanism, it should decay more rapidly than the bulk Si. Therefore, it could be that part of the Si interlayer has reacted with the bulk, so that both Si (the bulk Si and Si interlayer) are consumed in forming silicide while simultaneously being buried by the silicide at the surface. Again, the exact species of the silicides formed are uncertain and may consist of several species. However, these silicides peaks cannot be individually distinguished due to their small energy separation.

As observed for the 20Å case, Ni has again reacted with C, producing ternary phase silicide as discussed in section 6.4.2. This ternary silicide is observed to arise at exactly the same Ni thickness as with the 20Å case (5Å of deposited Ni), which indicates that the formation of the ternary phase silicide requires a minimum amount of Ni or C. The amount of free C at the interface and the ternary phase silicide in this case remains almost constant and is suspected to be located at the junction between the silicide layer and the bulk, as discussed previously in section 6.4.2. Simultaneously, the bulk C is covered up by the Ni overlayer, which explains the decrease in bulk C intensity.

When annealed at low temperature, further formation of Ni silicides is observed as described previously. However, as the amount of Si available is

slightly greater with a thicker Si interlayer than in the previous study, it is expected that the silicide formation would consume the Si interlayer rather than Si from the bulk SiC. However, in this case, bulk Si is seen to be more likely to be consumed. The intensity plot shown in Figure 6.28(b) clearly reveals the consumption behaviour, where the bulk Si decays more rapidly than the Si interlayer. Even with an increasing amount of silicides, the overall Si intensity is observed to decrease (see Figure 6.23(a)) with increasing annealing temperature. This event indicates the possibility of interdiffusion between silicides or diffusion of silicides into the bulk, similar to that what observed in the previous case. Again at 1200°C, re-evaporation of silicides is observed.

Although the behaviour of the Si core level has shown several changes from the 20Å case, the C core level shows a very similar behaviour than the previous case. However, the amount of free C generated in this case might be different than the previous case due to the different thickness of the Si interlayer. As the study emphasises on the C content of the interface and the effectiveness of the Si interlayer in reducing the amount of free C, the overall trend of the Si and C components of these two compositions (i.e. 20Å and 40Å of Si interlayer) will be evaluated and discussed later at the end of this chapter.

The electrical properties of this composition are straightforward and have been discussed previously in early section 6.4.3 (general observation). To summarise, a barrier of 0.3eV is formed during the interface formation, slightly different value from the 20Å case (0.2eV for 20Å Si). When annealed, downward band bending was also observed (also observed with the 20Å case). The reason for the differences in barrier are proposed to be the initiated from different chemical reactions between Si and C, as the silicides species changed drastically for a thicker Si interlayer. The comparison of the barrier height formed in between the 20Å and 40Å composition will be discussed and compared later at the end of this chapter.

6.4.4 60Å Si Interlayer

- **General Observation**

The study is extended to another thicker coverage of Si interlayer (60Å instead of 40Å). Similar to the both previous study, the experiment is conducted using the same technique and the overall trend of the results observed is presented to give a general impression of the effect of a thicker Si interlayer to the overall material composition.

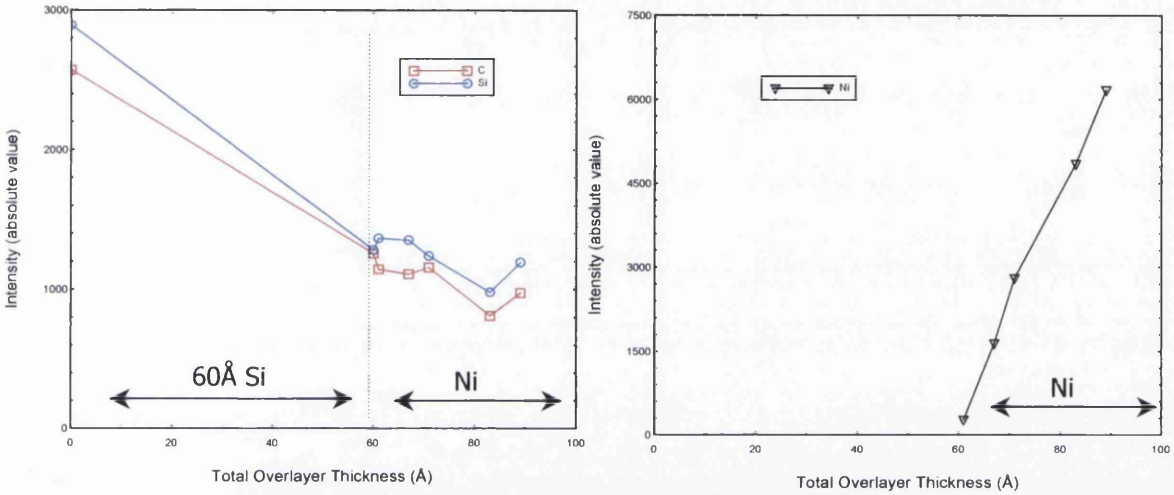

Figure 6.37: Overall peak intensity plots during interface formation (a) for *Si 2p* and *C 1s* (b) for *Ni 2p*.

The overall peak intensity plot for the Ni-60ÅSi-SiC interface is illustrated in Figure 6.37. The behaviour of the intensity plot can be explained by several stages throughout the interface formation. The initial single deposition of 60Å Si interlayer tends to cover up the bulk, which results in a massive decrease in both Si and C. Similar to the previous case studies, the outcome of deposition of Ni overlayers onto the Si-SiC interface is the formation of Ni silicides. Thus, Ni atoms bond with the Si atoms from the Si interlayer (especially for such a thick interlayer), hence we see an increase in Si intensity. Meanwhile, the formation of silicides on top of the surface then covers up the bulk, thus a decrease in C intensity is observed. Further

deposition of Ni overlayers will certainly produce more silicides. However, these silicides might also intermix and diffuse into the bulk as they form, which might be a possible explanation for the increase in intensity for both Si and C towards the end of the interface formation process. Obviously, with an increasing thickness of Ni, the intensity of Ni displays a persistent increasing trend (Figure 6.37(b)).

Electrically, the interface has displayed a similar behaviour to the previous study, forming a barrier of approximately 0.3eV. However, at the initial deposition of 60Å of Si, it is observed that the *Si 2p* and *C 1s* core level does not shift towards high binding energy as observed previously in the 20Å and 40Å case. Therefore, possible is Si passivation (observed previously in section 6.4.2 and 6.4.3) does not occur with the 60Å Si composition. This is probably cause by the thickness of the Si interlayer deposited in this case (thicker Si layer of 60Å), as Si passivation are more likely to occur with thinner layers. However, there is a stage where the C peak behaves slightly different than Si and Ni (see Figure 6.38 (b)). This behaviour might be associated with chemical reactions within the C components and will be considered in more detail in the next section when the spectra are deconvoluted.

At low temperature anneals, the overall intensity behaviour of the Si and C core levels are similar to the 20Å and 40Å interface, clearly shown in Figure 6.39(a). The intensity for both Si and C is seen to increase followed by an immediate decrease, which suggests surface reconstruction. Unlike the previous two cases, when annealed above 600°C, the overall intensity of C in this case greater than the Si intensity. The possible explanation for this incident could be C segregation towards the surface, revealing a stronger C signal while burying the Si intensity. Meanwhile, the intensity of the Si shows a gradual increasing trend, most possibly due to the formation of silicides. Another possible explanation for the increasing behaviour at higher annealing

temperatures (600°C to 1000°C) of both core level spectra is the interdiffusion of Ni silicides towards the bulk, revealing the bulk signals.

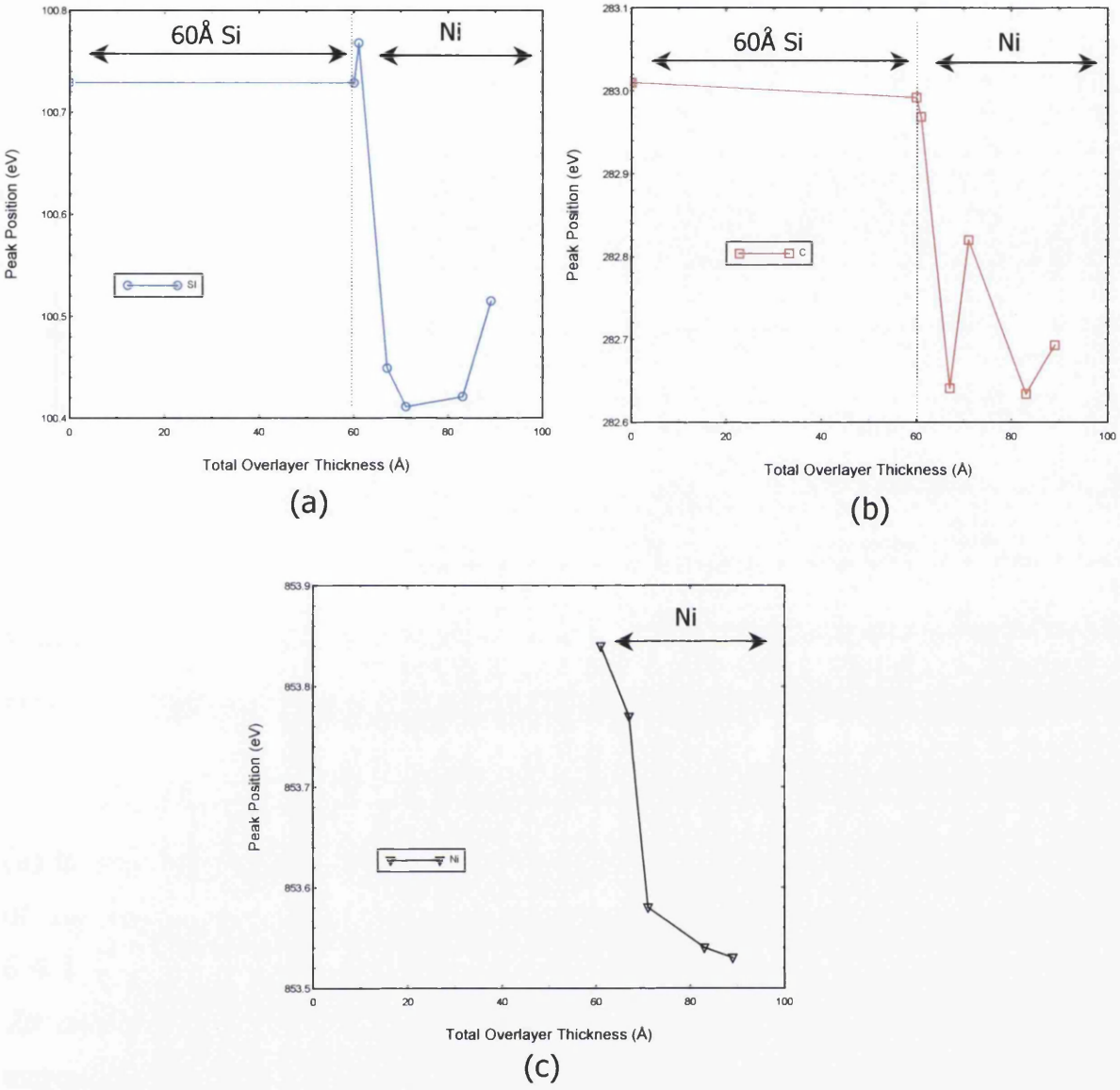

Figure 6.38: Peak position plots during interface formation for (a) *Si 2p* (b) *C 1s* (c) *Ni 2p*.

However, at this stage, these reactions are yet be established and will be further discussed later when the core level spectra are deconvoluted. Again,

as expected, the intensity of the Ni core level decreases with increasing annealing temperature as discussed previously in section 6.4.2 and 6.4.3.

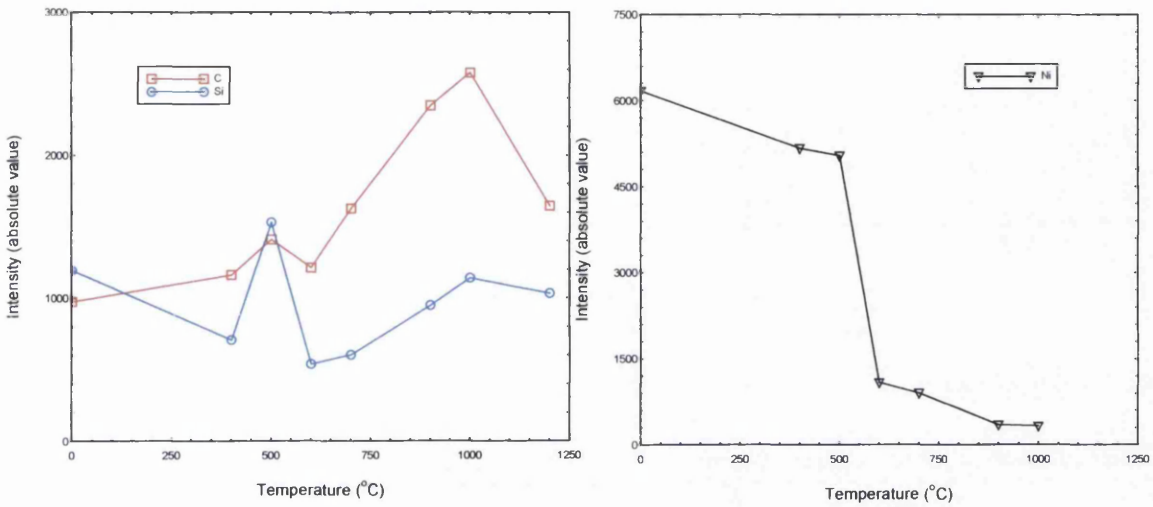

(a) (b)

Figure 6.39: Overall peak intensity plot at sequential anneals (a) for *Si 2p* and *C 1s* (b) for *Ni 2p*.

The peak position plot for all three components is shown in Figure 6.40 (a) to (c). Clearly, the peak shifts for all three components are similar to that of the 20Å and 40Å case and had been described earlier in section 6.4.2 and 6.4.3. However, it is observed that *C 1s* core level had a greater shift than *Si 2p* core level. This can be explained by the chemical reaction of the C, especially in this case where C is observed to segregate towards the surface, indicated by the intensity plot (Figure 6.39) discussed previously. Therefore, the peak shifts observed for *C 1s* core level spectra are more likely to correspond to chemical shift plus Fermi shift, giving a bigger shifts compared to *Si 2p* core level. Although shifted in a different trend, the *Ni 2p* core level shifts are similar to the results obtained from the 20Å and 40Å case, as discussed in section 6.4.2 and 6.4.3.

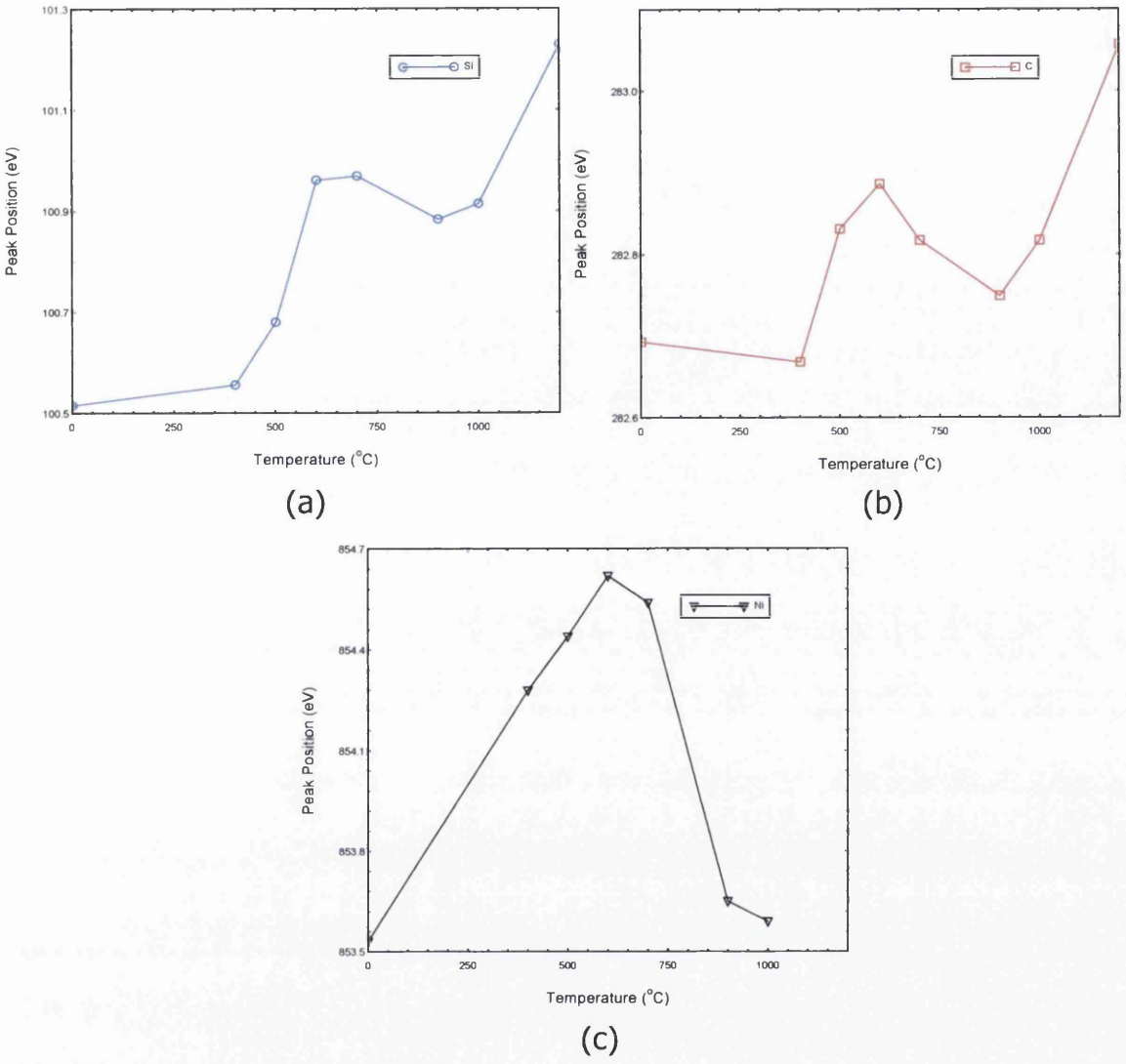

Figure 6.40: Peak position plot at sequential anneals for (a) *Si 2p* (b) *C 1s* (c) *Ni 2p*.

- ***Si 2p* core level**

The curve fitted *Si 2p* core level spectra is illustrated in Figure 6.41. From the initial atomically clean surface, the deposition of the 60Å Si interlayer followed by sequential Ni overlayers deposition results in the formation of silicides. The silicides are again observed to grow with increasing deposition of Ni overlayers, clearly indicated in the intensity plot shown in Figure 6.42(a). Meanwhile, the bulk Si and deposited Si are observed to

decrease, indicating the consumption of Si in the formation of silicides near the surface while burying the bulk Si.

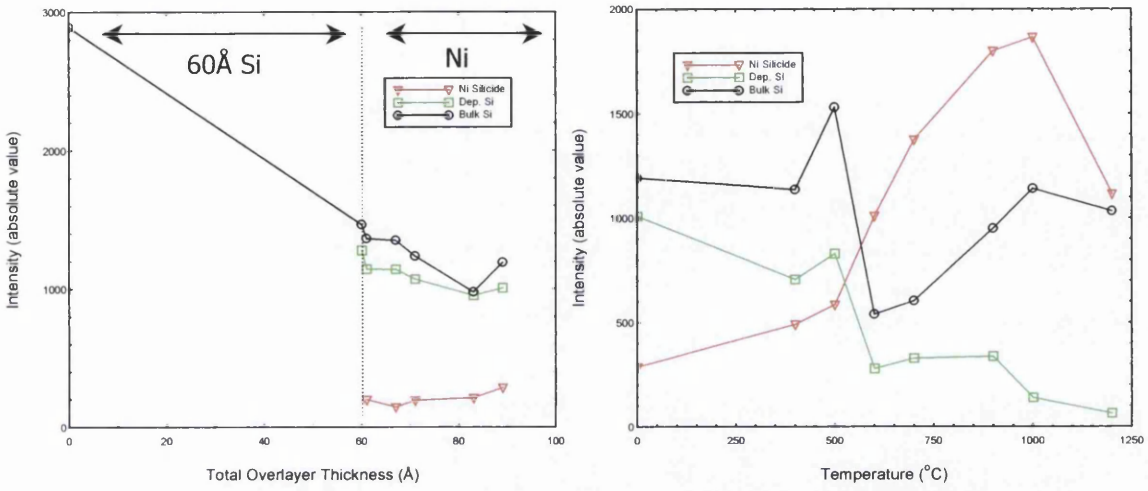

(a) (b)

Figure 6.42: Intensity plots of the deconvoluted Si components (a) during interface formation (b) at sequential anneals.

Electrically, the interface also exhibits a barrier formation indicated by binding energy shifts of the Si core level by 0.2eV. The peak position plot for the deconvoluted *Si 2p* core level spectra during interface formation is shown in Figure 6.43(a).

When annealed, the interface exhibits a slightly different behaviour than the two previous studies. The curve fitted *Si 2p* core level spectra during the heat treatment study are shown in Figure 6.44. Due to the presence of a thicker Si interlayer, the Ni silicide peak is seen to grow rapidly, indicated by the steep increase (red line) in the intensity plot in Figure 6.42(b). The formation of silicides obviously would consume Si. However, in this case, the Si interlayer (i.e. deposited Si, green line) is more preferable than the bulk. This reaction is clearly observable in the intensity plot, where the Si interlayer decays faster compared to the bulk Si.

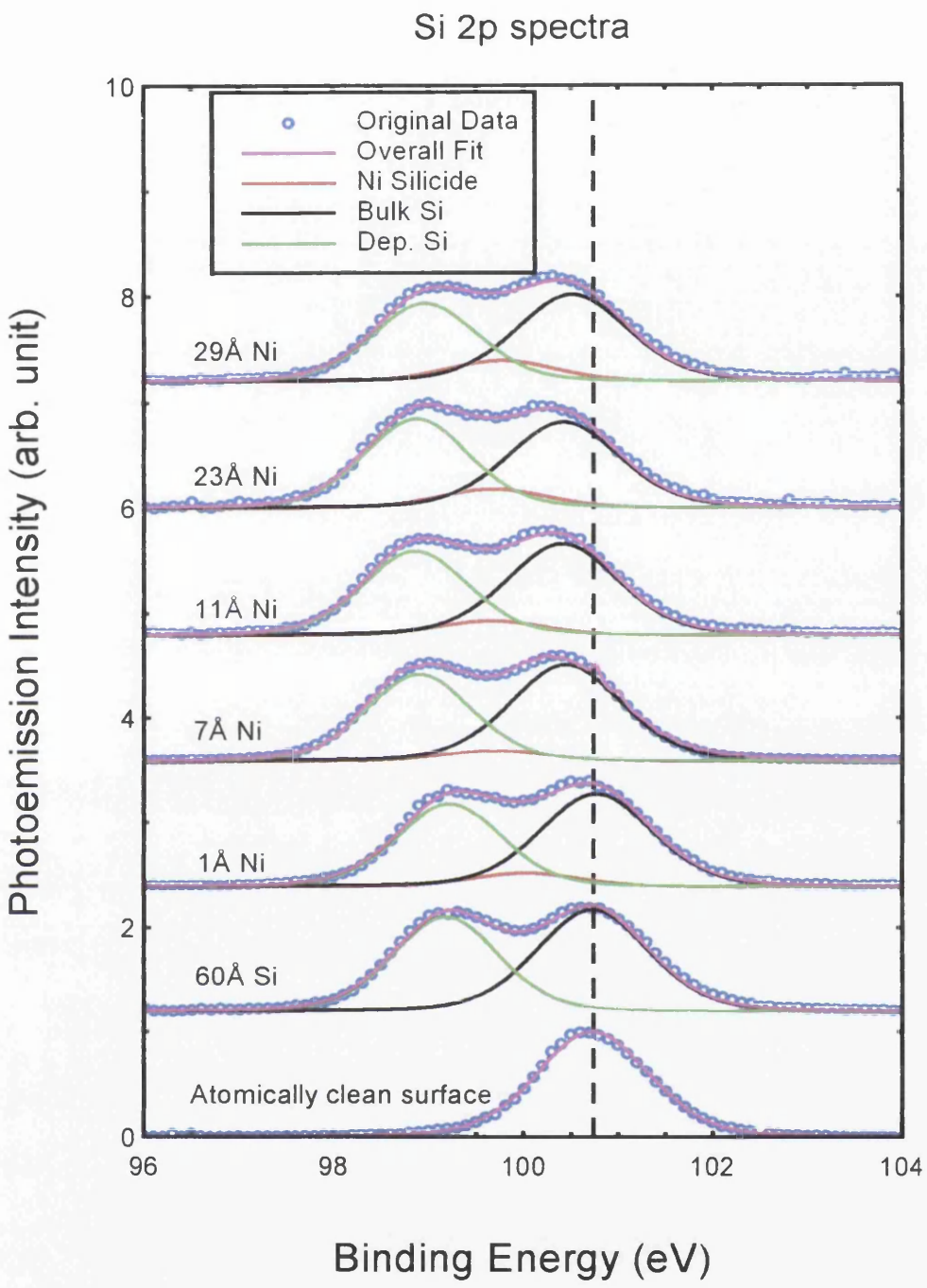

Figure 6.41: Curve fitted *Si 2p* core level spectra starting from the atomically clean surface to Si and sequential Ni overlayers deposition. The deconvoluted components including the original raw data are listed in coloured lines as described in the legend.

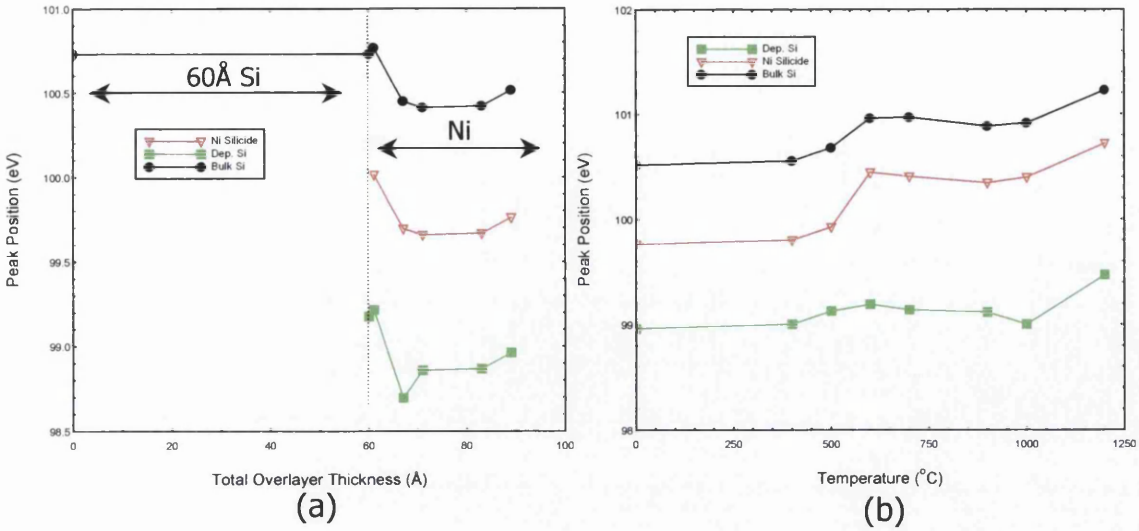

Figure 6.43: Peak position plots of the deconvoluted Si components (a) during interface formation (b) at sequential anneals.

In addition, the bulk Si is observed to increase at temperature above 600°C. The explanation for this behaviour is that apart from the formation of Ni silicides, intermixing or interdiffusion towards the bulk have also occurred, hence revealing a stronger bulk signal. Even so, at 1200°C, all Si components are observed to be re-evaporated, indicated by a decrease in all three components.

As discussed previously, the interface shows downward band bending throughout the annealing process. From the peak position plot in Figure 6.43(b), the Si components have shifted 0.4eV at low temperature anneal and further shifted by 0.2eV at 1200°C towards high binding energy.

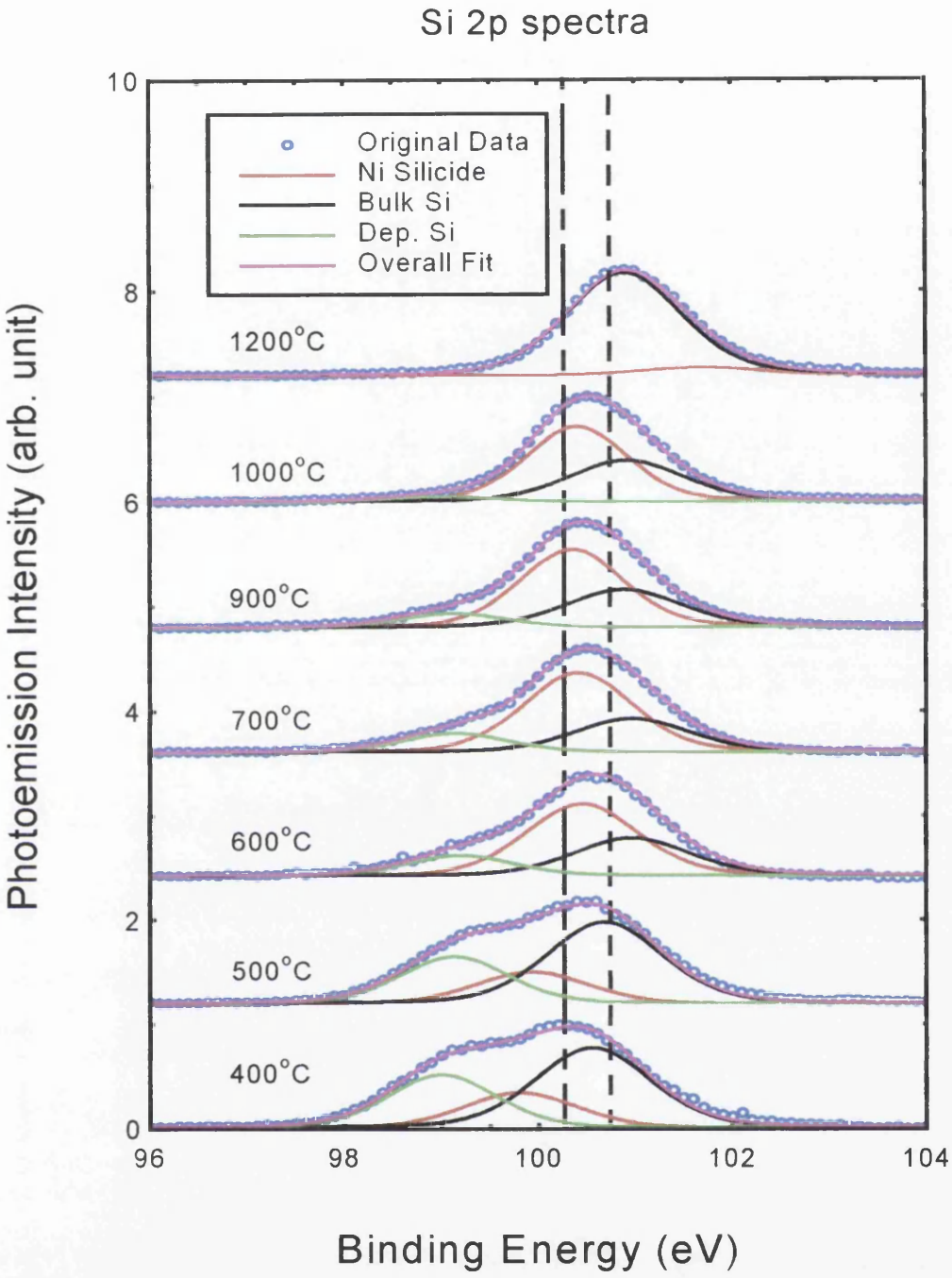

Figure 6.44: Curve fitted *Si 2p* core level spectra during sequential anneal starting from temperature of 400°C to 1200°C. The deconvoluted components including the original raw data are listed in coloured lines as described in the legend. The vertical dotted lines indicate peak movement in comparison to 400°C and the original clean surface.

- ***C 1s* core level**

The curve fitted *C 1s* core level is shown in Figure 6.45. As discussed previously in the general observation (section 6.4.4), the overall behaviour of the *C 1s* spectra is quite similar to that of the 20Å and 40Å thick Si interlayer case as discussed in section 6.4.2 and 6.4.3. However there are several differences in the chemical reactions occurring at the interface. The initial deposition of 60Å of Si again results in the formation of free C. However, the formation of ternary phase silicide arises immediately after the deposition of 1Å Ni, instead of 5Å, as observed in the previous two case studies. In addition, the overall intensity of the ternary phase silicide is greater than the intensity of the free C, clearly illustrated in the intensity plot (see Figure 6.46(a)). Nevertheless, the bulk C displays an identical behaviour to that of the previous study (see section 6.4.2 and 6.4.3).

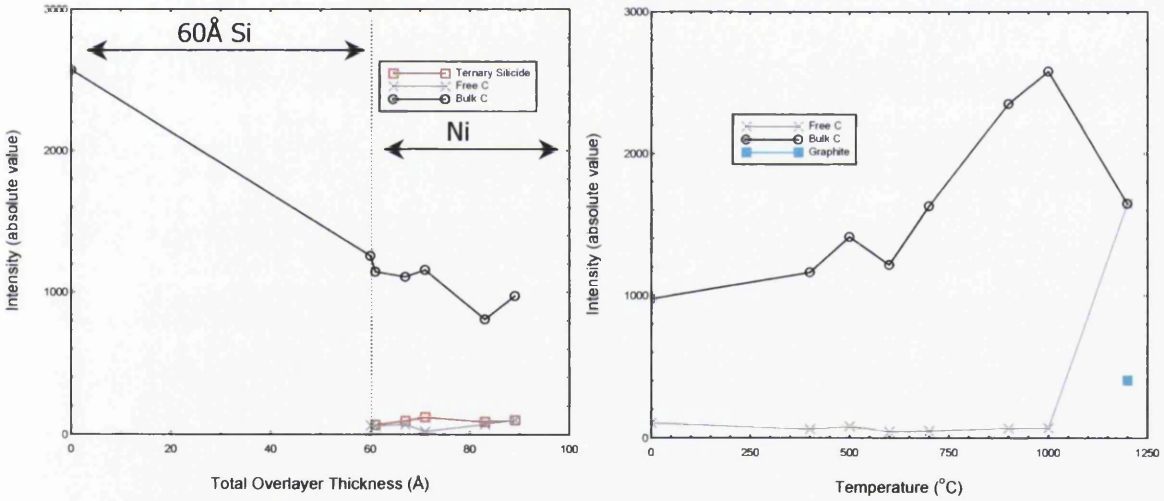

Figure 6.46: Intensity plots of the deconvoluted C components (a) during interface formation (b) at sequential anneals.

The peak position plot of the deconvoluted C components is illustrated in Figure 6.47(a). Clearly, the all C components shows a 0.3eV shifts towards

low binding energy, which indicates a barrier formation, similar to that of the 20Å and 40Å Si interlayer (section 6.4.2 and 6.4.3).

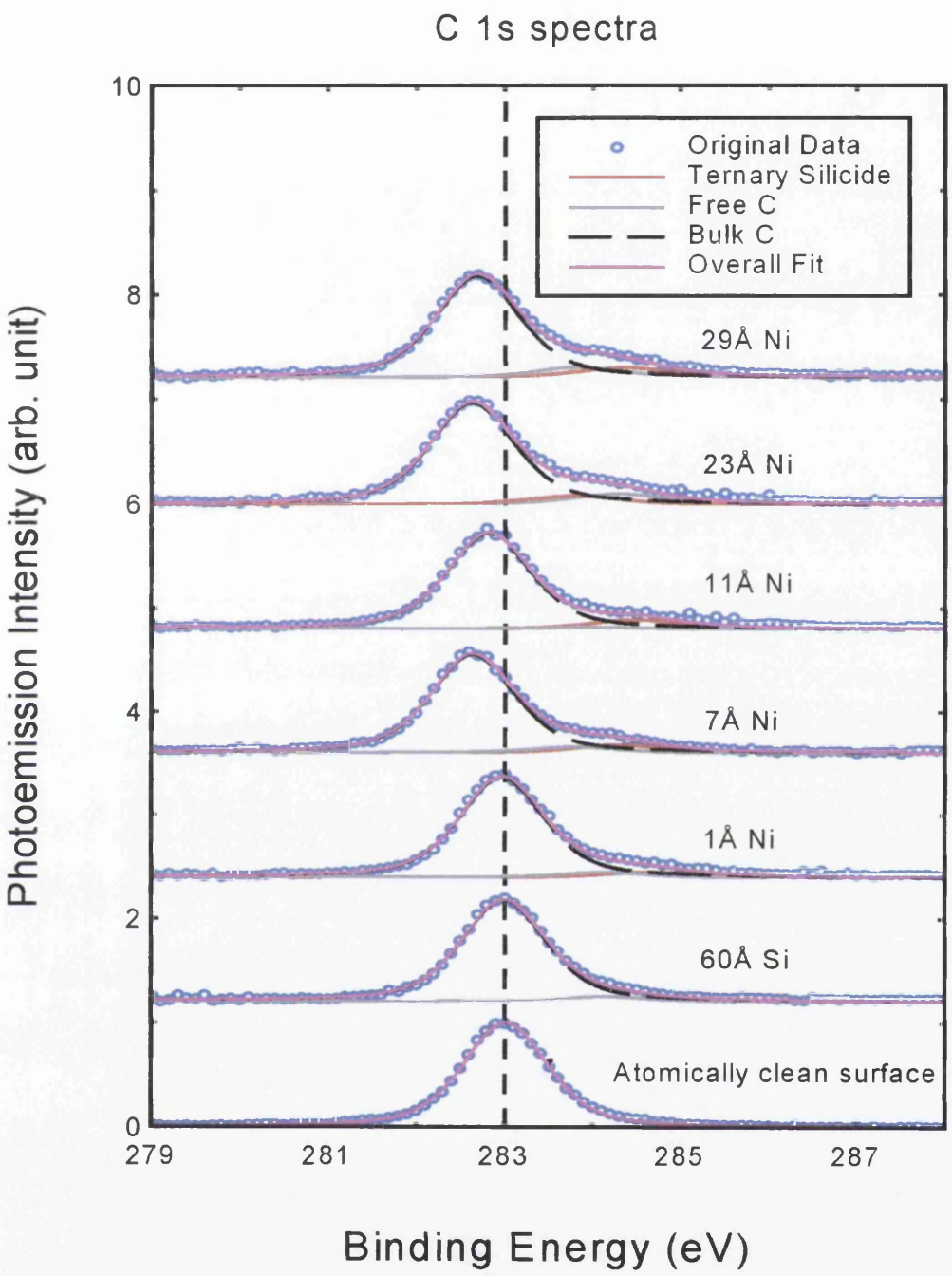

Figure 6.45: Curve fitted *C 1s* core level spectra starting from the atomically clean surface to Si and sequential Ni overlayers deposition. The deconvoluted components including the original raw data are listed in coloured lines as described in the legend.

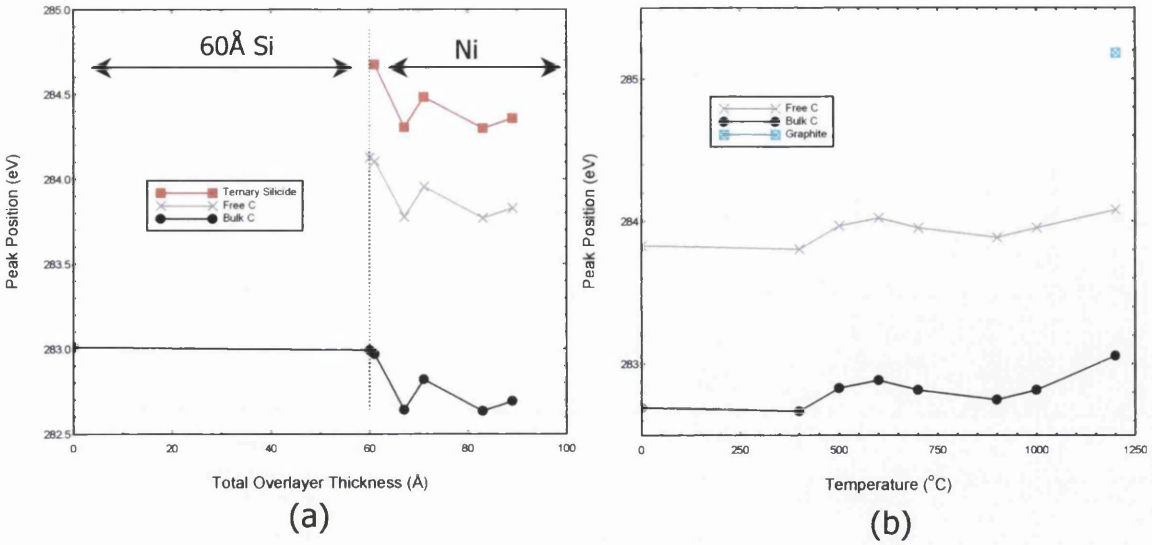

Figure 6.47: Peak position plot of the deconvoluted C components (a) during interface formation (b) at sequential anneals.

When the interface is annealed, the *C 1s* core level spectra behaves in the same way as for the 20Å and 40Å interlayers (section 6.4.2 and 6.4.3). Therefore, the discussion would not be repeated here. However, the final amount of free C formed at 1200°C is clearly seen to be greater than for the two previous case studies. Also, the C peaks position was observed to shift 0.2eV towards high binding energy at low temperature anneal and by 0.3eV at 1200°C. The comparison of all three cases of study investigated (20Å, 40Å and 60Å) will be included at the end of this chapter.

- ***Ni 2p* core level**

Generally, the behaviour of the *Ni 2p* core level is straightforward and has been discussed previously. The stack plot of the *Ni 2p* core level spectra is shown in Figure 6.49. During the interface formation, Ni overlayers with increasing thickness are deposited onto the Si-SiC surface. Hence, the intensity is expected to increase, which is clearly shown in Figure 6.37(b). The core level binding energy also shifted by approximately 0.3eV towards low

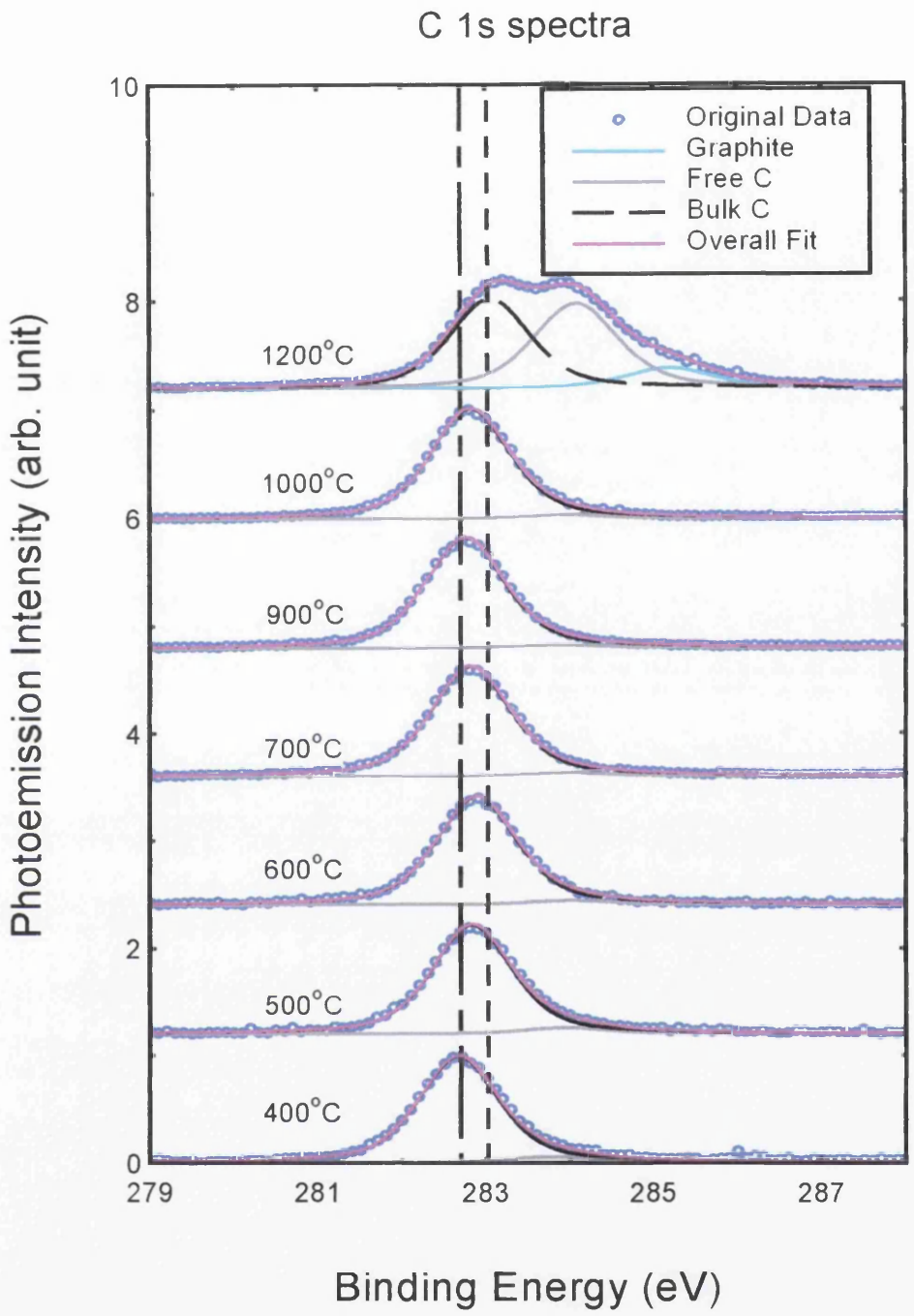

Figure 6.48: Curve fitted *C 1s* core level spectra during sequential anneals starting from temperature of 400°C to 1200°C. The deconvoluted components including the original raw data are listed in coloured lines as described in the legend. The vertical dotted lines indicate peak movement in comparison to 400°C and the original clean surface.

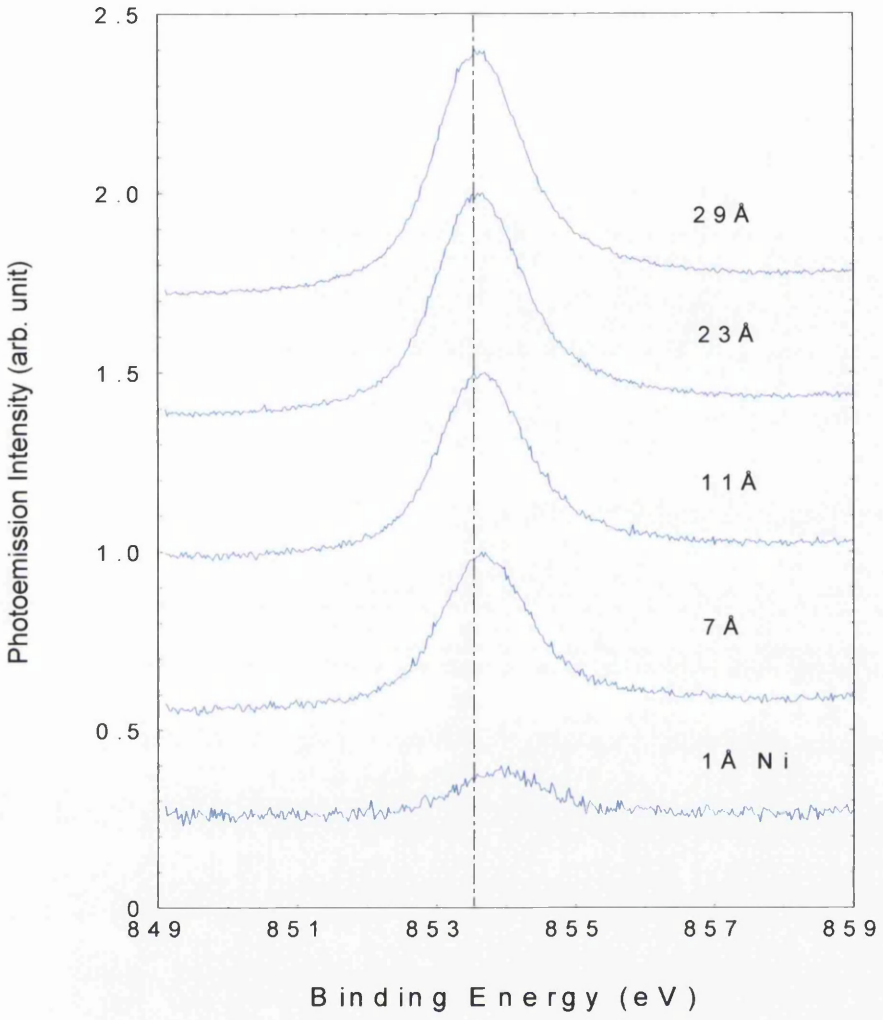

Figure 6.49: *Ni 2p* core level spectra during sequential Ni overlayers deposition.

binding energy, again confirming the formation of a barrier (see Figure 6.38(c)).

Upon annealing, the intensity of the *Ni 2p* peak decreases with increasing annealing temperature as shown in the stack plot in Figure 6.50. As described previously, the Ni is consumed in the formation of silicides, and together the silicides intermix with the Si interlayer and then diffuse towards the bulk, clearly indicated in the intensity plot shown in Figure 6.39(b). At

high temperature, the Ni is being re-evaporated as described in section 6.4.2. However, due to chemical reactions, the peak position is observed to shift in a different way than the bulk components (see Figure 6.40(c)).

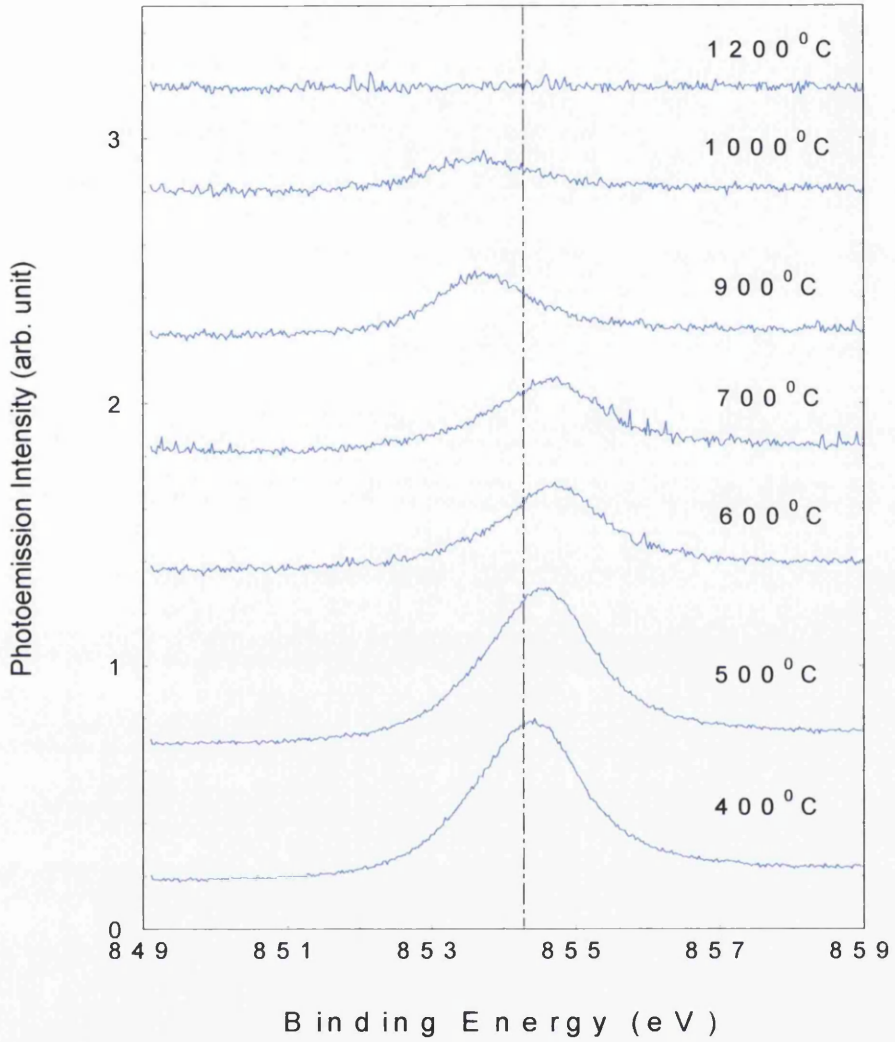

Figure 6.50: *Ni 2p* core level during sequential annealing temperatures.

Discussion

Generally, the experimental observation of the 60Å Si interlayer study again shows similarities to that of the 20Å and 40Å study. Although this is the case, the overall mechanism formation is slightly altered due to the thicker Si interlayer. Firstly, is the formation of Ni silicides. Although the exact species of

the silicides cannot be determined, the consumption of Si atoms in the silicides formation mechanism is assumed to be randomised between bulk Si and the deposited Si interlayer. Here, the rate of decay of the intensity is observed to be the same for both bulk Si and the deposited Si interlayer, as the formed silicides consumes Si and builds up on the surface.

The deposition of 60Å of Si interlayer also results in the formation of free C. However, the ternary phase silicide is observed to form immediately after the deposition of 1Å of Ni. Although this is not the case for the 20Å and 40Å Si interlayer, it is proposed that the formation of the ternary phase silicide requires a minimum amount of Ni or C (as described previously in section 6.4.3). This interpretation can be supported by the fact that for a 60Å Si interlayer, the free C created by the deposition of the Si interlayer onto the clean SiC might be slightly greater than for the two previous cases. The deposited Ni then reacts with this C, to produce enough ternary phase compound to be detected in the *C 1s* spectra (see Figure 6.45). The intensity of this ternary phase is observed to be slightly increased throughout the interface formation. Simultaneously, the free C remains almost constant, and is thought to be located at the intermediate junction between silicide and bulk. Plus, the bulk C behaves in a similar manner to that described in the two previous cases (as described in section 6.4.2 and 6.4.3).

As seen in section 6.4.3, annealing at low temperature results in further formation of Ni silicides. For the 60Å case, the deposited Si interlayer is more likely to be consumed in the formation mechanism, clearly indicated by the intensity plot in Figure 6.42(b). Here, the intensity of the deposited Si interlayer gradually decays to zero while the intensity of the bulk Si increases. Again, interdiffusion is expected to have occurred as described previously. Concurrently, the amount of Ni silicide is seen to increase rapidly. At 1200°C, the silicide intensity decreases, which corresponds to re-evaporation as discussed in section 6.4.2.

The reaction on the *C 1s* core level in this case is exactly the same as described in section 6.4.2, hence will not be repeated here. However, a point of interest is that at the very high temperature of 1200°C, the amount of free C and graphite formed at the surface is much greater than both previous cases. The comparison of the free C and graphite formation at such temperature will be presented later in the next section.

Electrically, the 60Å Si case has shown a similar behaviour to that of the 20Å and 40Å case. During the interface formation, an upward band bending was observed for *Si 2p* and *C 1s* core level, indicated by the peak position shifts towards low binding energy. When annealed, the peak shifts back to higher binding energy. However, it is important to note that these peak shifts may consists of both Fermi and chemical shifts due to the chemical reactions at the interface. The differences between the binding energy shifts between the core levels have already been discussed previously and will be compared in the next section.

6.5 Comparisons and Conclusion

So far, the results obtained has proven the efficiency of the Si interlayer in preventing free C formation at the contact layer even at temperatures up to 1000°C. Generally, the overall results for the three Ni-Si-SiC contacts have shown some common behaviours independent of the Si interlayer thickness as listed below.

1. The deposition of Si interlayer onto the atomically clean surface results in formation of a small amount of free C.
2. The deposition of Ni overlayers onto the Si-SiC interface results in the formation of Ni silicides, a ternary phase silicide and a slight increase in free C formation.
3. Fermi shifts towards low binding energy, which corresponds to the formation of a Schottky barrier are observed.

4. Further formation of Ni silicides at low temperature anneal, which simultaneously consumes Si atoms from either the bulk or the Si interlayer. In addition, at this stage, the ternary phase silicide disappears indicating intermixing between silicides or the interdiffusion of the silicides towards the bulk.
5. The formation of graphite and large amount of free C at temperature above 1000°C.
6. Barrier lowering with increasing annealing temperature, indicated by core level shifts towards high binding energy indication of ohmic behaviour of the Ni-Si-SiC contacts (see chapter 7).

Although the points listed above are common to the three Ni-Si-SiC contacts, the thickness of the Si interlayer is observed to influence the result of these reactions. In order to gain more understanding, these reactions associated with different thickness of Si interlayer are grouped into three main categories (free C formation, silicide formation and barrier formation). However, the main interest in this study is the behaviour of the contacts at elevated temperature. Hence, the comparison concentrates only on annealing conditions.

6.5.1 Free Carbon Formation

From Figure 6.51, it is clearly seen that the contact without a Si interlayer (Ni-SiC) is the worst, with the most free C formed between the contact layers. The 60Å interlayer is the second best with the 40Å interlayer resulting in the most free C of the three Ni-Si-SiC contacts, but it still much better than the contact without a Si interlayer. The 20Å Si interlayer composition is best among the four contacts investigated, displaying the least free C at the interface. Therefore, with presence of a Si interlayer, the amount of free C at the interface is greatly reduced, confirming the effectiveness of interlayer.

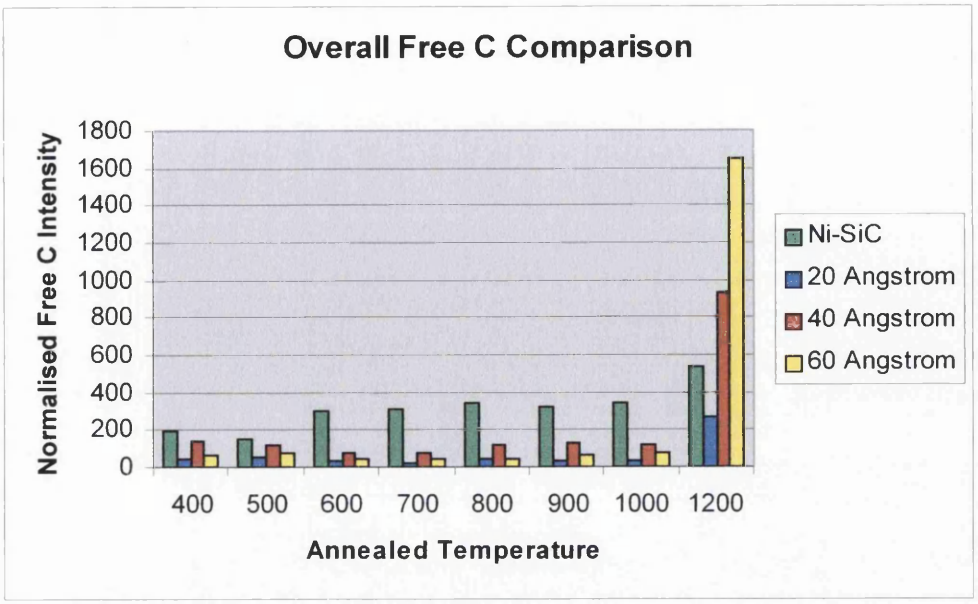

Figure 6.51: Comparison of free C formation at the contact layer for Ni-SiC and Ni - Si (20Å, 40Å, 60Å) –SiC composition under annealing conditions.

6.5.2 Silicide Formation

The C content at elevated temperature for all the experiments has been compared previously in section 6.5.1. However, the amount of silicides formed at the interface and the consumption behaviour of Si atoms from the bulk and Si interlayer are also points of interest in order to investigate the role of the Si interlayer in the Ni-SiC. Therefore, for the Si interlayer case studies (20Å, 40Å and 60Å), the silicides conditions at the interface under annealing conditions are compared in Figure 6.52.

From Figure 6.52, it can be clearly seen that the maximum amount of silicides occurs for the 40Å, Si interlayer, followed by 60Å and finally 20Å. The explanation for such behaviour is that the 20Å Si interlayer is not thick enough to provide enough Si atoms for silicide formation since the amount of Ni is greater than Si (30Å Ni > 20Å Si). With a limited source of Si atoms, the formation mechanism is limited even at low temperature anneals. For the case of 40Å where most silicides are formed, the possible reason is that there

is an adequate amount of Si atoms (as the amount of Si is more or less equal to that of Ni (30Å Ni: 40Å Si)) available for silicides formation. Therefore, the Si interlayer is fully utilised for silicides formation. Finally for the case of 60Å, the amount of Si is greater than Ni. In this case, there are not enough Ni atoms available for silicides formation. This again shows the importance of the Si interlayer thickness to the final contact.

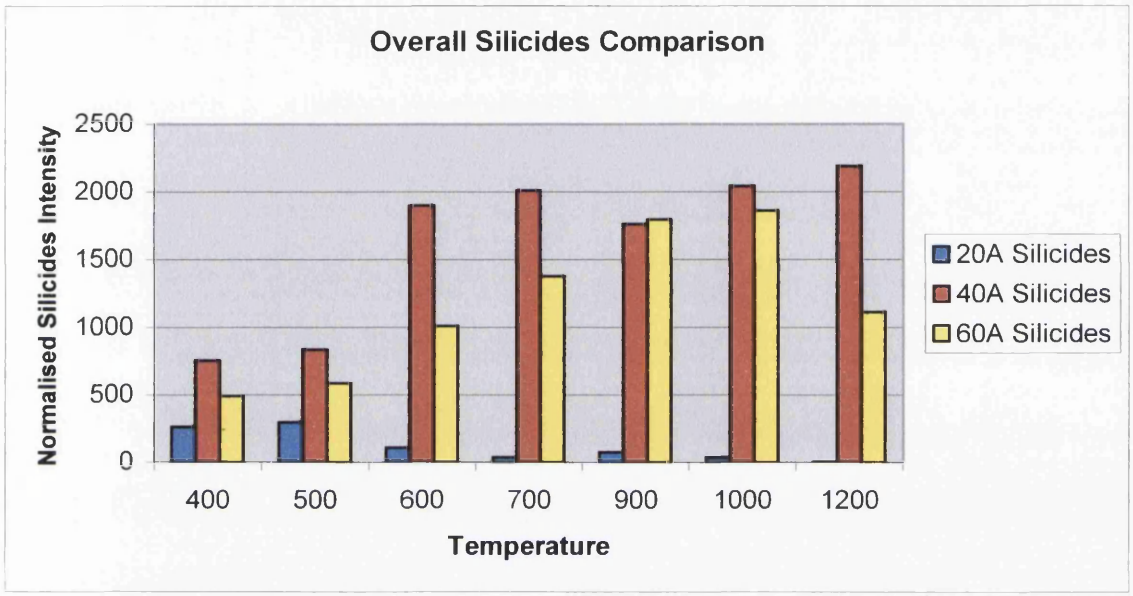

Figure 6.52: Comparison of silicides formation at annealing temperature for Ni-Si-SiC composition with 20Å, 40Å and 60Å Si interlayer.

6.5.3 Barrier Formation

Figure 6.53 (a) and (b) shows the overall core level shifts of the *Si 2p* and *C 1s* spectra during interface formation and sequential annealing stages. Note that for Figure 6.53(a), the overall peak shifts is taken with reference to the initial peak position of the clean surface to the peak position of the final deposition. For interface formation at room temperature, the 20Å case displayed an identical behaviour to that of the Ni-SiC interface, with a 0.5eV shift towards low binding energy, forming a Schottky barrier (as discussed previously in section 6.3 and 6.4.1). For the case of 40Å and 60Å, the core

level shift between the *Si 2p* and *C 1s* spectra is slightly different, which could be associated with difference in chemical environments (as discussed previously). However, for both cases, the overall shifts are the same with 0.2eV for *Si 2p* and 0.3eV for *C 1s* spectra. In general, the interface with a thin Si interlayer exhibits a higher barrier formation. However, the definite electrical properties cannot yet be concluded and will be further discussed in Chapter 7.

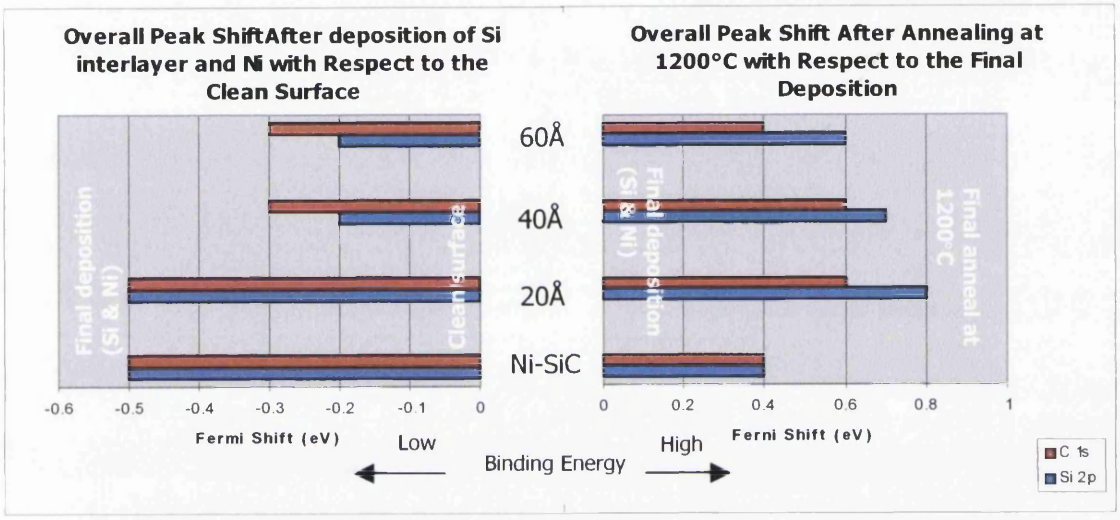

(a) (b)

Figure 6.53: Core level shifts of Ni-SiC and Ni-Si-SiC (with 20Å, 40Å, 60Å) contact (a) after final deposition of Si interlayer and 29Å of Ni (b) after annealing at 1200°C.

For Figure 6.53(b), the overall peak shifts is taken with reference to the peak position at the final deposition to the peak position of the last sequence of anneal at 1200°C. When annealed, it can be clearly seen that the Ni-SiC shifts the least towards high binding energy (i.e. barrier lowering, towards ohmic behaviour). The sequence is followed by the 60Å, 40Å and finally the 20Å interface (see Figure 6.53(b)). Again, we could see that there is a difference in core level shifts between *Si 2p* and *C 1s* spectra for all cases

with a Si interlayer, which indicates chemical reactions between the Si interlayer and Ni. However, it is important to note that the interface study is conducted with a very thin layer of Ni; hence the metallic behaviour is at its minimum. Although we have now observed a general trend of barrier lowering in these interfaces, it is important to fully evaluate their electrical properties as a function of the thickness of the Si interlayer. Therefore, it is essential to fabricate these structures into simple Schottky diodes and measure their current-voltage characteristics. The results of the current-voltage study performance will be discussed in the next chapter.

6.6 References

[1] J. R. Waldrop and R.W. Grant, Appl. Phys. Lett., **62**, 2685 (1993).

[2] M. I. Chaudhzy, W. B. Bezky and M. V. Zeller, Int. J. Electronics, **71**, 439 (1991).

[3] L. M. Porter and R. F. Davis, Mat. Sci. Eng., **B34**, 83-105 (1995).

[4] J. Crofton, L. M. Porter, J. R. Williams, Phys. Status Solidi, **202B**, 581-603 (1997).

[5] J. S. Park, K. Landry and J. H. Perepezko, Mat. Sci. and Eng., **A259**, 279-286 (1999).

[6] Ts. Marinova, V. Krastev, C. Hallin, R. Yakimova, E. Janzen, Appl. Surf. Sci., **99**, 119-125 (1996)

[7] Ts. Marinova, V. Krastev, C. Hallin, R. Yakimova, E. Janzen, Mat. Sci. Forum, **Vol. 207-209**, 293-296 (1996).

[8] Y. Hoshino, T. Nisimura, Y. Taki, Y. Asami, K. Sumimoto and Y. Kido, Surf. Sci. **511**, 112-120 (2002).

[9] M. P. Seah and W. A. Dench, 'Surface and Interface Analysis, Vol 1-Auger and X-ray Photoelectron Spectroscopy', Edition 2 (1990).

[10] A. Kakanakova-Georgieva, Ts. Marinova, O. Noblanc, C. Arnodo, S. Cassette, C. Brylinski, Thin Solid Films, **343-344**, 637-341 (1999).

[11] J. Acker, K. Bohmhammel, Thermochimica Acta, **337**, 187-193 (1999).

[12] B. Bokhonov, M. Korchagin, Journal of Alloys and Compounds, **319**, 187-195 (2001).

[13] B. A. Julies, D. Knoesen, R. Pretorius, D. Adams, Thin Solid Films, **347**, 201-207 (1999).

[14] E. H. Rhoderick and R. H. Williams, 'Metal- Semiconductor Contacts', Oxford University Press, (1988).

[15] L. N. Pauling, 'The nature of the chemical bond', 2nd edition, Cornell University Press, Ithaca, New York (1960).

[16] K. Bhanumurthy and R. Schmid-Fetzer, Composites, Part **A32**, 569-574 (2001).

[17] R. C. Jaeger,' Introduction to Microelectronic Fabrication', Addison Wesley, 1998.

[18] W. Y. Lee, K. S. Teng and S. P. Wilks, 'In-situ investigation of carbon reduction in 4H-SiC/Ni interface implementing Si interlayer', International Conference on Silicon Carbide and Related Material 2003 Proceedings, Trans Tech Publications Ltd.

[19] Ts. Marinova, A. Kakanakova-Georgieva, V. Krastev, R. Kakanakov, M. Neshev, L. Kassamakova, O. Noblanc, C. Arnodo, S. Cassette, C. Brylinski, B. Pecz, G. Radnoczi, Gy. Vincze, Mat. Sci. and Eng., **B46**, 223-226 (1997).

Chapter 7

Current – Voltage Characteristic of Ni-Si-SiC Contacts

7.1 Introduction

So far, the interface study discussed previously in Chapter 6 has demonstrated the effectiveness of the Si interlayer in carbon reduction at the metal-SiC surface at elevated temperature. However, it is important to notice that all the experiments conducted in Chapter 6 only consist of a thin metal layer (30Å of Ni). Thus, the overall metal contact may not be fully formed, as the metallic behaviour only arises when the metal coverage is thick enough. In addition, the performance of the Ni-Si-SiC contacts with various Si thicknesses (for our case 20Å, 40Å and 60Å) has to be gauged in terms of real device fabrication. In this chapter, the current-voltage (I-V) characteristic of Ni-Si-SiC diodes with three different Si interlayer thicknesses are measured and compared to each other. This process is repeated for all the annealing steps investigated in the XPS study. The results obtained from these diodes are presented below.

7.2 Experimental Procedures

The initial preparation of the 4H-SiC wafers is similar to that used in the interface study experiment, which is based on surface cleaning via the Si evaporation/re-evaporation technique, which has been discussed in Chapter 5. However, before admitting the sample into the UHV system for further cleaning purpose, a thick coverage of Ni was evaporated using an Edwards evaporator (see section 4.3.2) onto the backside of the sample to act as an Ohmic contact. As the UHV clean (see section 5.2.3) involves annealing cycles at temperatures up to 850°C, the back contact was annealed simultaneously, which neatly forms an Ohmic contact without additional annealing procedure. Next, the sample underwent the Si evaporation/re-evaporation cleaning process to produce an atomically clean surface. Subsequently, the desired thickness of Si interlayer (20Å, 40Å and 60Å) was evaporated onto the clean surface followed by the evaporation of the top Ni contact with thickness of approximately 3000Å via UHV e-beam evaporation sources (see section 4.3.1).

Subsequent to evaporation of all necessary materials for the contact formation, the sample was transferred to the clean room for device processing. Here, the sample was patterned into 650μm dots via a photolithography process described in section 4.4. The structures of the fabricated 650μm diodes are shown in Figure 4.7. The I-V measurement procedures are also described in section 4.5 and will not be repeated here. The sample was annealed sequentially starting from a temperature of 400°C to 1000°C for 10 minutes in the Edwards chamber under high vacuum conditions. At each stage, the diodes are measured using the I-V kit under dark conditions. The parameters ϕ_b and n are extracted from the I-V characteristic curve obtained based on the thermionic emission theory discussed in section 2.8.1.1 and the extraction procedure in section 2.9.1. Since each sample could be processed into 30-35 diodes, the best diode was chosen in each case. The results obtained for all three cases (20Å, 40Å and

60Å) are presented below. Note that the study on diode without Si interlayer had been conducted previously by a colleague [7], hence would not be repeated here. However, the comparison and discussion between diodes with and without Si interlayer will be included at the end of this chapter.

7.3 I-V Results

Figure 7.1 (a) to (g) show plots of the natural log of current density (Ln J) versus bias voltage (V) for the Ni-Si-SiC (Si interlayer thickness of 20Å, 40Å and 60Å) diodes at sequential annealing stages. For ease of discussion, the results of these diodes are presented in an increasing order of annealed temperature. The comparison for these diodes with the diode without a Si interlayer will be presented at the end of this chapter.

- **400°C**

At low temperature anneal, the 20Å and 40Å contacts exhibit a Schottky characteristic with a ϕ_b value of 1.31eV and 1.25eV respectively. Correspondingly, the ideality factor, *n*, for the diodes was approximately 1.6 and 2.5. The 'double bump' feature (see section 2.9.1) associated with the recombination effect is clearly observed for both contacts. The high *n* value for the 40Å contact is due to a strong recombination feature on the forward characteristic, which has a great influence to the linear region of the forward characteristic, giving a low value of slope, *m*. This incident also indicates that the 40Å contact does not obey the thermionic emission theory at this stage. Generally, at low temperature anneal, one would expect such behaviour as a result of surface reconstruction as observed in our interface study as discussed in Chapter 6. From the interface study results, surface reconstruction results in rapid silicide formation, usually more than one silicide species (although we only observed a single silicide peak within the *Si 2p* spectra as these silicides peaks are located very close to each other in terms of binding energy, hence cannot be distinguished).

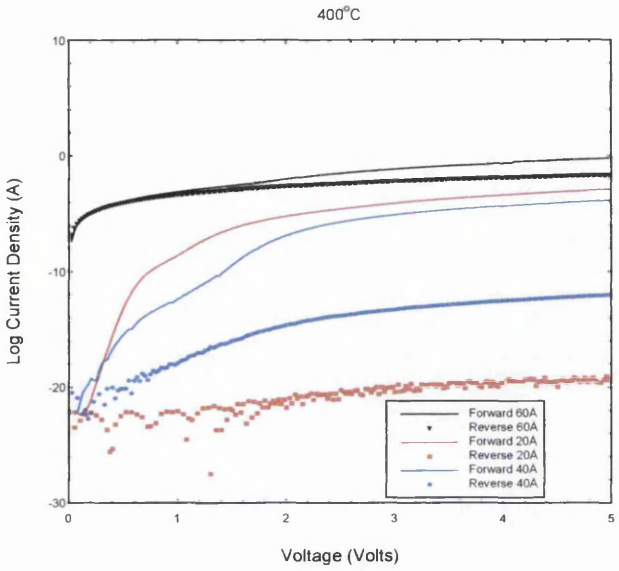
400°C
Log Current Density (A)
Voltage (Volts)
Forward 60A
Reverse 60A
Forward 20A
Reverse 20A
Forward 40A
Reverse 40A

(a)

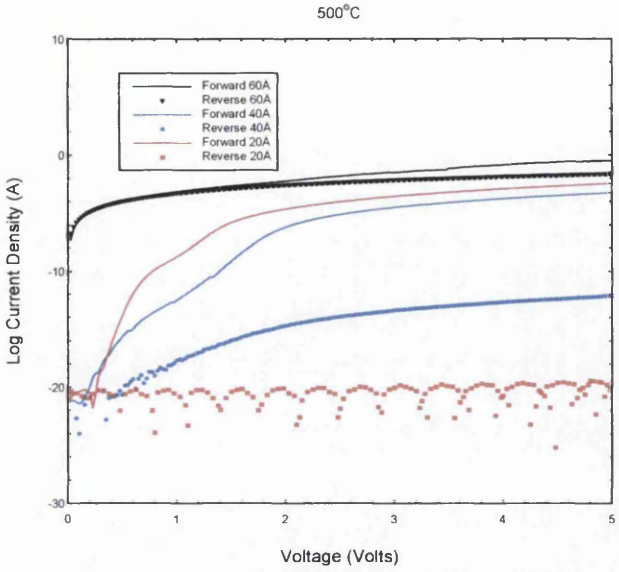
500°C
Log Current Density (A)
Voltage (Volts)
Forward 60A
Reverse 60A
Forward 40A
Reverse 40A
Forward 20A
Reverse 20A

(b)

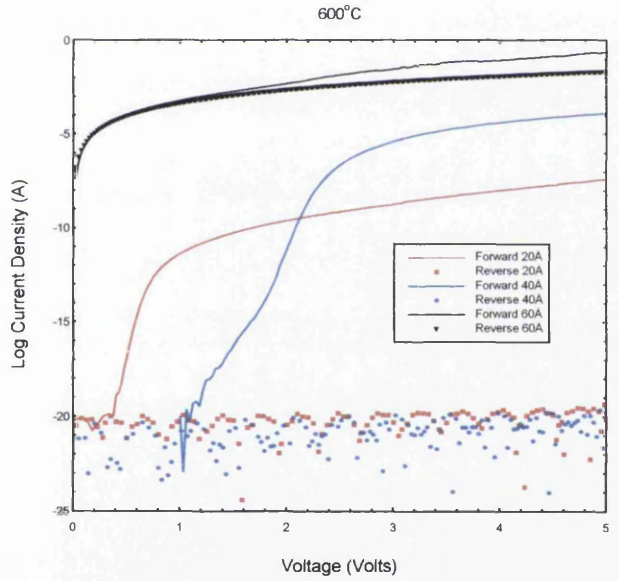
600°C
Log Current Density (A)
Voltage (Volts)
Forward 20A
Reverse 20A
Forward 40A
Reverse 40A
Forward 60A
Reverse 60A

(c)

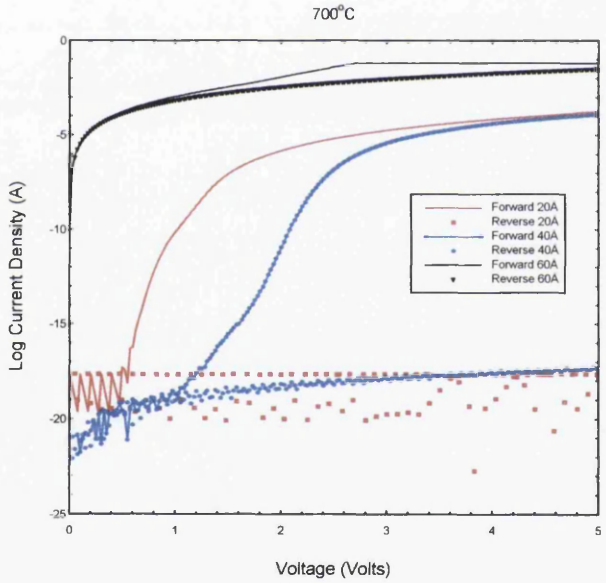
700°C
Log Current Density (A)
Voltage (Volts)
Forward 20A
Reverse 20A
Forward 40A
Reverse 40A
Forward 60A
Reverse 60A

(d)

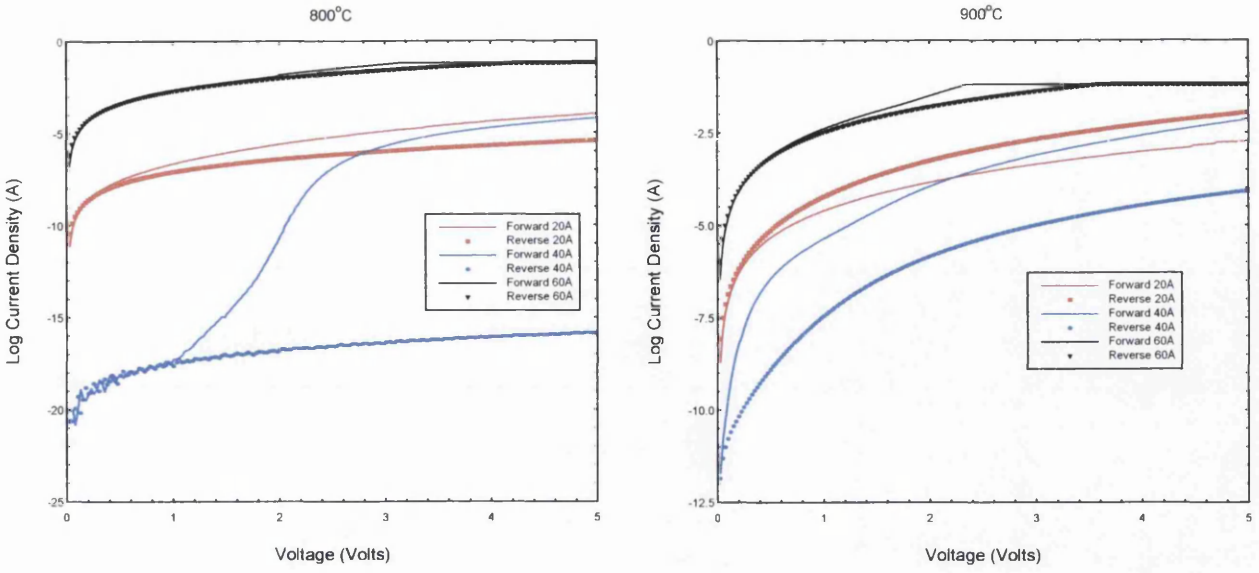

(e)

(f)

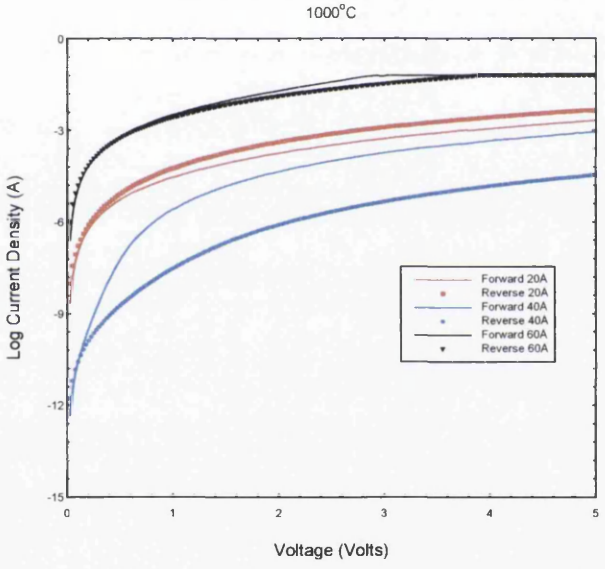

(g)

Figure 7.1: I-V results, log current density versus applied voltage plot for all three cases; 20Å, 40Å and 60Å Ni-Si-SiC contacts at annealed temperatures. (a) 400°C (b) 500°C (c) 600°C (d) 700°C (e) 800°C (f) 900°C (g) 1000°C. The forward and reverse characteristics are as described in legend.

In addition, the contact may also experience in surface relaxation. Therefore, the reactions within contact are dominated by surface reconstruction or re-ordering, hence the contact is not fully ready for current conduction. Although this is the case for 20Å and 40Å contacts, the 60Å contacts exhibit a drastically different behaviour. Even at low temperature, the contacts exhibit an Ohmic behaviour. The possible reason for that is the amount of silicides formed at the Ni-SiC junction. As seen in section 6.4.4, the amount of Ni atoms was not adequate for silicide formation; hence it was proposed to be a Si-rich silicide. Now, the Ni coverage is far thicker than for the interface study experiment. Thus, we would expect a lot of silicide at the Ni-SiC junction as a result of a resourceful Ni and Si environment. The formation of Ni-silicides has been proposed to play a critical role in forming Ohmic contact in SiC [1, 2]. Also, it is well known that Ni-silicides are a low-resistivity compound [3, 4], which explains the Ohmic behaviour of the 60Å contact.

- **500°C**

At 500°C, all contacts exhibit a similar behaviour to that observed at 400°C. The values of ϕ_b and n for the 20Å and 40Å contacts are also similar with values of ϕ_b of 1.32eV and 1.24eV and n of 1.6 and 2.9 respectively. The 60Å contacts remain unchanged, exhibiting an Ohmic characteristic.

- **600°C**

At this temperature, the most prevailing observation is the Schottky or rectifying behaviour for the 20Å and 40Å contacts. The forward characteristic of the contacts clearly shows a linear region, which corresponds to thermionic emission current. The linear region is curve fitted obtaining the value n, of 1.5 and 2.5 respectively and ϕ_b of 1.43eV and 1.72eV respectively. Again, the 40Å contact is observed to have a poor ideality factor but a high value of ϕ_b. This indicident can be explained by the remaining existence of the recombination current (although it had fully disappeared for the 20Å contact). Thus, the

current for the 40Å contact does not follow entirely thermionic emission theory. The reason for such behaviour can be possibly explained by the huge amount of silicides at the Ni-SiC junction, which is proposed to be more than one single species, although only a single silicide peak is observed due to small binding energy difference between these different silicide peaks (see *Si 2p* core level spectra in Figure 6.44). As discussed previously in section 6.5.2, the amount of silicides at the Ni-SiC junction for the case of 40Å contact is far greater than the 20Å contact. The recombination current is mostly associated with an interfacial layer between contacts. Hence, with a greater amount of silicides sandwiched between the contacts, recombination current is expected. For the case of 60Å contact, the Ohmic behaviour still persists without any change.

- **700°C**

The 20Å contact shows maximum performance at this temperature. Clearly seen from the forward characteristic, the 20Å contact exhibits a high forward current density with ϕ_b of 1.7eV and n of 1.71. Meanwhile, the 40Å contact I-V curve still consists of the recombination current, hence the linear region is again hidden by this recombination effect giving a high n value of 3.2 and ϕ_b of 1.56eV. Simultaneously, the 60Å contact remains unaltered, exhibiting an Ohmic behaviour.

- **800°C**

Despite having a good Schottky forward characteristic at 700°C, the 20Å contact has turned into an Ohmic contact at 800°C. However, the 40Å contact still exhibits a rectifying behaviour. The recombination current still persists, clearly seen on the forward characteristic. The ϕ_b is observed to be 1.5eV with n of 3.5. The 60Å contact remains unchanged.

- **900°C and 1000°C**

At these temperatures, all contacts have changed into Ohmic contact (see Figure 7.1 (f) and (g)). This reaction is expected as high temperature anneals usually results in Ohmic behaviour for all metal-semiconductor contacts [3]. The overall comparison and discussion for the performance of these contacts will be presented in the next section.

7.4 Discussions and Comparison

Until now, we have seen the gradual change of the 20Å and 40Å contacts from an initial rectifying to an Ohmic behaviour towards increasing annealing temperature. However, we have also seen that the 60Å contact exhibits an Ohmic behaviour throughout the annealing process. These behaviours are mostly associated with the thickness of the Si interlayer and its reaction product present at the Ni-SiC junction. As seen in Chapter 6, the reaction products of the Ni-Si-SiC interface were Ni silicides, ternary compound silicides and small amount of free C trapped between the Ni-SiC junctions. When annealed, the reactions products of silicides, proposed to be more than one species as a result of silicide enhancement at low temperature (although only a single peak is observed within the *Si 2p* spectra due to small energy separation between these silicide peaks) and a small amount of free C. We have also seen that the amount of silicides formed depends on the amount of Si and Ni atoms available. Although the 40Å case generates the most silicide (see section 6.5.2), one needs to be reminded that the interface study experiment were performed using only ~ 30Å of Ni. Hence, the Ni environment in the contact experiments is much richer than the interface experiments. Thus, with the thickest interlayer it is expected that the 60Å case form the most silicide. Therefore, the order of silicides formation would then be 60Å, 40Å and the least with the 20Å case.

Now, we have understood the silicide formation mechanism. The correlation between the contact behaviour and the amount of silicides formed

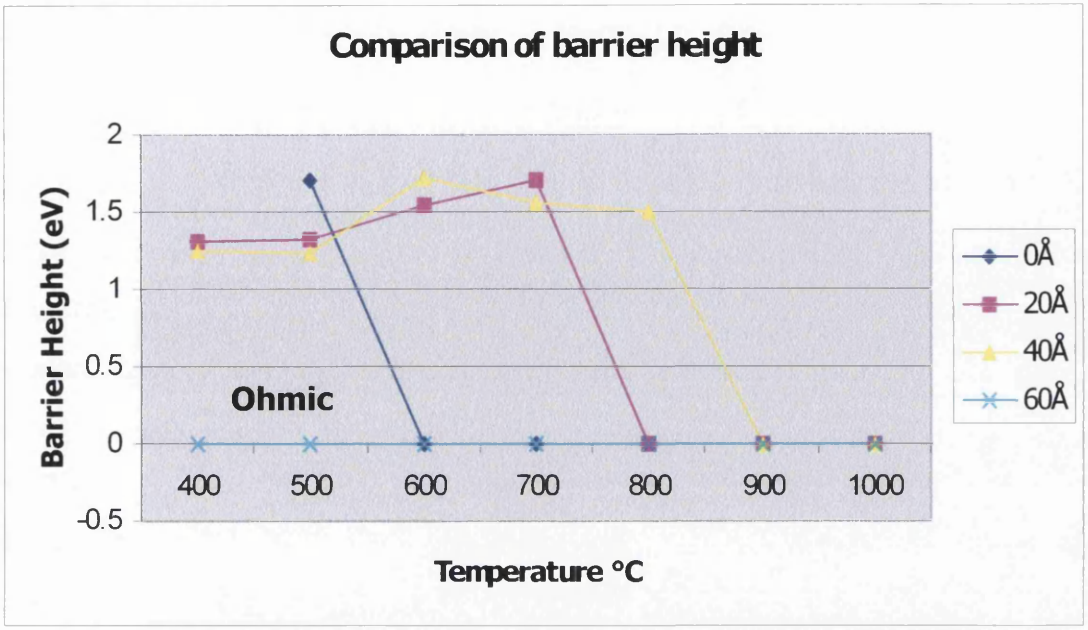

Figure 7.2: Comparison of barrier height, ϕ_b, of the Ni-SiC [7] and Ni-Si-SiC contacts at sequential annealed temperatures.

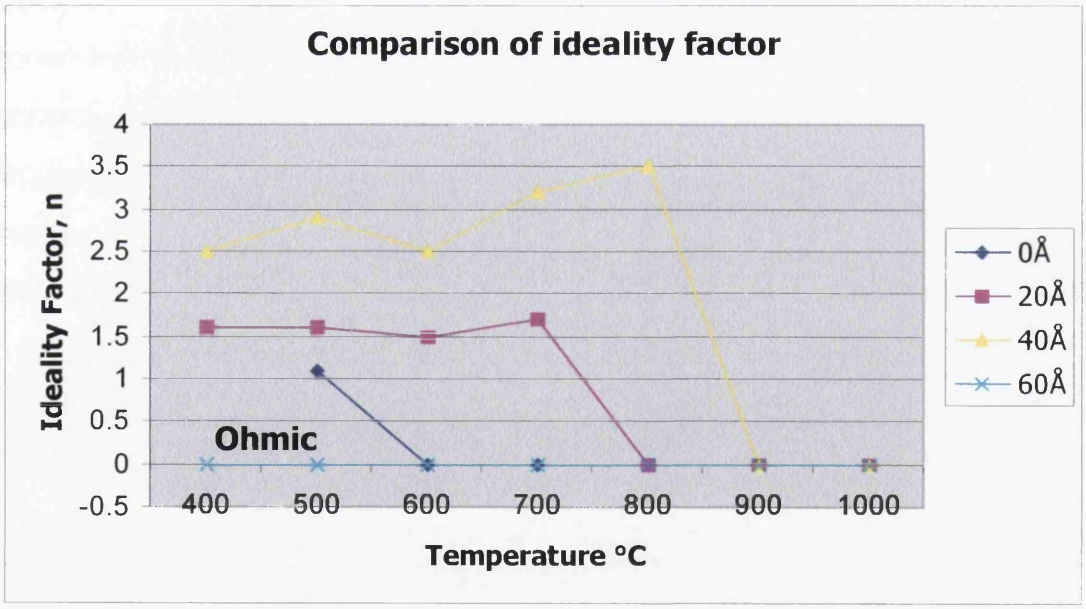

Figure 7.3: Comparison of ideality factor, *n*, of the Ni-SiC [7] and Ni-Si-SiC contacts at sequential annealed temperatures.

neatly explains the results observed. The comparison of barrier height and ideality factor of the contacts (with and without Si interlayer) is illustrated in Figure 7.2 and 7.3. First, let us consider the barrier height. Indicated by the blue line for Ni-SiC contact and pink line for the 20Å contact, a higher ϕ_b is exhibited compared to the 40Å contact (yellow line). This is in agreement with the results obtained from Chapter 6 (see section 6.5.3 and Figure 6.5.3(a)), which the shows that the Ni-SiC and 20Å interface had the largest Fermi shift, followed by the 40Å and the 60Å case. Note that the values of the barrier formed measured using XPS and I-V measurements cannot be compared directly as the initial barrier measured using XPS is unknown. However, the Fermi shift of the core levels spectra (*Si 2p*, *C 1s* and *Ni 2p*) can neatly confirms a barrier formation within the contact. The explanation for a higher ϕ_b for the Ni-SiC 20Å contacts can be clearly demonstrated in the forward characteristic of the contacts. At low temperature, recombination currents is clearly seen for both 20Å and 40Å contacts. At higher temperature, the recombination current disappears for the 20Å contact but remained throughout the annealing process for the 40Å contact. Here, the recombination current is possibly caused by an interfacial layer between the contacts [5]. In addition, low temperature anneals usually result in further silicides formation, as shown by the interface study results discussed previously in Chapter 6 [6]. From interface study (Chapter 6), the 20Å case had the least silicide formed at the interface and also consists of the least free C (see section 6.5.1). Also, the 40Å contact reacted at low temperature anneal giving even more silicides and also consist of free C greater than the 20Å contact, hence, the recombination feature remains, and also dominates throughout the annealing study. Meanwhile, it is observed that there is no recombination current for the Ni-SiC [7]. Therefore, the Ni-SiC contact and 20Å contact exhibits a better barrier formation, with a higher ϕ_b than the 40Å contact. For the case of 60Å contact, the amount of silicides formed is great enough that the contact had turned into a conducting or Ohmic contact even

at low temperature anneal and remain unaltered up to a temperature of 1000°C. At higher temperature where interdiffusion, re-evaporation of silicides and C segregation to the surface occurs, the contact exhibits a rectifying or Ohmic behaviour. This result is in agreement with the interface study for all three contacts (Ni-SiC, 20Å and 40Å), indicated by the shift of the core level spectra towards high binding energy, which corresponds to downward band bending (see Chapter 6). Nevertheless, the ' Schottky to Ohmic breakdown point' is among the point of interest in this study. Here, the contact without Si interlayer changes into an Ohmic at temperature above 500°C. Meanwhile, the 20Å contact changed into Ohmic behaviour 300°C later (i.e. at 800°C) and the 40Å contact turns Ohmic 400°C later (i.e. 900°C) than the Ni-SiC contact. This could be explained by amount of silicides that is still present within the contact at temperature range of 600°C to 900°C. Without the presence of a Si interlayer, the Ni-SiC contact had the least silicide, due to a limited formation of silicide, as there are only partial source of Si atoms from the bulk SiC. This is followed by 20Å contact and finally the 40Å contact (see Figure 6.52). With the interdiffusion and re-evaporation of silicides taking place at these temperatures, the quickest contact to be 'silicide-depleted' would then be the Ni-SiC, followed by 20Å and finally the 40Å contact. As the silicide disappears from the contact, the rectifying properties of contact are gradually turns into a conducting behaviour. This is in agreement with the XPS results obtained from the interface study, where further peak shifts towards high binding is observed for temperature of 800°C to 1000°C. Up to very high temperature (above 1000°C) almost all silicides had been re-evaporated, leaving huge amount of free C and graphite at the surface as observed with the XPS results (see Chapter 6 for *C 1s* core level spectra) [6]. The overall comparison of core level peak shifts during anneals is shown in Figure 6.53(b). Here, the total peak shifts observed from the final deposition to the final annealing step at 1200°C is 0.8eV (20Å) and 0.65eV (40Å) for *Si 2p* core level and 0.6eV for *C 1s* core level for both 20Å and 40Å interfaces. Meanwhile, from Figure 7.2,

the overall peak shifts taken from the lowest annealing step at 400°C to the final annealing step at 1200°C is ≈ 0.4eV for both 20Å and 40Å contacts. Note that the peak shifts observed from the XPS data consists of Fermi shifts and chemical shifts superimposed together. Therefore, taking into account of these chemical shifts, the peak shifts observed from the XPS data and the barrier height variations from the I-V characteristics for both 20Å and 40Å contacts are in agreement with the results observed.

Now, considering for the case of ideality factor, the Ni-SiC contact shows the best of all contact with n of 1.1. The 20Å contact shows a better n (1.5) than the 40Å contact (2.5). Theoretically, n is equal to unity if the contact is purely conducted by thermionic emission theory (see chapter 2). As we seen from the I-V characteristic, only the 20Å contact had displayed a proper linear region as a result of thermionic emission. On the other hand, the 40Å contact exhibits a more recombination current dominated curve, hence results in poor ideality factor as the linear region is hidden by the recombination current at low bias. Obviously for the 60Å case, the ideality factor cannot be determined due to the non-linear characteristic of the Log J-V curve.

In addition, it is important to note that all contacts are fabricated on an atomically clean surface. Hence, we assume that the diodes formed are in the form of intimate contacts. Even so, one could not simply neglect the other effects such as surface states, MIGS (metal-induced gap states), chemical reactivity and surface defects as discussed in section 2.3. However, in order to take into account of these effects, further studies involving complex calculations need to be carried out. This is however beyond the scope of this work and hence will not be included.

7.5 Conclusion

The presence of a Si interlayer at the Ni-SiC interface, apart from reducing the amount of free C at the interface, but also greatly influence the

properties of the contacts at high temperature [6]. These properties include the temperature of operation and the behaviour of the contact at room and elevated temperature. For example, an earlier work by a colleague shows that conventional Ni-SiC contact without Si interlayer would exhibit Schottky behaviour at temperature below 500°C with a ϕ_b of 1.7 and n of 1.1 [7]. Although the Ni-SiC contact produces a pure thermionic emission current, with a excellent ideality factor, at temperature above 500°C, the Ni-SiC turns into an Ohmic contact [7, 8]. But with the presence of Si interlayer, the contact is able to operate in a rectifying mode (with the same ϕ_b of 1.7) at higher temperature and this can be controlled via the Si interlayer thickness as discussed previously. In addition, the presence of a thick Si interlayer can effectively change the contact into an Ohmic contact without any annealing. Hence, by optimising a tailor-made central theme implementing a Si interlayer, the Ni-SiC contact properties can be controlled.

7.6 References

[1] J. Crofton, L. M. Porter and J. R. Williams, Phys. Stat. Solidi, **B202**, 581 (1997).

[2] J. Crofton, P. G. M. Mullin, J. R. Williams and M. J. Bozack, J. Appl. Phys., **77**, 1317 (1995).

[3] E.G. Colgan, J. P. Gambino and B. Cunningham, Mat. Chem. and Phys., **46**, 209-214 (1996).

[4] K. N. Tu, J. W. Mayer and L. C. Feldman, 'Electronic Thin Film Science for Electrical Engineers and Materials Scientists', Macmillan Publishing Company, (1992).

[5] E. H. Rhoderick and R. H. Williams, 'Metal- Semiconductor Contacts', Oxford University Press, (1988).

[6] W. Y. Lee, K. S. Teng and S. P. Wilks, 'In-situ investigation of carbon reduction in 4H-SiC/Ni interface implementing Si interlayer',

International Conference on Silicon Carbide and Related Material 2003 Proceedings, Trans Tech Publications Ltd.

[7] A. Kestle, S. P. Wilks, P. R. Dunstan, M. Pitchard and P. A. Mawby, Electronic Letters, Vol. 6, No. 3 (2000).

[8] J. R. Waldrop and R. W. Grant, Appl. Phys. Lett. **62**, 21 (1993).

Chapter 8

Conclusion

8.1 Conclusion

Over the past decade, the interest in SiC has grown extensively due to its attractive properties. The thermal and electronic properties of SiC have numerous applications for optoelectronics and high power, high frequency and strong radiation devices. The launch of SiC based products such as blue LEDs has indicated the beginning of a new generation of SiC based electronics devices. Yet, the working principle of such devices is rather new in the electronic industry when compared to the well-established Si based devices. The great potential of SiC in these devices applications is challenged by the difficulty of controlling metal contact properties. Hence, a solution to this challenges had to be formulated in order to realise high quality SiC based devices.

In Chapter 1, we have seen the basic requirements of controlling semiconductor-metal contacts. In order to gain a deep insight into development of Ni-semiconductor contacts, a step-by-step review was presented, starting from the well-established Ni-Si contact, to the Ni-SiC contact and to the main theme of this research; the control the metal contact via an introduction of a Si interlayer at the Ni-SiC interface. The review was centred on interface formation mechanism starting from Ni-Si a contact

towards Ni-Si-SiC contacts was discussed. In addition, the problems associated with Ni-SiC contact were also highlighted. The main objective of this work is clearly presented at the final section of the chapter. Several works related to this research theme are also discussed.

The theory of metal-semiconductor contacts studied using various models is presented in Chapter 2. Among the models proposed, the Schottky - Mott [1, 2] model predicts that the Schottky barrier height, ϕ_b, of the metal semiconductor contact is dependant on the work function of the metal, ϕ_m. Meanwhile, several independent studies [3 – 10] have shown that the value of ϕ_b in metal-semiconductor contact can be influenced by other factors such as Fermi level pinning via surface states, chemical reaction, defects at the interface and the electronegativity of the material. The electron transport mechanism across the metal-semiconductor contact was also discussed. The understanding of the theory in metal-semiconductor contact is concluded with Schottky barrier extraction techniques. Here, the two main techniques used throughout this work, current – voltage characteristics and photoelectron spectroscopy, are described. Apart from the understanding the theory of contact formation, it is also important to describe the experimental techniques used in the study. The working principles, theory, practical preparation plus calibration of the equipment used are presented in detail in Chapter 3 and 4.

The main objective of this work is to control and to improve the Ni-SiC contact using a Si interlayer. The study involves the understanding of the problems associated with Ni-SiC contacts in absence of the Si and the effect of the additional Si interlayer (i.e. forming Ni-Si-SiC contact) both chemically and electrically. Hence, the main frame of this work is divided into two sections, the interface study experiment to investigate the chemical properties and the fabrication of the Ni-Si-SiC contacts to gauge the electrical properties.

The first objective of this work was to prepare an atomically clean SiC surface as a starting platform for the Ni-SiC and Ni-Si-SiC contact formation studies. Thus, the first experiment was performed using XPS, LEED and STM

(described in Chapter 5) to achieve this goal. As this work is mainly based on the Si theme, a cleaning technique using a Si overlayer, known as Si evaporation/re-evaporation technique was employed. Here, the 4H-SiC sample is covered with a thin layer of Si after the wet chemical etch and UHV anneals. The deposited Si overlayer is then evaporated immediately giving a surface that consists of only bulk elements. This technique was carefully optimised, with the final optimal Si thickness of 40Å and a re-evaporation time of 7-8 minutes at 1000°C. The cleanliness of the surface produced was analysed and gauged by XPS, LEED and STM, confirming the cleanliness of the surface down to the atomic scale. The investigation was continued with a study on the effect of Si onto SiC. At this stage, the interface formation of Si-SiC junctions was studied in detail with XPS. Here, thin Si overlayers were sequentially deposited onto the atomically clean 4H-SiC sample and the surface was scanned with XPS in between each deposition. The *Si 2p* and *C 1s* core level spectra were recorded. The sample was then annealed sequentially from 250°C to 1050°C for 10 minutes, with the surface again monitored by XPS. The experiment was performed in such a way that every single stage of interface formation is investigated to observe surface chemical reactions and electrical changes by means of core level shifts. The analysis of the XPS data shows that deposition of Si onto the SiC surface resulted in no major chemical reaction but in a different bonding structure depending on the Si overlayer thickness. Thin Si overlayers were seen to bond to the bulk in a structure that follow the 4H-SiC hexagonal structure while thicker coverage exhibited a structure that follows the original zinc-cubic bonding of Si. This result has shown the possibility of controlling the structure and changing the polytypes of SiC via Si overlayers, which could to lead to useful applications in terms of material and solid-state studies. On the other hand, the Si-SiC interface study did not show any major chemical reactions at room or elevated temperatures. Hence, the property of overall Si-SiC structure is thermally stable.

Chapter 6 presents an XPS interface study of the effect of a Si interlayer in Ni-SiC contacts (i.e. forming Ni-Si-SiC contact) with three different thickness of Si interlayer (20Å, 40Å and 60Å). The core level analysis shows that with the presence of a Si interlayer, the products of the interface reactions consist of Ni silicides, a ternary compound of Ni-Si-C and a small amount of free C. The quantities of these reaction products are seen to be dependent on the thickness of the Si interlayer. Thicker Si interlayer produces a larger amount of silicides, free C and also the ternary compound (as described in Chapter 6). In addition, the analysis of the core level binding energy shows both Fermi shifts and chemical shifts. The chemical shifts are caused by the formation of silicide and the ternary compound. The Fermi shifts show upward surface band bending, indicating the formation of a barrier at the interface. The amount of upward band bending was found to depend on the Si interlayer thickness (0.5eV for 20Å and 0.3eV for 40Å and 60Å). The absolute value of the surface barrier cannot however be determined, as the initial (before deposition of Si and Ni) barrier at the surface is not known.

When annealed, the Ni-Si-SiC interface shows similar reactions but again they are seen to be dependent on the thickness of the Si interlayer. At low temperature, silicide enhancement is observed for all Ni-Si-SiC contacts. The formation of silicides is also observed to simultaneously consume Si from the Si interlayer and also from the bulk SiC. At temperatures above 600°C, interdiffusion between silicides and bulk SiC is observed. Until 800°C, it is likely that re-evaporation of silicides has occurred due to such a high temperature. The *C 1s* core level remained stable up 1000°C, consisting of only bulk C and a small of free C. Among the contacts, the 20Å contact exhibits the lowest quantity of free C at the interface, followed by the 60Å and finally the 40Å contacts. However, at 1200°C a huge amount of free C and graphite is observed as a result of Si depletion (re-evaporation of Si and silicides) for all thickness. Core level shifts towards high binding energy were

also observed, which indicates downward band bending. Again, this band bending is dependent on the thickness of the Si interlayer. Here, the 20Å contact shifts the most with –0.6eV, followed by 40Å and 60Å contacts with -0.55eV and –0.4eV respectively.

The investigation would not be complete without testing the electrical performances of the Ni-Si-SiC contacts. To this purpose, diodes are fabricated using the same interface composition as for the XPS (Ni-Si-SiC contacts with 20Å, 40Å and 60Å Si interlayer). These contacts were characterised using I-V measurement. The results obtained are presented in Chapter 7. From the I-V characteristics, again the thickness of the Si interlayer has a great influence on the performance of the diodes. With a thin Si interlayer (20Å and 40Å), the contacts exhibit a good Schottky behaviour at 600°C with ϕ_b of 1.7 and 1.5 and ideality factors of 1.7 and 3.2 for the 20Å and 40Å respectively. At 40Å, the contact still exhibits a rectifying behaviour up to a temperature of 800°C, 100°C higher than the 20Å case and 400°C higher than the contact without Si interlayer. On the other hand, the contact with the thickest Si interlayer (60Å) exhibits a constant Ohmic behaviour regardless of the annealing temperature.

The investigation on the effect of a Si interlayer presented in this thesis has resulted in significant advances in SiC technology. Firstly, a cleaning technique based on Si has been successfully established, which effectively produced an atomically clean surface [13]. Then, the Si interlayer reduced the free C content at the interface and the Ni-SiC surface dramatically up to temperature of 1000°C [11, 12]. In terms of device performance, the results from the Schottky diodes shows that the Si interlayer can be used to control the overall behaviour of the contact. The operating temperature or the breakdown temperature of the diode can be controlled by increasing the thickness of the Si interlayer. Finally, the contact can also made to be Ohmic via a thick Si interlayer, and this Ohmic behaviour remains stable up to 1000°C. In terms of overall performance, the 20Å thickness shows the best result, with the least amount of free C and the best ideality factor in diode

performance. However, the other two cases also displayed unique characteristics. The 40Å composition had shown the largest amount of free C, but when fabricated into a diode, the rectifying properties of the contact are seen to remain up to 800°C. Finally, the 60Å composition shows a moderate amount of free C at the interface but gives stable Ohmic properties up 1000°C even without annealing.

The ultimate goal of this work was achieved and showed the remarkable effectiveness of a Si interlayer in controlling Ni-SiC contacts. The investigation on the role of Si interlayer in the control of metal-SiC contacts can be extended by imaging the crystalline structure during the formation and annealing of the interface via Scanning Tunnelling Microscopy (STM) and Scanning Tunnelling Spectroscopy (STS). In contrast to XPS, STM/STS allows imaging of the crystalline structure of the interface at the atomic scale and also allows simultaneous current-voltage measurements. Therefore, electrical properties and topographical information such as defects and growth mode of the overlayers can be obtained and can be compared to those obtained from XPS and I-V measurements. In addition, the role of the Si interlayer can be extended in other metal-based SiC contacts such as tungsten (W) and titanium (Ti). The discovery of such useful Si interlayer-based theme in metal-SiC contacts would make a great impact in SiC technology. It is envisaged that this Si interlayer theme could enhance existing SiC based devices, which could lead to the production of devices with high reliability and performance especially at high temperature.

8.2 References

[1] W. Schottky, Naturwissenschaften, **26**, 843 (1938).

[2] N. F. Mott, Proc. Cambr. Phil. Soc., **34**, 568 (1938).

[3] J. Bardeen, Phys. Rev. Lett., **71**, 717-727 (1947).

[4] V. Heine, Phys. Rev., **A138**, 1689, (1965).

[5] W. E. Spicer, I. Lindau, P. Skeath and C. Y. Su, J. Vac. Tech., **17**, 1019, (1980).

[6] W. E. Spicer, I. Lindau, P. Skeath, C. Y. Su and P. W. Chye, Phys. Rev. Lett.,**44**, 420, (1980).

[7] K. N. Tu, J. W. Mayer and L. C. Feldman, 'Electronic Thin Film Science for Electrical Engineers and Materials Scientist', Macmillan Publishing Company, (1992).

[8] J. L. Freeouf and J. M. Woodall, J. Vac. Sci. Tech., **21**, 574 (1982).

[9] L. J. Brillson, C. F. Brucker, A. D. Katnani, N. G. Stoffel, R. Daniels and G. Margaritondo, J. Vac. Sci. Tech., **21**, 564 (1982).

[10] L. N. Pauling, 'The nature of the chemical bond', 2nd edition, Cornell University Press, Ithaca, New York (1960).

[11] W. Y. Lee and S. P. Wilks, 'In-situ investigation of the effect of Si interlayer in 4H-SiC-Nickel contact', Condensed Matter and Materials Physics 2002 conference, Europhysics Conference Abstracts Vol. 26A.

[12] W. Y. Lee, K. S. Teng and S. P. Wilks, 'In-situ investigation of carbon reduction in 4H-SiC/Ni interface implementing Si interlayer', International Conference on Silicon Carbide and Related Material 2003 Proceedings, Trans Tech Publications Ltd.

[13] W. Y. Lee, K. S. Teng, T. G. G. Maffeis and S. P. Wilks, 'The chemical, structural and electronic nature of atomically clean 4H-SiC surfaces: An XPS, LEED and STM/STS study', 13th Interdisciplinary Surface Science Conference 2001.